Université du Québec
Institut national de la recherche scientifique
Energie Materiaus télécommunications

ANTENNES AUX ONDES MILLIMÉTRIQUES AVEC FAISCEAU INCLINÉ EN UTILISANT DES STRUCTURES MÉTAMATÉRIAUX

Par:

Abdolmehdi Dadgarpour

Proposition du jury d'évaluation

Directeur de recherche :	Prof. Tayeb A. Denidni INRS-EMT
Examinateur interne et président du jury :	Prof. Serioja Tatu INRS-EMT
Examinateur externe :	Prof.Ahmed A.Kishk Concordia University
Examinateur externe :	Prof. Jean-Jacques.Laurin École Polytechnique de Montréal

Université du Québec
Institut national de la recherche scientifique
Energie Materiaus télécommunications

MILLIMETER-WAVE ANTENNA WITH BEAM-TILTING CAPABILITY USING METAMATERIALS

By:

Abdolmehdi Dadgarpour

A dissertation Submitted in partial fulfillment of the requirements for the degree of Doctor of Philosophy (Ph.D) in Telecommunications

Evaluation Jury

Research Director	Prof. Tayeb A. Denidni INRS-EMT
Internal examiner and Jury	Prof. Serioja Tatu INRS-EMT
External examiner	Prof.Ahmed A.Kishk Concordia University
External examiner	Prof. Jean-Jacques.Laurin École Polytechnique de Montréal

Dedication

This thesis is dedicated to my wife Naeemeh

TABLE OF CONTENTS

LIST OF TABLES

LIST OF FIGURES

ABSTRACT

The ISM frequency band at 60 GHz (57-64 GHz) has attracted much attention for its large frequency bandwidth (7 GHz). This band enables multi Gb/s data rate transmission and enhanced immunity as well as frequency re-use. However, due to the atmospheric absorption loss at this band the propagated signal degrades considerably. This issue can

be compensated by using high-gain antennas. Beam alignment is another challenge for high gain antennas where the location of transmitter or receiver is not fixed. This is due to narrow beamwidth of such antennas. The solution to resolve this issue is using beam switching or beam scanning networks such as phased antenna arrays. Existing beamforming systems based on phased antenna array incur large loss and are complex to implement in practice rendering them high-cost solution. An alternate solution proposed in this thesis is to realize beam tilting using metamaterials to minimize the loss and cost issues as well as obtain a low-profile structure.

In this dissertation, first and foremost, an array of meander line H-shaped resonators, which operate as an anisotropic metasurface at C-band, were integrated in front of a standard bow-tie antenna in order to tilt the direction of the antenna's main beam in the azimuth plane. In order to tilt the antenna's radiation beam in the elevation plane an array of inhomogeneous split-ring resonators are embedded in the H-plane of end-fire bow-tie antenna. The proposed designs are shown to provide a viable solution for next generation of base-station antennas that need to be capable of tilting the direction of the main beam under the horizon. This particularly includes 5G wireless cellular networks envisaged to operate at millimeter-waves. The proposed technique is also applicable at C-band (7-8 GHz) and WiMAX band (3.4-3.6 GHz).

The high-gain antenna proposed here for operation at millimeter-wave (57-64 GHz) is based on a bow-tie configuration which is fed by surface integrated waveguide (SIW). The technique proposed here to increase the antenna gain involves (i) embedding a split-ring resonator at the back side of bow-tie antenna, (ii) tilting the bow-tie radiators with respect to the end-fire direction, and (iii) integrating an array of folded H-shaped resonators to create a region of low refractive index in front of the bow-tie radiator in order to convert the antenna's spherical waves into planar waves. The measured results indicate that the antenna gain improves to 12 dBi over 57-64 GHz.

Another technique demonstrated here to deflect the main beam of a standard dipole antenna involves incorporating in the azimuth plane of the antenna a media with gradient index of refraction. This technique enables beam switching from -58 to +58 degrees over 57-64 GHz with maximum gain of 9.5 dBi at 60 GHz.

In order to obtain beam steering in the Elevation plane, the proposed folded H-shaped resonators are loaded in the E and H-plane of dipole. This arrangement is shown to provide two-dimensional beam tilting or beam switching at 60 GHz. However with this approach, the antenna gain is limited to 10 dBi and the beam deflection is limited to 17 degrees in both planes.

To achieve a higher gain and tilt angle an array of split-ring resonators (SRR) were integrated in front of a quasi TE-source generated by a dipole antenna at 60 GHz. The magnetic resonance of the SRRs result in a tilt angle of 34 degrees in both the azimuth and elevation planes with maximum peak realized gain of 14 dBi over 57-64 GHz.

Finally, to achieve a dual beam and broad beamwidth radiation in the azimuth plane of end-fire bow-tie antenna an array of stub-loaded H-shape resonators were integrated in front of the antenna. The measured results show beam deflection at +30 and -30 degrees with respect to the end-fire direction with the maximum peak realized gain of 9 dBi at 60 GHz.

ACKNOWLEDGMENTS

First of all, I sincerely wish to thank my supervisor Prof. Tayeb A.Denidni, who gave me the opportunity to join his group, and let me work on different projects. It was a real pleasure to for me to have such an exceptional scholar and it was my honor to be his PhD student.

Furthermore, I would like to thank my committee members, Prof.Tatu, Prof.Kishk,and Prof.Laurin for their review of my dissertation and their numerous constructive comments and feedback.

Finally, I want to thank my wife Naeemeh for her love and support, during this period of time.

Chapter 1 **INTRODUCTION**

1.1 Background and Motivation

With rapid development in wireless communication systems such as mobile communications, which is omnipresent everywhere in our daily life, a huge amount of information is accessible with high speed near the speed of light. Antenna is the key component of wireless technology which is utilized for different applications enabling high data rate transmission, point-to-point and mobile cellular communications.

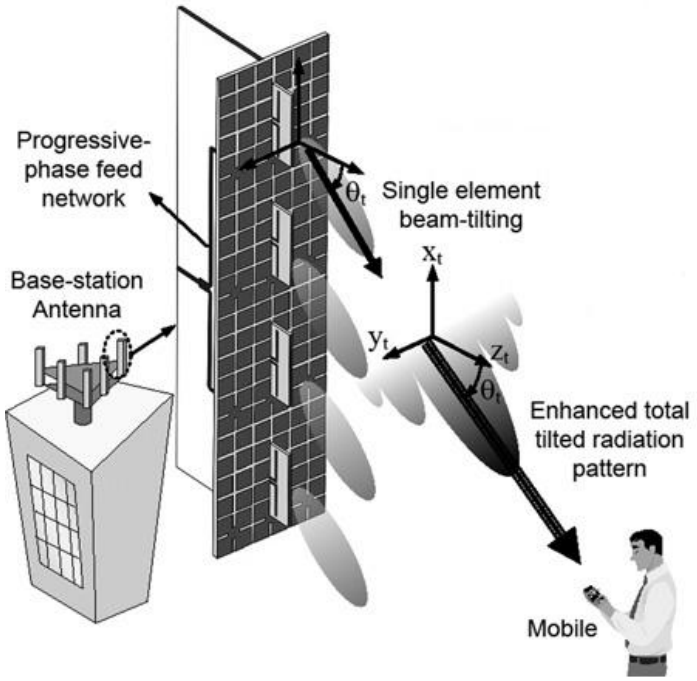

Figure 1-1: Configuration of the base-station antenna which is integrated by 1x4 EBG dipole antenna arrays to obtain a down tilt under horizon to cover the cell [1].

Antennas mounted on the base-stations normally consist of three or four antenna arrays that are arranged to project the main beam under the horizon to realize a small cell, as shown in Fig.1.1. This is necessary to improve the channel capacity and increase the coverage. In addition, this technique confines the power within the cell and therefore

minimizes adjacent channel interference. The radiation from the antenna can be tilted either by mechanical or electronic means. Mechanical tilting involves physically changing the position of the antenna element whereas electronic tilting can be achieved by using phased antenna arrays. One approach used to tilt the direction of the main beam electronically involves integrating a phase shifter, which can be designed using RF MEMS and PIN diodes, into the antenna element and change progressively the phase of each element so as to steer the main beam radiation into the pre-defined direction. Although, with this approach the radiation beam can be tilted at the desired angle, the gain of the antenna is severely degraded since the 3 dB beamwidth of the single radiating element is not broad enough to follow the overall radiation beam emanating from the array. The other drawback of electronic beam steering is the limited scan angle. Although the mechanical beam tilting option provides a fixed angle beam with no degradation in the antenna gain, however installation and implementation of the mechanical approach over the electronic approach in base-stations is very costly. To deal with this issue, an alternative method is suggested in this thesis that involves using metamaterials shown in Fig.1.2. Metamaterials are engineered structures which show exotic properties from microwave to optical frequencies that do not exist in nature. In fact, metamaterials are essentially periodic metallic structures on dielectric media whose periodicity is smaller than the Bloch wavelength. In other words, the composite structure is designed to interact with electromagnetic waves to exhibit a negative permittivity, permeability and index of refraction.

Metamaterials can be referred to as left-handed material (LHM) or negative index of refraction (NRI). The feasibility of this concept was first demonstrated by Smith et al. in 2001 by amalgamating parallel arrangement of wires, which act as electric resonators, with split-ring resonators (SRR), which act as magnetic resonators, as shown in Fig.1-2 to form a double negative permittivity and permeability. The main issue related to LHM is its narrowband and large loss which restrict its applications. It has been shown that the definition of metamaterial extends to materials with zero or low refractive index as well as high refractive index medium.

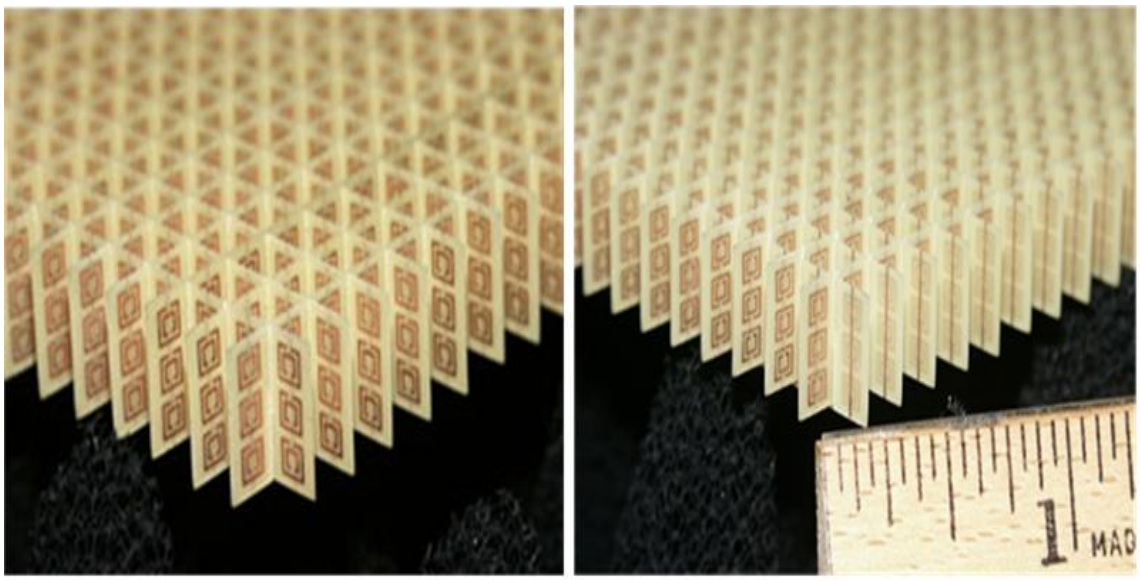

Figure 1-2: Homogenous metamaterial unit-cell comprised of DSR and wire as a double negative metamaterial region [2]

A great deal of work has been carried out to deploy metamaterials for beamforming applications. Metamaterials with negative index of refraction mostly find application in leaky wave antennas (LWAs) enabling wave propagation[3] in the structure backward, forward and broadside as shown in Fig.1.3. The peak of the radiation beam in this antenna structure however is affected by the frequency which restricts its application to fixed beam applications. A viable technique to obtain beam steering is to use tunable refractive index media implemented as a multilayer slab, where each slab consists of sub-wavelength electric resonators whose properties are controlled with varactor diodes, as shown in Fig.1.4. The purpose of varactor diode is to provide different phase shifts required for steering the incident wave into the desired angle. This structure is considered to be too bulky, large and expensive for practical purposes. Furthermore, the gain of this antenna severally drops when the beam is scanned from 0 to 30 degrees [4].

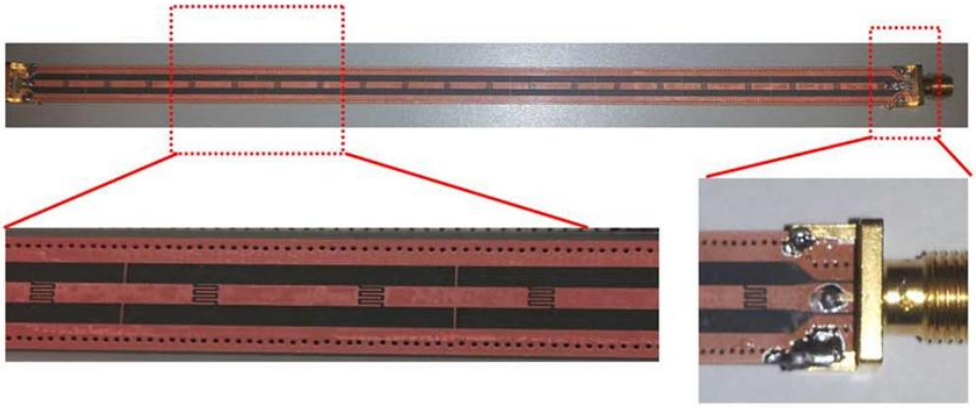

Figure 1-3: Leaky wave antenna realized by left handed metamaterial unit-cells [3]

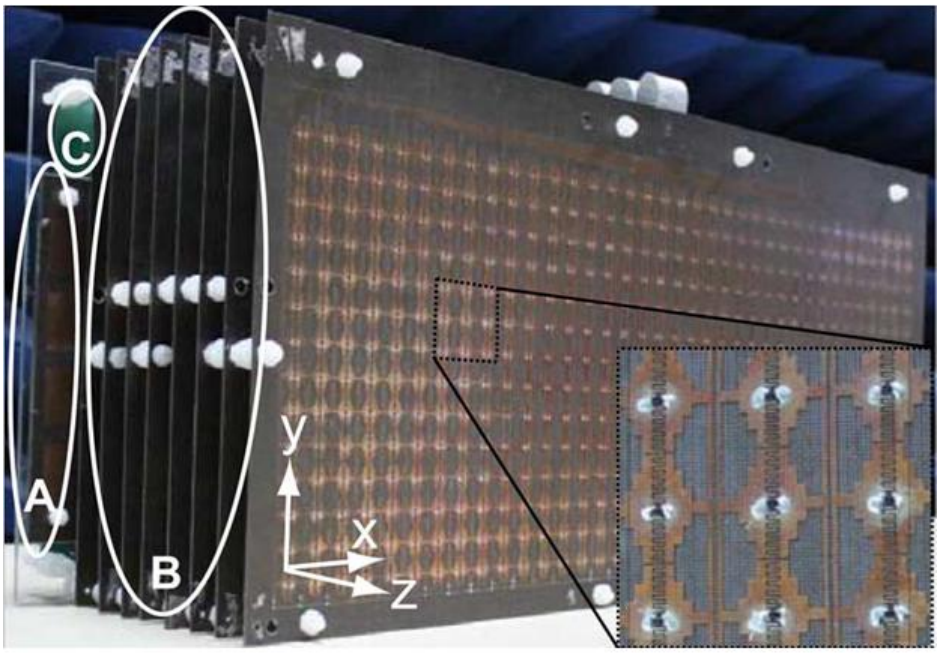

Figure 1-4: Electric resonance metamaterial unit-cell integrated by varator diode for beam steering applications [4].

The millimeter-wave frequency bandwidth is recognized to extend from 30-300 GHz with a corresponding wavelength of 10-1 mm wavelength. Recently, work at 60 GHz frequency band has attracted considerable attention for its large bandwidth from 57-64 GHz, which can enable wireless data transmission in excess of 1.5 gigabit per second for high definition video transfer, and high resolution imaging application. However, at this frequency the electromagnetic wave is absorbed greatly by oxygen molecules and hence the path loss is high (10–16 dB/km). To overcome this issue requires the use of a high-gain antenna which has the added benefit of minimizing channel distortion caused by multipath effects. Therefore directive antenna is a good candidate for the line-of-sight applications at 60 GHz. As the position of the receiver is not known precisely beam alignment between transmitter and receiver is another challenging requirement.

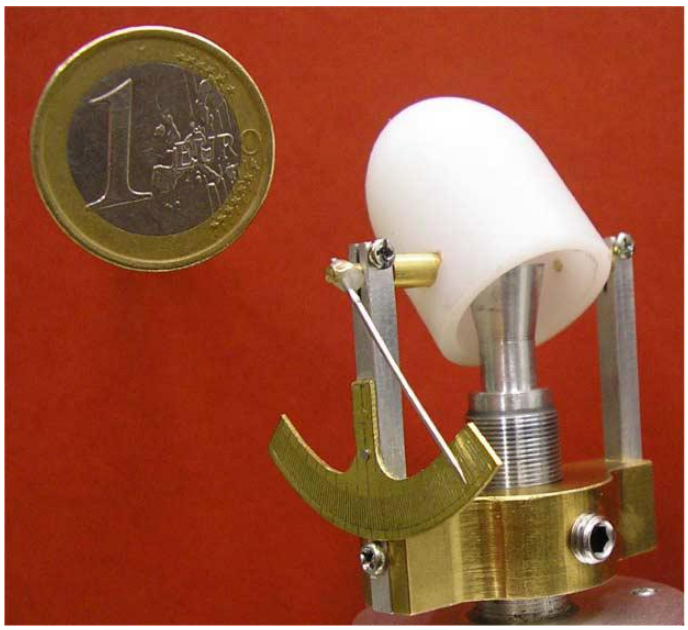

Figure 1-5: Dielectric lens antenna integrated by horn antenna for mechanically beam tilting at 60 GHz [5].

To deal with the latter issue, a steerable antenna is proposed here. A great deal of work has been carried out in this research to steer the direction of the radiation beam from an antenna at millimeter-wave. It is well known that phased antenna array or adaptive antenna array is a suitable technique for steering the beam, which enables sufficiently high signal-to-noise ratio to be established at the receiver. The deployment of phase antenna array requires the integration of many phase shifters, which introduces large loss in the system and is an expensive solution. Reconfigurable reflect array is another technique to scan the beam in both azimuth and elevation planes. This technique requires the integration of a large number of active elements such as PIN diodes in the antenna, which also makes it an expensive solution. Dielectric lens antenna, shown in Fig.1.5, is another technique for beam steering demonstrated at millimeter-wave frequencies [5]. These kinds of beam steering structures are bulky and appropriate for radar imaging systems.

1.2 **Dissertation Outline**

The dissertation is divided into 9 chapters with the abstract, publication list, and the reference. The contents of the dissertation charters are listed below. The main objective of the research was to develop a low-profile, low cost antenna which has the functionality to tilt the direction of the main beam in the azimuth and elevation planes without severely affecting its performance. For this purpose, an end-fire type of antenna was selected, in particular a classical dipole antenna which was a bow-tie antenna. The direction of radiation beam from the bow-tie antenna was steered in the E- and H-planes by integrating metamaterial or metasurface media, which were created with microstrip unit-cells.

- Chapter 2 presents a technique to re-direct the radiation beam from a planar antenna in a specific direction with the inclusion of metamaterial loading. The beam-tilting approach described here uses the phenomenon based on phase change resulting from an EM wave entering a medium of different refractive

index. The metamaterial H-shaped unit-cell structure is configured to provide a high refractive index which was used to implement beam tilting in a bow-tie antenna. The fabricated unit-cell was first characterized by measuring its S-parameters. Hence, a two dimensional array was constructed using the proposed unit-cell to create a region of high refractive index which was implemented in the vicinity bow-tie structure to realize beam-tilting. The simulation and experimental results show that the main beam of the antenna in the E-plane is tilted by 17 degrees with respect to the end-fire direction at 7.3, 7.5, and 7.7 GHz. Results also show unlike the conventional beam-tilting antennas, no gain drop is observed when the beam is tilted; in fact ,there is a gain enhancement of 2.73 dB compared to the original bow-tie antenna at 7.5 GHz. The reflection-coefficient of the antenna remains < -10 dB in the frequency range of operation.

- Chapter 3 presents a meta-surface implemented with magnetic resonance created with split-ring resonator unit-cells are used to realize wideband beam-tilting in an end-fire antenna. The end-fire antenna has rounded bow-tie configuration for wideband operation over 3.5–8 GHz. The antenna is integrated with 8×6 array of magnetic resonance unit-cells that are located off-axis in front of the bow-tie antenna in the azimuth plane. The interaction of the radiation beam with the meta-surface causes the direction of the radiation beam to be tilted in the E-plane. Measured results of the fabricated prototype antenna show the direction of the main beam in the E-plane is tilted by 12 and 21 degrees at 5.4 and 7.2 GHz, respectively, with respects to the end-fire direction. In addition, the antenna exhibits gain enhancement of about 5 dBi at 7.2 GHz compared to conventional rounded bow-tie antenna with no meta-surface.
- Chapter 4 describes a simple and effective beam tilting technique for planar end-fire antennas using an artificial dielectric layer. The proposed approach is based on the phase differential resulting from a high refractive-index medium that is achieved by using double G-shaped resonators (DGR) in a 5×4 array. The array is oriented normal to the direction of the main beam emanating from the antenna. To demonstrate the principle, the technique is applied to a Bow-tie antenna, which is

designed at the WiMAX frequency band (3.4–3.6 GHz). The antenna performance was verified practically, and the measured results confirm that the direction of the antenna's maximum beam can be refracted by 35^{o} in the H-plane, which is larger than conventional techniques. In addition, a maximum gain enhancement of 5 dB is achieved when the beam is tilted. Reflection-coefficient of the proposed structure is maintained better than -10 dB across its operational band.

- Chapter 5 presents a high gain bow-tie antenna that operates across 57 GHz–64 GHz for application in high data rate point-to-point communication systems. The proposed antenna consists of a pair of bow-tie radiators, where each radiator is etched on the opposite side of the common dielectric substrate and fed through substrate integrated waveguide (SIW) feed-line. The bow-tie radiators are arranged to cross each other symmetrically by tilting the feed-lines by 30 degrees in order to enhance the antenna gain and to obtain the required radiation pattern. The antenna is loaded with a pair of double G-shaped resonators (DGR) that are located in a region between the radiators and SIW in order to suppress the back-lobe level in the H-plane. Embedded in the E-plane of the antenna is an array of zero-index metamaterial (ZIM) unit-cells whose purpose is to effectively confine the electromagnetic waves in the end-fire direction in order to enhance its gain performance. A prototype antenna was fabricated and its performance was measured to validate the simulation results. The proposed structure exhibits a gain of 11.8–12.5 dBi over the frequency range of 57 GHz–64 GHz with reflection-coefficient less than -11 dB. In addition, the proposed antenna exhibits good cross-polarization which is less than -17 dB in both E- and H-planes at 60 GHz.
- Chapter 6 describes a beam tilting technique for planar dipole antennas utilizing gradient refractive-index metamaterial (GRIM) unit-cells. The beam deflection mechanism is based on the phase shift phenomena resulting from the interaction of the EM waves with media of different refractive-indices implemented using GRIM unit-cells. The GRIM unit-cell comprises of a stub loaded I-shaped resonant structure that is directly integrated onto the dipole antenna. The simulation and experimental results show that an antenna with a 5×4 array of

GRIM unit-cells can steer the main beam in the E-plane by +26^{o} with respect to the end-fire direction over 57–64 GHz. The antenna exhibits 4 dB gain enhancement and S_{11} better than -10 dB from 57–64 GHz. It is also shown that a quad-feed dipole antenna with GRIM arrays can deflect the beam by ±56^{o}.

- Chapter 7 demonstrates elevation-plane beam tilting for a printed dipole antenna operating over 57–64 GHz. This is achieved using a 3×4 array of high refractive-index metamaterial (HRIM) unit-cells. The unit-cell comprises a modified H-shaped structure with stub loading to control the refractive-index of the unit-cell over a finite frequency range. Integration of the 3×4 array in the H-plane of a dipole antenna is shown to deflect the main beam by +30 degrees with respect to the end-fire direction over 57–64 GHz. In addition, the proposed technique provides 5 dB gain enhancement.
- Chapter 8 presents 1D and 2D-beamforming for a planar dipole antenna operating at millimeter-wave bands. 1D-beamforming was achieved by using mu-near-zero (MNZ) metamaterial slabs that were integrated in the dipole antenna, where each slab was loaded with an array of low refractive-index unit-cells. The resulting radiated beam can be scanned by 34 degrees due to the phase shift in the beam introduced by its interaction with the metamaterial slabs. In addition, the proposed antenna configuration provides gain improvement of 8 dB as the slabs effectively increase the aperture size of the antenna. An array of MNZ inclusions in the E-plane of a double dipole antenna is shown to provide scanning from -34 to +34 degrees with respect to the end-fire direction over 57-64 GHz. 2D-beam scanning was realized by increasing the number of MNZ unit-cells in the elevation plane of double dipole antenna. Loading the slabs in front of the double dipole antenna with 7×10 array of MNZ unit-cells are shown to provide a beam deflection of 34 degrees in the azimuth and elevation planes.
- Chapter 9 presents a technique to generate dual-beam radiation in the E-plane of a printed bow-tie antenna operating over 57–64 GHz. This is achieved by artificially modifying the dielectric constant of the antenna substrate using arrays of metamaterial inclusions realized using stub-loaded H-shaped unit-cells to provide a high index of refraction. The metamaterial inclusions are tilted with

respect to the axis of the antenna and embedded in the direction of the end-fire radiation. The resulting dual-beam radiation in the E-plane has maxima at +60 and 120 degrees with respect to the end-fire direction (90 degrees) with a maximum peak gain of 9 dBi at 60 GHz.

- Chapter 10 concludes the dissertation. The future work in the proposed research area is included in this chapter.

Chapter 2 BEAM TITLTING ANTENNA USING METAMATERIAL LOADING

2.1 Introduction

Adaptive antennas with reconfigurable pattern have been extensively deployed in the wireless communication systems in order to improve the transmission quality and increase the channel capacity. In fact base stations of wireless communication systems comprise of antenna arrays that are mounted on towers and high buildings which makes it necessary for the antenna to have main beam titling below the horizon. Main beam titling can be accomplished either electronically or mechanically. Electronic beam steering techniques use agile elements such as electronically controlled transmission-lines [6], varactor diodes [7] and RF micro-electromechanical (MEMS) switches [8]. Unfortunately, these techniques suffer from a noticeable gain drop when the beam is tilted. Although the mechanical beam tilting approach [9] shows a better performance at higher tilt angles, however it requires a complicated mechanical installation framework that increases the system size as well as its weight. Another promising technique reported in [10] achieves beam steering by pivoting an appropriately shaped dielectric substrate in front of a single fixed feed.

In this case a dielectric substrate is shaped in the form of an elliptical lens that is placed over the antenna to tilt the main beam towards a certain direction. The main disadvantage of this technique is that the dielectric lens is large and bulky. Leaky-wave antennas are also employed for beam tilting applications. Recently, a beam scanning leaky-wave slot antenna using a composite right/left-handed (CRLH) technique was reported in [11]. The antenna has a beam scanning angle between -31^{o} to $+52^{o}$ in the frequency range from 9.5 to 12.4 GHz. However, the tilt angle is a function of the frequency which restricts the application of the antenna. Another drawback of this antenna is its bulky structure resulting from the three-dimensional waveguide framework.

Recently, metamaterials have attracted considerable attention in the light of their unique properties and unprecedented applications in changing the effective properties of materials. Metamaterials have been applied in different antenna applications to realize

e.g. bandwidth enhancement, beam focusing, gain enhancement, and polarization efficiency [12-13].

In this paper, we propose a new solution for beam-tilting applications, in which an integrated metamaterial loading (IML) is implemented directly onto the antenna. This integrated metamaterial loading results in no impact on the antenna's profile, and exhibits necessary refractive index to re-direct its beam.

In the following sections, we first describe the proposed H-shaped metamaterial unit-cell structure, and extract its characterizing parameters. Then a 2D array of the unit-cell is applied to the bow-tie antenna. Finally, the tilting effect of IML on the antenna's main beam is investigated. To validate the results, a prototype of the new IML structure was fabricated, and its S-parameters are measured using a modified version of the free space measurement (FSM) method described in [14]. Then, the characterizing parameters of the media are extracted using a well-known algorithm described in [15]. Finally, two bow-tie antennas with and without the IML structure are fabricated and their return-loss and radiation patterns measurements are presented. The unit-cell's refractive-index is verified over the antenna's operating frequency range. The measured results show the main beam of the antenna is tilted by 17 degrees in the E-plane, i.e. towards the direction of the metamaterial inclusion. The results also show unlike conventional tilted-beam antennas, there is no gain drop when the beam is tilted. In fact, there is a 2.73 dB increase in the gain of the antenna at 7.5GHz.

2.1.1 Beam Tilting Mechanism

The mechanism of beam-tilting involving two layered media that are deployed in the antenna is explained in this section. This approach was used to develop a low-profile antenna with a tilted main beam. In Fig.2.1 an electromagnetic (EM) point source is placed in the vicinity of a two-layered medium with two different refractive indexes. The EM wave that exits in each layer undergoes a different phase shift. The scenario depicted in Fig.2.1 is analogous to a two-element antenna array with a phase shift of β between the elements, which is given by:

$$\beta = k_o(n_2 - n_1)d \qquad (1)$$

The relation between β and the radiation angle φ, which is derived from the antenna theory [16], is given by:

$$\beta = k_o l sin\varphi \qquad (2)$$

Therefore, from Eqns. (1) and (2) the tilt angle is given by:

$$\varphi = sin^{-1}\left[\frac{d(n_2 - n_1)}{l}\right] \qquad (3)$$

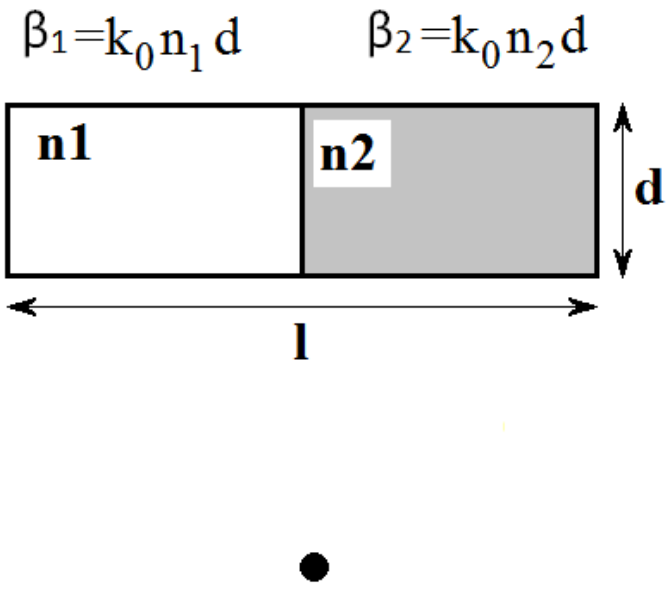

Figure 2-1: Mechanism of beam tilting using two layered dielectric media.

According to Eqn.(3) the tilt angle of the beam is determined by the difference in the refractive index of the two media and its dimensions. As we intend to use this technique for an end-fire planar bow-tie antenna, the above two layered media needs to be located on the substrate of the antenna. The best solution for changing the refractive index of a limited region of the antenna's substrate was to load the antenna with a suitably designed

metamaterial unit-cell. The unit-cell had to (1) provide a high refractive index compared to the substrate, and (2) could be directly integrated onto the dielectric substrate without affecting the antenna's profile. The next section describes the unit-cell structure and its characterizing parameters, which were validated with measured results.

2.1.2 Metamaterial Unit-cell

The proposed metamaterial unit-cell structure, shown in Fig.2.2, is in fact a modified version of the H-shaped resonator reported in [17]. The difference between the H-shaped resonator and the unit-cell presented here is that the structure includes meandered lines and whose thickness has been modified to realize a higher refractive index. This structure was chosen because it can be easily integrated within the planar bow-tie antenna. The geometry of the antenna determines the polarization of the EM wave which is along the x-direction; it was therefore necessary to design an electric resonator so as to take advantage of the unit-cells' resonance.

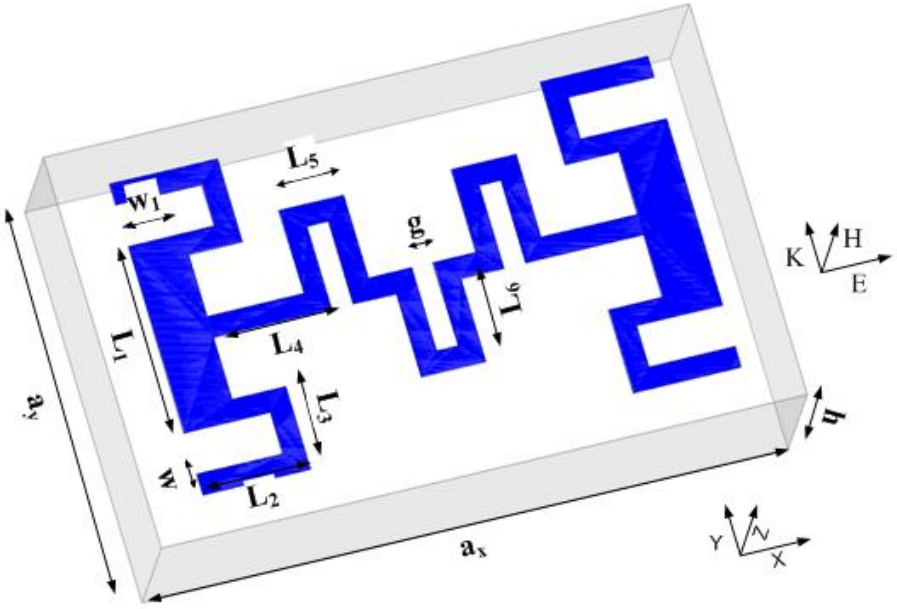

Figure 2-2: Geometry of the proposed unit-cell implemented on a dielectric substrate.

The H-shaped meandered line structure was fabricated on a Rogers RT5880 substrate with the thickness of h=1.575 mm, permittivity of 2.2, and loss-tangent of 0.0009. The dimensions of the unit-cell structure are: a_x=6 mm, a_y=3.77 mm, w=0.2 mm, w_1=0.5 mm, L_1=1.8 mm, L_2=1 mm, L_3=0.8 mm, L_4=1.1 mm, L_5=0.6 mm, L_6=0.8 mm, g=0.2 mm.

The unit-cell was simulated using HFSS with PEC and PMC boundary conditions applied to yz and xy-planes, and the two ports were located in Y-direction. S-parameters S_{11} and S_{12} of the unit-cell structure were simulated, and its characterizing parameters were extracted using the algorithm described in [15]. To validate the simulated S-parameters, the measurement setup in Fig. 3 was used. In this setup, which is a modified version of the free space measurement (FSM) method in [14], a box was designed to contain a 30×35 array of the unit-cell, as well as two standard horns acting as transmitter and receiver antennas. Fig.2.3 shows a photo of the fabricated array of the proposed unit-cell.

Figure 2-3: Measurement setup for acquiring the S-parameters of the unit-cell array.

The simulated and measured S-parameters of the unit-cell are shown in Fig.2.4 (a) and (b). These results were used to extract the array's effective relative permittivity, permeability and refractive-index.

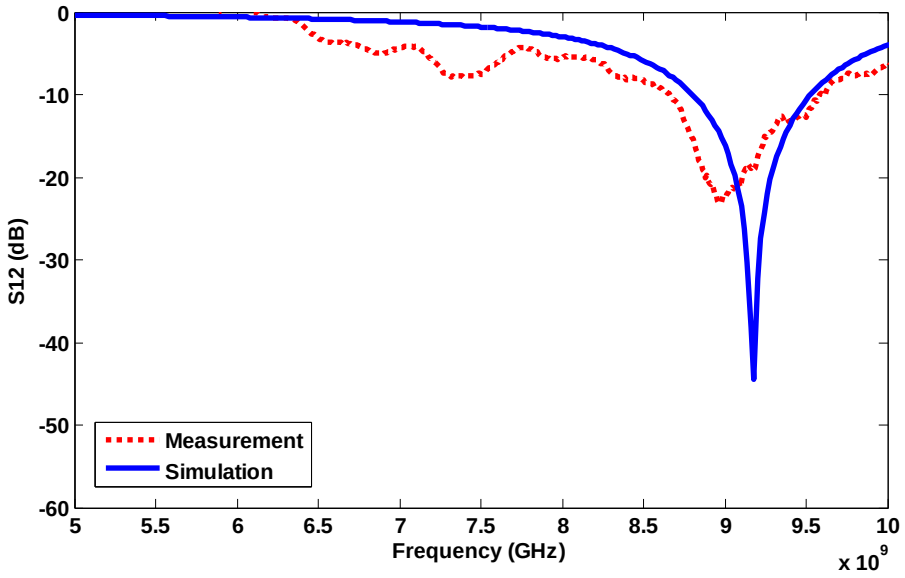

(a)

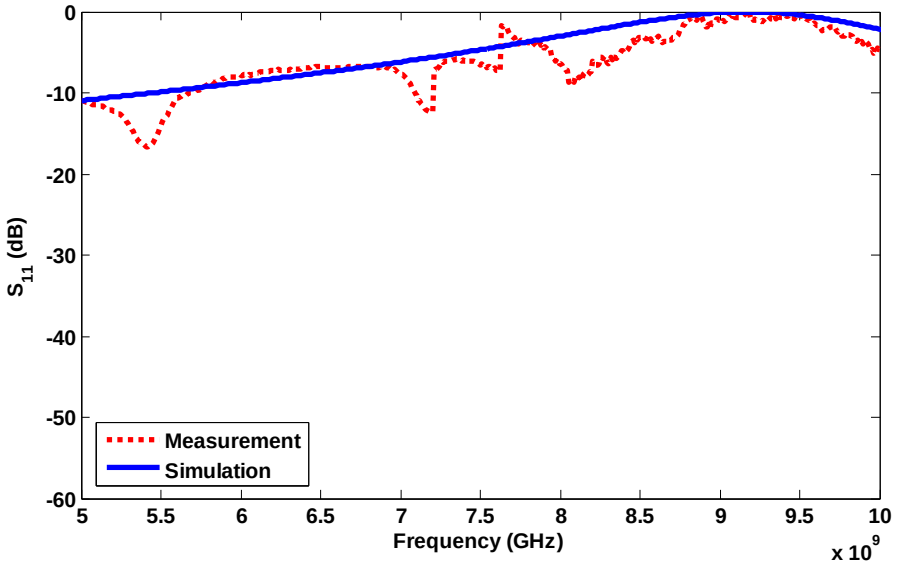

(b)

Figure 2-4: The S-parameters of proposed unit-cell structure.

Fig.2.5 shows the extracted aforementioned parameters from the measurement results. The results show the unit-cell has a high permittivity (epsilon) and low permeability (mu) behavior across the frequency range 7-8 GHz, while the magnitude of the refractive-index varies between 2.1 and 2.4.

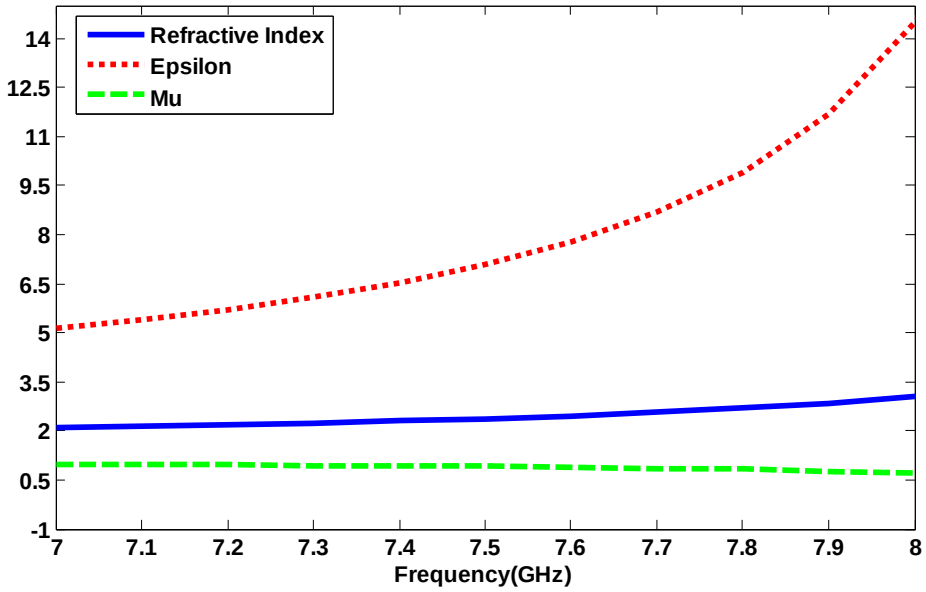

Figure 2-5: Retrieved parameters (n, ε, and μ) of meandered-line H-shape unit-cell.

The actual substrate's refractive index n_{sub} is 1.6. By applying the metamaterial unit-cell we have effectively increased the refractive index for a portion of the substrate. The proposed meandered line H-shaped unit-cell is compact in size as well as exhibits a relatively high refractive index compared to the substrate over a wideband operating range compared to its H- shaped counterpart in [17]. Fig. 6 compares the meandered line unit-cell to its equivalent H-shaped resonator.

Fig.2.6 shows the frequency of the permittivity spike shifts from 11.2 GHz to 8 GHz, which corresponds to a miniaturization factor of 0.7 for the proposed unit-cell structure compared to the conventional H-shaped resonator in [17]. Also across the frequency range of 7-8 GHz, which is the operating range of the antenna, we can see that the effective permittivity of the structure is about 7.5, which is nearly twice as higher than the effective permittivity of the conventional H-shaped structure.

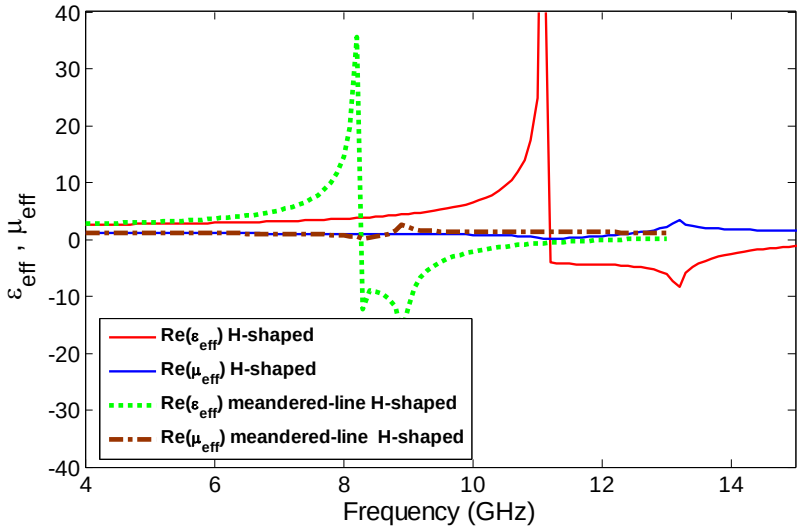

Figure 2-6: The extracted permittivity and permeability of the H-shaped and proposed meandered-line unit-cell.

2.1.3 BOW TIE ANTENNA WITH IML

Fig.2.7 depicts the layout of the proposed antenna with metamaterial unit-cells integrated on the same substrate.

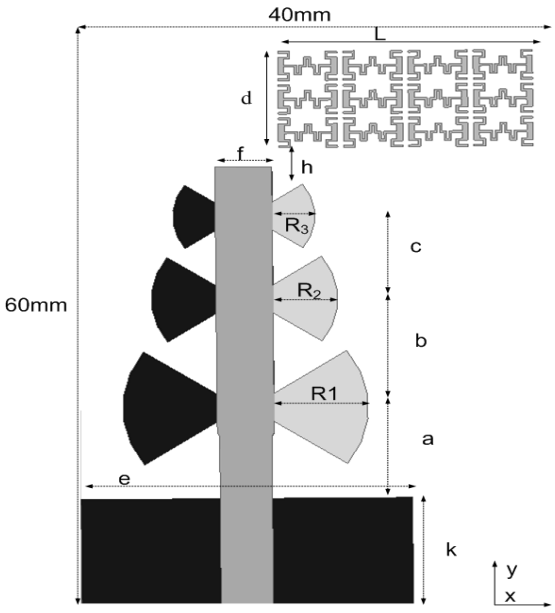

Figure 2-7: Configuration of proposed antenna embedded with IML unit-cells on the top surface of substrate.

In this design, the reference antenna was a three-element array of bow-tie radiators connected to a microstrip feed-line [18]. A 3×4 array of the proposed metamaterial unit-cells were printed on the antenna's substrate and located in front of the antenna. The integrated metamaterial loading (IML) on the antenna was printed on a Rogers RT5880 substrate with thickness of 1.575 mm. The dimensions of the proposed antenna are: a=9.2 mm, b=11 mm, c=8.4 mm, k=10.8 mm, e=28 mm, f=4.4 mm, R_1=7.9 mm, R_2=5.4 mm, R_3=3.6 mm. Coupling between the IML and the antenna is through electromagnetic interaction. Fig.2.8 shows the radiation pattern of the bow-tie antenna with and without IML structure in the E-plane of the antenna.

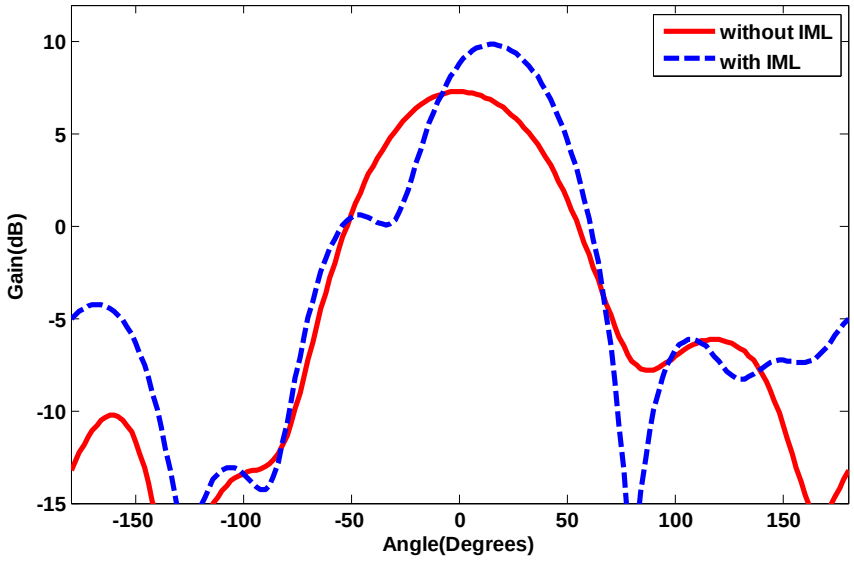

Figure 2-8: Radiation patterns of proposed antenna in the E-plane (xy) with IML unit-cells and a conventional bow-tie antenna at 7.5 GHz.

Fig.2.8 shows that when the IML is included in the antenna substrate the main beam of the antenna is tilted by an angle of 17 degrees. The tilt angle can be calculated using Eqn. (3), where $n_2=n_{IML}$=2.2, $n_1=n_{sub}$=1.6, d=9.7 mm and l=21.5 mm which gives us $\varphi = 17$. Fig.2.9 (a) and (b) shows the Poynting vector and electrical-field distribution over the antenna structure with and without IML inclusion, respectively, at 7.5 GHz. These figures show that when there is no IML the antenna's energy is radiated predominately in a vertical direction, but when the IML inclusion is added to the structure the radiation is tilted towards the location of the IML.

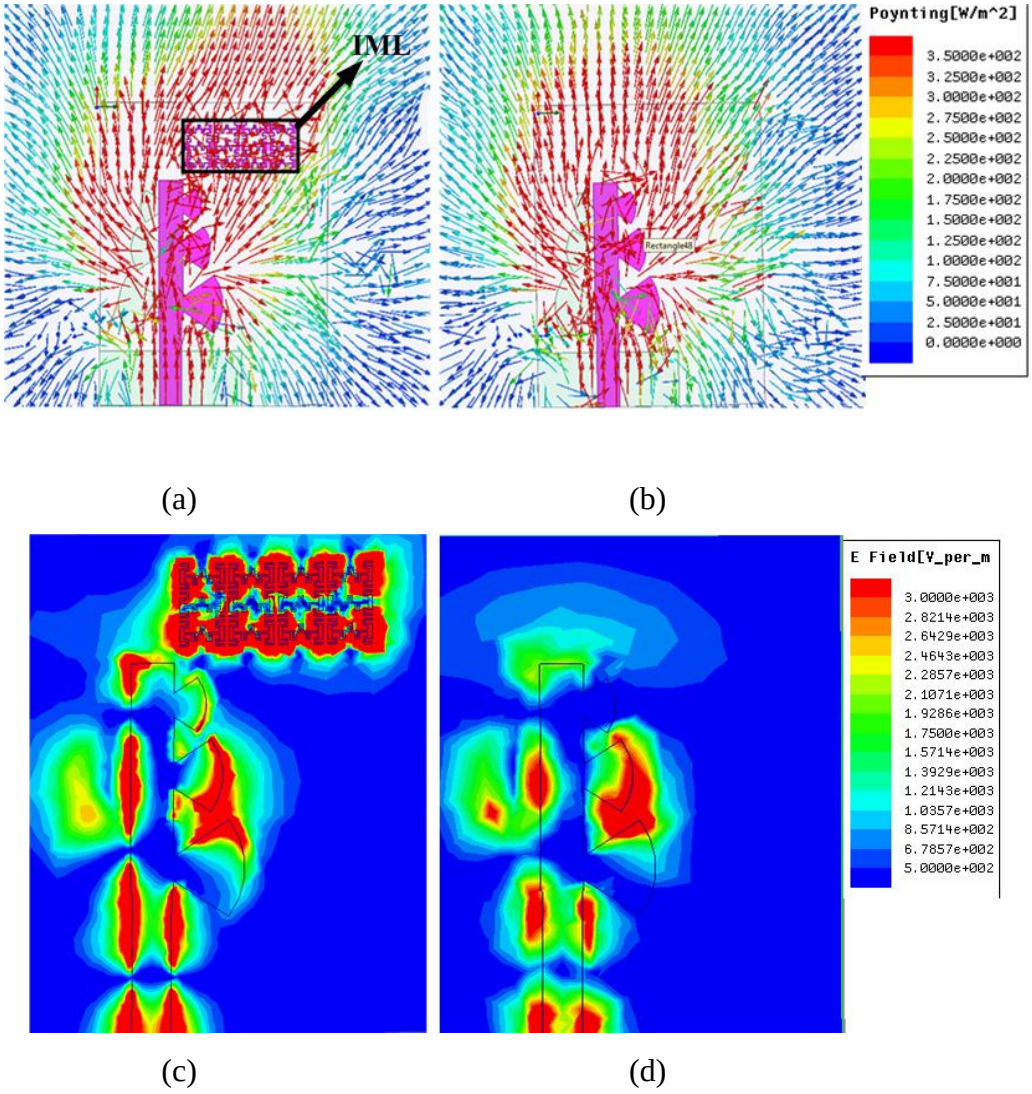

Figure 2-9: Radiation Poynting vector and E-field distribution over the antenna at 7.5 GHz (a) & (c) with IML, and (b) & (d) without IML.

According to Fig.2.9 (c) and (d), the distribution of the electrical-field is completely modified in presence of the IML structure. The modified E-field induces current in the unit-cells that make it behave like a parasitic element to re-direct the antenna's main beam as well as enhancing its gain [16].

2.1.4 PARAMETRIC STUDY

This section describes the results of a study to determine how different numbers of unit-cells affect the tilt angle performance in the E-plane. In this study, the antenna was simulated with an IML inclusion having 2, 3, 4 and 5 columns, and in each case the effect of the IML on gain, main beam directivity, and side-lobe level (SLL) of the antenna was investigated.

Fig.2.10 shows the radiation pattern of the antenna in the E-plane (xy) at 7.7 GHz for various levels of unit-cell loading. The results clearly show the incorporation of the IML structure increases the gain of the antenna. Gain enhancement is due to the parasitic effect of unit-cells printed on the substrate which act as parasitic directors. These results are summarized in Table I.

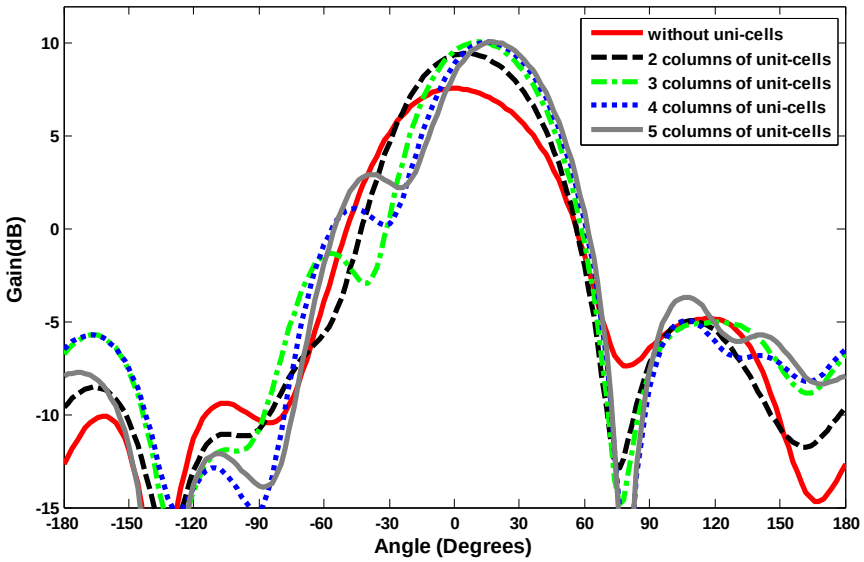

Figure 2-10: Radiation pattern of proposed antenna with different columns of unit-cell loading in the y-direction.

It is clear from Table I that when the number of the unit-cell columns is increased a higher tilt angle is observed. However, there is a trade-off between the tilt angle and the SLL, and as we can see from Table I that with 5 columns the SLL is -7 dB, which is unacceptable. The other effect of the IML is gain enhancement, which increases with

increase in the number of the columns. The parametric study in this case shows the best performance of the antenna can be achieved when four columns are used in the structure of IML. Another parameter that was investigated was the distance (*h*) between IML and the end bow-tie radiator, as shown in Fig.2.7. In this study, *h* was varied from 1 mm to 5 mm, and the resulting radiation patterns are shown in Fig.2.11. These results indicate that the distance *h* does not have any significant effect on the beam tilting angle.

The parametric study shows that the main beam angle can be tilted from 6 to 19 degrees when the IML columns are increased from 2 to 5. Therefore, if a reconfigurable IML is used in the antenna's structure the main beam can be steered from 6 to 19 degrees. A reconfigurable structure can be realized using active elements such as PIN diodes, and investigation of this is under progress.

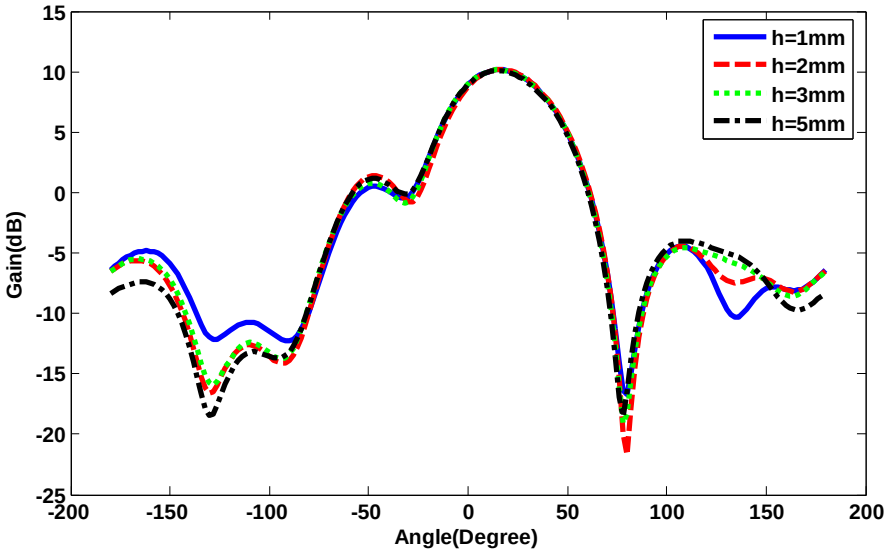

Figure 2-11: The radiation pattern of antenna in the E-plane as a function of Parameter h

Table 2-1: The effect of IML on antenna performance

No. of unit-cell columns in IML structure	2	3	4	5
Tilt angle (degree)	6	12	17	19
Gain (dB)	9.45	10.07	10.05	10
Side-lobe level (dB)	-14.5	-11.38	-9	-7

2.1.5 Experimental Results

The proposed antenna design with the embedded IML structure was validated practically. The bow-tie antenna with a 3×4 array of meander-line metamaterial unit-cells were fabricated and measured. A photograph of the fabricated prototype is shown in Fig.2.12.

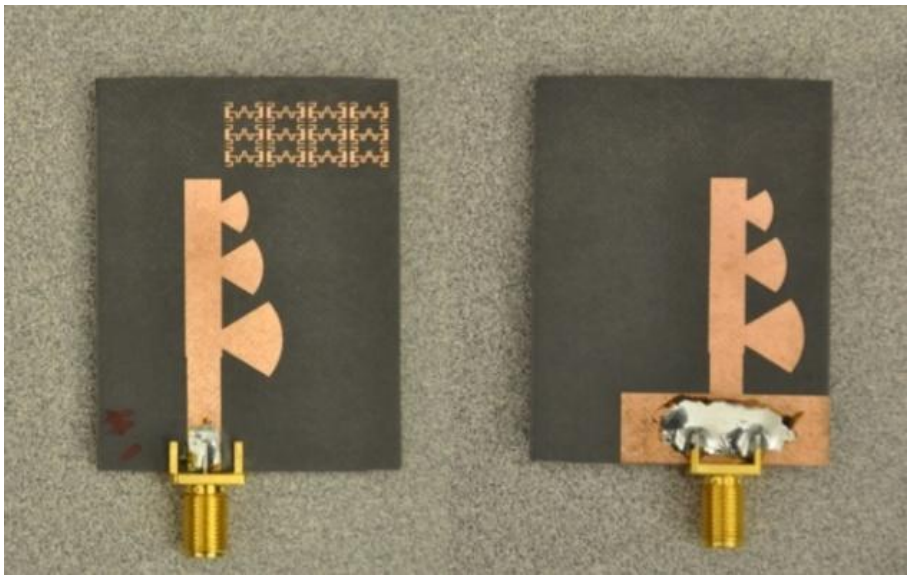

(a) *(b)*

Figure 2-12: Photograph IML antenna, (a) top view, (b) bottom view.

The measured and simulated reflection-coefficient of the antenna with and without IML inclusion is shown in Fig.2.13. The reflection-coefficient is altered in presence of the IML, which is due to the mutual coupling effect between the bow-tie radiators and the unit-cells. However, the magnitude of S_{11} remains lower than -10 dB in the frequency range of 7-8 GHz.

The simulated and measured normalized radiation patterns of the proposed antenna with IML structure in the E-plane are plotted in Fig.2.14 (a-c) at 7.3, 7.5, and 7.7 GHz. Fig.2. 14 (d) shows the simulated and measured radiation pattern of the antenna in the H-plane at 7.5 GHz, where the main beam is oriented in the end-fire direction without tilting.

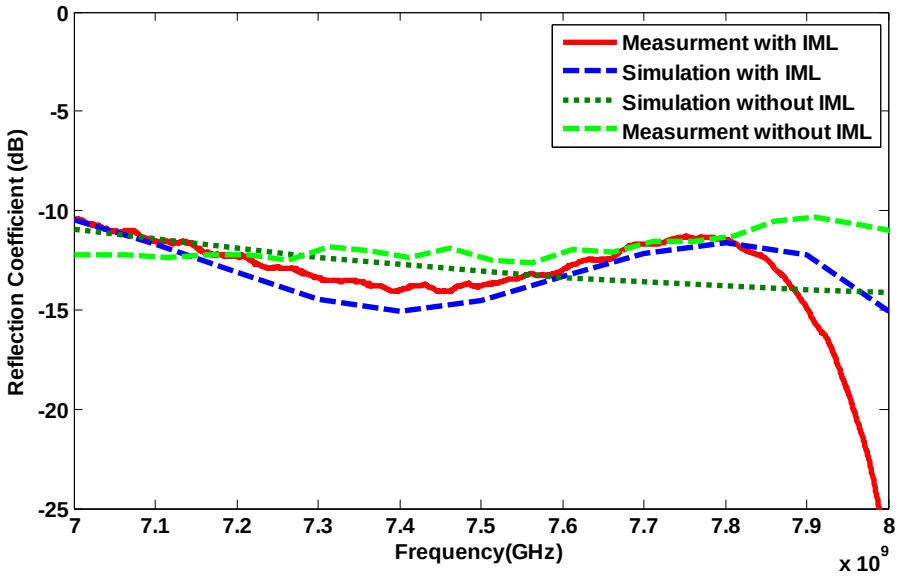

Figure 2-13: Reflection-coefficient of bow-tie antenna loaded with IML.

The peak gain measurement at different frequencies was carried out using the gain comparison method with a known standard horn antenna, which can be calculated using the following expression:

$$G_{AUT} = G_{GS} + 10log\left(\frac{P_{AUT}}{P_{GS}}\right) \quad (4)$$

Where $G_{AUT\ dB}$ is the gain of IML bow-tie antenna, and $G_{GS\ dB}$ is the gain of standard horn antenna with specification of EMCO model operating in the frequency range of 5.85-8.2 GHz. The measured peak gain can be obtained by calculating the receiving

power of the antenna under test (P_{AUT}) and the standard horn's power in receiving mode (P_{GS}). From the results given in Table II the measured gain of the proposed antenna with IML at 7.5 GHz is 9.23 dB, which is 2.73 dB more than the conventional bow-tie antenna.

Table 2-2: Measured peak gain of antenna at different scan angles

Freq. (GHz)	Simulated peak gain without IML	Measured peak gain without IML	Simulated peak gain with IML at 17^o	Measured peak gain with IML at 17^o
7.3	6.44	5.71	8.9	8.7
7.5	7	6.5	9.5	9.23
7.7	7.40	7.84	10	9.25

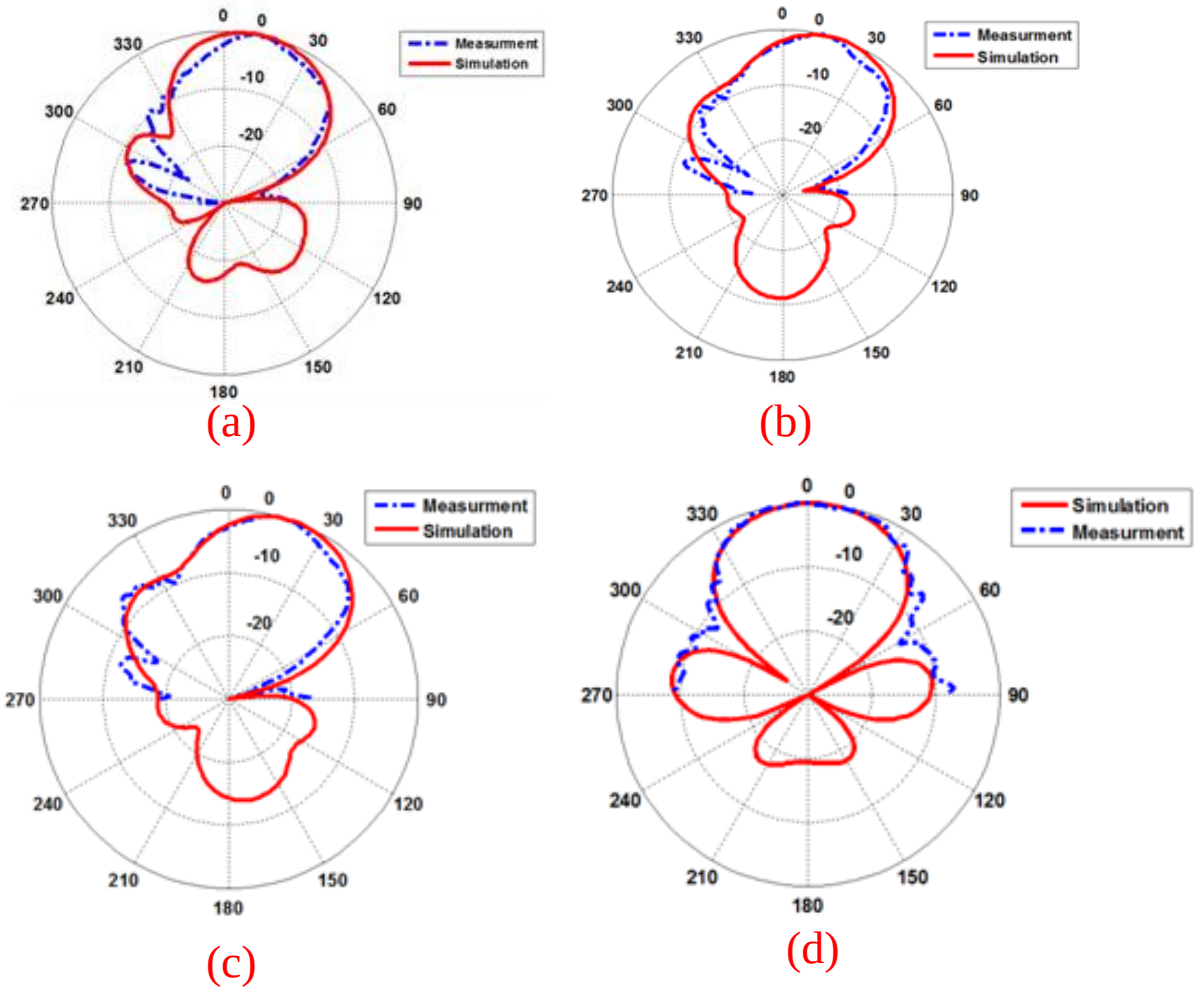

Figure 2-14: Radiation pattern of proposed antenna with IML at: (a) 7.3 GHz, (b) 7.5 GHz, (c) 7.7 GHz, and (d) with IML in the H-plane at 7.5 GHz.

2.1.6 Conclusion

A novel technique is presented that uses metamaterial unit-cell loading, which is implemented onto the planar antenna, in the vicinity of radiating element to re-direct its main beam in a specific direction. The antenna employed comprises of a three-element array of bow-tie radiators, and the beam tilting method employed is based on the application of metamaterial inclusions to realize a region of high refractive index. The metamaterial unit-cell structure was characterized and its behavior and performance including its high refractive-index was verified through fabrication and measurement. Compared to a conventional H-shaped resonator the proposed unit-cell provides a

miniaturization factor of 0.7 as well as a higher refractive-index. A 3×4 array of metamaterial unit-cell loading was integrated within a bow-tie antenna. The simulation and experimental results show that the antenna's main beam tilted by 17 degrees in a direction towards the location of the metamaterial loading in the E-plane, while the H-plane radiation pattern remains unchanged. The tilt angle observed correlates with the predicted value. Unlike other conventional methods of tilting, the method described here results in no degradation in gain, in fact a gain enhancement of 2.73 dB is observed, which is due to parasitic behavior of the metamaterial unit-cell inclusion.

Chapter 3 **RADIATION BEAM TILTING OF END-FIRE ANTENNA WITH META-SURFACE**

3.1 **Introduction**

Adaptive antennas with beam-steering capability provide advantages of increased signal gain, greater range of the signal path, reduced multipath reflection, improved spectral efficiency, and increased network capacity. Various techniques have been reported to steer the direction of the main beam of planar antennas including RF varactor diodes [19] and RF MEMS phase shifter [20]. When these techniques are implemented in array antennas the associated large loss renders them unsuitable for applications especially at millimeter-wave bands. The direction of the main beam can be steered mechanically however this is undesirable for numerous applications. More recently, the authors in [1] have incorporated an electromagnetic band-gap (EBG) structure in the orthogonal plane around an array of four printed dipole antennas. With this technique the EBG structure needs to be placed in close proximity to the dipole antennas in order to tilt the direction of the antenna's main beam by 28 degrees at 3.5 GHz. Although the technique is simple it requires each conductor element constituting the EBG unit-cell to be short-circuited to ground, which can complicate its construction and impact on the cost of the antenna. To circumvent this shortfall the authors in [21] have demonstrated that by loading a bow-tie antenna with an array of sub-wavelength meander-line metamaterial unit-cells can tilt the main beam of the antenna by 17 degree in the azimuth plane over 7.2-7.5 GHz. Greater tilt angle has be reported by the same authors in [22] using gradient index of refraction implemented with metamaterial unit-cells that are integrated in the azimuth plane of printed dipole antenna. They have shown the direction of the main beam can be deflected by 26 degrees in the E-plane at millimeter-wave frequencies. This technique offers a low-profile structure with good gain and tilt angle. To obtain a beam deflection of 30 degrees in the elevation plane at 60 GHz the authors in [23] employed an array of folded H-shaped resonators.

In this chapter meta-surface is used to tilt the direction of the bow-tie antenna, where the meta-surface is realized by magnetic resonance created with split-ring resonators (SRR).

The SRR structure is designed to provide an operational bandwidth over 5.4–7.5 GHz. The antenna consists of a microstrip to slot transition-line as a balun connected to the rounded bow-tie radiators. The direction of the antenna's main beam was tilted by integrating the array of SRR unit-cells off-axis of the bow-tie antenna with respect to end-fire direction. The measured results confirm the antenna's radiation in the azimuth plane is deflected from 12 to 22 degrees over 5.4–7.2 GHz, and the antenna offers a maximum peak gain of 11 dBi at 7.2 GHz.

3.2 **Beam Tilting Approach**

To deflect the direction of the main beam of the antenna it is necessary to integrate the meta-surface of SRR unit-cells with a refractive index greater than the antenna substrate in the azimuth plane. The array of SRR unit-cells need to be placed off-axis to the bow-tie antenna along the end-fire direction, as illustrated in Fig.3.1. The beam tilting mechanism results from the phase differential created in the radiation by meta-surface [21-22].

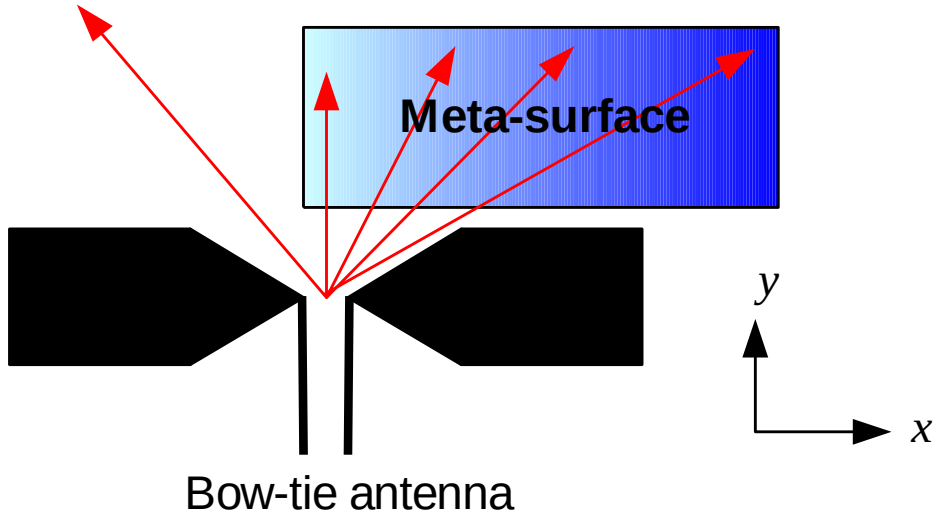

Figure 3-1: Mechanism of beam-tilting in the E-plane of the bow-tie antenna.

The split-ring resonator in [24] was modified to create a meta-surface with broadband performance. The proposed SRR unit-cell, shown in Fig.3.2, was fabricated on RO5880 with relative permittivity 2.2 and thickness of 0.51 mm. To extract the salient parameters characterizing the unit-cell such as permeability, permittivity and refractive index it was necessary to assign the PEC and PMC boundary conditions in the *yz* and *xy*-planes, respectively. Two wave ports are located into the *y*-direction to excite the EM wave.

The S-parameters result of proposed unit-cell in Fig.3.3 shows that the EM waves pass unimpeded through the array of SRR unit-cells except at 2.97 GHz.

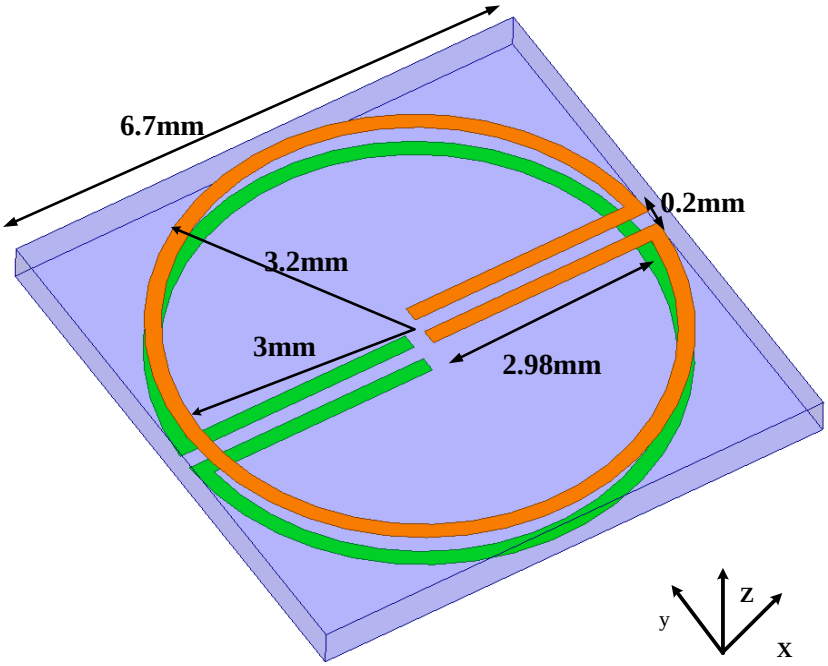

Figure 3-2: Configuration of proposed split-ring resonator (SRR) on the top and bottom surface of RO 5880 substrate.

The results in Fig.3.4 show that over the frequency range of 5–8 GHz the magnitude of permeability and permittivity are 0.7 and 1.87–2.4. The corresponding refractive index varies from 1.18–1.32 over the frequency range of 5–8 GHz.

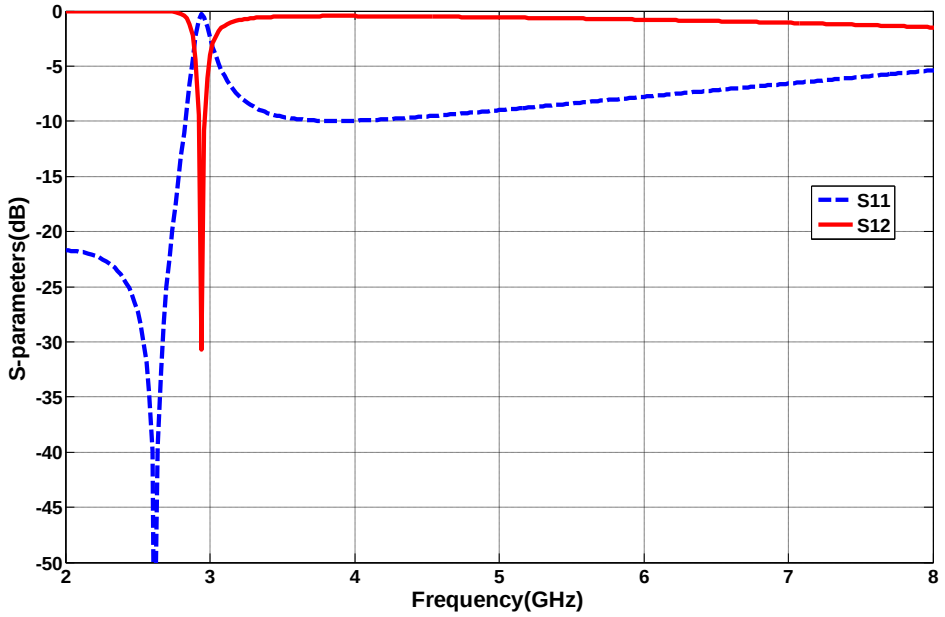

Figure 3-3: The S-parameter response of the proposed SRR unit-cell.

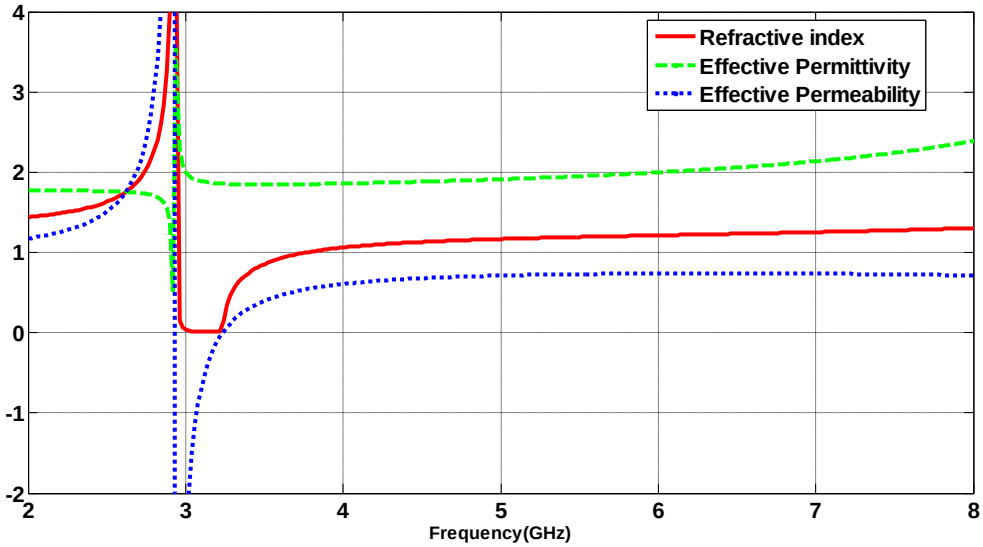

Figure 3-4: The extracted effective permittivity, permeability and refractive index of the split ring resonator.

3.3 **Bow-Tie Antenna with Array of SRR Unit-Cells**

In this section the properties of a rounded bow-tie antenna are studied when combined with the array of SRR unit-cells. The bow-tie antenna employed here is a modified Yagi antenna in [25]. The bow-tie antenna was constructed on RO5880 substrate with relative dielectric constant of 2.2 and thickness of 0.51. A 8×6 array of SRR unit-cells were integrated onto the antenna substrate and located in front of the bow-tie in the E-plane, as illustrated in Fig.3.5. The SRR unit-cell was implemented on the top and bottom layers of antenna substrate. Dimensions of the bow-tie antenna are annotated in Fig.3.5. Effect of SRR loading on the radiation pattern of the bow-tie antenna is shown in Fig. 6 at 5.4, 6.2, and 7.2 GHz. The SRR was loaded in the E-plane (azimuth-plane) of the antenna. Fig.3.6 shows the SRR loading deflects the direction of the main beam in the E-plane by 12, 18, and 21 degrees at 5.4, 6.2, and 7.2 GHz, respectively, with respect to the *y*-axis (end-fire direction).

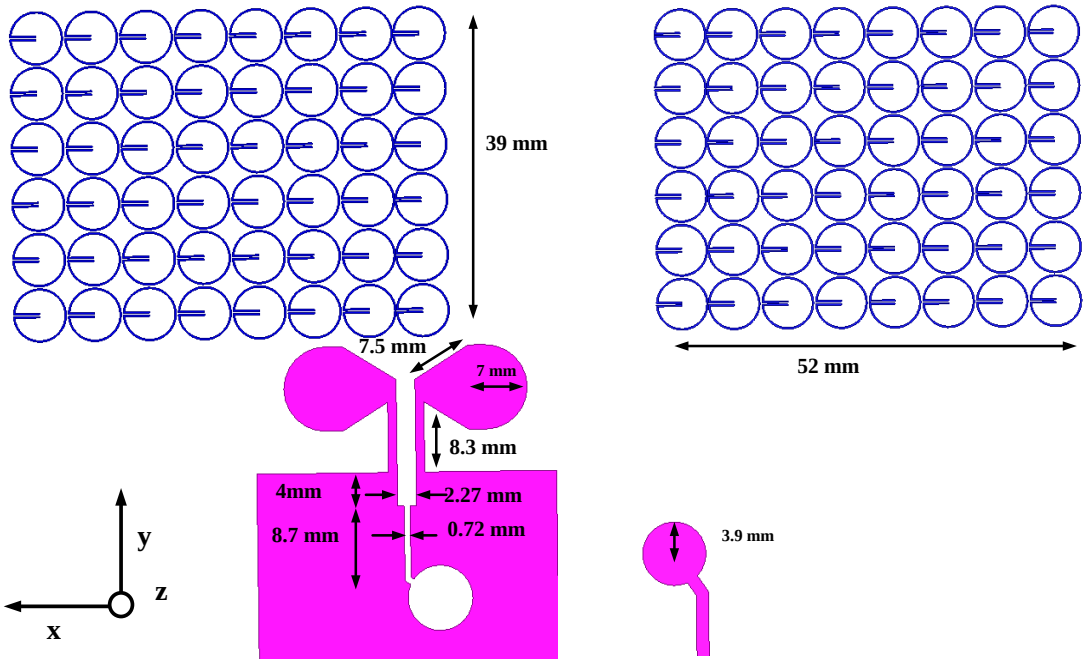

Figure 3-5: Configuration of proposed antenna embedded with SRR unit-cells, (a) on the bottom, and (b) on the top surface of substrate.

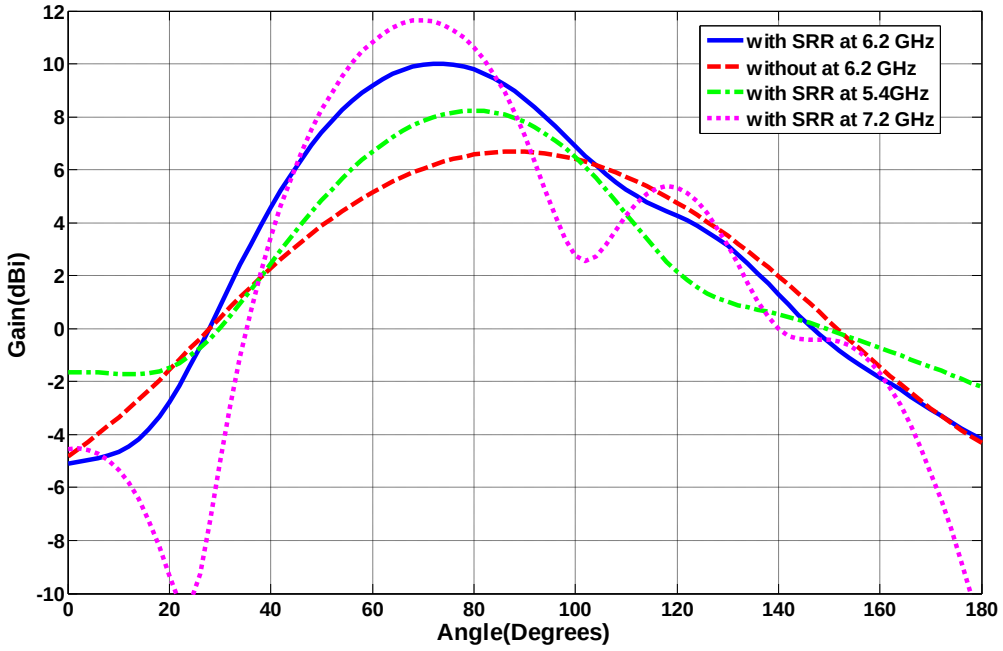

Figure 3-6: Radiation patterns of proposed antenna in the E-plane (xy) with SRR unit-cells and a conventional bow-tie antenna at 5.4, 6.2, and 7.2 GHz.

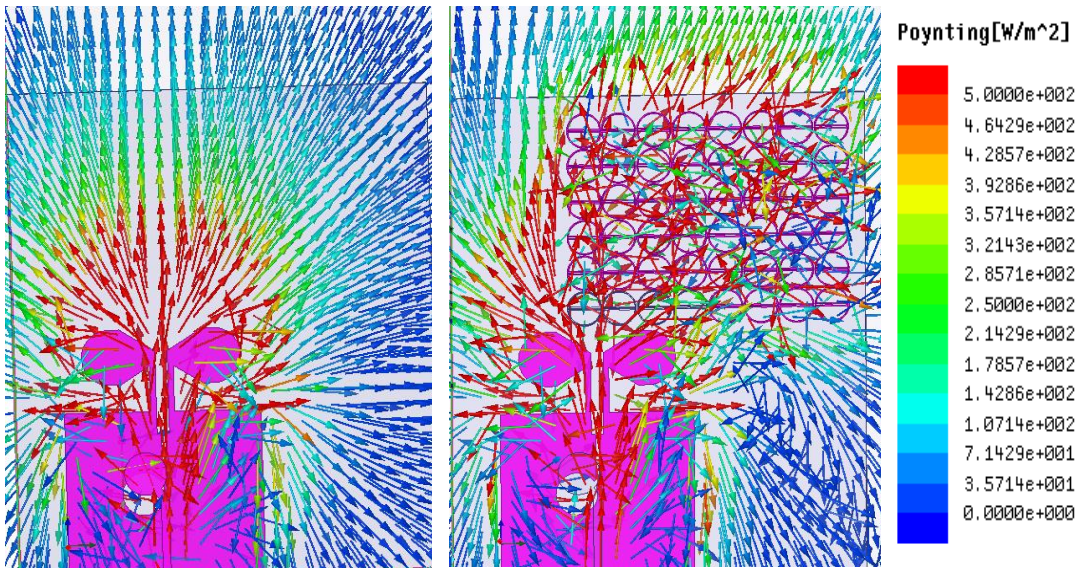

(b) (a)

Figure 3-7: Poynting vector distribution over the antenna at 6.2 GHz, (a) without SRR, and (b) with SRR.

The gain of the antenna is increased by 5 dBi at 7.2 GHz compared to a conventional bow-tie antenna with no meta-surface. This is attributed to the enhanced aperture size of the proposed antenna. The change in the tilt angle at different frequencies is due to the variations of the refractive index. The Poynting vector distribution on the lower surface of antenna at 6.2 GHz is shown in Fig.3.7. It can be observed the SRR unit-cells strongly influence the radiation emanating from the bow-tie antenna. The EM radiation veers towards the meta-surface in the *x*-direction.

3.4 **Experimental Results**

The proposed bow-tie antenna with 8×6 array of SRR unit-cells was fabricated and its performance measured. The photograph of the prototype antenna is shown in Fig.3. 8.
The simulated and measured reflection-coefficient of proposed antenna is shown in Fig.3. 9. The measured results indicate that the magnitude of S_{11} is better than -10 dB over 3.5–8 GHz.

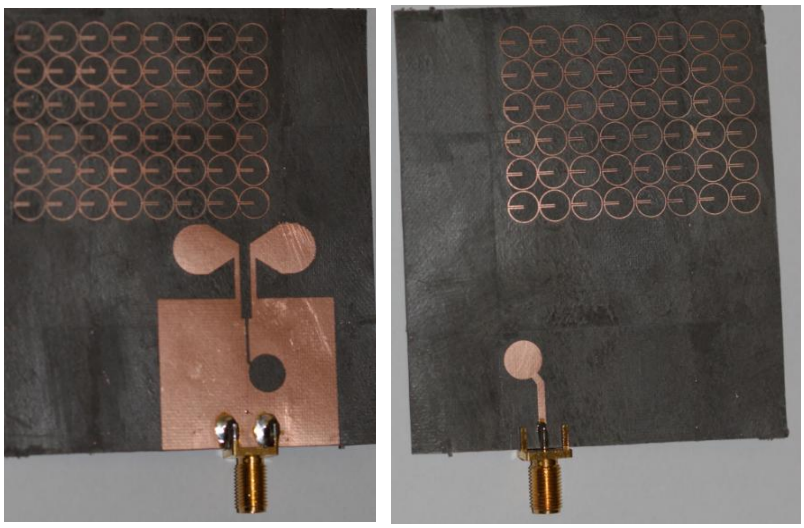

Figure 3-8 Photograph of SRR bow-tie antenna, (a) bottom view, and (b) Top surface of substrate.

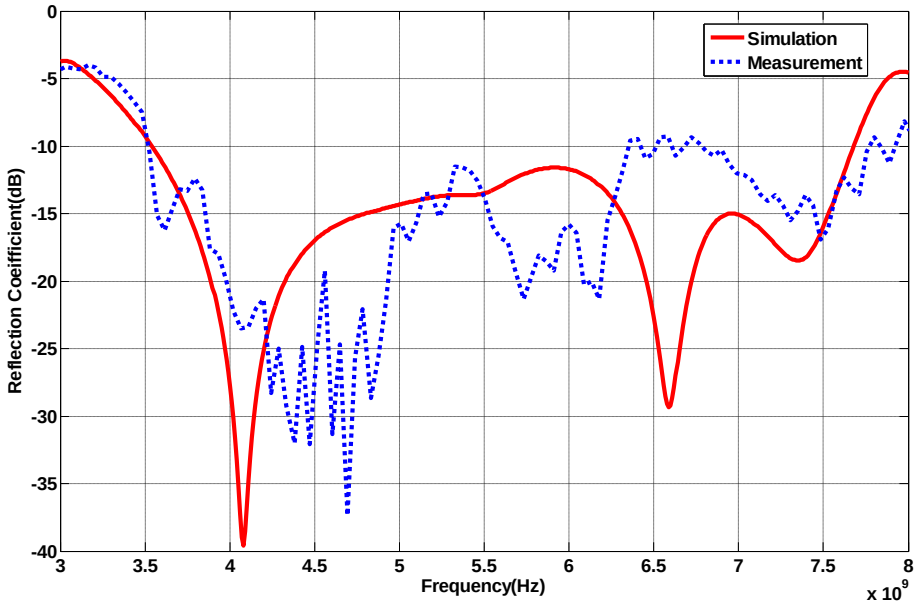

Figure 3-9 The simulation and measured reflection-coefficient of the SRR rounded bow-tie antenna.

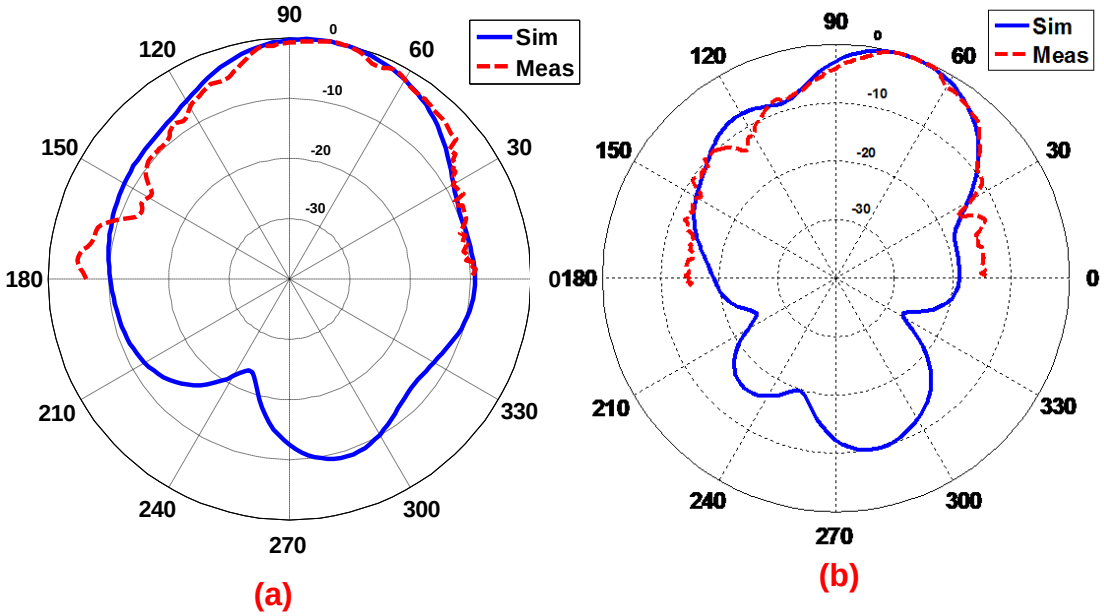

Figure 3-10: The normalized radiation patterns of the rounded bow-tie antenna with 8×6 SRR in the E-plane (xy) at: (a) 5.4 GHz, and (b) 7.2 GHz

The simulated and measured radiation pattern of the proposed antenna in the E-plane (*xy*) at 5.4 and 7.4 GHz, in Fig.3.10, shows the direction of the antenna's main beam is deflected by 12 and 21 degrees at 5.4 and 7.2 GHz, respectively. The change in the deflection angle at the two frequencies is attributed to the variation in the refractive index of the meta-surface as in Fig.3.4. The measured antenna gain at 5.4 and 7.2 GHz are 8.2 and 11 dBi, respectively.

3.5 **Conclusion**

Meta-surface created with magnetic resonance using an array of split-ring resonators was employed to steer the direction of a bow-tie antenna's main beam in a predefined angle. The meta-surface comprised 8×6 array of split-ring resonators that were integrated on the bow-tie antenna. The measured results validate the proposed technique. Beam deflection of 12 and 21 degrees were achieved at 5.4 and 7.2 GHz, respectively, with a corresponding maximum peak gain of 8.1 and 11 dBi.

Chapter 4 **Enhancement of tilted beam in elevation plane for planar End-fire antennas using artificial dielectric medium**

4.1 **Introduction**

Adaptive antennas with reconfigurable radiation patterns are extensively deployed in the wireless communication systems to minimize the effect of co-channel interference when base-stations are located in densely populated urban environments. An effective technique to control the radius of coverage and reduce co-channel interference is to use down tilt antenna technology.

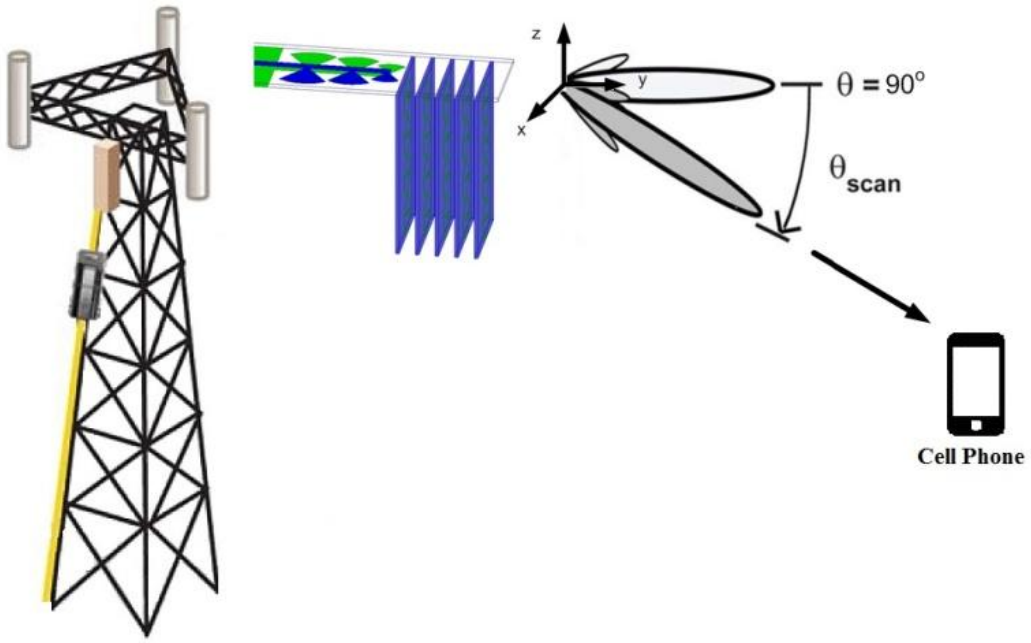

Figure 4-1: Base-station dipole antenna array which can be substituted with the proposed double G-shaped bow-tie antenna.

Hence, the beam tilt angle of base-station antennas is an important design parameter for cellular networks to improve channel capacity [26]. A base-station system usually use a 1

×4 antenna arrays mounted on a tower to tilt the main beam below the horizon, as illustrated in Fig.4.1.Beam tilting in conventional systems is typically implemented either mechanically or electronically. Electronic techniques are usually realized using electronically controlled transmission-lines [6], varactor diodes [7] and RF micro-electromechanical systems (MEMS) [8], [27]. Although these techniques provide an agile beam tilting system, one major drawback observed with them is a severe drop in gain performance when the beam is steered. On the other hand, the mechanical beam tilting approach suffers from the difficulty in installation due to the inclined structure of the antenna arrays.

Zhang et al. [28] has proposed a Yagi-Uda parasitic array for beam-steering applications that employs a driven part and parasitic elements using electronic switches. By controlling the switches, the antenna's main beam can be steered however with no gain enhancement. In [29], a 1×4 base-station antenna array has been reported using a low-pass RF MEMS phase-shifter that can scan the radiation beam by 9^o with a gain of 8.3–8.6 dB at 2 GHz. Another valid approach for beam-tilting involves the use of a dielectric lens in front of the antenna [30-31]. However, this kind of set-up is too large and bulky for modern communication systems.

Recently, the authors in [32] have reported a 3D antenna array of EBG loaded dipoles that provide beam tilting of 24^o with SLL of -5.5 dB at 3.5 GHz and maximum directivity of 11.2 dB. Protrusion dimension of this antenna is 72 mm. Beam steering of the 4×16 antenna array in [4] is achieved using active metamaterial unit-cells with different refractive-index, where varactor diodes are employed to control the refractive-index of the array. This configuration provides scanning over $\pm 30^o$ at 5 GHz, but its side-lobe-level (SLL) is -4 dB when the beam is tilted by 30^o, and its gain drops severely by 3 dB from 8 to 5 dB when the beam is scanned from 0 to 30^o with protrusion dimension of 150 mm. Authors in [33] use a partially reflective surface antenna to steer the main beam by 15^o at 2 GHz in the H-plane which has a protrusion dimension of 78 mm.

In this chapter, a novel approach is described based on the application of high refractive-index metamaterials to tilt the radiation beam of planar end-fire antennas. Proof-of-concept is demonstrated using a Bow-tie antenna designed to operate at the WiMAX frequency band. The proposed antenna consists of Bow-tie radiators similar to

the one in [25] along with a 5×4 array of double G-shaped resonator (DGR) mounted asymmetrically in the antenna's H-plane. The DGR array is used to create a high refractive-index medium, which plays a key role in the beam tilting mechanism. To validate the proposed tilting technique, a prototype of the DGR antenna was fabricated and measured. It is shown the DGR Bow-tie antenna provides a larger than normal tilt angle of 35^{o} in the elevation plane and also offers a maximum gain of 10.4 dB at 3.6 GHz while maintaining a reflection-coefficient better than -10 dB.

The protrusion dimension of the proposed DGR antenna is 79+35=114 mm which is in fact composed of two main sections: first the antenna section which is a wide-band bow-tie antenna array with protrusion of 79 mm, and then a custom-designed metamaterial section with protrusion of 35 mm. It is important to mention that this section is the main contribution of this paper, and it can be added to any type of end-fire antenna to generate the beam-tilting in the H-plane.

4.2 Bow-tie Antenna

The geometry of the proposed planar Bow-tie antenna shown in Fig.4.2(a) essentially consists of three circular sector patches that are attached to the microstrip feed-line. This structure is printed on both sides of the dielectric substrate to create a symmetrical Bow-tie radiator. The Bow-tie antenna was selected because of its end-fire radiation pattern, shown in Fig.4.2(b), which makes it ideal for integration with beam switching networks. Moreover, the Bow-tie antenna has a wide radiation beamwidth in its H-plane, which is necessary for achieving higher tilt angles.

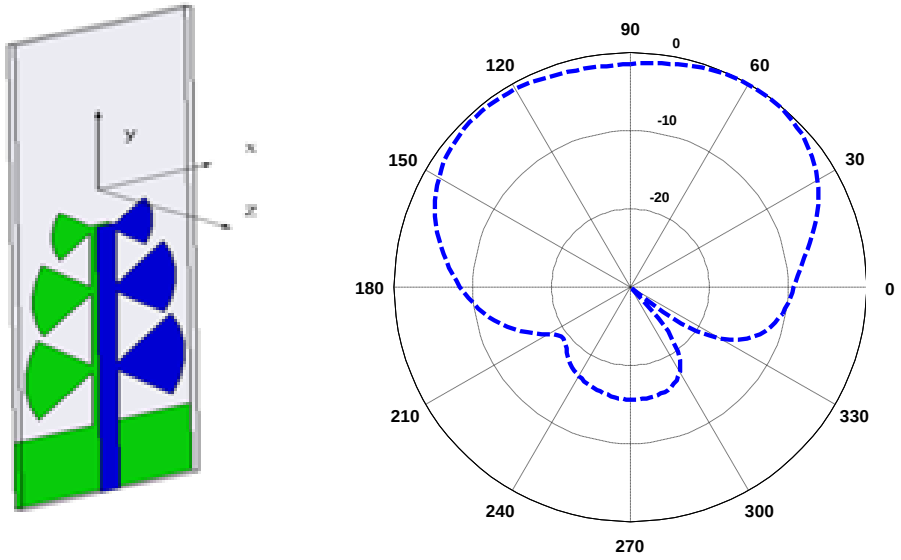

Figure 4-2: (a) Geometry of the planar Bow-tie antenna, and (b) its normalized radiation pattern in the H-plane.

4.3 Beam Tilting Mechanism

The main goal of this investigation was to introduce beam tilting functionality in the H-plane (elevation plane) of a planar end-fire antenna like a Bow-tie. The beam tilting approach employed here is based on the phase shift property resulting from the interaction of the electromagnetic wave (EM) emanating from the antenna with different media.

To realize beam tilting, two media are used with different refractive-indices in the antenna's H-plane (*yz*), as illustrated in Fig.4.3. The first medium is the substrate on which the antenna is constructed, whilst the second medium is an artificial dielectric that is placed on the other side of the first substrate. The artificial dielectric is implemented using a novel electric resonator based on a metamaterial unit-cell to provide a low-profile structure whose characteristic parameters can be finally controlled. As will be shown in Section IV, the proposed metamaterial unit-cell is used to create a region of high refractive-index medium compared to the antenna's substrate.

The beam tilt angle (θ) of the Bow-tie antenna can be calculated from the refractive-indices of the two regions (n_{sub} and n_{DGR}) and the different optical path lengths of the rays traversing the two media. In fact, the EM waves reaching points A and B have equal phase angles so that the beam deflection angle can be determined using:

$$\left[\left(\sqrt{L^2 + a^2} - a\right) - d(n_{DGR} - n_{sub})\right]/L = sin\theta \qquad (1)$$

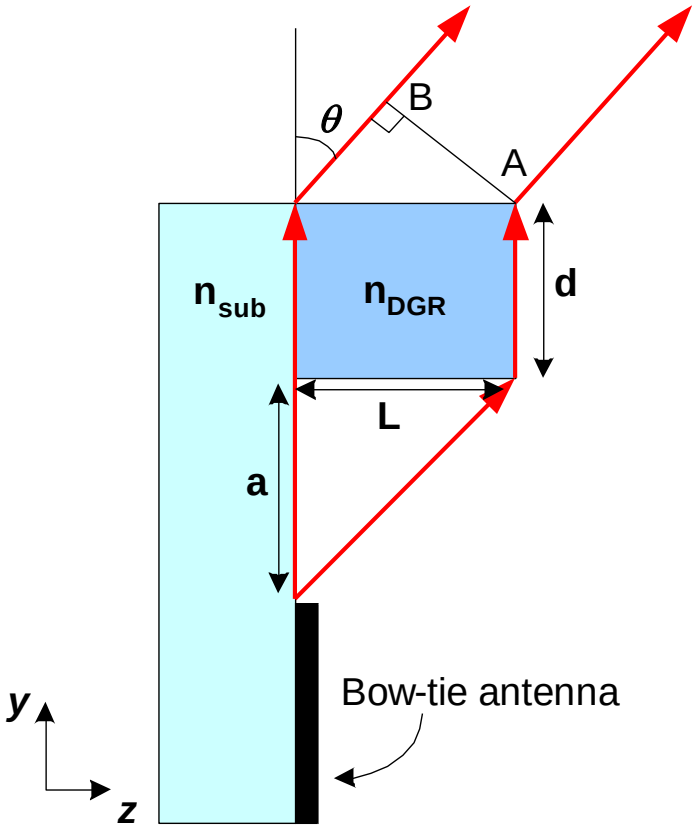

Figure 4-3: Mechanism of beam tilting in the H-plane of Bow-tie antenna.

Where d is the thickness of the artificial medium consisting of a 5×4 DGR unit-cells; a is the distance of the radiating antenna to the DGR slab; n_{DGR} is the refractive-index of the artificial medium; n_{sub} is the refractive-index of the antenna substrate; and L is the length of the high refractive-index medium in the direction of the beam deflection (z-direction). Eqn. (1) indicates that the tilt angle of the beam is a function of the difference in the refractive-indices of the two media. Thus, by increasing the refractive-index of the

artificial medium, a larger phase difference can be achieved and consequently a larger tilt angle.

4.4 **Metamaterial Unit-cell**

The high refractive-index medium was realized using an electric resonator based on a metamaterial unit-cell. A conventional ring resonator (CRR) for the radius given in Fig.4.4 (i.e. average of R_1 and R_2) has a resonant frequency of 5.72 GHz, which is further away from the WiMAX operating frequency of 3.5 GHz. Hence, it was necessary to modify the CRR configuration to obtain a structure that exhibits a higher refractive-index and therefore results in a smaller structure that resonates at the desired WiMAX frequency. The resulting electric resonator, shown in Fig.4.4, is referred to here as a double G-shaped resonator (DGR).

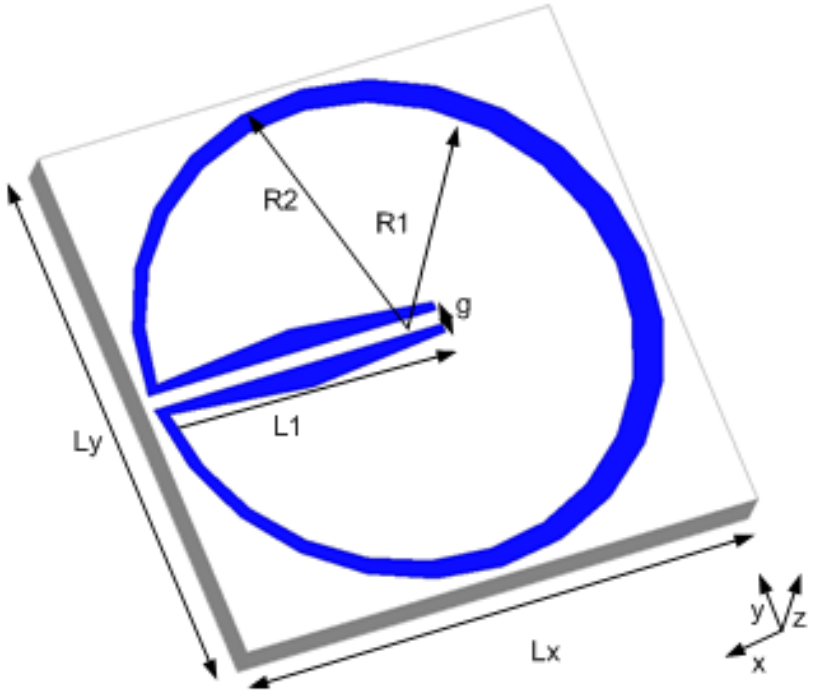

Figure 4-4: The proposed double G-shaped resonator (DGR) unit-cell fabricated on a dielectric substrate.

The proposed DGR unit-cell was fabricated on a Rogers RT/Duroid 5880 substrate with the thickness of h = 1.575 mm, permittivity of 2.2, and tangent-loss of 0.0009. The dimensions of the unit-cell are: L_x = 18 mm, L_y = 18 mm, L_1 = 9.7 mm, R_1 = 8 mm, R_2 = 8.7 mm, and g = 0.5 mm. The effective constitutive parameters of the proposed unit-cell were determined using HFSS software based on the standard procedure described in [34]. The perfect electric conducting (PEC) and the perfect magnetic conducting (PMC) boundary conditions were assigned in the *yz* and *xy* planes defined in Fig. 4.4, and the two ports were located in *y*-direction.

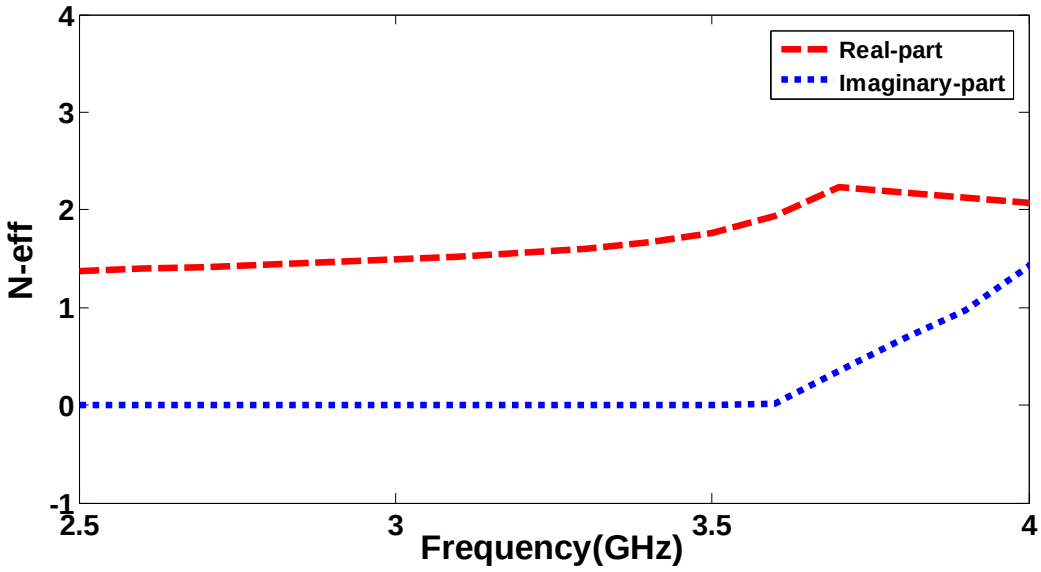

Figure 4-5: Refractive-index of proposed DGR unit-cell as a function of frequency.

The extracted effective index of refraction of the DGR unit-cell as a function of frequency, shown in Fig.4.5, confirms the unit-cell provides a higher refractive-index across the WiMAX frequency range (3.4–3.6 GHz), i.e. 1.68–1.95 than the antenna substrate (n_{sub} = 1.26). The maximum refractive-index of the unit-cell is 2.23 at 3.7 GHz. Fig.4.6 reveals that the electric resonance frequency of the CCR unit-cell shifts from 4.35 GHz to 3.7 GHz when it is converted to a DGR configuration. In addition, across 3.4–3.6 GHz, corresponding to the WiMAX band, we can observe that the effective permittivity of the DGR unit-cell at 3.6 GHz is about 9, which is three times higher than the effective

permittivity of the CCR unit-cell. In the next section, the artificial medium is placed in the antenna's boresight to tilt the direction of the main beam.

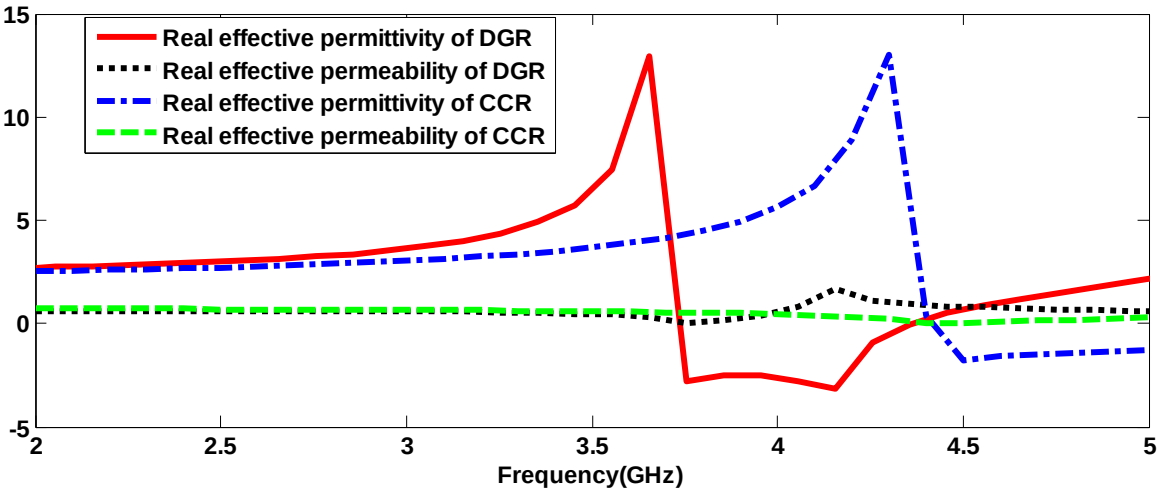

Figure 4-6: Extracted permittivity and permeability of the CCR and DGR unit-cell.

4.5 **Bow-Tie Antenna with DGR Unit-Cell**

In this section, the antenna's characteristics are studied when the metamaterial lens is placed in the H-plane of the antenna. A 1×2 and 1×4 array constituted from the DGR unit-cells are placed in the vicinity of the antenna, as shown in Fig.4.7. The overall length of 1×2 and 1×4 arrays are 36 mm and 72 mm, respectively. According to the simulation results, the 1×4 array tilts the main beam peak by 38° in the H-plane, and the 1×2 array tilts the main beam peak by 25° compared to the antenna without the lens. It is observed in Fig.4.7 that gain enhancement of 1.7 dB is realized due to the metamaterial lens. In order to achieve a maximum gain enhancement and tilt angle at the same time, four lens layers were deployed. The optimum gap between the layers was deduced using the optimization tools in HFSS. The final DGR configuration is a 5×4 array integrated with the Bow-tie antenna, shown in Fig.4.8. The dimensions of the antenna are: w_1 = 45 mm, w_2 = 72 mm, h = 7 mm, W = 45 mm, L = 114 mm, L_1 = 75.5 mm, L_2 = 17.5 mm, R_1 = 17 mm, R_2 = 15 mm, and R_3 = 9.6 mm. Fig.4.9 shows the direction of the main beam is tilted by 31° at 3.5 GHz, which has a maximum gain of 11 dB using the proposed metamaterial

lens. The tilt angle at 3.5 GHz can be calculated using Eqn. (1), which is $\theta = 36.6^{o}$ given that $n_{sub} = 1.26$, $n_{DGR} = 1.815$, $d = 37$ mm, $a = 8$ mm, and $L = 72$ mm.

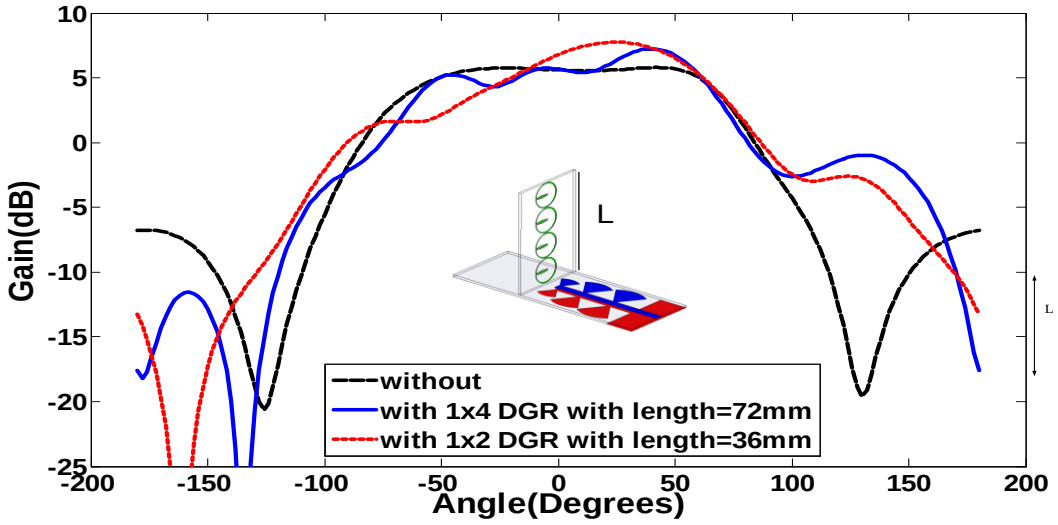

Figure 4-7: Radiation pattern of the antenna with 1×2 and 1×4 DGR unit-cells placed on the substrate.

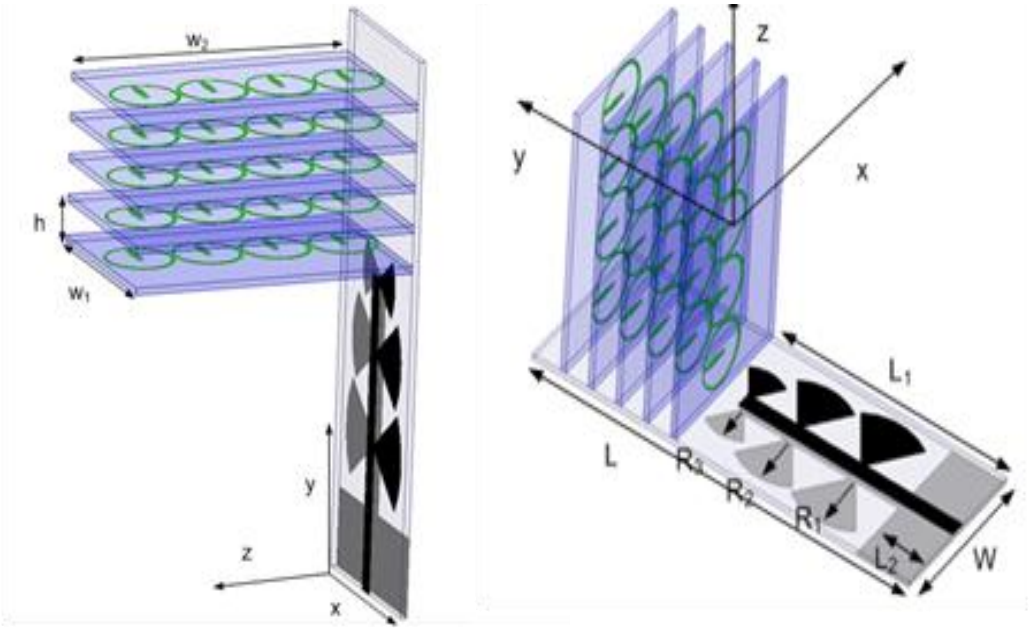

Figure 4-8: 3D configuration of proposed antenna with 5×4 array of DGR antenna.

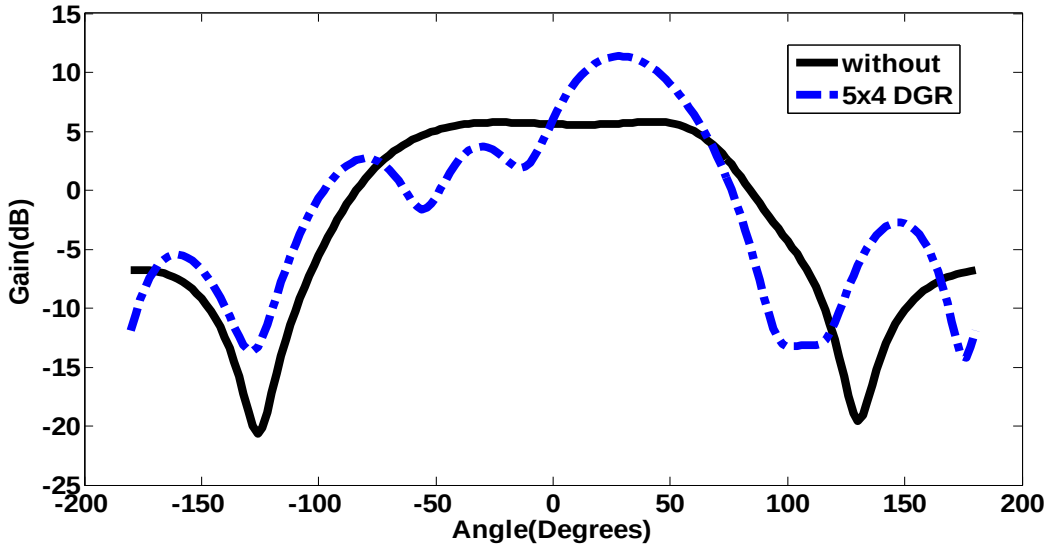

Figure 4-9: Radiation pattern of the antenna in the H-plane with and without DGR loading.

The Poynting vector distribution over the antenna shown in Fig. 4.10 reveals that when the DGR arrays are vertically mounted on the antenna substrate, the maximum beam direction is tilted towards the DGR slab. The tilting mechanism can be explained by Snell's law, i.e. $n_{DGR}\sin\theta_1 = n_{air}\sin\theta_2$ which applies at the boundary of the DGR lens and air. According to this equation, the angle θ_2 of the exiting wave from the DGR array into the air is refracted at a greater angle than the incident wave angle θ_1. The radiation from the antenna is refracted from end-fire (+*y*) to a broadside direction (+z) when the antenna is loaded with DGR array. This phenomenon can be clearly observed in Fig.4.10 (b), confirming the proposed DGR medium exhibits a high refractive-index.

To verify the proposed DGR antenna array acts as an artificial dielectric material of high refractive-index, the layers of the DGR array were replaced with a dielectric substrate of $\varepsilon_r = 9.1$. The dimensions of the structure were identical in the investigation. The resulting normalized radiation pattern in Fig.4.11 shows the direction of the main beam is tilted by 31^o, which is the same as the DGR array implemented on a dielectric material with a lower dielectric constant of $\varepsilon_r = 2.2$. This confirms the DGR array behaves like an artificial dielectric material with higher dielectric constant. The resonant nature of the DGR structure has an effect of increasing the peak gain of the antenna by 3 dB.

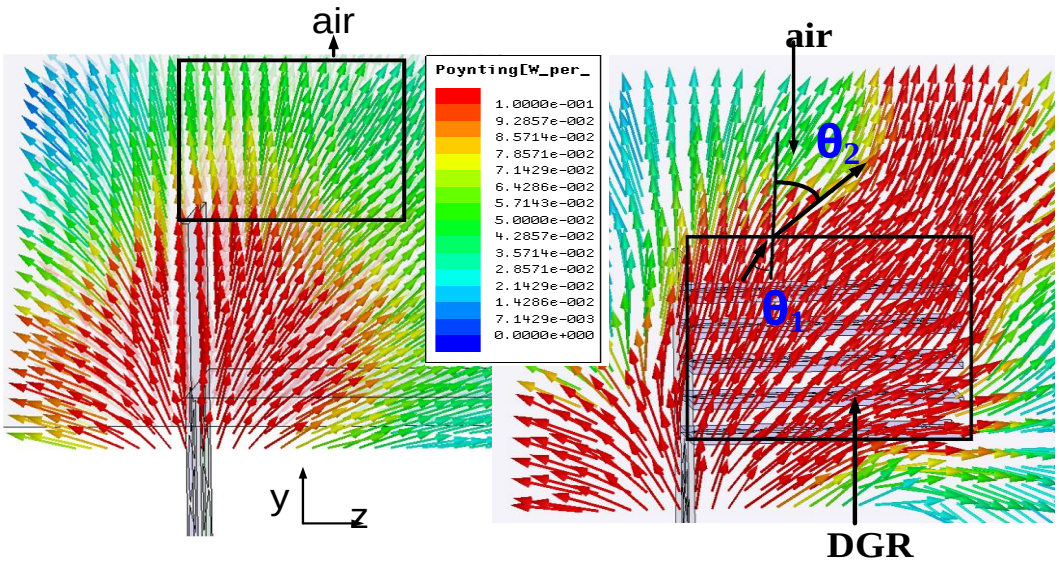

(a) (b)

Figure 4-10: Poynting vector distribution over the antenna in the H-plane (yz) at 3.5 GHz, (a) without DGR loading, and (b) with DGR loading.

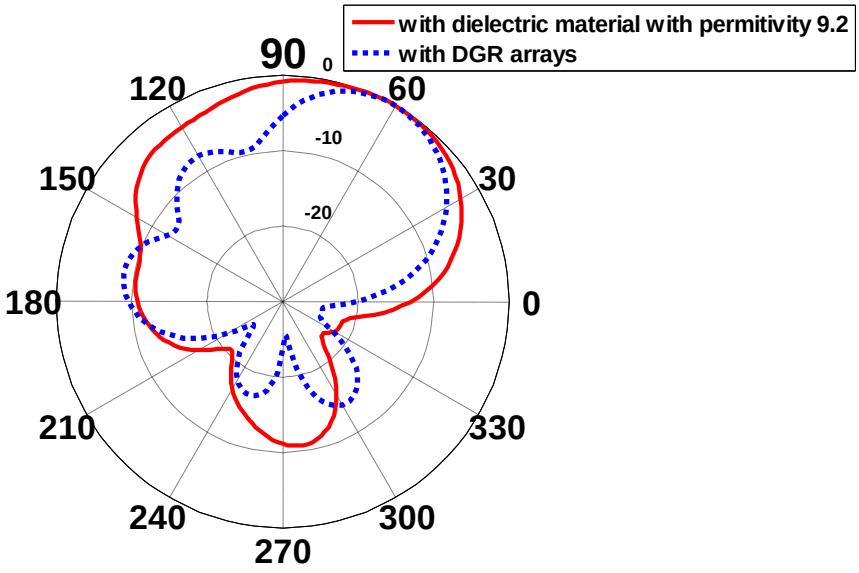

Figure 4-11: Normalized H-plane radiation pattern of the antenna loaded with the DGR array and implemented on a substrate having ε_r = 2.2; and when the DGR array is replaced with a plain dielectric substrate of ε_r = 9.1

4.6 **Parametric Study**

In this section, the results of a parametric study are presented on the number of the DGR unit-cell loading in each layer and their effect on the beam tilt angle. An investigation on the antenna was performed with a five-layer lens, but the number of the DGR unit-cells in each layer was varied from 1 to 4. Fig.4.12 shows a schematic view of the antenna with a five-layer lens, where each layer consists of one DGR unit-cell. The effect of different number of DGRs in each layer on the antenna gain, tilt angle and side-lobe level is given in Table I.

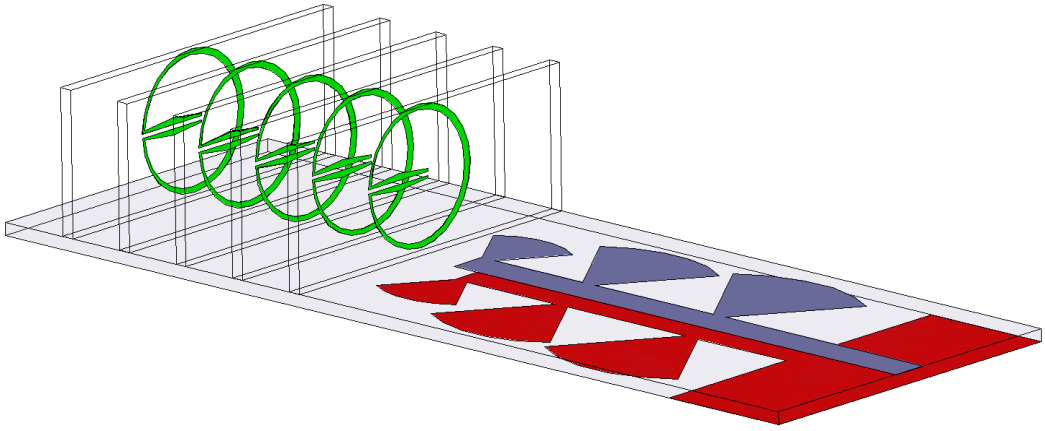

Figure 4-12: Bow-tie antenna with 5-layer lens where each layer comprises of one DGR unit-cell.

The H-plane radiation pattern of the antenna with different number of DGR unit-cells in the lens layer at 3.5 GHz is shown in Fig.4.13, whose main features are summarized in Table I. The results indicate that when the number of the DGR unit-cells in each layer is increased a higher tilt angle is produced. In particular, with five layers each of which is loaded with one DGR unit-cell (i.e. 5×1 array) the tilt angle is 8^{o}; however a 5×4 array exhibits a tilt angle of 31^{o}. The results in Table I show no discernible improvement in side-lobe-level when 5 layers are added. In Fig.4.13 the SLL of 8×1 array is -10.24 dB compared to -8 dB for the 5×1 array, which constitutes an improvement of 2.24 dB by using the 8×1 array. Hence some improvement in the SLL can be achieved by increasing

the number of DGR arrays in the +*y* direction. The results also show a reduction in the 3 dB beamwidth (BW) with increase in the number of DGR unit-cells. In fact, there is an average reduction in the 3 dB beamwidth by 10.6% with the addition of an extra DGR unit-cell. This is attributed to the resonant nature of the DGR structure resulting in higher quality-factor with increasing rows. From Fig.4.13 it can be observed that one feasible solution to maintain a larger beamwidth would be to use fewer layers in the end-fire direction. This technique can be applied for different number of DGRs to compensate the variation in the beamwidth. The parametric study reveals that the best performance of the antenna can be achieved when four rows (i.e. 5×4 DGR unit-cells) are employed.

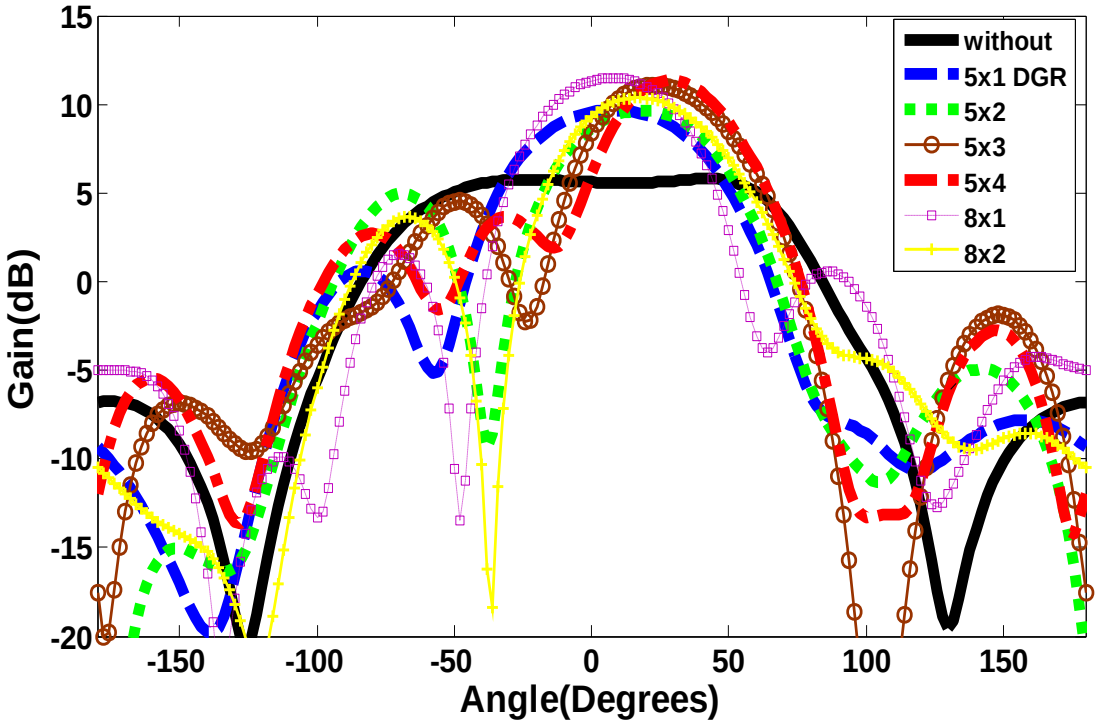

Figure 4-13: Radiation pattern of proposed antenna with different number of unit-cell loading in the z-direction

Table 4-1: The effect of DGR unit-cells on the antenna performance

No. of DGRs	Gain (dB)	Tilt angle (degree)	3 dB - BW (degree)	Side-lobe level (dB)
5×1	10.00	8	70	-8.0
5×2	9.65	19	64	-5.0
5×3	10.30	23	58	-7.0
5×4	11.00	31	50	-8.5
8×1	11.5	8	60	-10.24

The results in Table I indicate that the tilt angle can be varied from 8 to 31° when the DGR unit-cells are increased in the *z*-direction. This implies in a reconfigurable DGR the main beam can be steered electronically from 8 to 31°. This can be achieved by embedding PIN diodes in the structure of the DGR unit-cells.

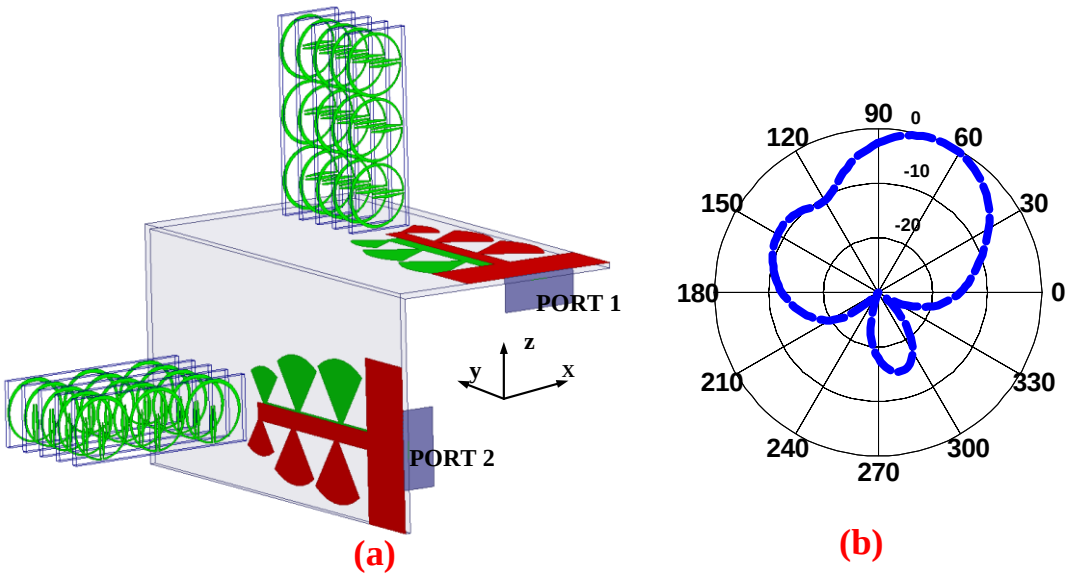

Figure 4-14: (a) Dual-polarized 5×3 DGR antenna array, and (b) H-plane radiation pattern of dual-polarized antenna at 3.5 GHz.

Dual-polarization can be achieved by setting up the proposed antenna in the orthogonal arrangement shown in Fig. 4.14(a). When port 1 is excited, the radiation pattern tilts by

30° in the H-plane at 3.5 GHz, as shown in Fig.4.14 (b). Cross-polarization level of the dual-polarized antenna is lower than the co-polarization by 20 dB.

The antenna tilt angle is a function of refractive-index however the refractive-index is a function of frequency, as is evident in Fig. 4.5. It is therefore inevitable the tilt angle will vary with frequency. The effect of frequency on the tilt angle can be minimized over a short frequency range by employing a DGR unit-cell that is non-resonant at the desired frequency of operation. This was demonstrated by loading the Bow-tie antenna with a 5×3 array of DGR unit-cells whose dimensions have been modified so that its refractive-index remains almost constant at 1.58 over 3.4–3.6 GHz. The simulation results in Fig. 4.15 shows the beam tilt is virtually fixed at 32° across 3.4–3.6 GHz.

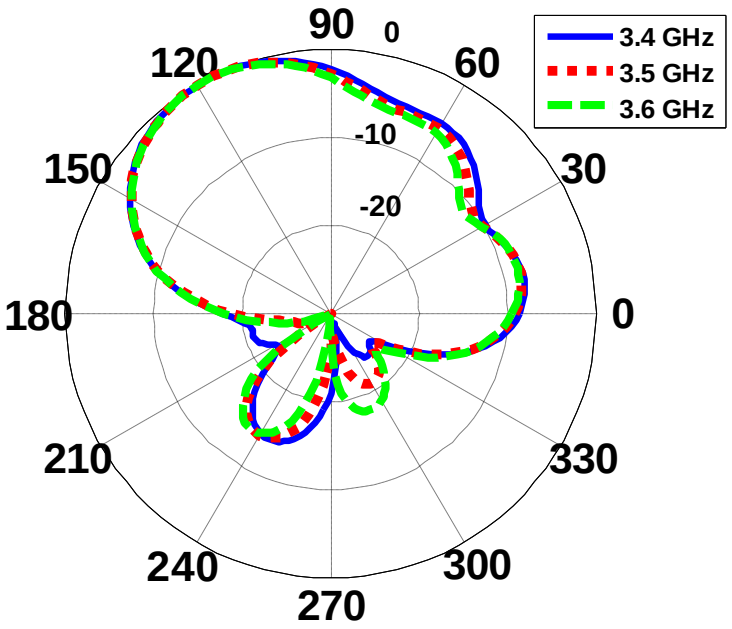

Figure 4-15: Radiation pattern of antenna when integrated with 5×4 CCR arrays.

4.7 **Experimental Results**

To verify the beam-tilting approach described above, a Bow-tie antenna was embedded with DGR unit-cells. The prototype was fabricated and its performance measured. The photograph of the fabricated prototype is shown in Fig. 4.16.

The measured reflection-coefficient of the antenna with and without metamaterial lens is shown in Fig.4.17. According to this figure, the DGR lens affects the reflection coefficient of the structure compared to the conventional antenna without metamaterial, albeit the reflection-coefficient of the antenna is better than -10 dB in the WiMAX band. The measured radiation patterns of the proposed structures with and without the DGR lens in the H-plane is plotted in Fig.4.18 at 3.4, 3.5, and 3.6 GHz. The results presented in Fig.4.18 are summarized in Table II. The measured gain enhancement at 3.5 GHz is 5.1 dB. The measurement of the peak gain at various frequencies was carried out using the gain-comparison method with a known standard horn antenna. Unlike conventional beam tilting methods, the proposed beam tilting technique is accompanied by increase in the antenna gain. The antenna gain can be increased by increasing the number of the unit-cells in the $+y$ direction. Fig.4.19 shows the measured radiation pattern of the proposed antenna with DGR unit-cells in the E-plane (xy) at 3.5 GHz.

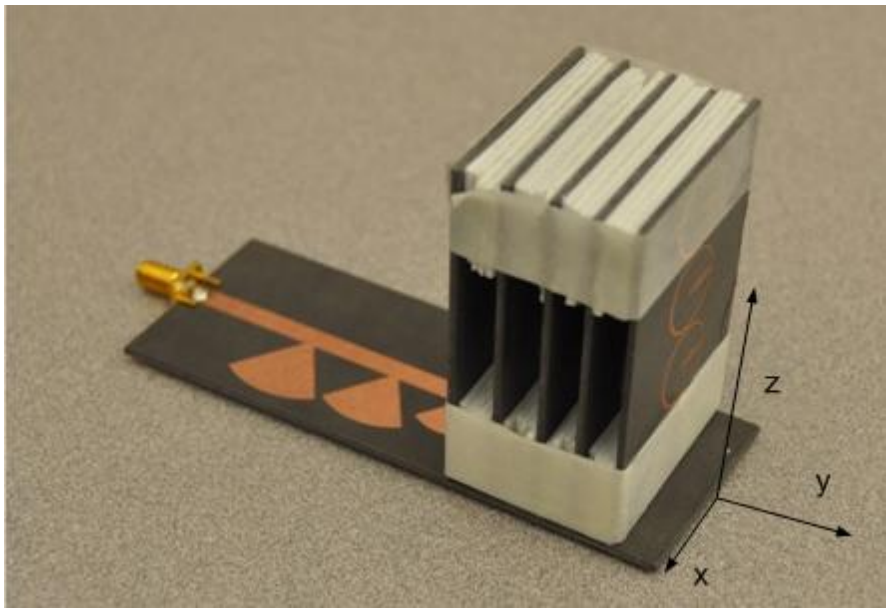

Figure 4-16: Photograph of the fabricated antenna loaded with 5×4 DGR unit-cells.

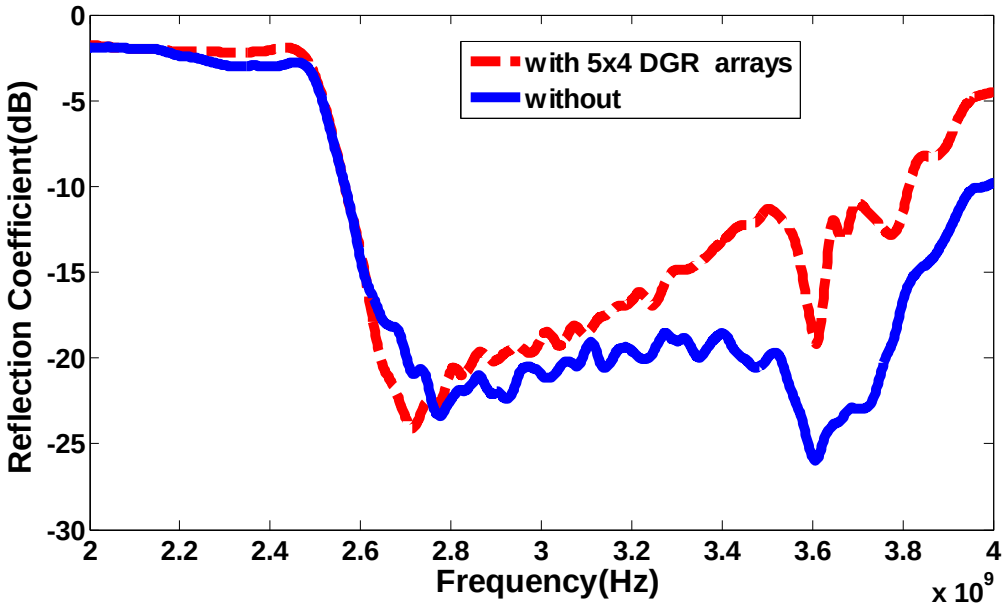

Figure 4-17: Measured reflection-coefficient of the Bow-tie antenna with and without DGR array loading.

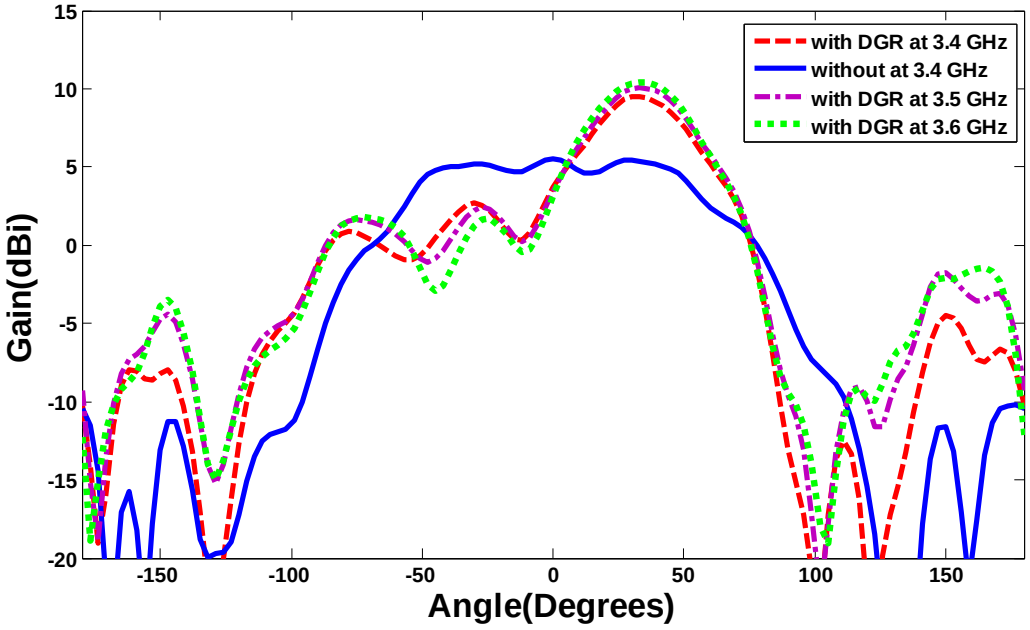

Figure 4-18: Measured radiation pattern of the proposed antenna in the H-plane with and without DGR loading at: 3.4 GHz, 3.5 GHz, and 3.6 GHz

Table 4-2: Measured peak gain of antenna at different scanned angles

Freq. (GHz)	Beam tilt angle with DGR (degree)	Measured peak gain without DGR (dB)	Simulated peak gain with DGR (dB)	Measured peak gain with DGR (dB)
3.4	30	5.1	10.0	9.8
3.5	33	5.1	11.0	10.2
3.6	35	5.2	11.2	10.4

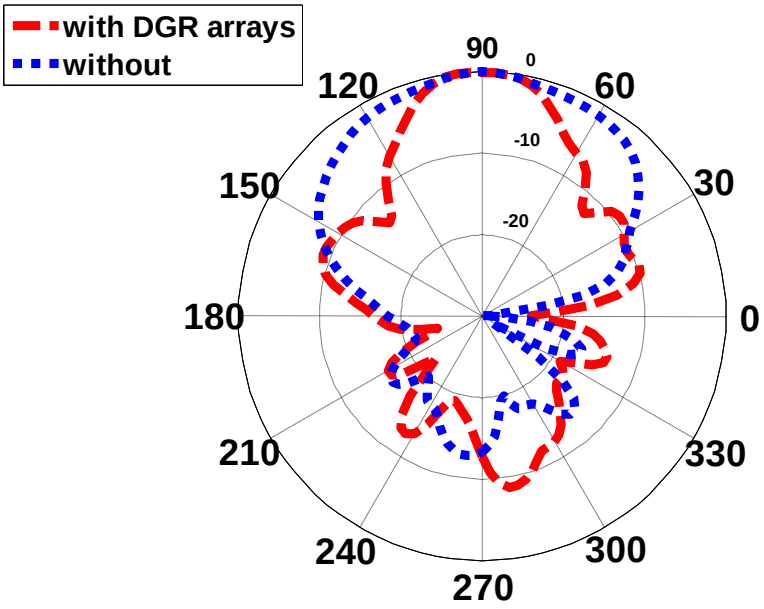

Figure 4-19: Measured radiation pattern of the proposed antenna in the E-plane with and without DGR unit-cells at 3.5 GHz.

4.8 **Electronic Beam switching in the Elevation plane**

In order to electronically switch the orientation of the main beam from -32 to +32^{o} with respect to the end-fire direction (+*y*), an additional Bow-tie antenna was added to the other side of DGR array, as shown in Fig.4.20(a). When port 1 is excited with port 2 terminated, the main beam tilted to 32^{o} towards the +*z* direction. The converse applies when port 2 is excited with port 1 terminated. As a result, by utilizing SP4T switch at the ports, the beam can be electronically tilted from -32 to +32^{o}. The proposed structure was validated practically. The measurement results shown in Fig.4.20 (b) confirm that the main beam of this structure can be switched from -32 to +32^{o} with respect to end-fire direction (+*y*) at 3.5 GHz and has a peak realized gain of 10.35 dBi. The S21 plot in Fig. 4.21 shows how much energy is absorbed into port 2 when radiated from port 1. The magnitude of S21 at 3.5 GHz is -16 dB which indicates that 2.5 percent of the power is absorbed at port 2 when power is radiated from port 1.

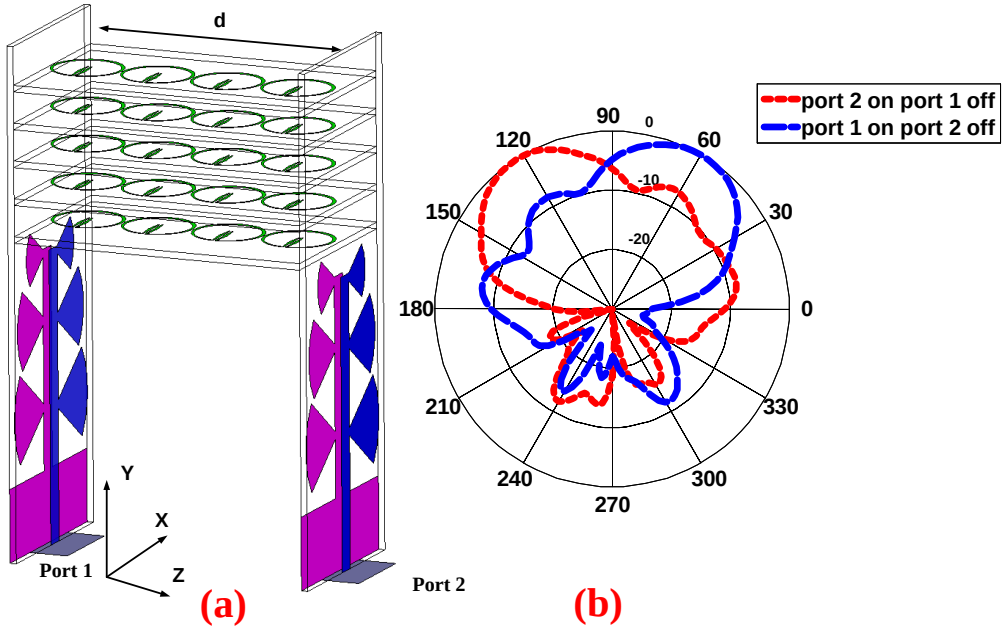

Figure 4-20: (a) DGR antenna array arrangement to deflect the beam from -32 to 32o respect to the end-fire direction (+y), (b) measured radiation pattern of the dual-feed Bow-tie antenna with DGR loading in the H-plane.

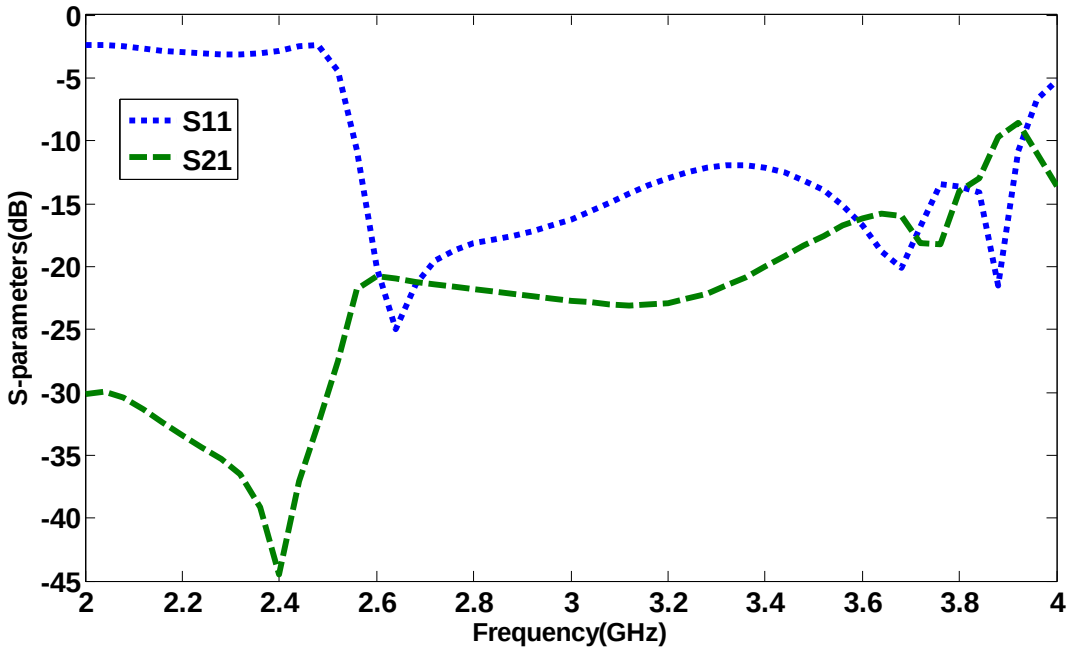

Figure 4-21: Insertion and reflection-coefficient of the DGR antenna array arrangement in Fig. 4-19.

4.1 Conclusion

A novel beam-tilting technique has been described for planar end-fire antennas like the Bow-tie. The technique uses an artificial composite structure with a high dielectric constant. Proof-of-concept is demonstrated at the WiMAX band (3.4–3.6 GHz). The proposed structure consists of three Bow-tie radiators connected symmetrically to a microstrip-line, and included in the vicinity of the radiators in the H-plane is a 5×4 array of DGR unit-cells that act as high refractive-index medium. The measured results show that the proposed lens tilts the antenna main beam by 35^{o} in the H-plane at 3.6 GHz. The maximum measured gain of the beam-tilting antenna is 10.4 dB at 3.6 GHz compared to 5.2 dB without the lens. Unlike conventional tilting methods, the proposed technique is accompanied by a gain enhancement. The magnitude of the reflection-coefficient is maintained better than -10 dB in the WiMAX band when the beam is tilted. The validity of the proposed technique for electronic beam switching networks was verified. A prototype of a double Bow-tie antenna arrangement using a 5×4 DGR array was fabricated and its performance measured. It was shown the main beam of the prototype is electronically switchable from -32 to $+32^{o}$ at 3.5 GHz. The proposed DGR Bow-tie antenna presents a viable candidate for future cellular or WiMAX applications

Chapter 5 **Millimeter-wave High-Gain SIW End-fire Bow-tie Antenna**

5.1 **Introduction**

The unlicensed industrial, scientific and medical (ISM) band centered at 60 GHz (57 GHz–64 GHz) provides a large bandwidth of 7 GHz however signals at these frequencies incur high loss due to atmospheric absorption. These characteristics make it suitable for high data rate (in the order of multiples of Gbps) applications over a short-range including the transmission of uncompressed high definition video streaming and wireless point-to-multipoint connections. High propagation loss at these frequencies makes the design of high-gain antennas crucial. For such antennas to be commercially viable they need to be compatible with low cost technologies. Numerous antenna designs at 60 GHz have been previously proposed and implemented using multi-layer technology including low temperature co-fired ceramic (LTCC), liquid crystal polymer (LCP) and high end hydrocarbon ceramic printed circuit boards (PCB) [35]-[43]. In [44] the authors have described a high gain antenna operating at 60 GHz using dielectric resonator antenna (DRA) which is surrounded with an electromagnetic band-gap (EBG) structure to provide a maximum peak gain of 8.7 dBi. The aforementioned antenna designs are complex and expensive to fabricate. In addition, they have a broadside radiation pattern that restricts their application in beam-switching systems.

In this chapter a planar bow-tie antenna is presented that uses an amalgamation of different techniques to realize a high gain structure for operation over 57 GHz–64 GHz. Work in this paper is inspired by reference [45]. Configuration of the proposed antenna, shown in Fig.1, comprises a pair of bow-tie radiators. Each radiator is etched on the opposite sides of the substrate and arranged to cross each other symmetrically. The radiators are tilted by 30 degrees with respect to the end-fire direction (+*y*) to increase the antenna gain and determine its radiation pattern. The antenna is loaded with double G-shaped resonators (DGR) that have a band-stop property. The two DGR structures are located in the vicinity of the bow-tie radiators and SIW in order to suppress the back-lobe level in the H-plane. An array of zero-index metamaterial (ZIM) unit-cells is embedded laterally in the E-plane above the bow-tie radiators to convert the spherical waves into uniform field distribution. The fabricated bow-tie antenna provides a gain of 11.5–12 dBi

over 57 GHz–64 GHz, and a reflection-coefficient of less than -11 dB. Although the proposed antenna exhibits a comparable gain performance to previously reported millimeter-wave antenna designs [35]-[45], it has the advantage of being a simpler structure that is cost effective to fabricate.

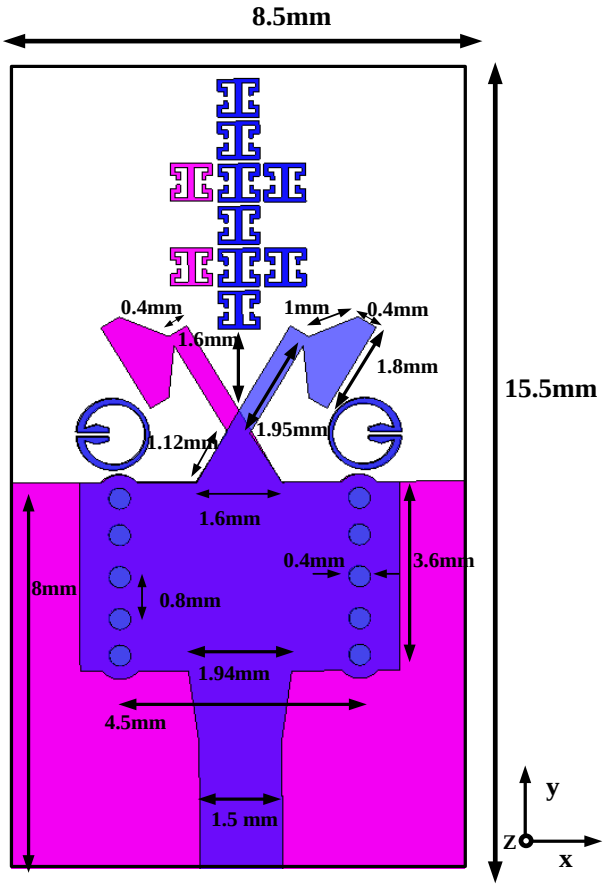

Figure 5-1: Configuration of the proposed tilted bow-tie antenna with DGR and an array of ZIM unit-cells

In the following section, we first propose the initial design of the bow-tie antenna with SIW feed-line. The antenna's characteristics are then investigated when the bow-tie radiator is tilted with respect to the end-fire direction. It is shown that when the antenna is loaded with double G-shaped resonators its back-lobe level in the H-plane and gain are enhanced. Lastly, we propose a zero-index metamaterial unit-cell structure. An arrangement of these ZIM unit-cells are embedded laterally in the E-plane of the tilted bow-tie antenna to realize a high gain response over 57 GHz–64 GHz.

5.2 **Antenna Design**

The geometry of the proposed antenna in Fig.5.1 consists of a SIW structure resembling a rectangular tunnel created between the top and bottom copper foils of the dielectric substrate that is surrounded by the two rows of metallic vias. The tunnel is equivalent to a dielectric-filled rectangular waveguide, where the two rows of metallic vias are equivalent to its side walls. The SIW configuration that is depicted in Fig. 1 is a modified version described in [46]. This configuration creates a 180 degree phase difference between the currents along the top and bottom layers of the SIW structure. The lower end of the SIW structure is tapered to a microstrip feed-line, and the upper end tapered to a bow-tie radiating element. The bottom of the substrate comprises a truncated ground plane with an identical bow-tie antenna that is arranged to symmetrically cross with the dipole antenna on the top metallic layer of the substrate.

The SIW structure was fabricated on RT 5880 dielectric substrate with relative permittivity of 2.2, thickness of 0.5 mm and loss tangent of 0.0009. The feed-line to the SIW structure has a tapered transition to provide a good impedance match over the required frequency range of 57 GHz–64GHz.The normalized E-plane (*xy*) and H-plane (*yz*) radiation patterns of this structure at 60 GHz are shown in Fig.5.2. The worst case back-lobe level (BLL) in H-plane is about -0.6 dB which is not appropriate for practical purposes. The worst case side-lobe level (SLL) in the E-plane (*xy*) is about -7 dB. Improving the BLL in the H-plane will result in more power being directed into the end-fire direction. Since the antenna gain is inversely related to its beamwidth, so improving the SLL in the E-plane (*xy*) will result in a narrower beamwidth and enhanced gain performance.

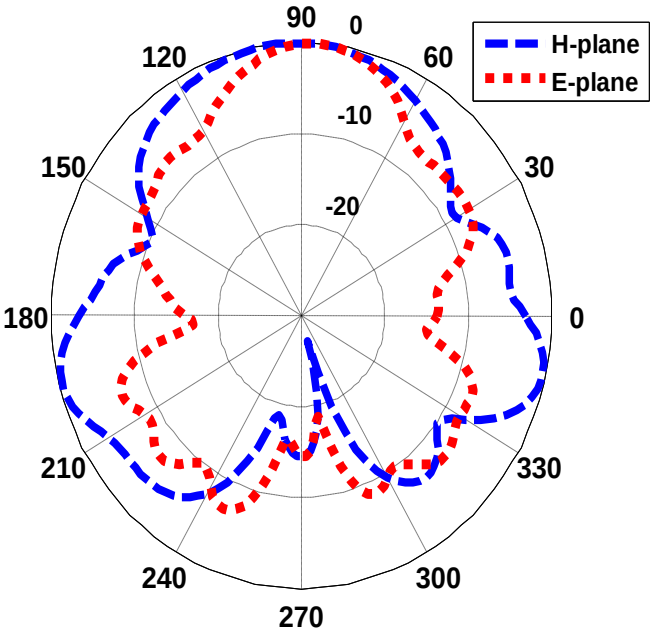

Figure 5-2: The normalized radiation patterns of the un-tilted bow-tie antenna in the E- and H-planes at 60 GHz. Angle is in degrees and radius in dB.

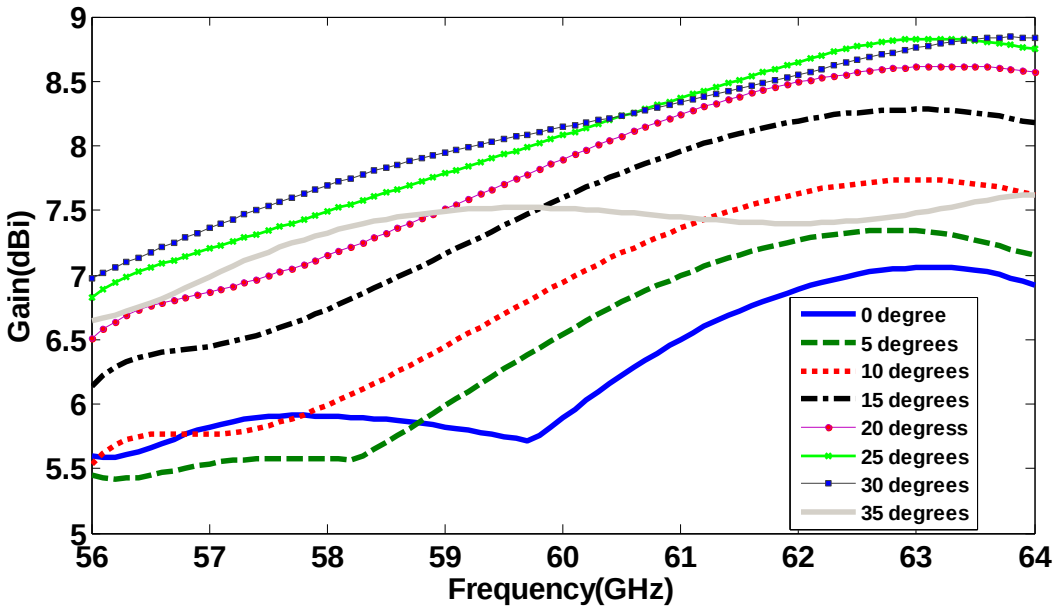

Figure 5-3: Antenna gain response as a function of bow-tie tilt angle.

5.3 **The Effect of bow-tie radiator tilt angle**

The tilt angle of the bow-tie radiators with respect to *y*-axis was investigated. The results of this study in Fig.5.3 show that increasing the tilt angle from 5 to 30 degrees has a direct effect on the antenna gain. Certain tilt angles improve the antenna gain over the frequency range of 56 GHz–64 GHz, which is equivalent to enlargement of the antenna aperture. A tilt angle of 30 degrees is observed to provide an optimum gain performance. At a tilt angle of 30 degrees, the gain varies between 7–8.8 dB, which corresponds to a gain enhancement of 1.5–2.0 dB over frequency band of 57 GHz–64 GHz compared with the antenna with 0 degree tilt angle.

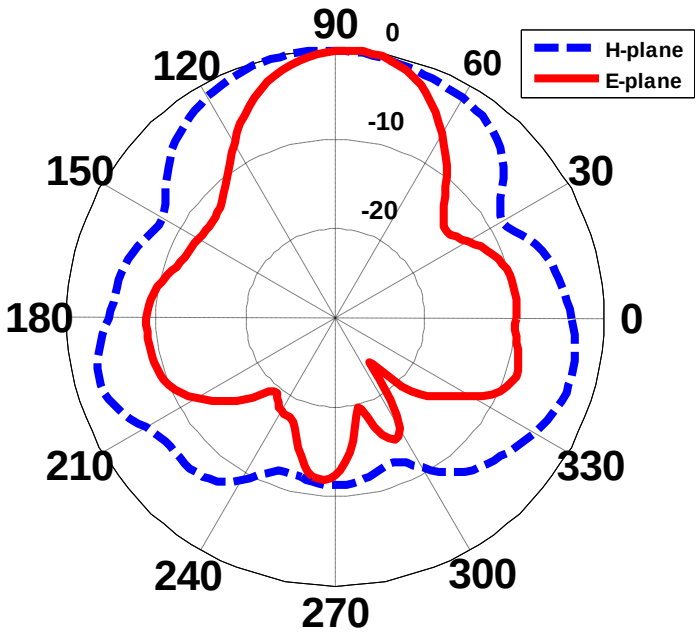

Figure 5-4: The normalized radiation patterns of the tilted bow-tie antenna in the E- and H-planes at 60 GHz. Angle is in degrees and radius in dB.

The radiation patterns of the antenna with the bow-tie radiators tilted by 30 degrees are shown in Fig.5.4. This result shows there is a distinct improvement in the SLL in both E-

plane (*xy*) and H-plane (*yz*) however there is degradation in BLL compared with the un-tilted radiators in Fig. 2.

5.4 **The Effect of DGR loading**

In order to reduce the back-lobe radiation in the H-plane (*yz*), the double G-shaped resonator, shown in Fig.5.5, was employed. This resonator is based on the broadside coupled split-ring resonator structure described in [47]. The DGR structure is constructed on both layers of the substrate in the vicinity of the bow-tie radiating elements. This is necessary to couple the DGR with the electromagnetic field emanating from the radiating elements in order to induce current along the perimeter of DGR structure. The DGR behaves equivalently to an LC resonant circuit which is excited by an EM wave source.

The S-parameters of the DGR structure in Fig.5.5 were established by applying the ports on both sides of the resonator along the *xy*-plane. Application of a plane wave along the *y*-axis results in the electric and magnetic field polarized in the *x*- and *z*-axis, respectively.

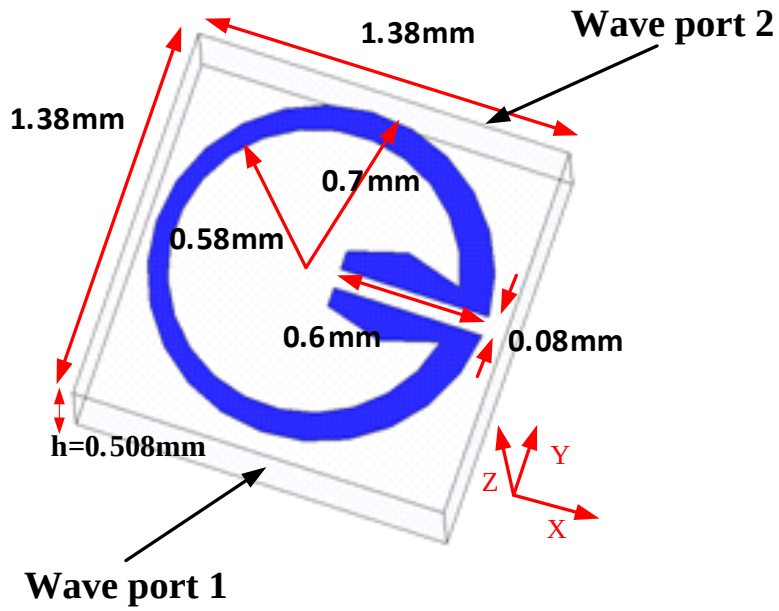

Figure 5-5: The structure of the double G-shaped resonator.

The S-parameter response of the DGR structure in Fig.5.6 exhibits a wide bandstop response over 55.4 GHz–65 GHz for a rejection level greater than -10 dB. Embedding the proposed DGR structure on both sides of the substrate and next to the tilted bow-tie radiators, results in reduction of the BLL. In the H-plane (*yz*) BLL is reduced by about 4 dB and in the E-plane (*xy*) by about 3dB, as shown in Fig.5.7. The E-field distribution over the antenna, which is shown in Fig.5.8, clearly demonstrates there is a reduction in the E-field intensity at the sides of the tilted bow-tie radiators in the locality of the DGR structures.

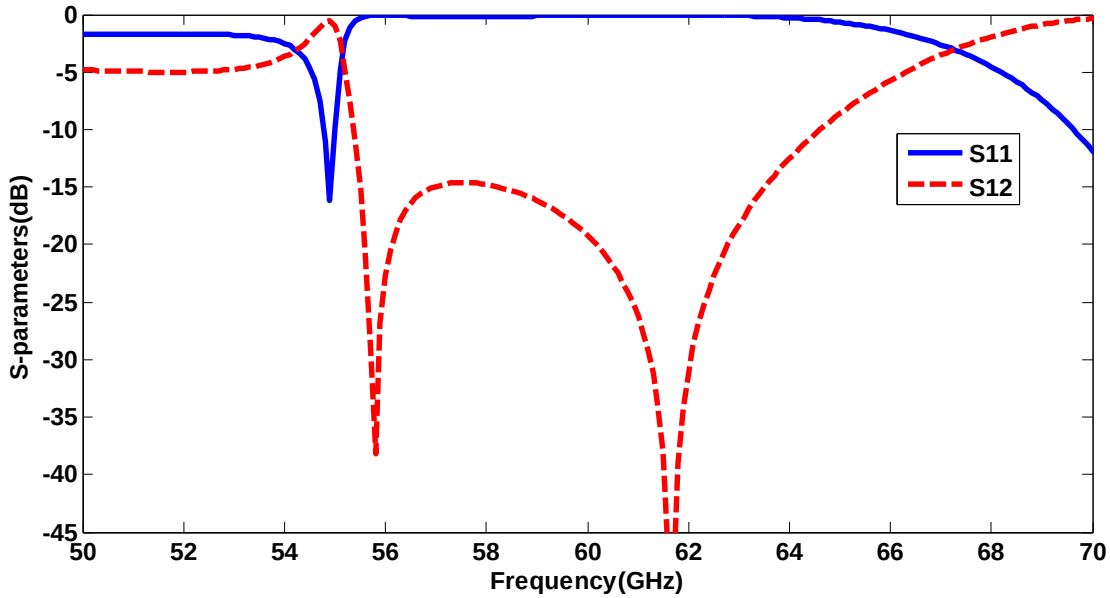

Figure 5-6: S-parameter (|S12| and |S11|) response of the DGR configuration.

With DGR loading, the antenna gain varies from 9.57 to 8.14 dB over 57 GHz–64GHz, as shown in Fig.5.9. Gain enhancement of 2.14–0.28 dB is observed across 57 GHz–62 GHz compared with the bow-tie antenna without DGR loading. However, above 62.5 GHz the gain begins to decline and reduces by 0.7 dB at 64 GHz.

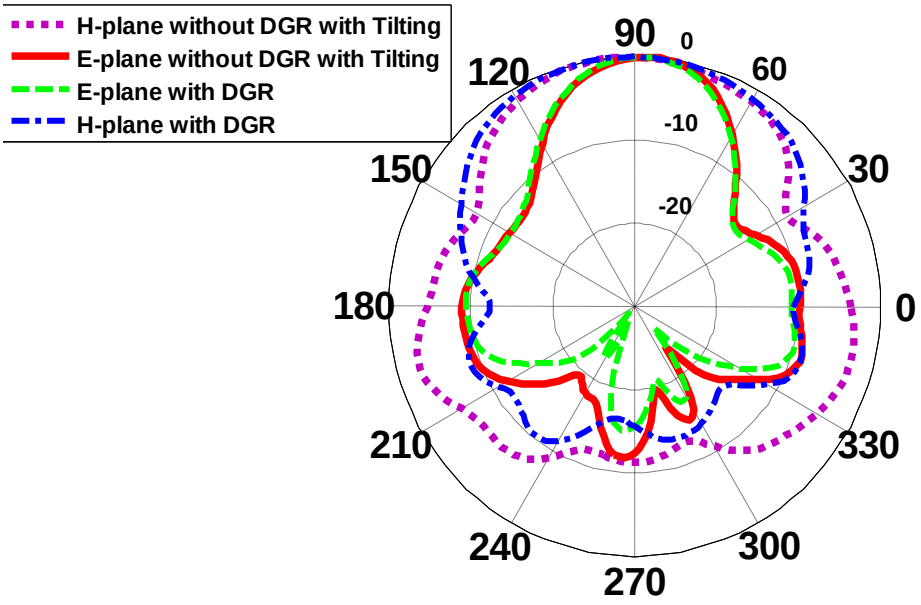

Figure 5-7: The normalized radiation patterns of the proposed antenna with and without DGR loading in the E-and H-planes. Angle is in degrees and radius in dB.

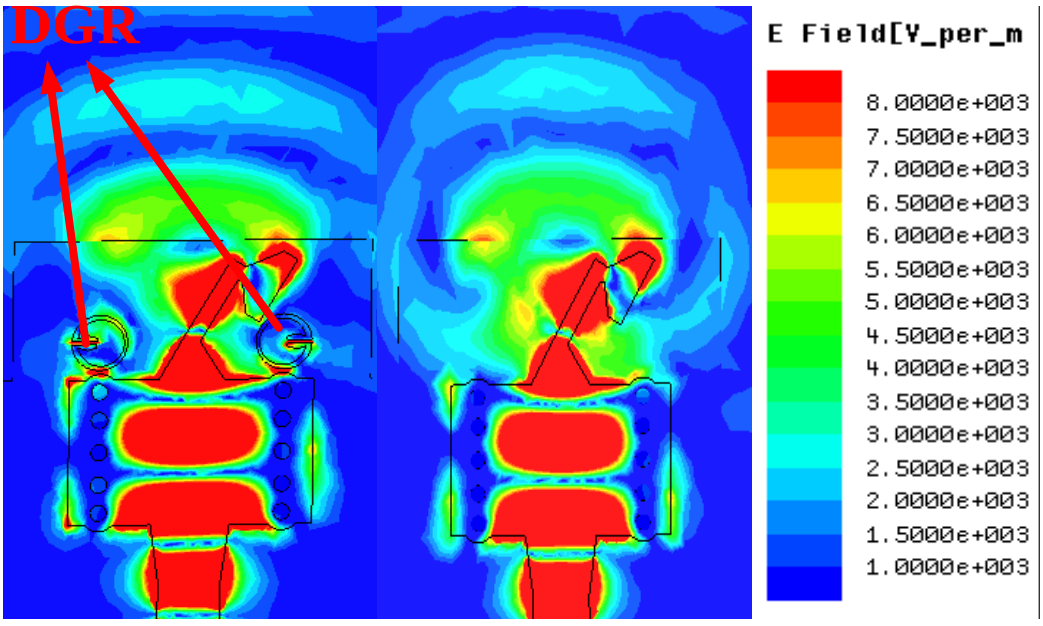

Figure 5-8: The E-field distribution over the tilted antenna: (a) with DGR loading, and (b) without DGR loading.

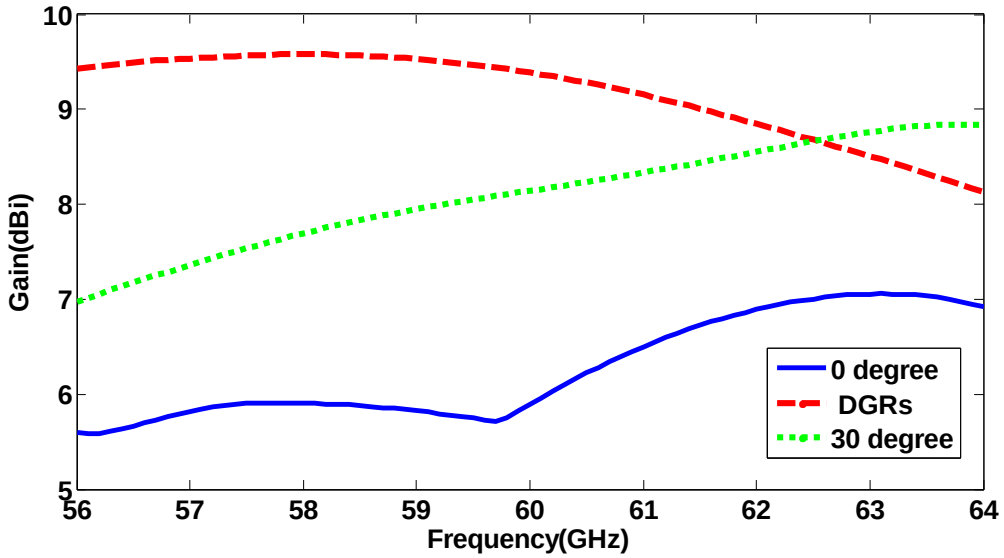

Figure 5-9: Comparison of bow-tie antenna gain for un-tilted and tilted radiators, and the antenna gain for a tilted bow-tie antenna with DGR loading.

5.5 **ZIM Unit-Cell**

In order to enhance the gain of the antenna a zero-index metamaterial unit-cell structure, shown in Fig.5.10, was embedded in the antenna. The ZIM unit-cell structure is a modified version of the electric LC resonator described in [48]. Here we have increased the effective inductance and capacitance of the structure so that its resonant frequency is lower and it exhibits near zero permittivity over frequency range 57 GHz–64 GHz.

The intrinsic electrical parameters of the ZIM unit-cell (effective permittivity and permeability) were determined using a standard extraction algorithm which is described in [49] and is based on the S-parameters. This involves assigning a perfect electric conducting (PEC) and the perfect magnetic conducting (PMC) boundary conditions in the *xz*-plane and *xy*-plane to the ZIM structure in Fig.5.10. The transmission and reflection-coefficient response of the ZIM unit-cell in Fig.5.11 shows the signal is uninhibited to pass through the structure over the required operating frequency range of 57 GHz–64 GHz.

The extracted effective permittivity, permeability and refractive-index of the proposed ZIM unit-cell are shown in Fig.5.12. The simulation results show that the refractive-index

of the ZIM unit-cell is less than unity over the frequency range of 55 GHz–65 GHz. It also shows the permittivity is less than 0.75 over the frequency range of 55 GHz–64 GHz.

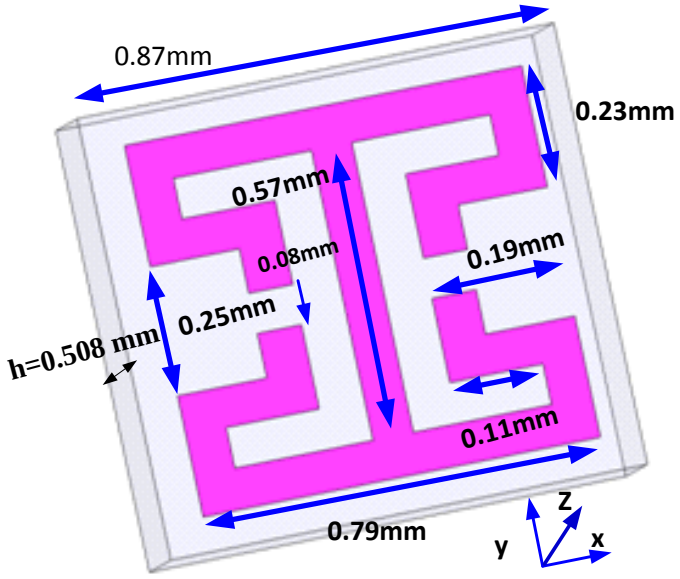

Figure 5-10:The configuration of the ZIM unit-cell.

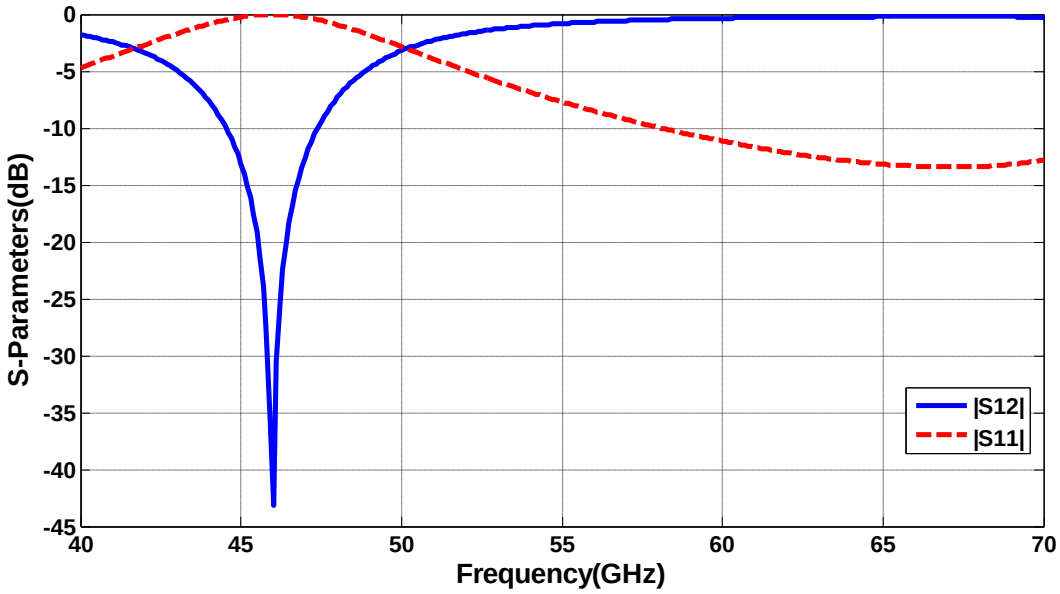

Figure 5-11:S-parameter (|S12| and |S11|) response of the proposed ZIM bow-tie antenna.

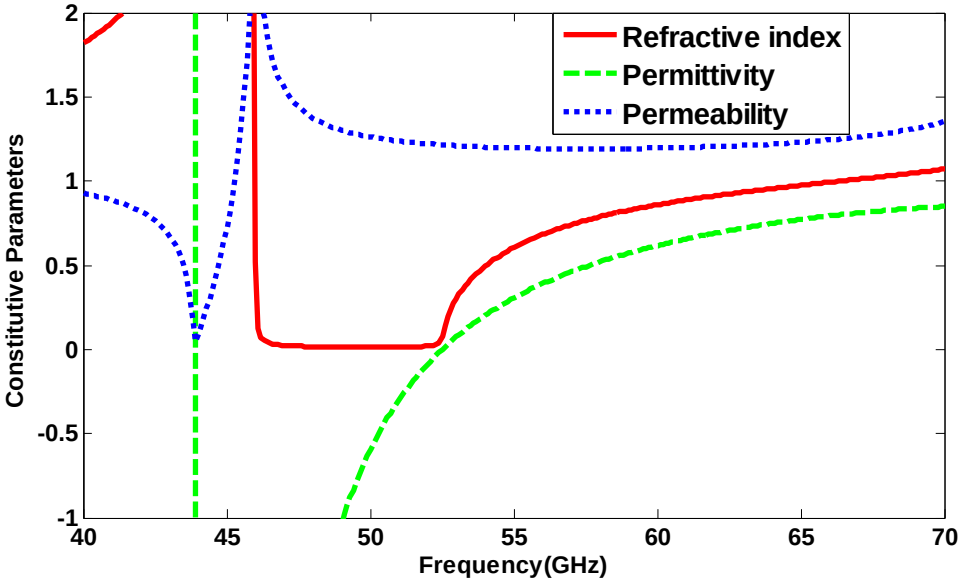

Figure 5-12: Retrieved characterizing parameters of the ZIM unit-cell, i.e. permittivity, permeability, and refractive index.

5.6 **Antenna with Array of ZIM Unit-Cell**

In this section, various combinations of ZIM unit-cell arrangements etched on the antenna are investigated. The ZIM unit-cells are embedded laterally in the E-plane above the tilted bow-tie antenna which is loaded with DGR structures. The initial antenna design is loaded with the number of ZIM unit-cells (1,3,5) from the bow-tie antenna to $+y$ direction. The antenna gain of this array configuration varies between 11.8-11.3 dB over 57 GHz –64 GHz, as shown in Fig.5.13. An array configuration of (1,3,1,3,1,1) ZIM unit-cells provides a gain variation of 11.8–12.5 dB between 57–64 GHz, which corresponds to an average gain enhancement of 3.95 dB compared with the tilted bow-tie antenna without ZIM unit-cells. An array configuration of (1,3,1,3,1,1) ZIM unit-cells is used in the final antenna design.

The radiation patterns in the E-plane (xy) and H-plane (yz) of the final antenna consisting of tilted bow-tie radiators with embedded DGR structures and ZIM unit-cell arrays are shown in Fig.5.14. Compared with the radiation patterns of the initial bow-tie

antenna in Fig.5.2, it can be observed that the side-lobe and back-lobe level in both planes are improved considerably by approximately 10 dB.

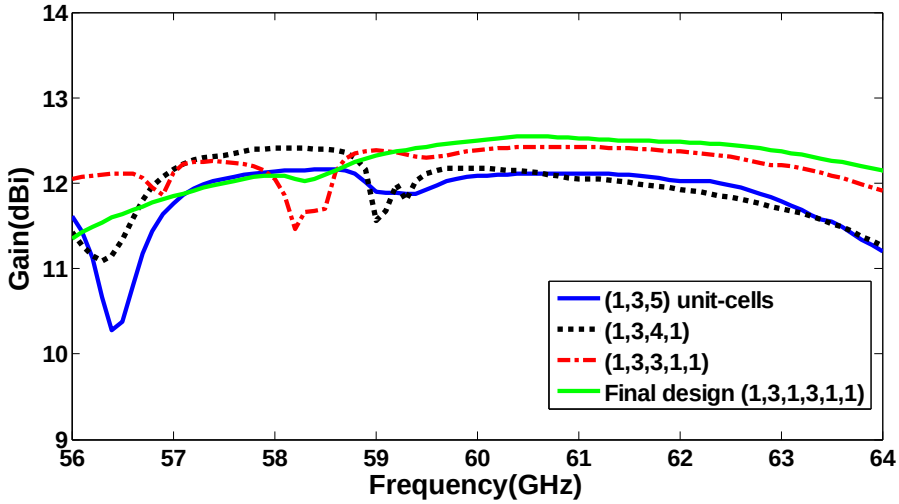

Figure 5-13: Antenna gain with various ZIM unit-cell arrangements.

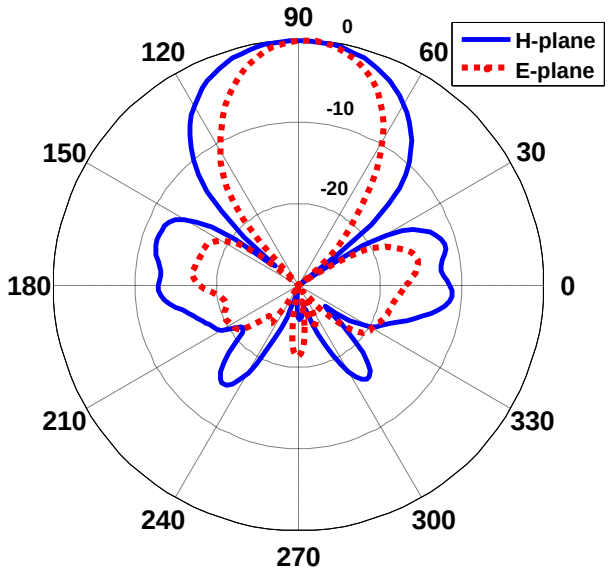

Figure 5-14: The normalized radiation patterns of the final antenna in the E- and H-planes at 60 GHz. Angle is in degrees and radius in dB.

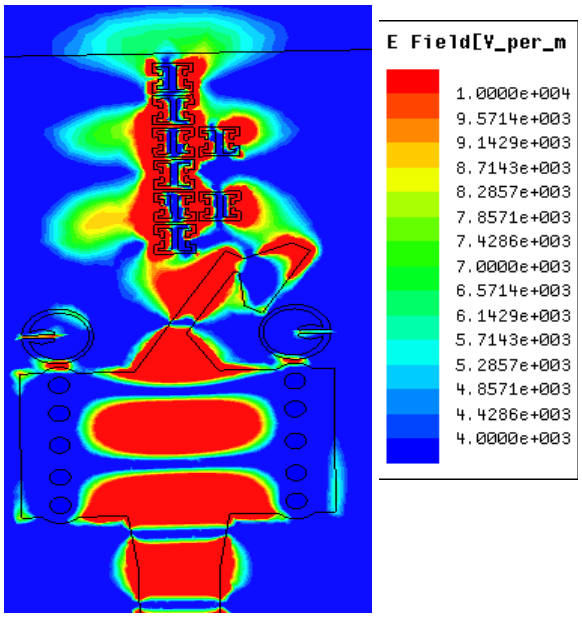

Figure 5-15: The E-field distribution over the antenna at 60 GHz.

The E-field distribution over the final antenna in Fig.5.15 confirms that the DGR and ZIM unit-cell loading has a great impact on confining the radiation beam to end-fire direction and suppressing the antenna's side and back-lobes.

5.7 **The Experimental Results**

The proposed tilted bow-tie antenna incorporating an array of ZIM unit-cells and a pair of DGR structures was fabricated and its performance was measured. The photograph of the fabricated prototype antenna is shown in Fig.5.16. The magnitude of S11 was measured using an Anritsu 3739C Vector Network Analyzer. The 1.85 mm end-launch connector was utilized to measure the reflection-coefficient. The measured reflection-coefficient of the antenna, shown in Fig.5.17, is less than -15 dB over 59 GHz–64 GHz. The radiation patterns were measured using MI Technology anechoic chamber using the antenna test arrangement shown in Fig.5.18, where a horn antenna was located at the focal point of the reflector to generate a plane wave towards the antenna under test.

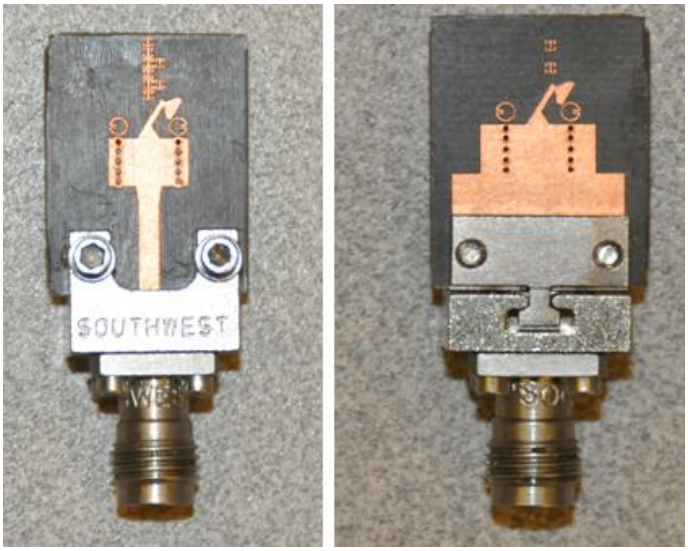

(b) (a)

Figure 5-16: Photograph of the fabricated prototype antenna, (a) top, and (b) bottom.

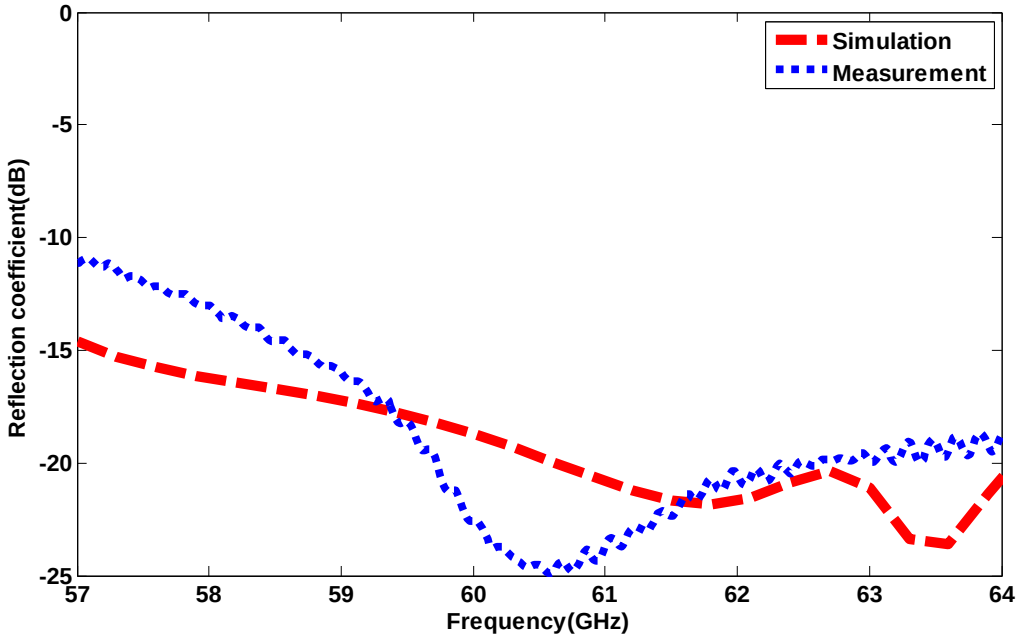

Figure 5-*17*: Measured and simulated reflection coefficient of the ZIM tilted bow-tie antenna.

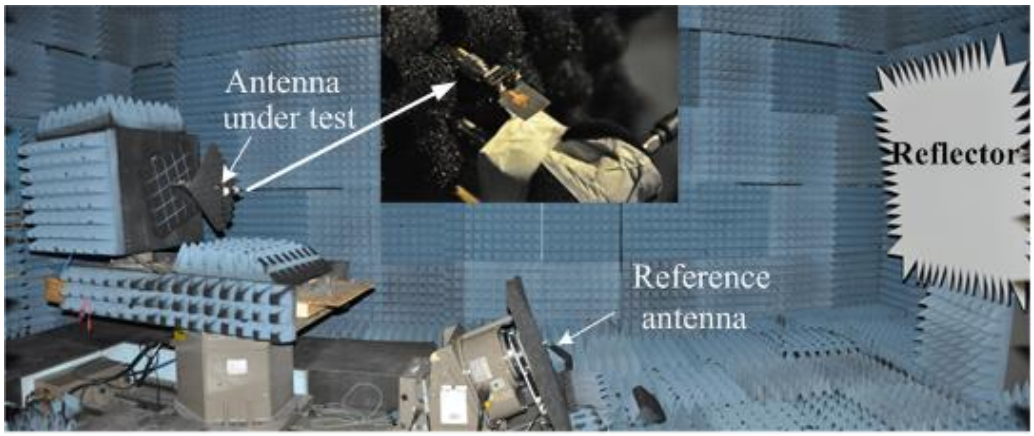

Figure 5-18: Photograph of the antenna measurement set-up.

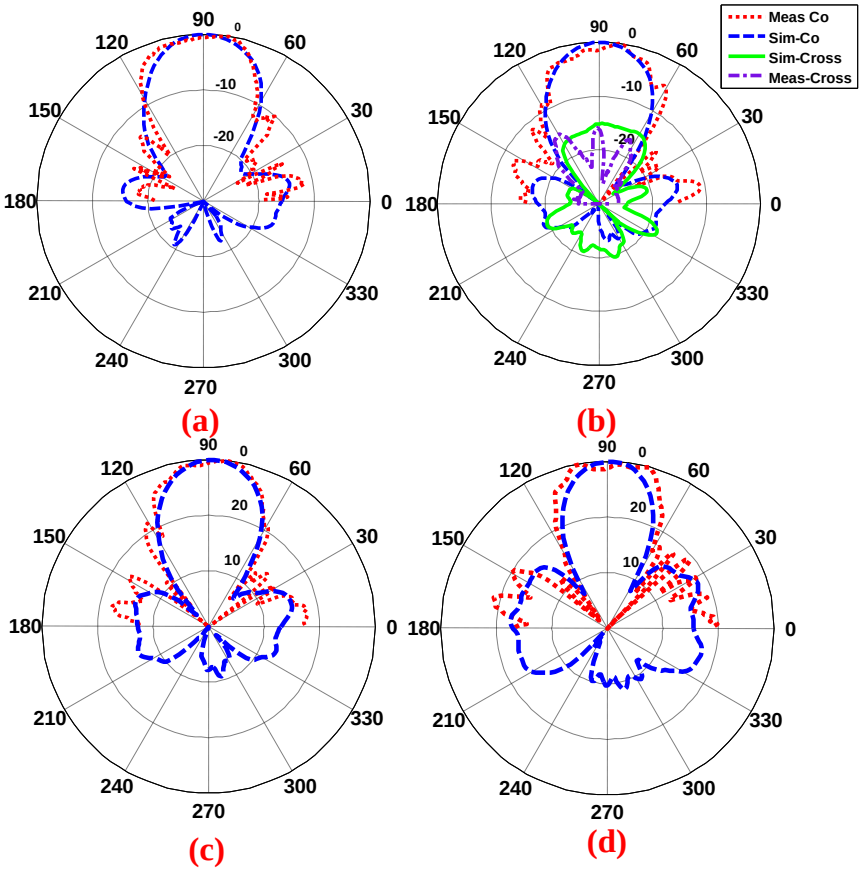

Figure 5-19: Normalized simulated and measured radiation patterns of the proposed antenna in the E-plane(x-y) at: (a) 58 GHz, (b) 60 GHz (c), 62 GHz, and (d) 64 GHz. Angle is in degrees and radius in dB.

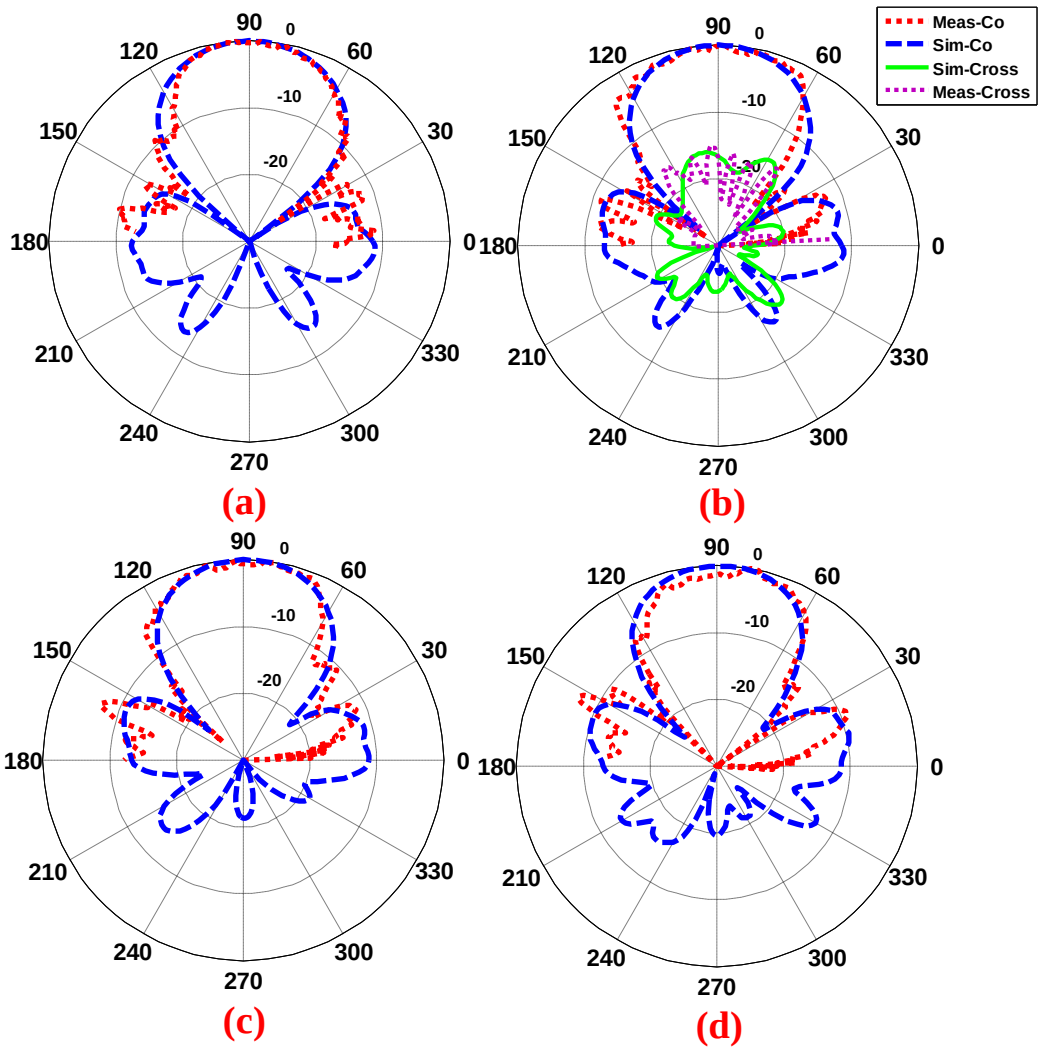

Figure 5-20: Normalized simulated and measured radiation patterns of the proposed antenna in the H-plane (yz) at: (a) 58 GHz, (b) 60 GHz, (c) 62 GHz (d), and 64GHz. Angle is in degrees and radius in dB.

The measured radiation-patterns of the ZIM bow-tie antenna in the E-plane (*xy*) and H-plane (*yz*) at 58, 60, 62 and 64 GHz are plotted in Fig.5.19 and 5.20. Correlation between the simulated and measured results is good. The results indicate that the side-lobe level of the antenna in the H-plane is less than -11.5 dB at 60 GHz and less than -9.7 dB at 64 GHz, which is better than that of Yagi-Uda design in [50] that has SLL of -5 dB; and the front to back radiation in both planes is better than -20 dB. Additionally, the cross-polarization of the antenna in the E-plane (*xy*) and H-plane (*yz*) is better than -17 dB at 60

GHz, which is better than ZIM Vivaldi antenna in [45] with -10 dB cross polarization. The measured radiation efficiency of the antenna is 91% at 60 GHz.

The antenna gain was measured using the comparative method that involves measuring the signals received by the reference horn antenna and the test antenna, and determining the relative difference in the gain of both antennas. The measured loss due to SIW and 1.85 mm end-launch connectors, shown in Fig.5.21, is 2–2.5 dB over the frequency range of 57 GHz –64 GHz. This loss was taken into account in the gain measurement. It is important to mention that in the simulation we have used wave ports on both ends of the SIW structure shown in Fig.5.21, and the simulated antenna gain takes into account the SIW loss.

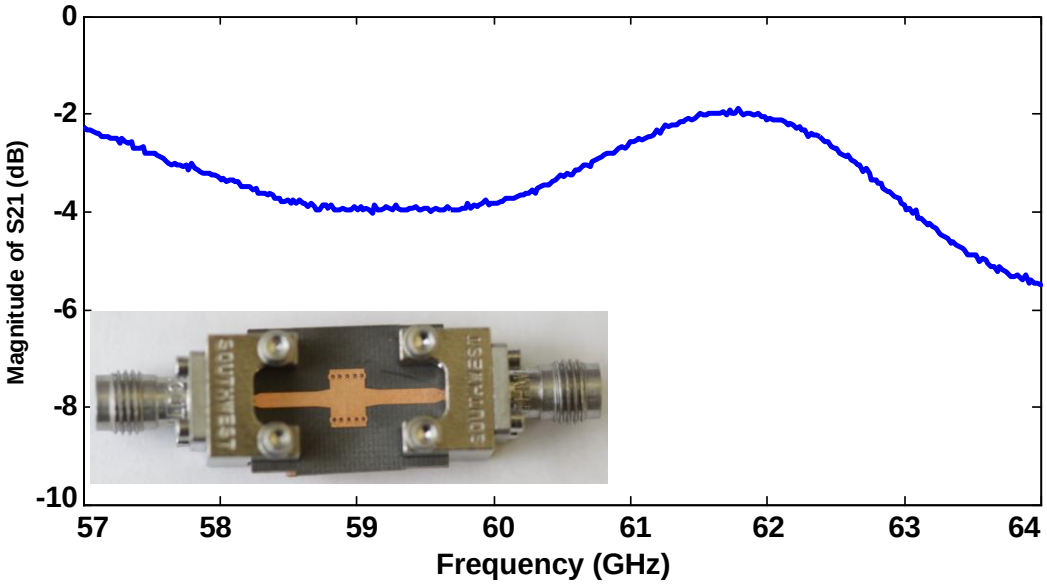

Figure 5-21: Measured insertion-loss of back-to-back end-launch connectors along with SIW microstrip line.

The measured peak gains of the proposed antenna are given in Table I. The discrepancy between simulation and measurement results is about 0.5 dB.

Table 5-1: Measured and simulated gain of the proposed tilted bow-tie antenna at various frequencies

Freq. (GHz)	Simulated peak gain (dB)	Measured peak gain (dB)
58	11.9	11.5
60	12.4	12.0
62	12.5	12.0
64	12.1	11.7

5.8 **Conclusion**

A modified bow-tie antenna structure is proposed for high gain performance across 57 GHz–64 GHz. The antenna consists of a pair of tilted bow-tie radiators, where each radiator is etched on the opposite side of the common dielectric substrate and fed through substrate integrated waveguide (SIW) feed-line. The bow-tie radiators are arranged to cross each other symmetrically in order to enhance the antenna gain and to obtain the required radiation pattern. It is shown that the antenna gain can be significantly enhanced by loading the antenna with an array of ZIM unit-cells that are implemented laterally to the radiators. In addition, double G-shaped resonators are employed to reduce the back-lobe level of the antenna. The antenna exhibits a measured gain of 11.5–12 dBi over frequency range of 57 GHz–64 GHz with reflection-coefficient less than -11 dB. The proposed antenna is simple to design and inexpensive to fabricate. The characteristics of the antenna make it suitable for application in 60 GHz indoor wireless communication systems.

Chapter 6 **Beam Deflection Using Gradient refractive index media for 60 GHz end-fire antenna**

6.1 **Introduction**

The 60GHz unlicensed frequency band has attracted considerable attention in the light of its large frequency band (57–64 GHz) and high absorption loss. Operation at this frequency band enables reduction of interference as well as greater frequency reuse factor. These characteristics make it very attractive for short-range wireless indoor communication and multi Gb/s data rate systems. One major challenge in the implementation of 60GHz wireless systems is high path-loss, which can be compensated using high gain antennas. However, high gain antennas possess a narrow beamwidth that makes beam alignment difficult, especially where the location of transmitter or receiver is not fixed. Adaptive antennas provide a solution to negate this issue but this is costly [51]-[52]. Another viable technique to re-direct the main beam towards specific direction is based on liquid crystal phased array using reflection-type phase shifter [53] however the scanning is limited to 27^{o}. This can be overcome using a beam forming network like the Butler matrix [54]-[56] but this can increase the overall system size.

The planar 60 GHz switched beam patch antenna in [54] is implemented using a 4×4 Butler matrix that can switch the direction of the main beam in four directions. This antenna has dimensions 13.1×9.75 mm^2.To realize 2D beam scanning, the authors in [55] used a switched beam network using a pair of 4×4 Butler matrix interconnected to four hybrid couplers, which are connected to a 2×4 patch array to produce eight beam-states. Loading a varactor diode between parasitic elements is another approach to steer the main beam in the azimuth plane with maximum peak gain of 5.9 dB [57]. Another promising method involves integrating a dielectric lens in front of an antenna array for implementing beam steering at millimeter-waves [58,5 9].

More recently, the authors in [21] integrated a 4×3 array of high refractive-index metamaterial unit-cells with a bow-tie antenna to demonstrate the feasibility of tilting the

direction of the antenna main beam for C-band applications; however the refractive index of the unit-cell could not be altered. With this technique, the antenna exhibits a gain enhancement of 1.5–2.5 dBi over the frequency range of 7.3–7.7 GHz but the angle of the main beam is limited to 17^{o}.The authors in [60] presented a passive fixed beam forming network (BFN) by applying a 4×4 Butler matrix consisting a SIW phase shifter and coupler to tilt the main beam in both E- and H-planes by 20^{o}. The antenna consists of a multi-layer structure which is complex to construct and occupies a volume of $2.86\lambda_o \times 2.86\lambda_o \times 0.22\lambda_o$.

This chapter presents an inexpensive beam tilting technique using a gradient refractive-index metamaterial (GRIM) unit-cell to deflect the direction of the main beam of a 60 GHz end-fire dipole antenna at angles of $\pm 56^{o}$, $\pm 26^{o}$, and 0^{o}. The unique feature of the GRIM unit-cell is its refractive-index can be altered by varying the stub loading without affecting the overall dimensions of the unit-cell. The proposed antenna consists of a printed dipole antenna incorporating 5×4 array of GRIM unit-cells which are directly integrated onto the antenna along the azimuth plane. Measurements show the deflection of the main beam at angle $+26^{o}$ and -26^{o} with respect to the end-fire direction is accompanied by peak gain of 10.2 dB and 9.7 dB, respectively. The antenna radiates with an efficiency of 88% at 60 GHz, which is much higher than the BFN structure in [60] that has an efficiency of 70% at 26.5 GHz. In addition, the proposed antenna exhibits a higher beam tilt angle and a gain enhancement of 4 dB over the frequency range of 57–64 GHz than that in [21] which operates at C-band.

6.2 **Beam deflection technique**

When an electromagnetic wave (EM) in one medium enters another medium of a different refractive index the wave refracts as predicted by Snell's law. In [61] it is shown that a 2D array of resonators with subwavelength separation results in phase discontinuities in the propagating EM wave as it traverses the interface between two media as predicted by the generalized Snell's law:

$$\sin(\theta_t)n_t = \sin(\theta_i)\, n_i + \frac{\lambda_o}{2\pi}\frac{d\varphi}{dx} \qquad (1)$$

Where θ_i and θ_t are angle of incidence and refraction, respectively, and $d\varphi/dx$ is the gradient of phase discontinuity. This principle is employed here to steer the EM radiation emanating from a printed dipole antenna. This is achieved by embedding an artificial media with a higher refractive-index than the antenna, which effectively increases the aperture of the antenna and enhances its gain performance. Authors in [59] have shown it is necessary to offset the antenna from the center of a dielectric lens to create phase differential needed to deflect the waves from the antenna. This approach was implemented here on the printed dipole antenna, as illustrated in Fig.6.1. In the initial design a medium of identical refractive-index created using 5×4 array of Type A unit-cells (described in Section III) was integrated in front of an antenna.

Both arms of the dipole antenna launch the EM rays, where each ray has proper effective path length in the aperture of the radiating antenna. The resultant effect of each ray at the far-field can be determined by calculating the array factor (AF) as described in [57] using:

$$AF = 1 + e^{j(kd_1 cos\alpha_1)} + e^{j(kd_2 cos\alpha_2)} \ldots + e^{j(kd_5 cos\alpha_5)} \qquad (2)$$

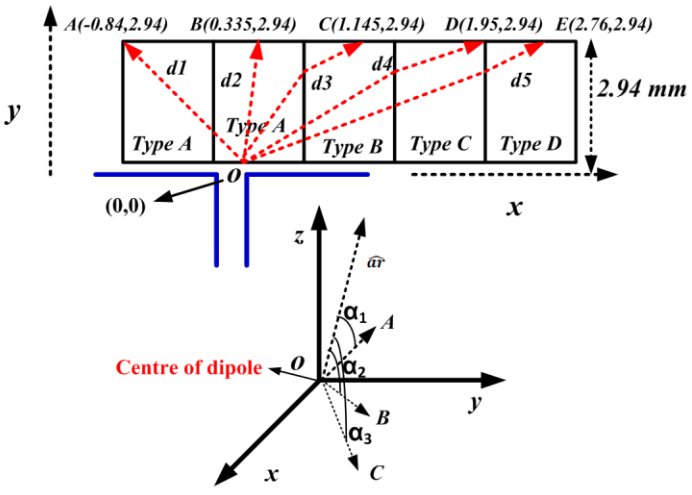

Figure 6-1: Ray paths from the offset axis of dipole antenna with 5×4 array of GRIM.

Where $d_1, d_2 \ldots d_5$ are the effective path lengths of each ray emanating from locations *A*, *B*…*E*, which can be calculated from the centre of dipole (*O*) toward the locations *A*, *B*…*E*, as shown in Fig.6.1, where angles $\alpha_1, \ldots \alpha_5$ can be obtained from:

$cos\alpha_1 = \hat{a}_{ro}.\hat{a}_{ra}$=-0.158 $cos\varphi$+0.99 $sin\varphi$
$cos\alpha_2 = \hat{a}_{ro}.\hat{a}_{rb}$=+0.109 $cos\varphi$+0.96 $sin\varphi$
$cos\alpha_3$= 0.363 $cos\varphi$+0.93 $sin\varphi$
$cos\alpha_4$ =0.553 $cos\varphi$+0.83 $sin\varphi$
$cos\alpha_5$ =0.684 $cos\varphi$+0.729 $sin\varphi$

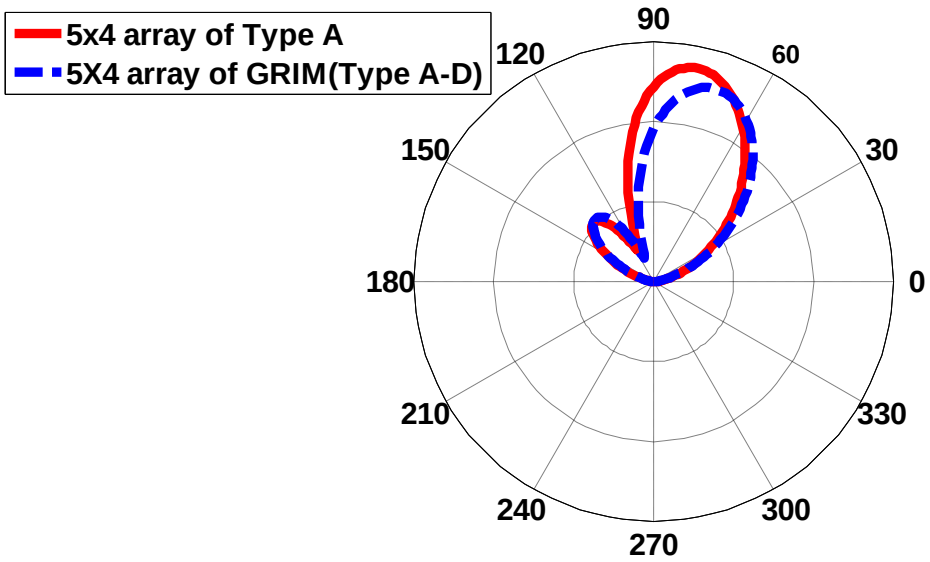

Figure 6-2: Radiation patterns of the dipole antenna with dielectric slab constituted from 5×4 array of GRIM unit-cells, and dielectric slab with identical loading.

The far-field radiation pattern of the proposed structure in the azimuth plane was calculated as described in [57] by multiplying AF with the element factor of dipole antenna, i.e. $F(\varphi) = \left[\cos\left(\frac{\pi}{2}\cos(\varphi)\right)/\sin(\varphi)\right]$. When the antenna was loaded with identical unit-cells (5×4 array of Type A) the main beam tilted at an angle of 78.5°, as shown in Fig.6.2; however when the antenna was loaded with a dielectric slab with 5×4

array of GRIM unit-cells (Types A-D), the main beam deflected to 68^{o}. This is attributed to the phase discontinuity in the GRIM region according to the generalized Snell's law in Eqn. (1), where the effective path length of each ray traversing in GRIM region is different than for identical unit-cell loading.

6.3 **Metamaterial Unit-Cell**

The configuration of proposed GRIM unit-cell structure, shown in Fig.6.3, is in fact a modified version of the I-shaped resonator in [21] which is loaded with a rectangular stub to provide a specific refractive-index. The dimensions of the stub (L_{load},W_{load}) determine the refractive-index of the medium within its locality over a specific frequency range. This structure was selected because of its ease of integration onto the antenna substrate without altering the antenna profile.

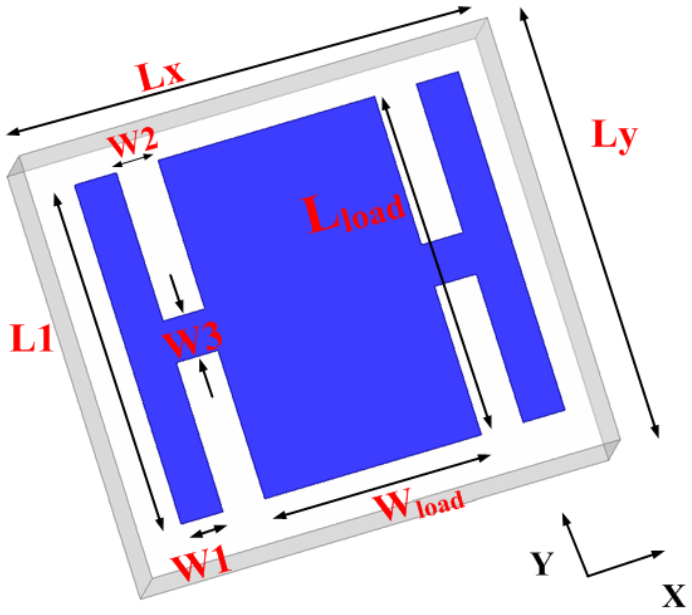

Figure 6-3: Geometry of the proposed GRIM unit-cell implemented on a dielectric substrate.

The GRIM unit-cell was constructed on a Rogers RT5870 substrate with the thickness (h) of 0.254 mm, permittivity (ε_r) of 2.3, and loss-tangent of 0.0009.Although the manufacturer recommends the substrate be used for applications up to 40 GHz, the

simulated and measured results presented later show it is indeed suitable for applications up to 64 GHz.

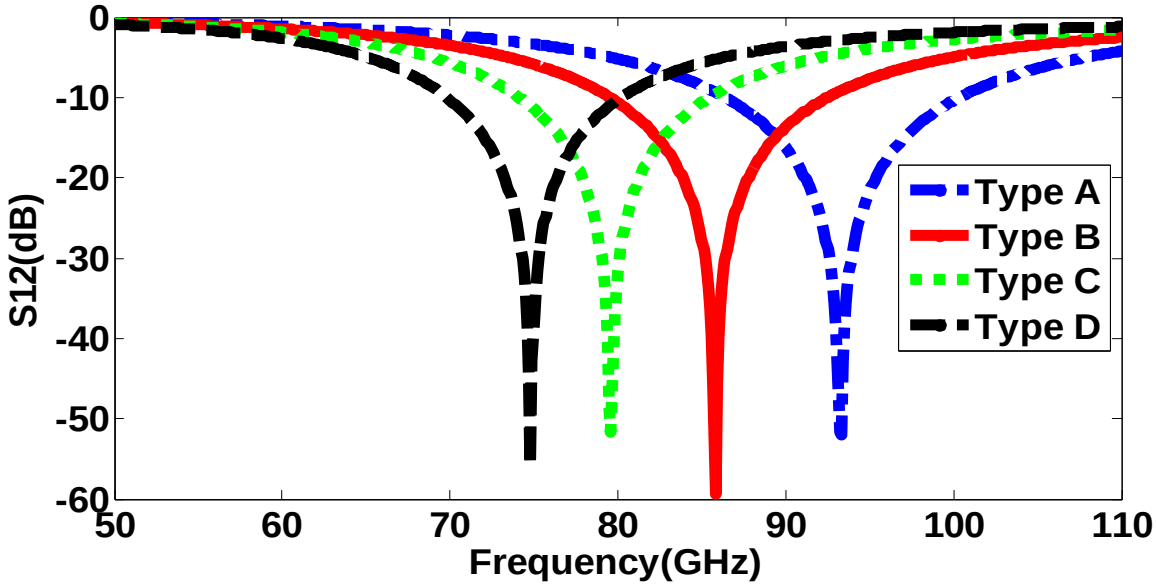

Figure 6-4: Magnitude of S12 of the proposed GRIM unit-cell structure .

The constitutive parameters of GRIM unit-cell, i.e. permittivity, permeability as well as refractive-index, were extracted using Ansoft HFSS, where the PEC and PMC boundary conditions were applied along the *yz* and *xy*-planes, and the two ports were located in *x*-direction. The GRIM unit-cell's effective magnetic permeability and electric permittivity were extracted from the structures transmission and reflection coefficients using the algorithm in [34] which employs Kramers–Kronig relations to estimate the real part of the refractive-index. In order to determine how the refractive-index is influenced by loading the I-shaped unit-cell with a rectangular stub, various unit-cells were developed whose dimensions (in mm) are given in Table I.

The insertion-loss (S_{12}) response for the various GRIM unit-cells is shown in Fig. 4. Contrary to conventional behavior it is observed that as the dimensions of the stub loading are reduced the structures anti-resonant frequency shifts downwards in frequency from 93 GHz to 74.5 GHz.

Table 6-1: Dimensions of GRIM unit-cell of various sizes

Type A	$L1$=0.63, $W2$=0.07, $W1$=0.077, L_x=0.80, L_y=0.72, $W3$=0.08 W_{load}=0.40, L_{load}=0.65, α=(L_{load}/W_{load})=1.62
Type B	W_{load}=0.35, L_{load}=0.56, α=1.62
Type C	W_{load}=0.29, L_{load}=0.47, α=1.62
Type D	W_{load}=0.23, L_{load}=0.37, α=1.62

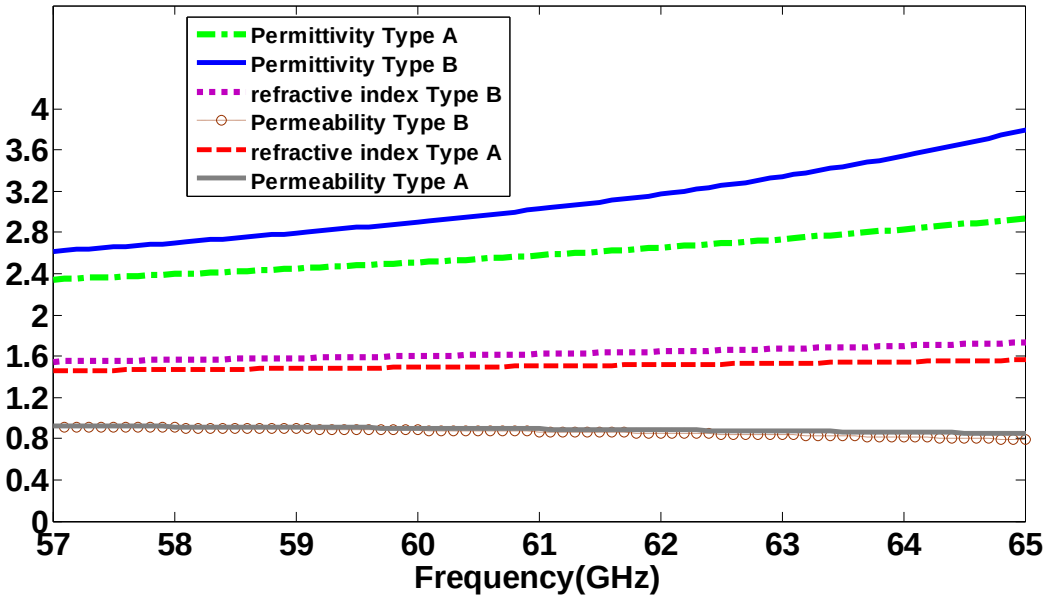

Figure 6-5: Relative permittivity, permeability and refractive-index of Type A and B elements.

This is achieved without affecting the overall dimensions of the GRIM unit-cell. Fig.6. 4 shows the anti-resonant frequency of Type A unit-cell is far away from the operating band (57–64 GHz), and its effective refractive-index over 57–64 GHz shown in Fig. 5 varies between 1.44 and 1.57, which can be considered virtually constant. However, a larger variation in the effective refractive-index is observed when the unit-cell's anti-resonance is located closer to the operating band, as exemplified by Type D unit-cell. In this case the magnitude of the effective refractive-index varies between 1.73 and 2.4 over 57–64 GHz, as shown in Fig.6.6. The above results confirm a graduated refractive-index

can be achieved by controlling the length and width of loaded rectangular stub in the I-shaped unit-cell.

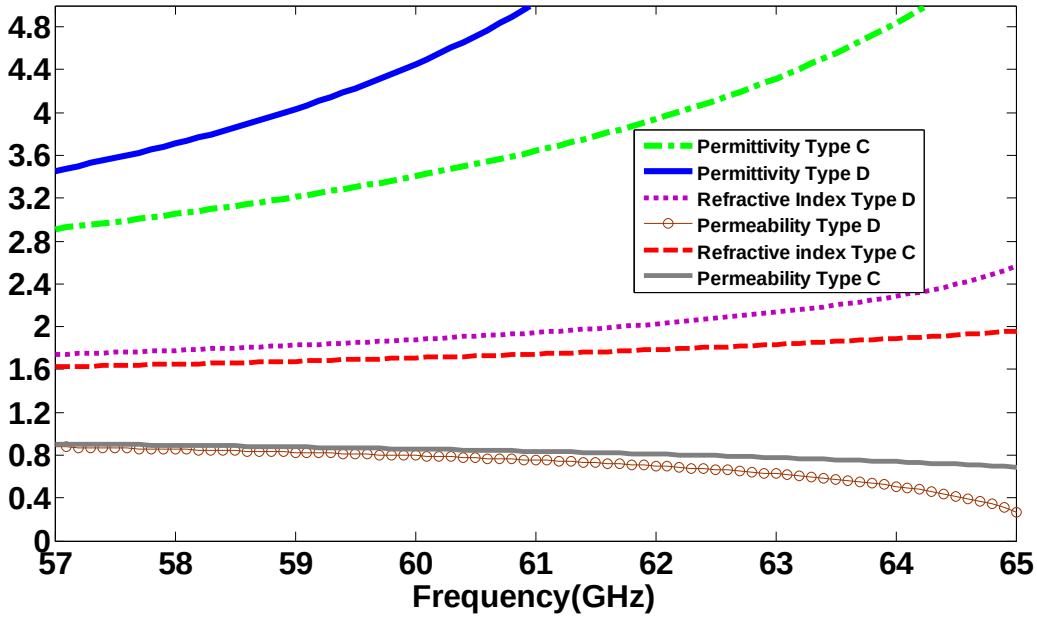

Figure 6-6: Relative permittivity, permeability and refractive-index of Type C and D elements.

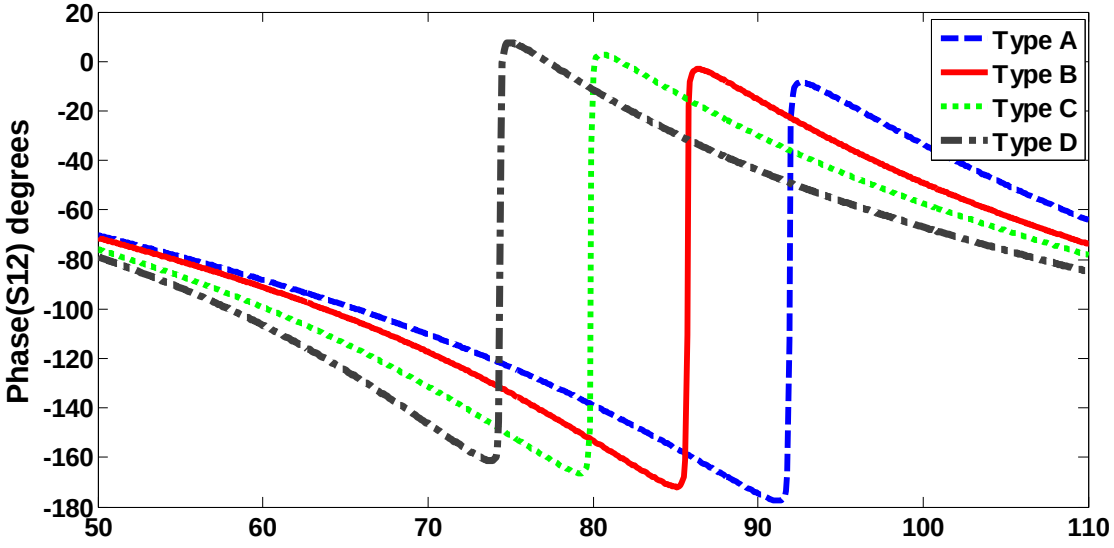

Figure 6-7: Phase of the proposed GRIM unit-cell structure .

The GRIM structures exhibit a different phase response across 50–73 GHz, as shown in Fig.6.7, where the phase of Type D element lags C, Type C lags B, and Type B lags A. The results show proposed Type of unit-cell has different phase response and therefore will contribute towards a larger tilt angle according to the generalized Snell's law.

6.4 Single Dipole Antenna with GRIM unit-cell

In this section, the characteristics of a single-dipole antenna are explored when integrated with the proposed gradient refractive-index GRIM unit-cell. The dipole antenna used here is a modified version of the dipole antenna reported in [50]. A 5×4 array of GRIM unit-cells were incorporated into the antenna substrate and laid in front of the dipole-antenna in the azimuth plane, as shown in Fig.6.8. The structure of GRIM was separated into the top and bottom layers to enhance coupling with the dipole arms and ensure GRIM effectively interacted with radiation on both sides of the antenna.

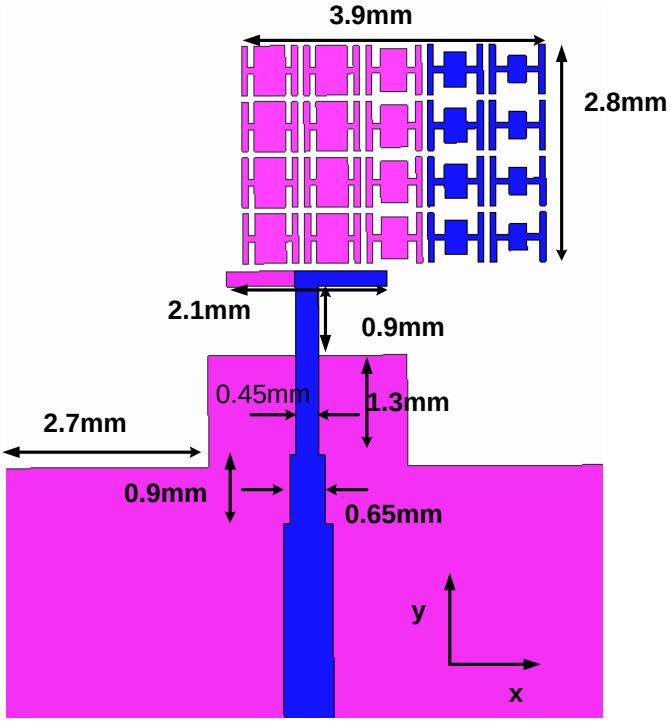

Figure 6-8: Configuration of proposed antenna embedded with GRIM unit-cell on the top and bottom surface of the substrate.

The dimensions of the proposed antenna are annotated in Fig.6.8. The radiation pattern of the printed dipole antenna is shown in Fig.6.9 with and without GRIM inclusions in the E-plane of the antenna. The results in Fig.6.9 show that when the GRIM is integrated into antenna substrate the direction of the main beam in the E-plane is tilted by 26^{o} with respected to the end-fire direction. In addition, this is accompanied by 4 dB gain enhancement compared to the dipole printed-antenna with no GRIM loading since the radiating aperture size is larger.

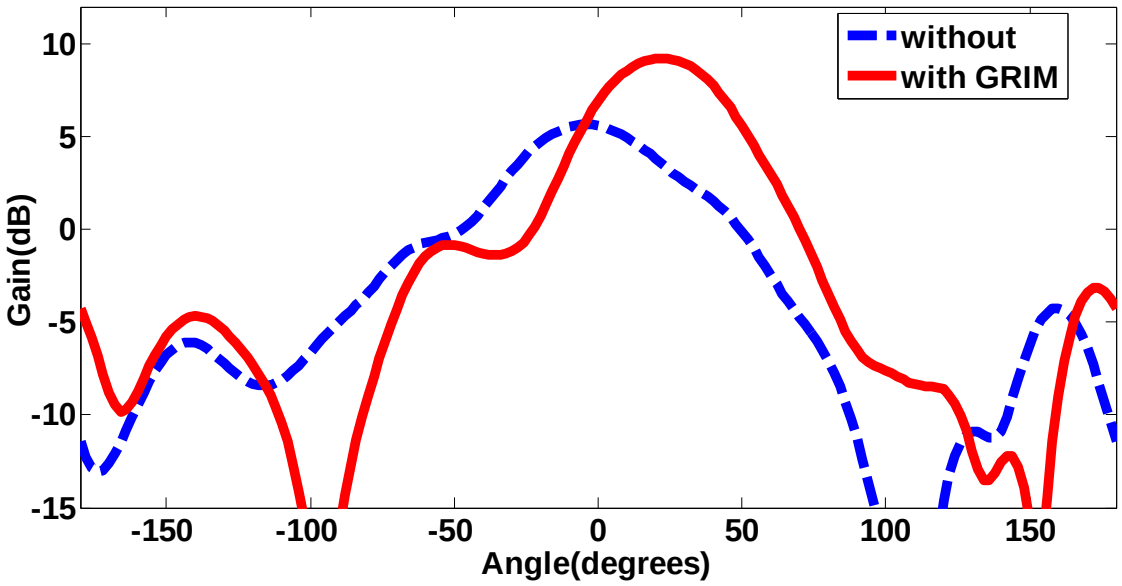

Figure 6-9: Radiation patterns of proposed antenna in the E-plane (xy) with GRIM unit-cells and a conventional dipole antenna at 60 GHz

In order to gain a better understanding of the mechanism behind beam tilting, the antenna's Poynting vector was computed with and without GRIM loading using 3D full-wave simulator EM simulation. The results in Fig.6.10 show that the presence of GRIM causes the EM waves to deflect towards the metamaterial region.

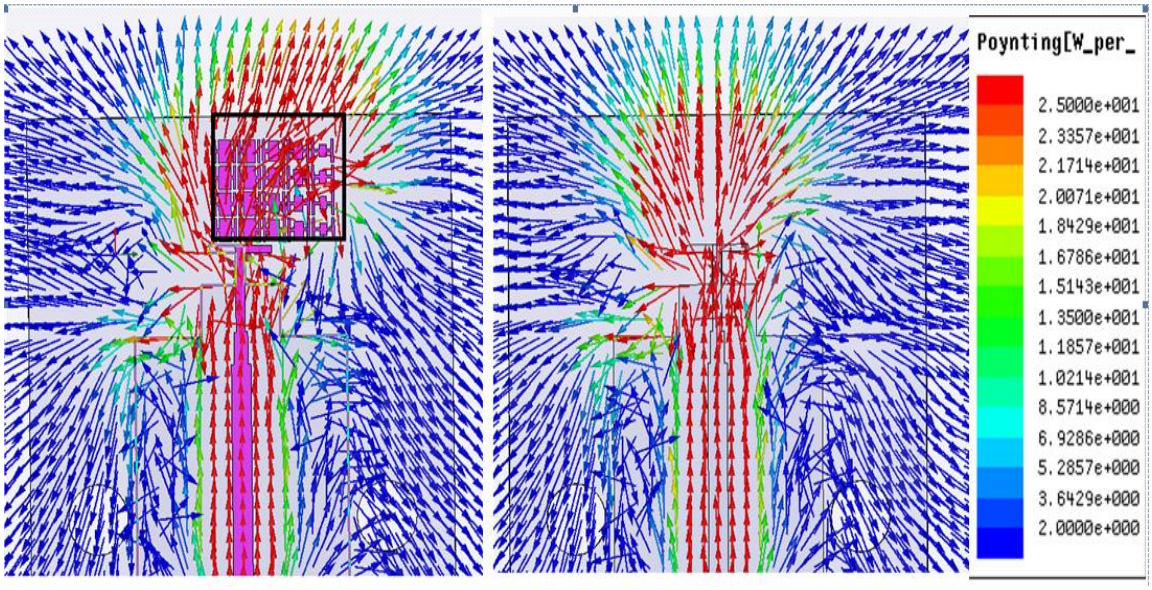

(a) *(b)*

Figure 6-10: Poynting vector distribution over the antenna at 60 GHz: (a) with GRIM, and (b) without GRIM

6.5 **Parametric Study**

The effect of GRIM unit-cell columns on the beam tilting is now investigated. Initially the antenna was loaded with two columns of four unit-cells (4×2 arrays of Type A unit-cell) with the same refractive-index (n_1) in front of dipole antenna. The configuration directs the radiation pattern towards the end-fire direction as shown in Fig.6.11. By increasing the columns to 3, 4, and 5 with different refractive indices (n_3,n_4,n_5) results in the main beam to tilt by 8^o, 16^o, and 26^o, respectively, as shown in Fig. 11. Six GRIM columns provide a beam tilt of 29^o, however this is accompanied by a marginal gain dropped and deterioration in SLL. Hence 5 columns (5×4 GRIM) were selected in the final design.

The effect on the beam angle by offsetting the dipole feed along the *x*-direction was investigated. The feed of the dipole antenna with 5×4 GRIM was offset in the +*x* direction in steps of 0.5 mm from 0 to 3 mm which resulted in the main beam shifting from -25^o to 25^o as shown in Fig.6.12.

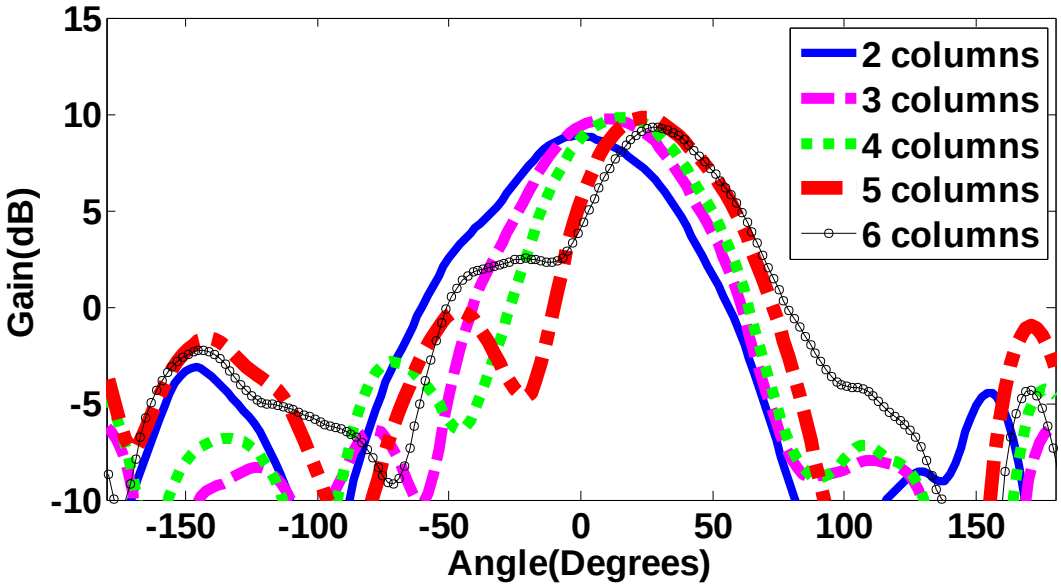

Figure 6-11: Radiation pattern of antenna as a function of number of GRIM unit-cell columns

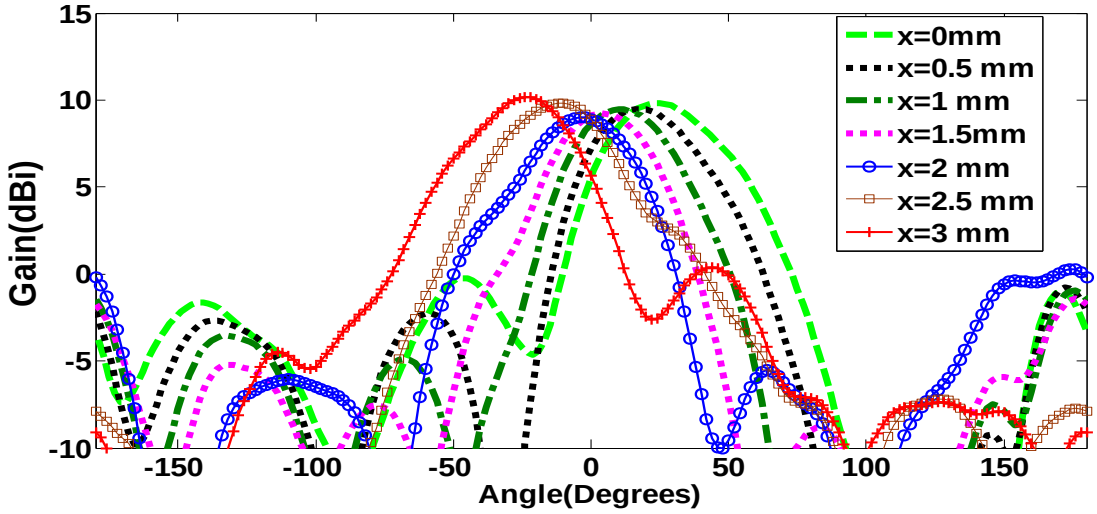

Figure 6-12: Radiation pattern for a 5×4 GRIM as a function of feed-line offset along the x-direction at 61 GHz unit-cell columns

The E-plane (*xy*) radiation pattern at 61 GHz of the dipole antenna with a dielectric slab loaded with 5×4 array of GRIM unit-cells (Types A-D), and with 5×4 array of identical unit-cells (Type A) is shown in Fig.6.113. This figure shows the main beam of the antenna is deflected by 29^{o} when an array of GRIM unit-cells is integrated on dielectric

slab. There is a 9^{o} difference between the two scenarios, and the antenna with GRIM loading provides 1.1 dBi more gain than when loaded with an array of identical unit-cells.

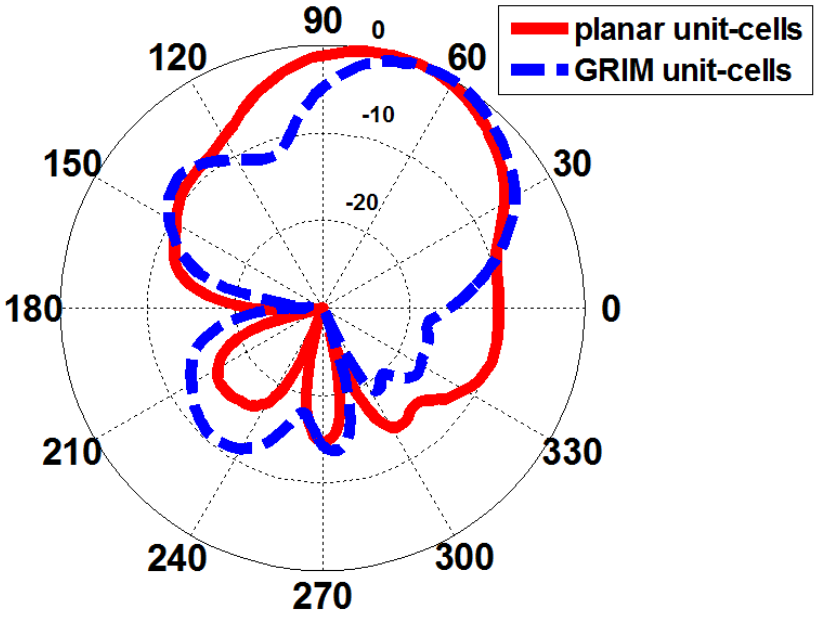

Figure 6-13: Radiation pattern of antenna having dielectric slab loaded with GRIM unit-cells and slab with identical unit-cells.

6.6 Experimental Results

The proposed single dipole-antenna with a 5×4 array of gradient refractive-index metamaterial unit-cells was fabricated and its performance measured. The photograph of the prototype dipole antenna with GRIM loading is shown in Fig.6.14(a).There is good correlation between the simulated and measured reflection-coefficient results, shown in Fig.6.14(b), and the discrepancy in the measured response is attributed to the fabrication tolerance. The results confirm that the reflection-coefficient is better than -10 dB between 57–64 GHz. A 1.85 mm end-launch connector (model no.1893-03A-5) was used for the measurement.

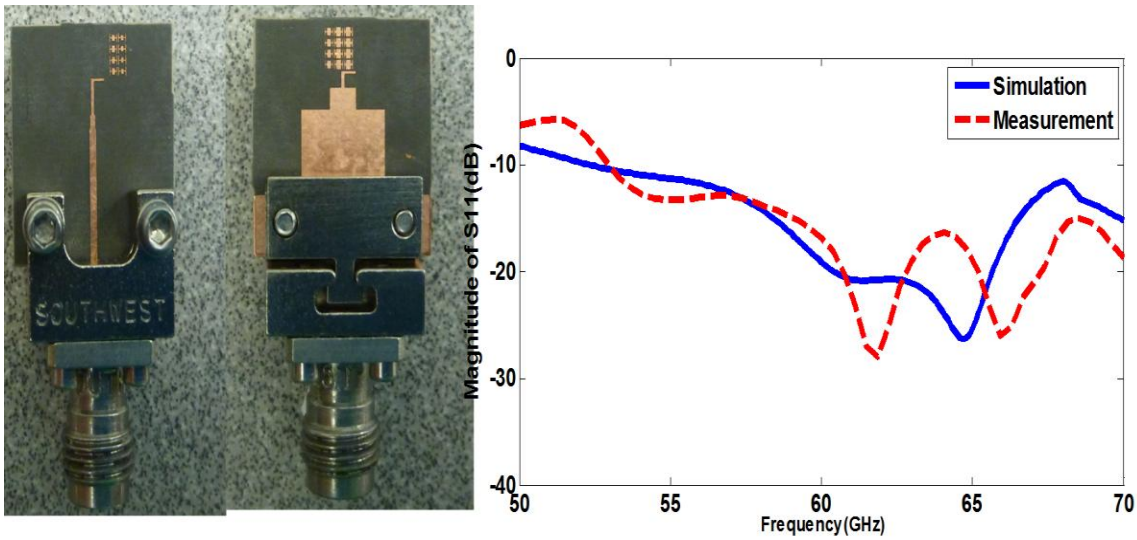

(a) (b)

Figure 6-14: (a) Photograph of dipole antenna with GRIM array, and (b) simulated and measured reflection coefficient

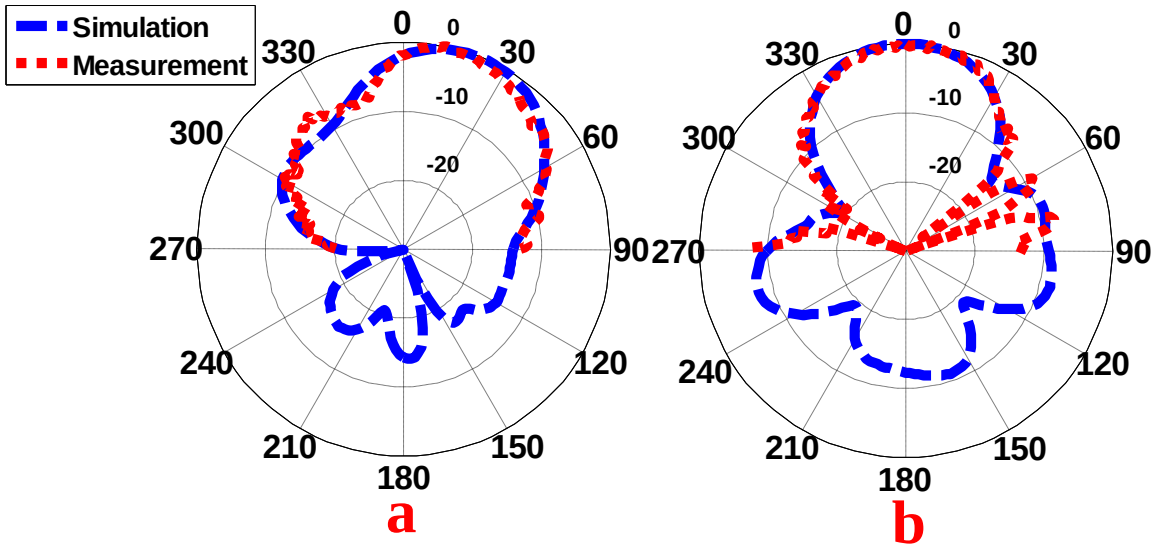

Figure 6-15: The normalized radiation pattern of single dipole-antenna with a 5×4 array of GRIM loading at 60 GHz in the (a) E-plane (xy), and (b) H-plane (yz).

The simulated and measured radiation pattern of the single dipole antenna with GRIM loading in the E-plane at 60 GHz is shown in Fig. 6.15(a). The main beam of the antenna

is confirmed to tilt by 26°. The radiation pattern in the H-plane at 60 GHz remains unchanged, as shown in Fig.6. 15(b), and is oriented towards the end-fire direction.

6.7 **Double Feed Antenna with 5x4 array of GRIM**

The versatility of proposed approach can be demonstrated by using a beam switching network to steer the main beam from +26° to -26°. To achieve this requirement an additional dipole-antenna was added to the proposed single GRIM loaded dipole-antenna, as shown in Fig.6.16. This configuration includes of a double-dipole antenna with a 5×4 array of GRIM unit-cells.

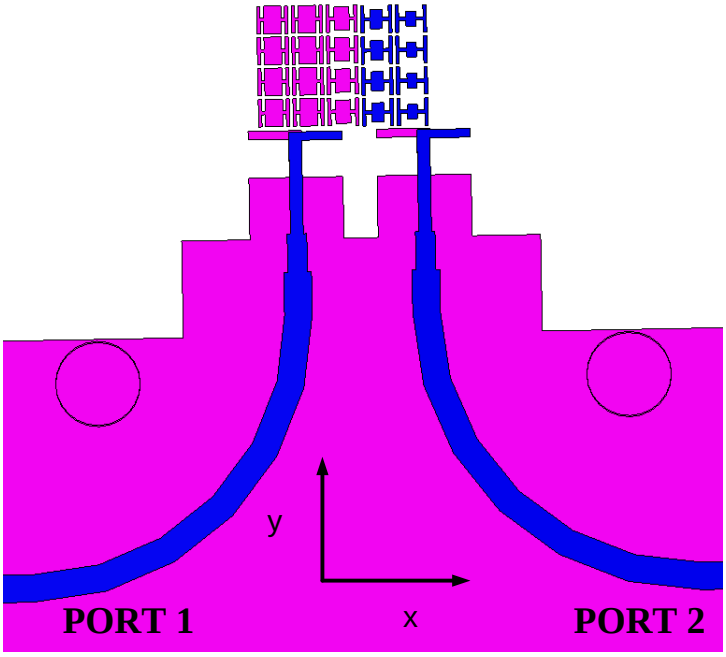

Figure 6-16: Geometry of double-feed antenna with 5×4 array of GRIM unit-cells

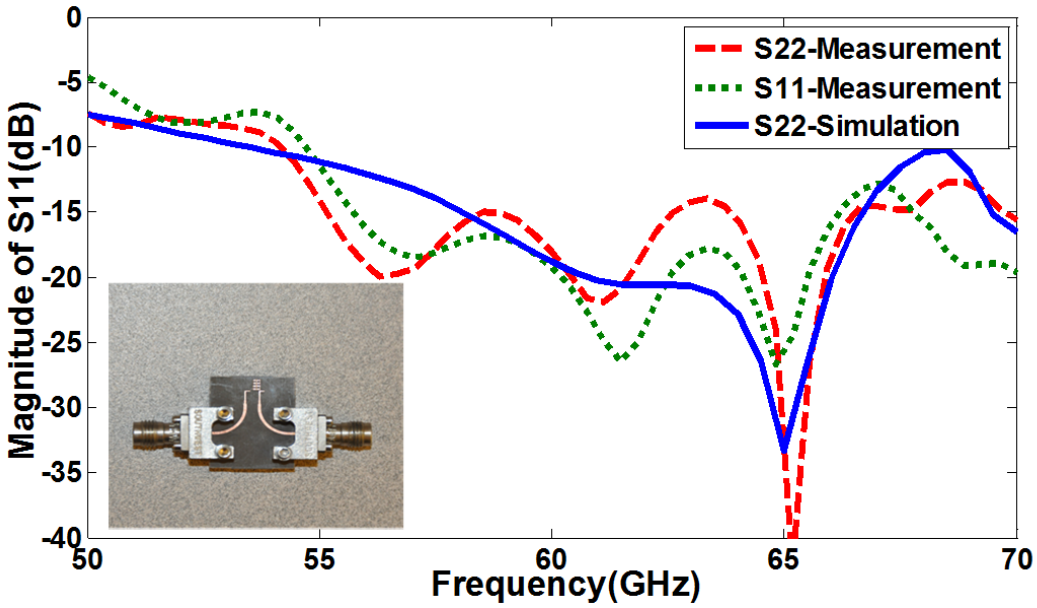

Figure 6-17: The measured reflection coefficient of the double dipole GRIM antenna with inset photograph of fabricated antenna.

The operation of this structure is based on the concept explained in Section II. When antenna-1 is excited with the GRIM loading placed off-center to the right of dipole antenna then the main beam is tilted towards the GRIM region by $+26^{o}$. When port 1 is terminated with a 50 ohm load and antenna-2 is excited, as the GRIM unit-cells are off-center to left of antenna-2, the main beam tilts towards the GRIM region by -26^{o}. When both ports are excited the main beam propagates towards the end-fire direction (+*y*).

The measured reflection-coefficient of the two ports, shown in Fig.6.17, is better than -10 dB in the frequency range of 57–64 GHz. The results of simulated radiation pattern of three states (-26^{o}, 0^{o}, $+26^{o}$) at 61 GHz are shown in Fig.6.18.

The radiation pattern in the azimuth plane was measured by exciting one port at a time using an end-launch connector while the other connector was terminated. The measured and simulated normalized radiation pattern in the azimuth plane (E-plane) at 58, 61, and 63 GHz is shown in Fig.6.19 (a-c). There is good correlation between the simulation and measured results. Fig.6.19 (d) shows the normalized radiation pattern in the H-plane at 60 GHz is oriented along the end-fire direction.

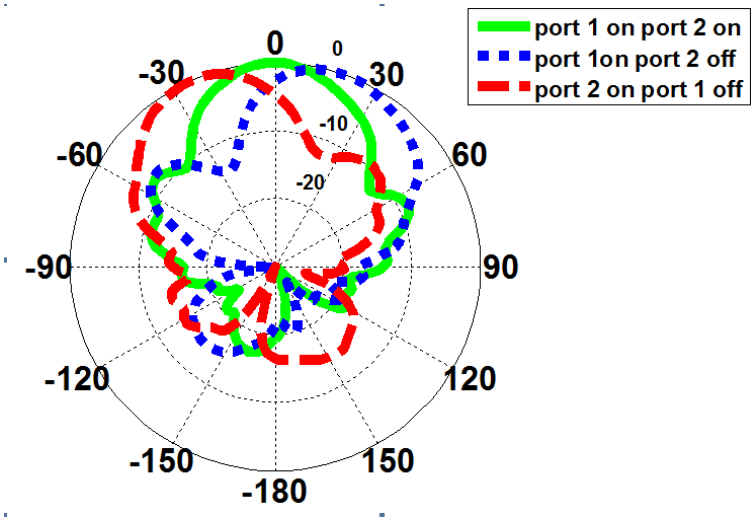

Figure 6-18: The simulated normalized radiation pattern when beam is switched in three states +26^{o}, 0^{o}, and -26^{o} at 61 GHz

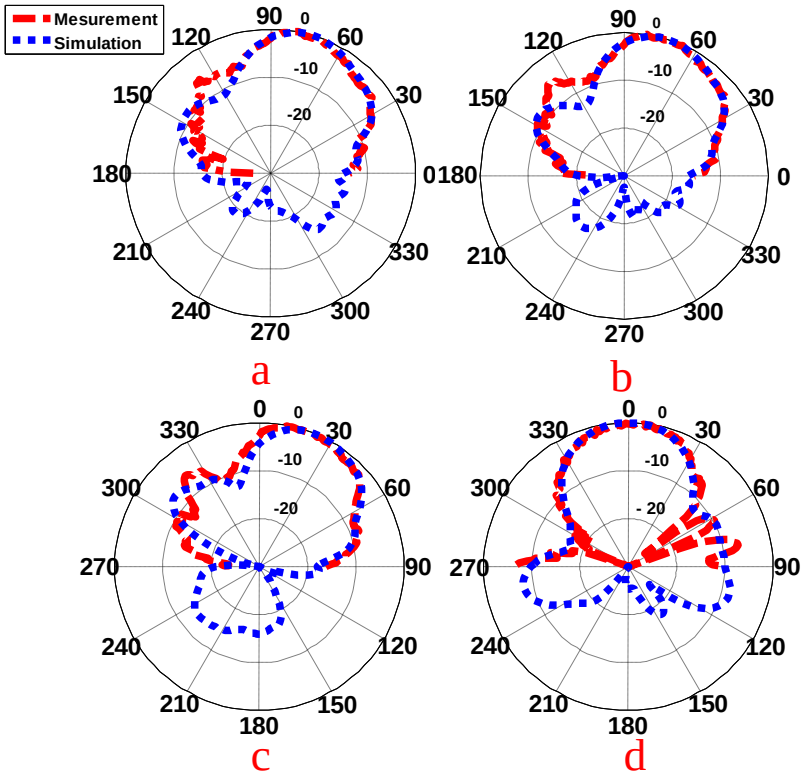

Figure 6-19: Normalized radiation pattern of proposed antenna with GRIM loading in the E-plane when port 1 is excited at: (a) 58 GHz, (b) 61 GHz, (c) 63 GHz, and (d) with GRIM loading in the H-plane at 60 GHz

The simulated and measured radiation pattern of the antenna when port 2 is excited and port 1 is terminated is shown in Fig. 6.20. The result confirms that the main beam direction is tilted by -26^{o} as expected. The antenna gain was measured using the comparative method that involves measuring the signal received by the reference antenna and the test antenna, and determining the relative difference in the gain of both antennas. With this information the gain of the test antenna was determined. The measured radiation efficiency was calculated as explained in [16]. The measured gain of double feed antenna at different beam scan angles along with efficiency are given in Table II. The measured result indicates that there is a maximum peak gain of 10.2 dB at 61 GHz, when the beam is tilted by +26^{o}.

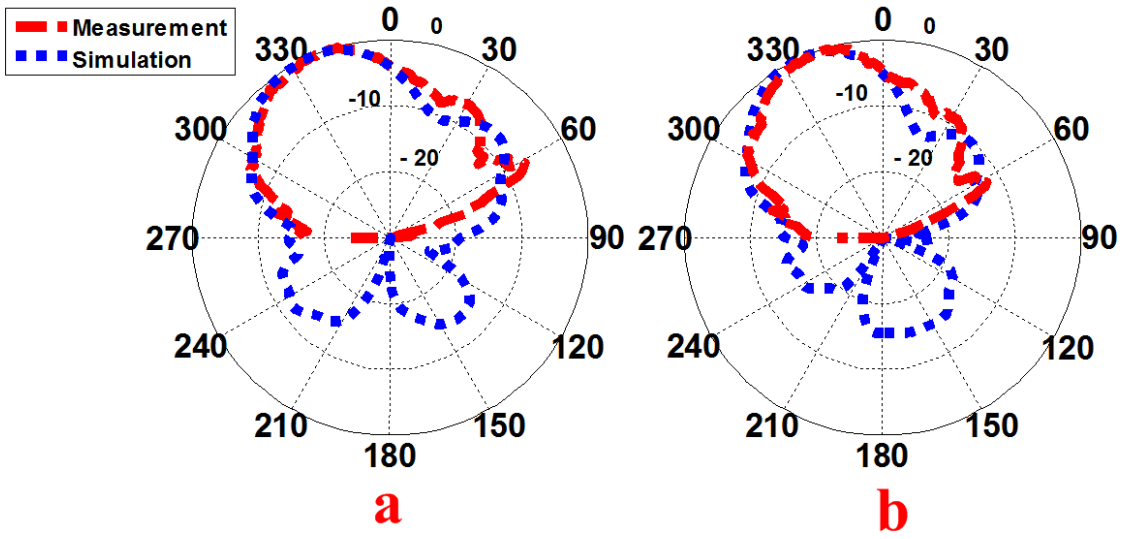

Figure 6-20: Normalized radiation pattern of proposed antenna with GRIM loading in E-plane when port 2 is excited at: (a) 59 GHz, and (b) 63 GHz.

Table 6-2: Measured peak gain and efficiency of double feed GRIM antenna

Freq.(GHz)	Simulated peak gain at angle $+26^{o}$(dBi)	Measured peak gain at angle $+26^{o}$(dBi)	Simulated peak gain at angle -26^{o}(dBi)	Measured peak gain at angle -26^{o}(dBi)	Measured radiation efficiency (%)
58	9.60	9.4	9.30	9.40	87.5
61	9.90	10.2	9.72	9.70	88.0
63	9.70	10.0	9.75	9.70	84.0

6.8 **Fourth-Feed Antenna with GRIM array**

In Section VII it was shown that a double feed antenna with 5×4 GRIM enables the main beam of antenna to be steered from -26^{o} to $+26^{o}$. In order to achieve greater scan coverage the configuration in Fig.6.21 is proposed.

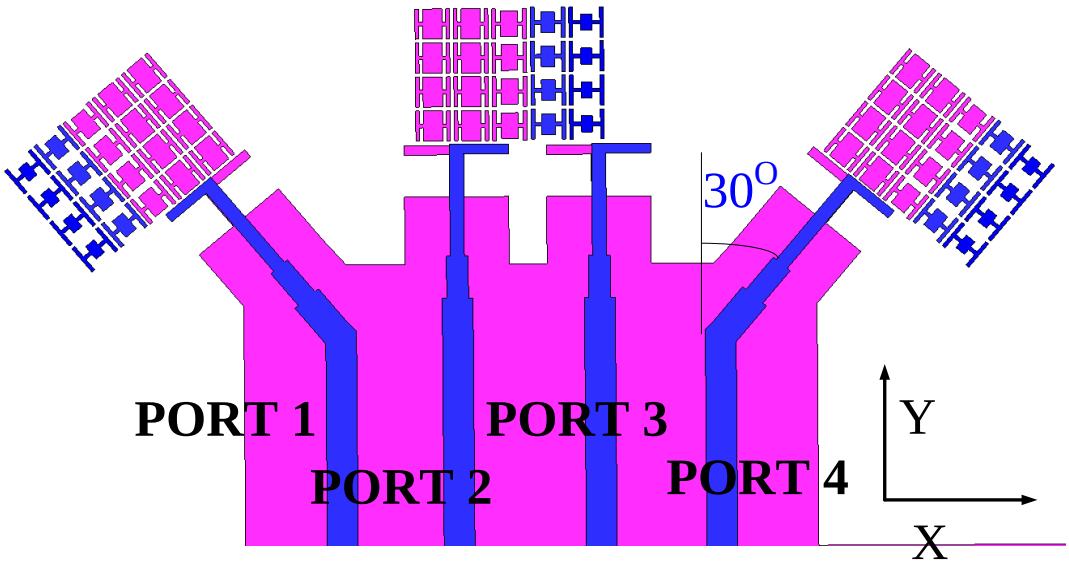

Figure 6-21: Configuration of fourth-feed antenna with 5×4 GRIM unit-cells.

The structure consists of four feed-lines where the outer two feed-lines are tilted by 30^{o} with respect to the *y*-axis. The associated 5×4 array of GRIM unit-cells is also tilted by 30^{o}. The operation of quad-feed structure is similar to the double-feed configuration. Fig.

6.22 shows the total radiation pattern of antenna configuration in different states, proving that beam switching is achievable at ±56°, ±26°, and 0°.

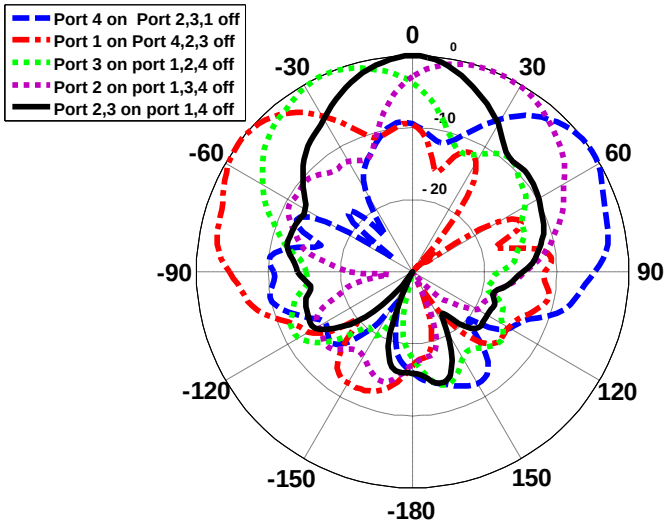

Figure 6-22: Radiation pattern of proposed four-feed antenna with GRIM array in E-plane to realize five angle beams switching at 61 GHz.

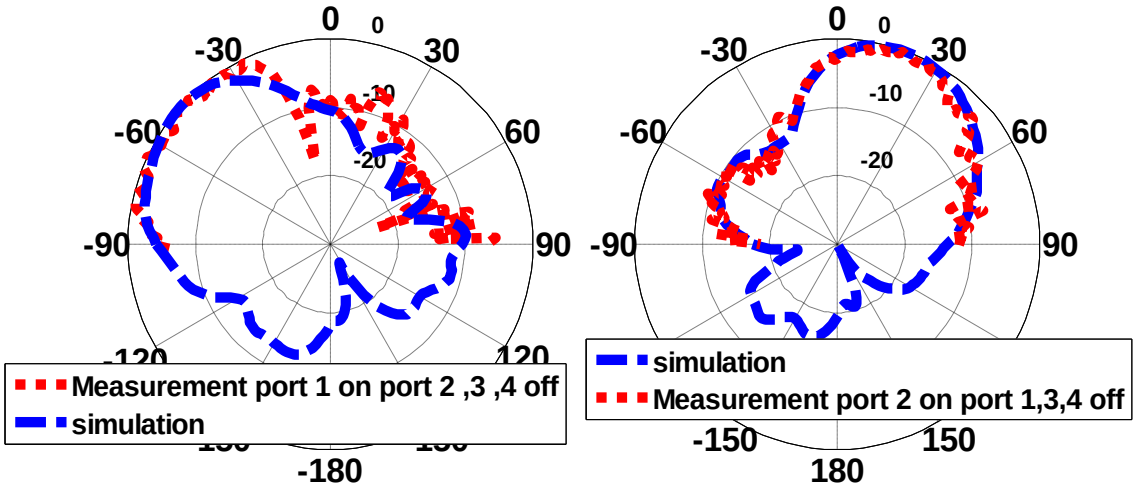

(a) (b)

Figure 6-23: Radiation pattern at 60 GHz of the quad-feed antenna when (a) port 1 is excited, and (b) port 2 is excited.

In order to validate the simulation results the radiation pattern of two states was measured at 60 GHz as shown in Fig. 23. In the first state, port 1 is excited and the other ports are

terminated, resulting in the main beam deflecting by -56^{o}. A piece of absorbing material was attached to the other ports to prevent the radiation from other ports. In the second state, port 2 was excited and the other ports were terminated. In this case the main beam tilted by +26^{o}.

6.9 **Conclusion**

Gradient refractive-index metamaterial (GRIM) structure was used to deflect the direction of the main beam of a dipole antenna by a specified angle. This was achieved by integrating 5×4 array of GRIM unit-cells on the planar antenna. The GRIM unit-cell comprise of an I-shaped structure loaded with a rectangular stub, where the dimensions of the stub loading determine the refractive index of the unit-cell. The measured results confirm the direction of the main beam to deflect by +26^{o} in the E-plane with gain enhancement of 4 dB resulting from the increased size of the radiating aperture. A double-feed dipole with 5×4 GRIM unit-cells was used to demonstrate scanning of the main beam in the E-plane from -26^{o} to +26^{o}. Using the proposed technique a quad-feed antenna was shown to provide beam tilt angles of ±56^{o}, ±26^{o}, and 0^{o}.

Chapter 7 IMPROVEMENT OF GAIN AND ELEVATION TILT ANGLE USING METAMATERIAL LOADING FOR MILLIMETER-WAVE APPLICATION

7.1 Introduction

Communication in the unlicensed 60 GHz band (57–66 GHz) has attracted great attention for short range multi-Gbps data rate applications such as high definition video streaming using the IEEE 802.11ad WiGig standard. One distinguishing feature of the 60 GHz communication is its high propagation loss due to the extremely high carrier frequency and the oxygen absorption peaks at this frequency band. To combat this, directional antenna with high directivity gain can be adopted to obtain sufficient link budget [62]. This can be accomplished using antenna arrays that provide advantages of interference mitigation and multipath suppression [63]. The challenge with directional antennas is beam alignment between the communication pair. Hence, different approaches have been proposed to achieve electronic beam steering such as integrated lens antenna technique for 1-D and 2-D beam scanning at millimeter-wave [64-65]. The drawback feature of this approach is its overall bulky framework.

1-D and 2-D beam scanning at 30 GHz has been presented in [66] by applying a 2×2 SIW antenna array implemented with a combination of couplers and phase shifters to tilt the main beam direction in E-and H-plane by 15 and 45 degrees respectively .

Applying a Butler matrix is another technique to implement a beam forming network at millimeter wave[67-71].For instance,1D and 2D beam forming network has been introduced by the authors in [67] utilizing a 1x4 dielectric rod antenna integrated by SIW folded butler matrix. However the proposed structure has a large dimension and is so complicated.

The authors in [70] reported a 60 GHz active switched beam antenna consisting of a 4×1 quasi-Yagi array incorporating a 4×4 butler matrix network to obtain a beam steering of $\pm 40^{o}$. The overall dimensions of structure are 1.5×1.4 cm.

In [71] folded Butler matrix and substrate integrated waveguide radiators are integrated as a whole by employing the LTCC fabrication process to implement a miniature substrate integrated multi-beam array antenna. The drawback of this approach is it's a complicated structure and the circuit area is 16.5×14.6 mm^2 excluding the additional feeding structures.

In [32] an array of dipole antenna is mounted perpendicular to an EBG ground-plane to realize beam tilting for mobile base-stations. With this technique the beam tilt angle is limited to 25 degrees. The physical size of the antenna at 3.5 GHz is 2.6λ×0.63λ×0.84λ Comb-line antenna array in [13] provides a tilt angle of 30 degrees at 76 GHz. This antenna is composed of several rectangular radiating elements directly connected to a straight feeding microstrip line. The radiating elements are inclined 45 degrees from the feeding line. The drawback of this configuration is its large physical size, i.e. 15.2λ×2.5λ×0.03λ ,as it requires two lines of 26-element linear array and its side-lobe is -5 dB. Authors in [21] have demonstrated the beam tilting phenomenon can be realized using high refractive-index metamaterial loading which is integrated within the antenna structure. With this technique the beam tilt angle is limited to 17 degrees in the azimuth-plane at C-band. In addition, over its operating frequency range the gain of the antenna is restricted to 1.1–2.4 dB. To increase the tilt angle along with the gain, array of gradient index of refraction media was embedded in front of a classical dipole antenna at 60 GHz to deflect the main beam direction in the azimuth plane by 26 degrees in the azimuth plane with measured gain of 9.45 dBi [22].Additionally, in order to deflect the radiation pattern of the bow-tie antenna arrays under the horizon an array of split-ring resonator was integrated in the elevation plane of bow-tie antenna arrays with 30 degrees tilt angle at 3.5 GHz suitable for next generation of base-station antenna [72].

This chapter presents results on 1-D and 2-D beam deflection over 57-64 GHz using a novel 3×4 array of high refractive-index metamaterial (HRIM) unit-cells.In section II, the mechanism behind beam titling is explained followed by the structure of the unit-cell used in the implementation of high refractive-index. In section III a 3×4 array of HRIM unit-cells is integrated in the elevation plane of printed single dipole antenna to achieve a 30 degree beam titling. In section V, the proposed technique is applied to a double-feed dipole to demonstrate the beam deflection cover angles of -30^o and $+30^o$ in the elevation

plane. Lastly, in section VI, a 2×4 array of HRIM unit-cells is integrated into the antenna substrate to obtain a beam titling in the azimuth plane to provide simultaneous beam deflection in both elevation and azimuth planes. A prototype antenna incorporating HRIM unit-cell arrays in the elevation plane was fabricated and its radiation pattern and gain performance was measured to verify the proposed technique. Measurement results show the deflection of the main beam at 30^{o} with respect to the end-fire direction is accompanied by peak gain of 10.34 dBi at 60 GHz.

7.2 Mechanism of Beam tilting

It has been shown in [65] that by placing a dielectric hemispherical lens over an antenna results is in beam deflection. The angle of deflection can be controlled by using lenses of different radii. In this paper we have realized beam deflection in the elevation-plane of a planar dipole antenna by loading it with an array of HRIM unit-cells.

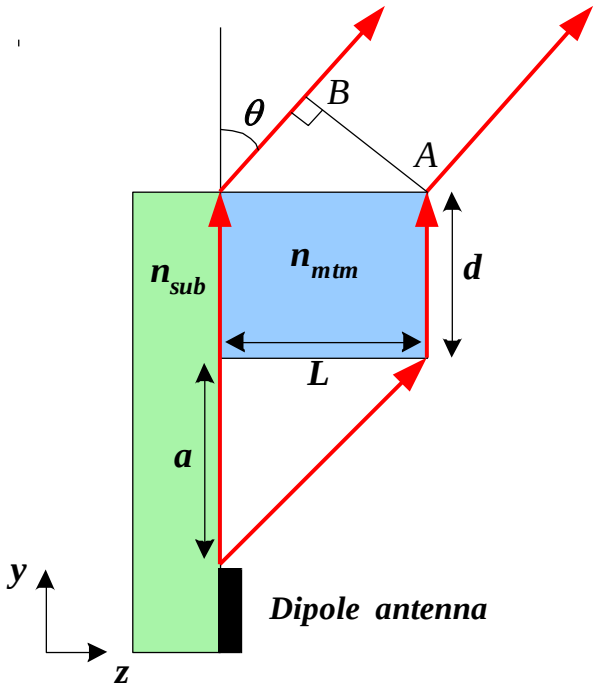

Figure 7-1: Mechanism of beam-tilting in the H-plane of the dipole antenna.

The metamaterial array is loaded directly onto the dipole antenna in the elevation-plane in the path of the radiation. The array effectively acts like a hemispherical lens that deflects the radiation beam. Moreover the array effectively increases the antenna aperture to enhance its gain performance.

Beam tilt angle can be determined from the geometry of the HRIM loaded dipole antenna, shown in Fig.7.1, where there is phase difference between the paths of lengths "*a*" along the substrate surface which guides a TE surface wave and the free-space path of length $\sqrt{(L^2 + a^2)}$. Where *a* is the distance of dipole antenna to the HRIM region, and *L* is the length of HRIM region in the *z*-direction.

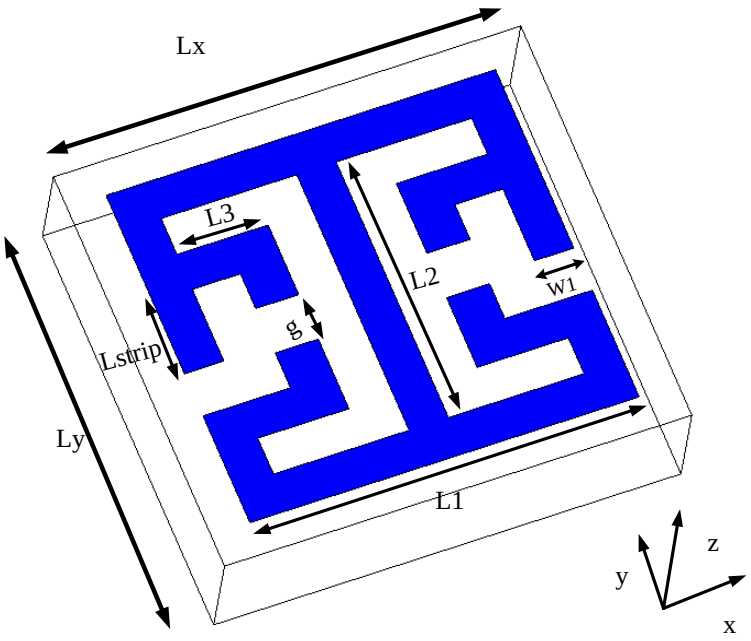

Figure 7-2: Geometry of the proposed HRIM unit-cell implemented on a dielectric substrate.

In order to implement the proposed technique the metamaterial unit-cell structure, shown in Fig.7.2, is employed. This is a modified version of the H-shaped meandered line metamaterial structure described in [21]. The proposed unit-cell structure includes inter-

coupling gap (g) and open-circuited stub loading of length L_{strip} that is used to control the refractive-index of the unit-cell over a specific frequency range.

Table 7-1: Metamaterial unit-cells (dimensions in millimeter)

Type A	*L1*=0.79, *L2*=0.57, *L*3=0.186, *W1*=0.08, *Lstrip*=0, *Lx*=0.83, *Ly*=0.81, *g*=0.08
Type B	*L1*=0.79, *L2*=0.57, *L*3=0.186, *W1*=0.08, *Lstrip*=0.08, *Lx*=0.83, *Ly*=0.81, *g*=0.08
Type C	*L1*=0.79, *L2*=0.57, *L*3=0.186, *W1*=0.08, *Lstrip*=0.16, *Lx*=0.83, *Ly*=0.81, *g*=0.08

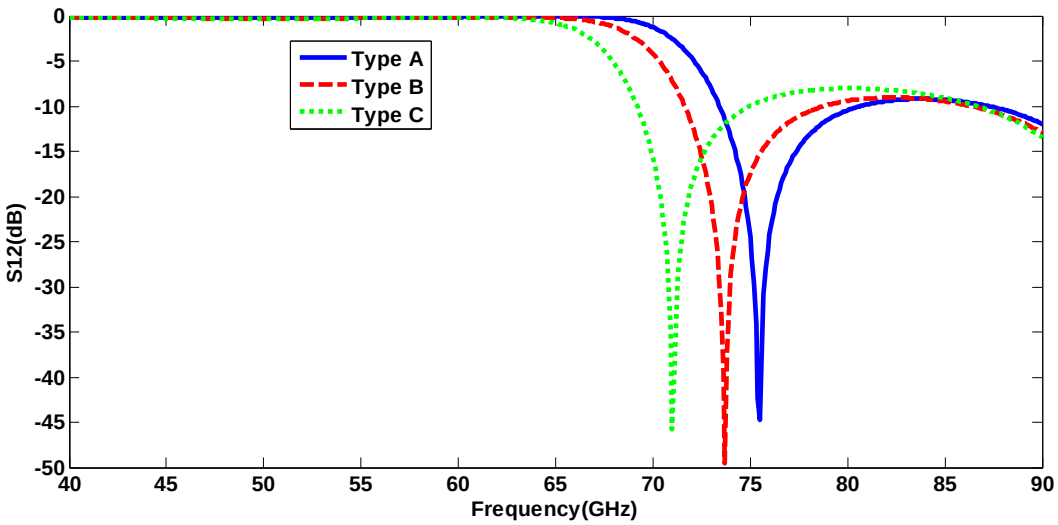

Figure 7-3: Insertion loss response Geometry of the proposed HRIM unit-cell structure.

The unit-cell is constructed on a Rogers RT5880 substrate with the thickness (h) of 0.508 mm, permittivity (ε_r) of 2.3, and loss-tangent of 0.0009. The unit-cell's effective permittivity, permeability as well as refractive-index were extracted by modeling the structure on Ansoft HFSS, where the perfect electric conductor and perfect magnetic conductor boundary conditions were applied along the *yz* and *xy*-planes, and the two ports were located in *x*-direction. S-parameters of the unit-cell structure and its characterizing parameters were extracted using the algorithm in [34].

The effect of the stub loading on the unit-cell's refractive-index was investigated. Various sizes of the stub loading are referred to here as Type A, B and C whose dimensions are given in Table 1.

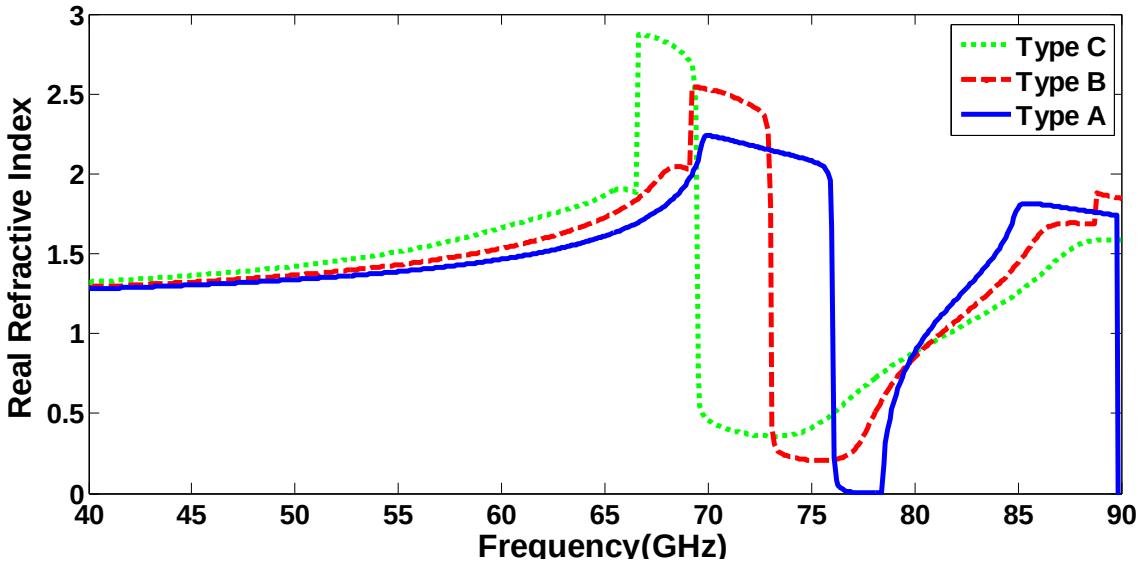

Figure 7-4: Real part of effective refractive index of the HRIM unit-cell

The insertion-loss response of the HRIM unit-cell with various lengths of stub loading is shown in Fig.7.3. It is observed that when the length of stub loading is increased from 0–0.16 mm, the anti-resonant frequency of the unit-cell shifts downwards in frequency from 77–71 GHz. The results show the anti-resonant frequency of Type A unit-cell is further away from the required operating band (57–64 GHz). The effective refractive-index of Type A unit-cell over this frequency band varies from 1.41–1.57, as shown in Fig.7. 4. However, a larger variation in the effective refractive-index is realized when the unit-cell's anti-resonance is located closer to the operating band, as exemplified by Type C unit-cell. In this case the magnitude of the effective refractive-index varies between 1.56 and 1.85 over 57–64 GHz. Type B unit-cell providing an effective refractive-index between 1.46–1.71 was selected for integration in the elevation-plane of the dipole antenna which is larger than effective refractive-index of antenna substrate (i.e. 1.28).

7.3 **Beam Deflection on a single Dipole Antenna**

In this section, the characteristics of a single dipole antenna is investigated when it's loaded with a 3×4 array of HRIM unit-cells in the elevation plane (*yz*), as shown in Fig. 7.4. The dipole antenna was constructed on Rogers RT5870 substrate with thickness of 0.254 mm and permittivity of 2.3. The index of refraction plotted in Fig.7.4 is applicable to an infinite volume of HRIM unit-cells.

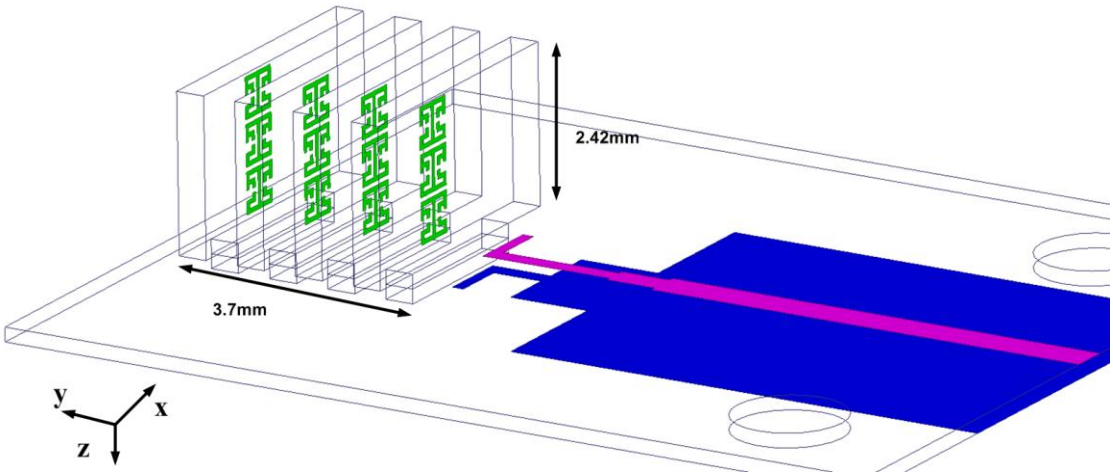

Figure 7-5: Configuration of the antenna embedded with a 3×4 array of the proposed HRIM unit-cells on upper surface of antenna substrate

However, what has been built is only a small slice, or a limited volume, of the array of slabs shown in Fig.7.5. Most of the volume of this array of slabs has a lower index of refraction, and it is described by: $[(\varepsilon_{r1}t_1 + \varepsilon_{r2}t_2)/(t_1 + t_2)]^{1/2}$, where ε_{r1} (ε_{r2}) is the relative permittivity of the dielectric slabs (of the air region) and t_1 (t_2) is the thickness of the slab region (air region). As constructed, the HRIM metamaterial is really an array of resonant scatterers which lie in a plane (the H-plane) as opposed to occupying the entire volume of the region associated with the slabs.

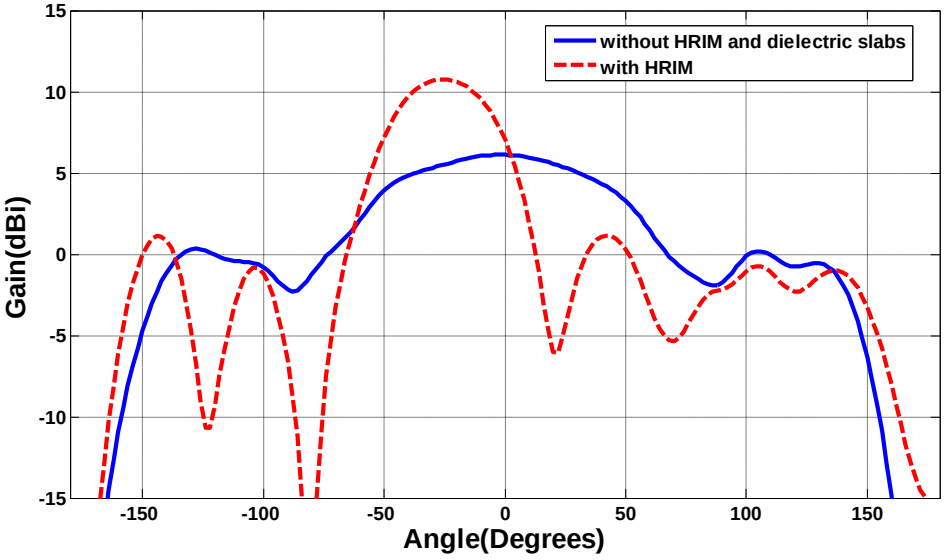

Figure 7-6: Radiation patterns of proposed antenna in the H-plane(yz) with proposed unit-cell and a conventional dipole antenna with no loading HRIM at 60 GHz.

The radiation patterns of the antenna with and without unit-cell loading in the H-plane (*yz*) of the antenna is shown in Fig.7. 6. The results show the direction of the main beam in the H-plane tilts by -30 degrees with respected to the end-fire direction. In addition, this deflection is accompanied by 5 dB gain enhancement compared to dipole antenna with no HRIM loading. This indicates the HRIM loading essentially behaves as a meta-lens that effectively increases the aperture size of antenna yielding antenna gain enhancement.

7.4 Parametric Study

In order to investigate the mechanism of beam titling explained in section II and show how the increase in the number of unit-cells in the z-direction results in a more tilt angle, a parametric study here is investigated. In initial design a 1x4 array of Type B unit-cell is included in front of the dipole antenna in the y-z direction. The result of radiation pattern in the H-plane is demonstrated in Fig.7.7. Loading a 1x4 array of abovementioned inclusions make to re-direct the beam direction up to 9 degrees from 90 to 81degrees.If a

2×4 array of unit-cell is added in the y-z direction, the beam is deflected by 18 degrees with respect to the end-fire direction. Finally increasing the array of unit-cells from 2x4 to 3x4 by integrating brings about a 30 degrees tilt angle. As a result this study proves this fact that the refractive index along with the length of artificial medium as explained in Section II are two key factors to realize more tilt angle since the increase in the length of metamaterial unit-cell.

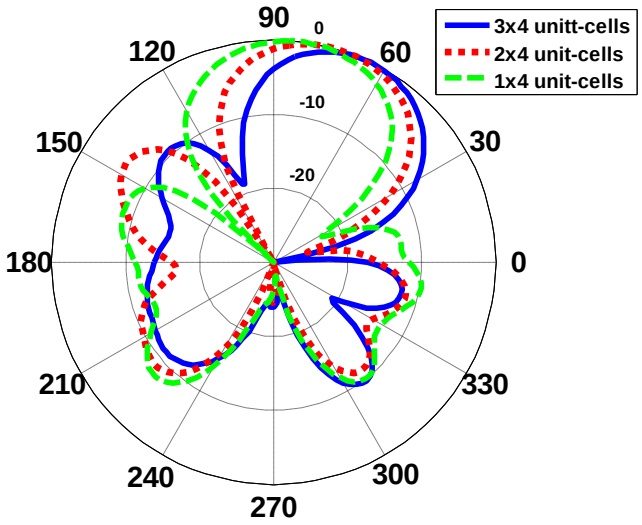

Figure 7-7:Radiation pattern of antenna in terms of different unit-cells loaded in the y-z direction

7.5 **Beam Switching Network in the elevation plane**

For a beam switching network to scan the main beam in the elevation plane from -30 to +30 degrees, it was necessary to include another dipole antenna in the opposite side of metamaterial unit-cells as shown in Fig.7.8. When port 1 is excited ‘on’ the main beam is directed to +30 degrees with port 2 terminated; conversely, when port 2 is excited ‘on’ the main beam deflects to -30 degrees with port 1 terminated. The radiation pattern of proposed structure is shown in Fig.7.9.These results suggest the direction of the beam can be electronically switched from -30 to +30degrees.

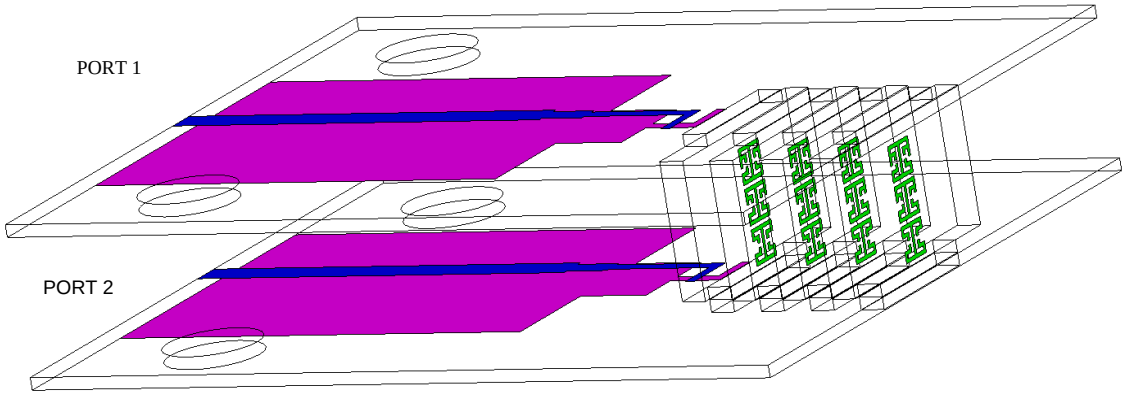

Figure 7-8: Configuration of two-dipole antenna when integrated with HRIM unit-cells.

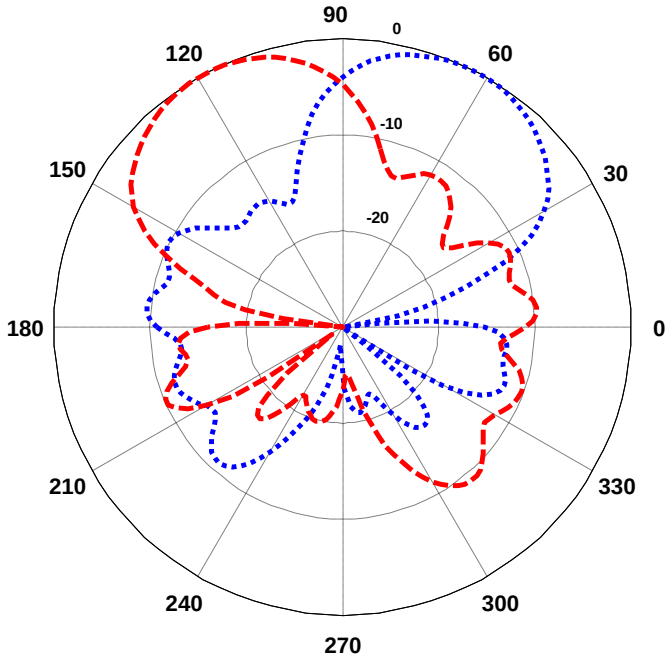

Figure 7-9: The normalized radiation pattern of elevation plane(H-plane) when working in two states at 60 GHz

7.6 **Two Dimensional Beam Tilting**

To achieve a 2-D beam scanning, a 2×4 array of Type B unit-cell was integrated in the azimuth plane of dipole antenna, as shown in Fig.7.10.This arrangement provides beam deflection of 17 degrees in the E-plane. To achieve -17 degree another dipole antenna is added on the opposite side of unit-cells. It is important to mention that a 3×5 array of H-shaped unit-cells was integrated in the elevation plane of both antennas so that a 2-D beam deflection can be implemented.

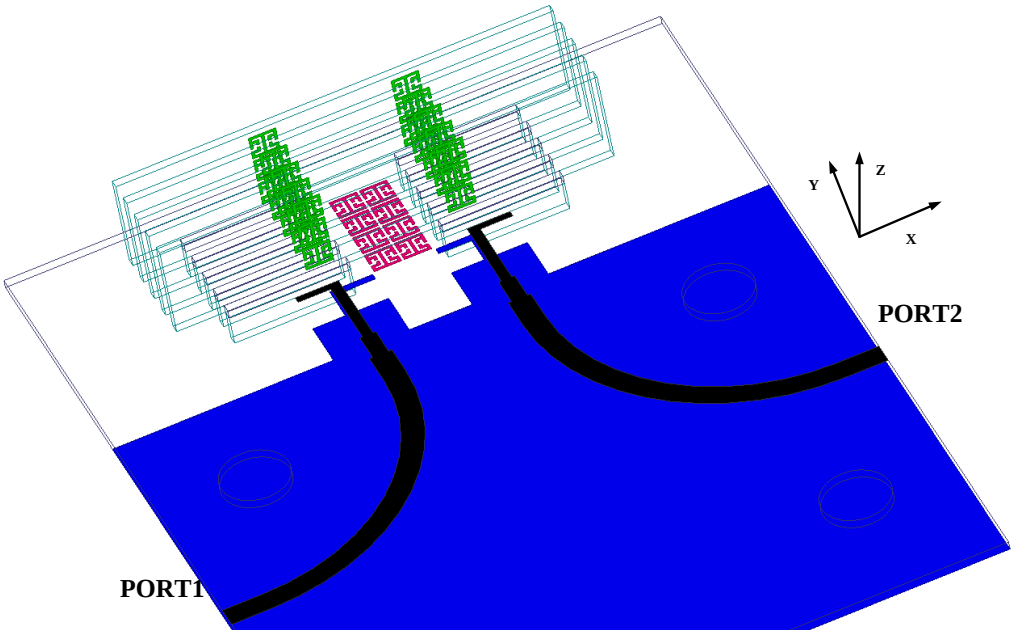

Figure 7-10: Configuration of two dipole antenna when integrated with HRIM in the azimuth and elevation planes .

The radiation pattern in Fig.7.11 shows that when antenna port 1 is excited and port 2 terminated with a 50 ohm load, the main beam in the azimuth and elevation planes tilts by 17 degrees. Conversely, when port 1 is terminated and port 2 is excited the main beam in the E-plane is directed to -17 degrees while the direction of beam in H-plane tilts by +17 degrees.

Fig.7. 11 shows the radiation pattern of the antenna when it is working in E and H-planes. This verifies that loading the antenna with an array of metamaterial unit-cells in both planes can bring about the implementation of 2-D beam tilting.

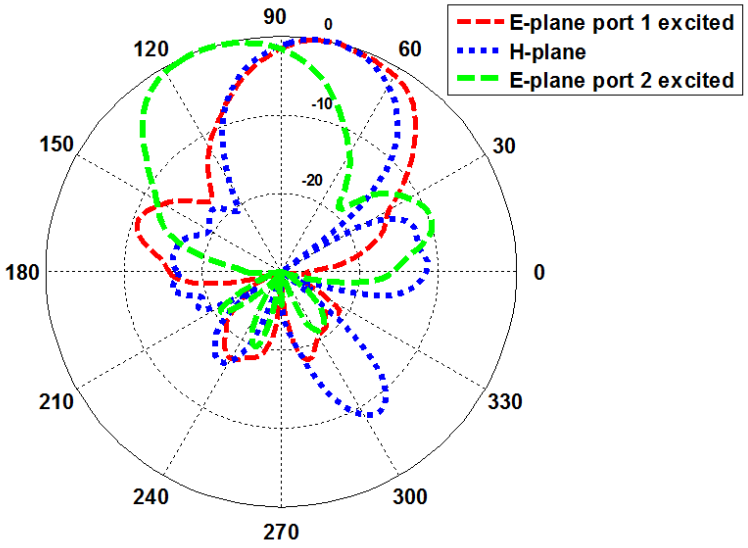

Figure 7-11: Radiation pattern of the antenna in E and H-plane when is loaded with metamaterial unit-cells in the azimuth and elevation plane at 60 GHz

To achieve a 2-D beam scanning, a 2×4 array of Type B unit-cell was integrated in the azimuth plane of dipole antenna, as shown in Fig.7.10.This arrangement provides beam deflection of 17 degrees in the E-plane. To achieve -17 degree another dipole antenna is added on the opposite side of unit-cells. It is important to mention that a 3×5 array of H-shaped unit-cells was integrated in the elevation plane of both antennas so that a 2-D beam deflection can be implemented.

The radiation pattern in Fig.7.11 shows that when antenna port 1 is excited and port 2 terminated with a 50 ohm load, the main beam in the azimuth and elevation planes tilts by 17 degrees. Conversely, when port 1 is terminated and port 2 is excited the main beam in the E-plane is directed to -17 degrees while the direction of beam in H-plane tilts by +17 degrees.

Fig.7. 11 shows the radiation pattern of the antenna when it is working in E and H-planes. This verifies that loading the antenna with an array of metamaterial unit-cells in both planes can bring about the implementation of 2-D beam tilting.

7.7 **Experimental Results**

Photograph of the fabricated single dipole-antenna with a 3×4 array of metamaterial unit-cells is shown in Fig.7.12. The HRIM unit-cells were constructed on a Rogers RT5880 dielectric slab with thickness of 0.508, and the four slabs are integrated in the H-plane of the antenna. A 1.85 mm end-launch Southwest connector was used in the antenna measurements.

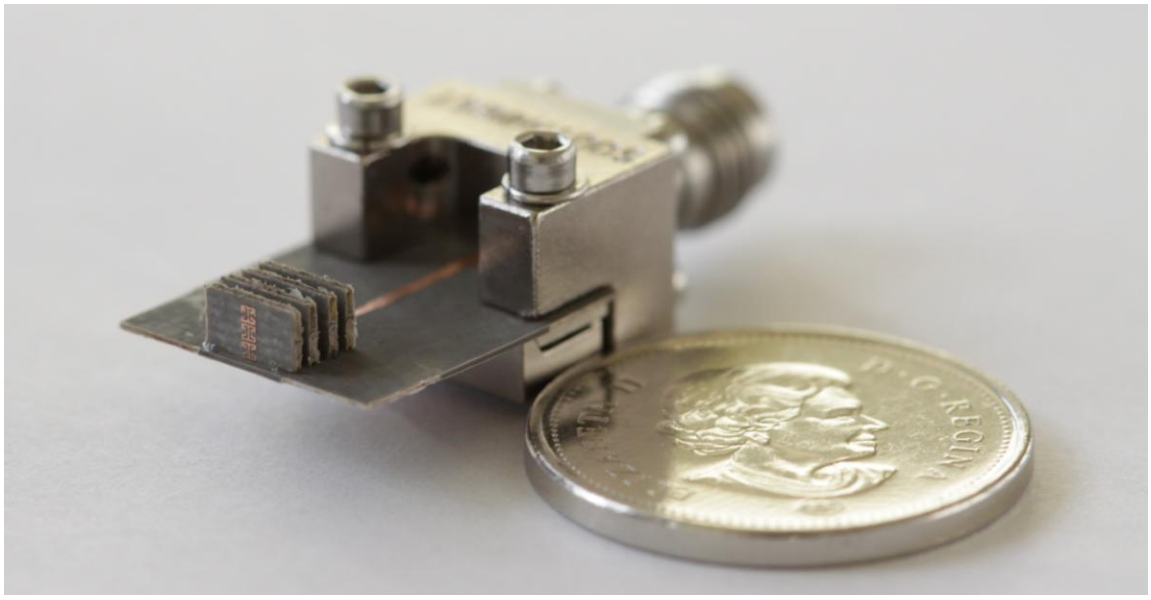

Figure 7-12: Photograph of the single-feed antenna with HRIM loading in elevation plane.

The measured reflection-coefficient of the antenna, shown in Fig.7.13, is less than -15 dB between 55–65 GHz. The simulated and measured radiation patterns of the dipole antenna in the H-plane (yz) with HRIM loading at 58, 60, and 62 GHz are shown in Fig. 7.14. The measured results confirm the main beam of the antenna tilts by 30^{o}.

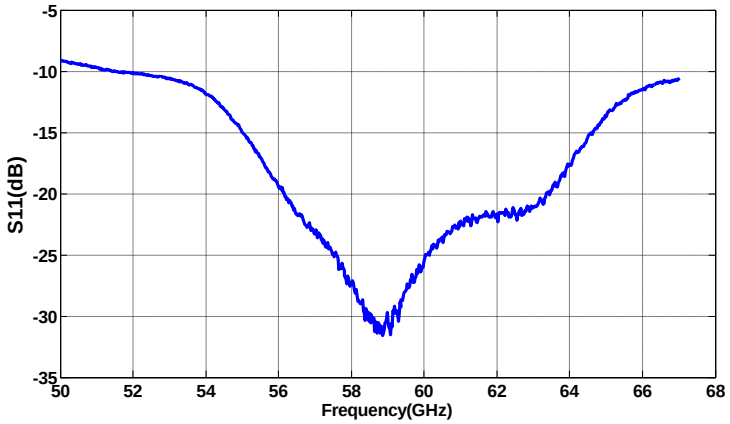

Figure 7-13: The measured reflection-coefficient of the single dipole antenna with HRIM unit-cell loading.

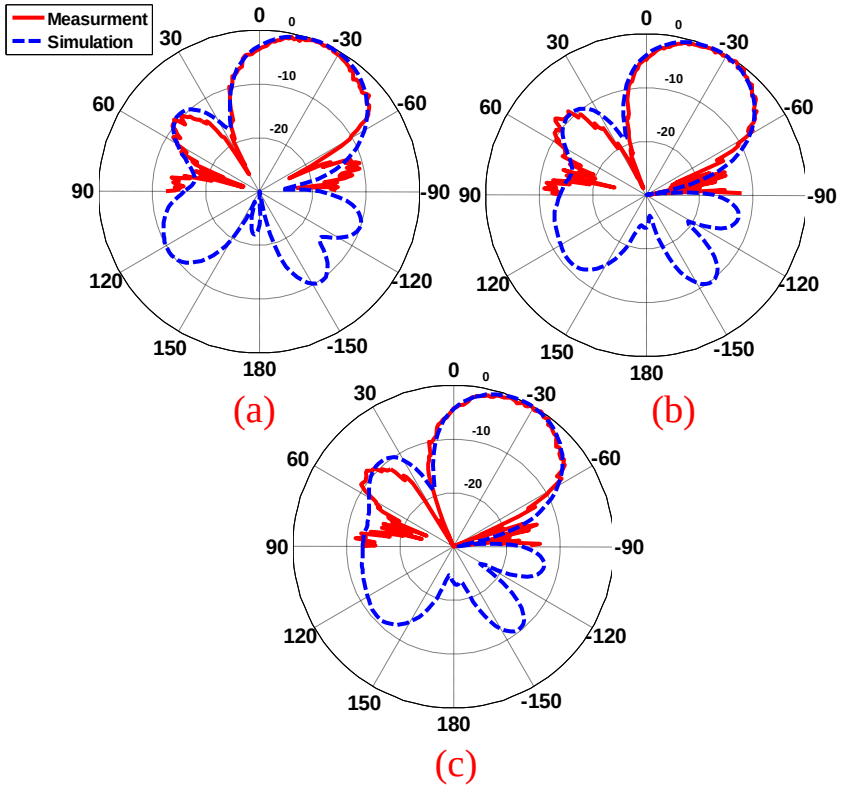

Figure 7-14:The normalized radiation patterns of the single dipole-antenna with 3×4 HRIM in the H-plane (yz) at: (a) 58 GHz, (b) 60 GHz, and (c) 62 GHz.

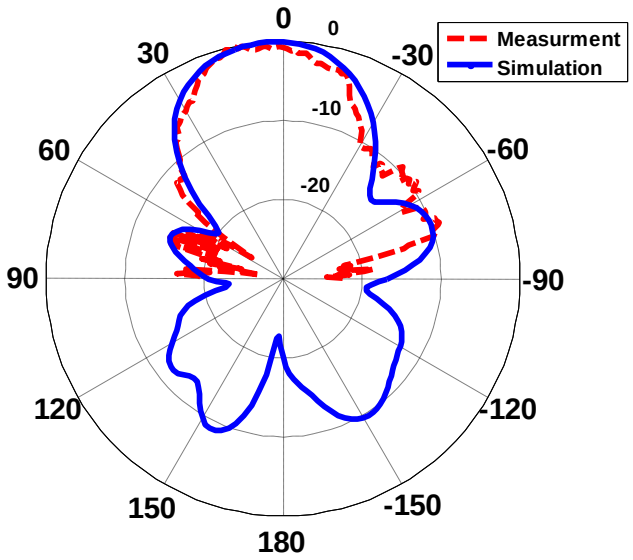

Figure 7-15: The normalized radiation pattern of the single dipole antenna with 3×4 array of HRIM unit-cells in the E-plane (xy) at 60 GHz.

The radiation pattern in the E-plane at 60 GHz, shown in Fig.7.15, remains virtually unaffected and is directed towards the end-fire direction.

The antenna gain was measured using the comparative method that involves measuring the signal received by the reference antenna and the test antenna, and determining the relative difference in the gain of both antennas when both the reference antenna and antenna under test are working in the received mode. With this information the gain of the test antenna can be determined. The measured gain of single feed antenna at beam scan angle of 30 degrees is shown in Fig.7.16. The measured result shows a peak gain of 12dB at 63 GHz, when the beam is tilted by +30 degrees in elevation planes. In addition, the measured gain is more than 10 dBi over operating range of 57-64 GHz.

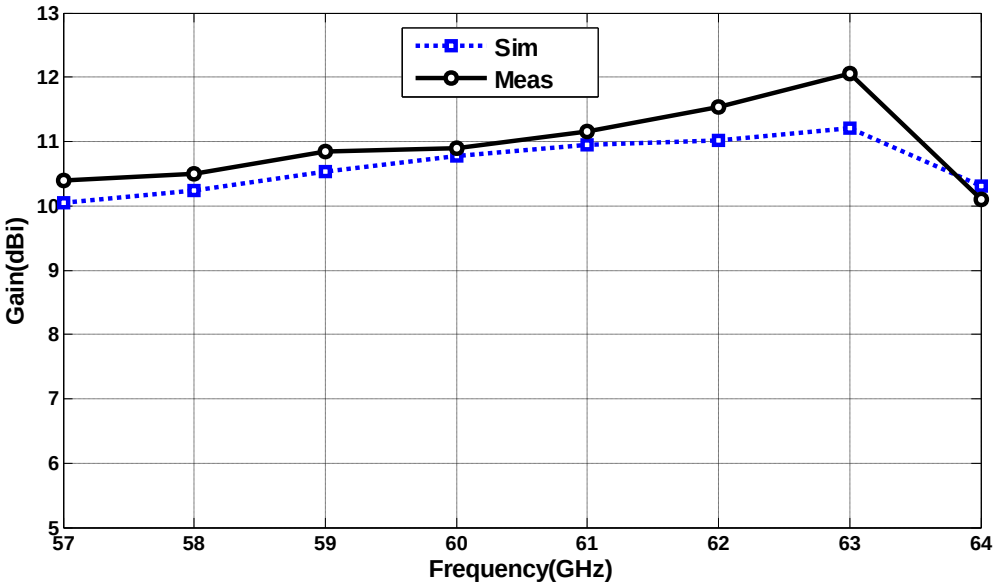

Figure 7-16: The measured and simulated antenna gain.

7.8 **Conclusion**

High refractive-index metamaterial (HRIM) unit-cells are shown to tilt the direction of a dipole antenna's main beam by a prescribed angle. This was accomplished by using an array of HRIM that were directly embedded in the elevation-plane of the planar antenna. A 3×4 array of inclusions was loaded in the elevation plane of a single dipole antenna. The simulated and measured results confirm the direction of the main beam can be deflected by +30 degrees in the H-plane (elevation plane), where the direction of main beam in the E-plane remains unchanged. The peak gain of the antenna is 12 dBi at 63 GHz when the beam was tilted by 30 degrees. To scan the main beam in the H-plane from -30 to +30 degrees a double-feed dipole with a 3×4 HRIM unit-cell was proposed. A double-feed antenna incorporating HRIM unit-cells into the azimuth and elevation plane was designed to steer the main beam direction in the E and H-plane by 17 degrees. Unlike other conventional methods of tilting, such as phased array antenna the approach proposed here leads to no degradation in gain, in fact a gain enhancement of 5 dB is observed.

Chapter 8 ONE AND TWO DIMENSIONAL BEAM SCANNING ANTENNA FOR MILLIMETER-WAVE MIMO APPLICATIONS

8.1 Introduction

60 GHz unlicensed band is attracting significant attention as it offers a huge frequency band (57–64 GHz) and signals incur large loss due to atmospheric absorption. Other characteristics that make this frequency band attractive are lower interference and greater frequency reuse. The 60 GHz frequency band promises data rates greater than 1 Gb/s over a short distance and highly compact and miniaturized systems. Although the major issue associated with working at 60 GHz is the large path-loss attenuation encountered, this can be compensated by using high-gain antennas. Since the antenna gain is inversely proportional to beamwidth, therefore high-gain antennas are associated with narrow beamwidth. This property can effectively be used to mitigate interference and multipath effects. However, such antennas make the beam alignment challenging where the location of transmitter or receiver is not fixed [62].

The antenna radiation beam can be steered using various techniques such as integrated lens antenna at millimeter-waves [73-75]; however, this approach results in a bulky antenna. The 1D and 2D beam-scanning at 30 GHz reported in [66] uses a 2×2 substrate integrated waveguide (SIW) antenna array implemented with a combination of couplers and phase shifters to provide a gain of about 8.5 dBi. The 8-port hybrid coupler employed results in a very large antenna structure ($20\lambda \times 16.766\lambda \times 0.07\lambda$).

The authors in [76] have utilized the integrated waveguide phase shifter to achieve 2D beam-scanning by using a 2×2 microstrip ring antenna array. This technique enables the main beam to be deflected by 20 degrees in both planes. The beamforming structure was implemented on a multilayer substrate which makes its construction complicated. This antenna provides a gain and radiation efficiency of 8.3 dBi and 70%, respectively, when the beam is scanned. The dimensions of structure are $2.86\lambda \times 2.86\lambda \times 0.22\lambda$. Adaptive

antennas or phased array antennas is another approach reported in [77],[78] to re-direct the beam direction in a desired angle. The above techniques require using many antenna elements, which introduces large losses and lead to costly systems.

Metamaterials have received considerable attention for applications in beamforming networks. For instance, metamaterial based phase shifters using a conventional negative reflection-index phase shifter which is fed by a 3-element leaky wave CPW-CTS antenna array provides a scanning angle of 66 degrees in the E-plane with maximum gain of 11 dBi at 2.4 GHz [79]. In [4], an active metamaterial with tunable refractive-index is shown to scan the main beam of patch antenna from 0 to 30 degrees where a gain of 5 dB is obtained at 30 degrees. However, this antenna produces large side-lobe levels, and the structure is physically large. In order to obtain a low-profile structure, the authors in [21] introduced a high refractive-index metamaterial unit-cell integrated in the azimuth plane of a printed bow-tie antenna arrays to achieve 17 degrees beam tilt angle with maximum peak gain of 9.45 dB. However, the beam deflection is fixed and the maximum scan angle is limited to 17 degrees.

This chapter presents results on 1D and 2D beam scanning technique using a mu (μ) near-zero (MNZ) metamaterial unit-cell configuration using end-fire antenna for application in millimeter-wave MIMO systems operating over 57–64 GHz. End-fire antenna was selected for this investigation as it facilitates beam-switching compared to broadside radiating antennas, especially at millimeter-wave frequencies. To the authors' knowledge, this is the first time that MNZ unit-cells have been used for 2D beam-scanning MIMO antenna at 60 GHz. The proposed structure is adaptable for mechanical scanning in both planes.

8.2 **Mechanism of Beam scanning**

It has been demonstrated in [65] that by integrating a dielectric lens in front of the antenna, which is offset from the center of the antenna, cause radiated EM waves to be refracted in a pre-defined angle. This phenomenon is due EM waves traversing in two media of different refractive indices as predicted by Snell's law. This concept has been applied here however the dielectric lens has been substituted for a metamaterial lens. The proposed metamaterial lens is used in the azimuth and elevation planes of the dipole antenna in order to refract the direction of the main beam in both planes. Unlike the dielectric lens [80]-[81] the incorporation of the metamaterial lens provides 2D beam scanning and facilitates the realization of a miniaturized structure.

Anisotropic metamaterial unit-cells are integrated onto the dipole antenna, as illustrated in Fig.8.1, where the unit-cells essentially act as a metamaterial lens. In the analysis the dipole antenna is regarded as a quasi TE source that emits EM rays. Each ray emanating from the source has an effective path length to the antenna's radiating aperture, and therefore different phase shift angles.

It is evident from Fig.8.1 that the position of the dipole antenna determines the scan angle in both azimuth and elevation planes since the movement of antenna changes the effective path length of each ray over its radiating aperture. Better understanding of the mechanism of this phenomenon can be obtained by calculating the array factor as described in [57]. The dipole antenna is considered to be a quasi TE source and the polarization of the E-field is along the azimuth plane. The dispersion equation for TE polarization to calculate the wave vector inside the metamaterial region is [14]:

$$\frac{{\beta_z}^2}{\mu_T} + \frac{{\beta_T}^2}{\mu_z} = {k_{die}}^2 \varepsilon_T \qquad (1)$$

Where the permeability along the optical axis is denoted by μ_z, which has a different value to the permeability along the transverse axes ($\mu_x = \mu_y = \mu_T$).

Transfer function of the configuration in Fig.8.1 is obtained by calculating the transmission and multiple reflection-coefficients on the top and back surface of metamaterial region when the EM wave is obliquely incident on it. Transfer function is given by:

$$T = \frac{t_1 t_2 e^{(-i\beta_z t)}}{1 - r_2{}^2 e^{(-2i\beta_z t)}} \quad (2)$$

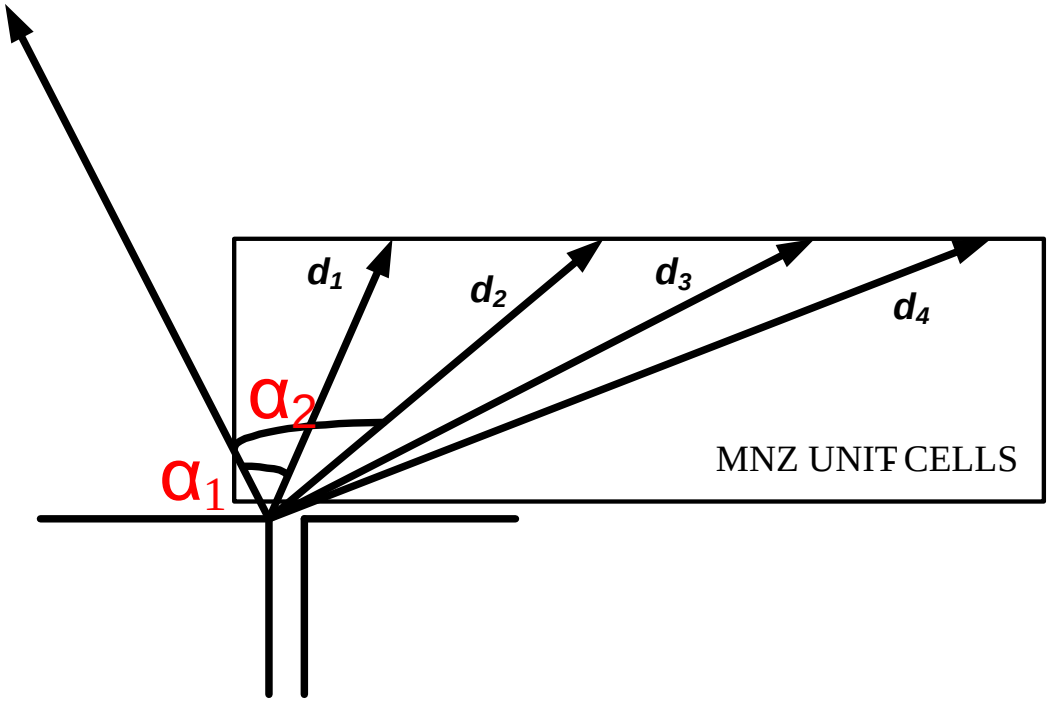

Figure 8-1: The dipole antenna loaded by MNZ unit-cells in the azimuth plane.

The transmission and reflection-coefficients are given by:

$$t_1 = \frac{2\mu_t k_z}{\mu_t + \beta_z},\ t_2 = \frac{2\beta_z}{\mu_t k_z + \beta_z},\ r_2 = \frac{\beta_z - \mu_t k_z}{\mu_t + \beta_z},\ r_1 = \frac{\beta_z - \mu_t k_z}{\mu_t + \beta_z}$$

Where $k_z = k_{die}\ \sin(\varphi)$ and β_z can be obtained from Eqn.(1). Transverse permeability is equal to 1 and the permeability in the direction of propagation is equal to 0.4.

The array factor calculation takes into account the transfer function and different path lengths (d_1,d_2,..d_5) and is given by:

$$AF = 1 + Te^{j(kd_1 cos\alpha_1)} + Te^{j(kd_2 cos\alpha_2)} + Te^{j(kd_3 cos\alpha_3)} + Te^{j(kd_4 cos\alpha_4)} \quad (3)$$

Where angle $\alpha_1 - \alpha_4$ can be obtained from [14]:

$cos\alpha_1 = \hat{a}_{ro}.\hat{a}_{d1},\ cos\alpha_2 = \hat{a}_{ro}.\hat{a}_{d2},\ cos\alpha_3 = \hat{a}_{ro}.\hat{a}_{d3}$

$cos\alpha_4 = \hat{a}_{ro}.\hat{a}_{d4}$

The total E-field of antenna in the far-field can be obtained by multiplying the element factor of dipole antenna $F(\varphi) = \cos\left(\frac{\pi}{2}\cos(\varphi)\right)/\sin(\varphi)$ in Eqn.(3).

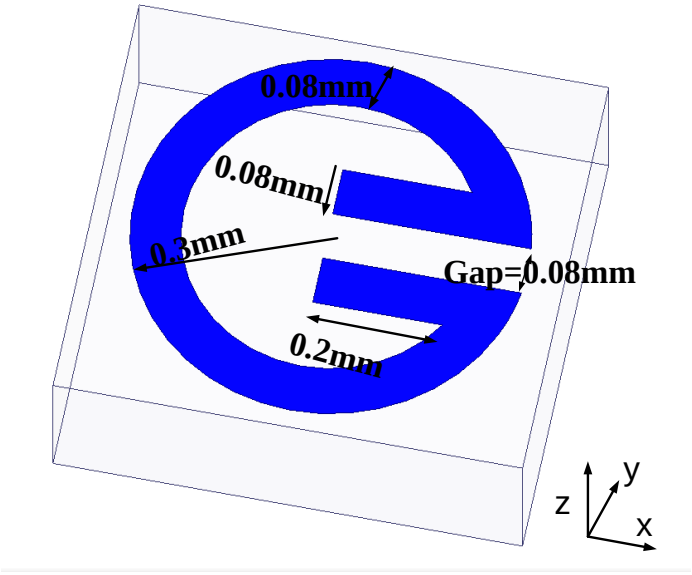

Figure 8-2: Geometry of the proposed MNZ unit-cell implemented on a dielectric substrate.

The metamaterial lens was implemented using the unit-cell configuration shown in Fig.8.2, which was derived from the capacitively loaded loop (CLL) structures in [82]. When the metamaterial unit-cell is excited by EM waves at an angle normal to the unit-cell (i.e. *z*-direction) this creates a magnetic resonance in the unit-cell whose frequency is dependent on the radius of the split-ring. The structure essentially behaves as an *LC* circuit, where the inductance is determined by the circumference of the ring and the capacitance by the gap between the parallel strips. It is important to mention that the H-field should be normal to the axis of unit-cell (along the *z*-direction) to create a magnetic resonance.

The unit-cell was constructed on a Rogers RT5870 substrate with the thickness (h) of 0.254 mm, permittivity (ε_r) of 2.3, and loss-tangent (δ) of 0.0009.The electrical parameter of MNZ unit-cell, i.e. permeability, was extracted from its model using Ansoft HFSS, where the PEC and PMC boundary conditions were applied along the *yz* and *xy*-planes, and the two ports were located in the *y*-direction. The polarization of E-field is horizontal (*x*-direction). The S-parameters (S_{11} and S_{12}) of the unit-cell structure and its characterizing parameters were extracted using the algorithm in [34].

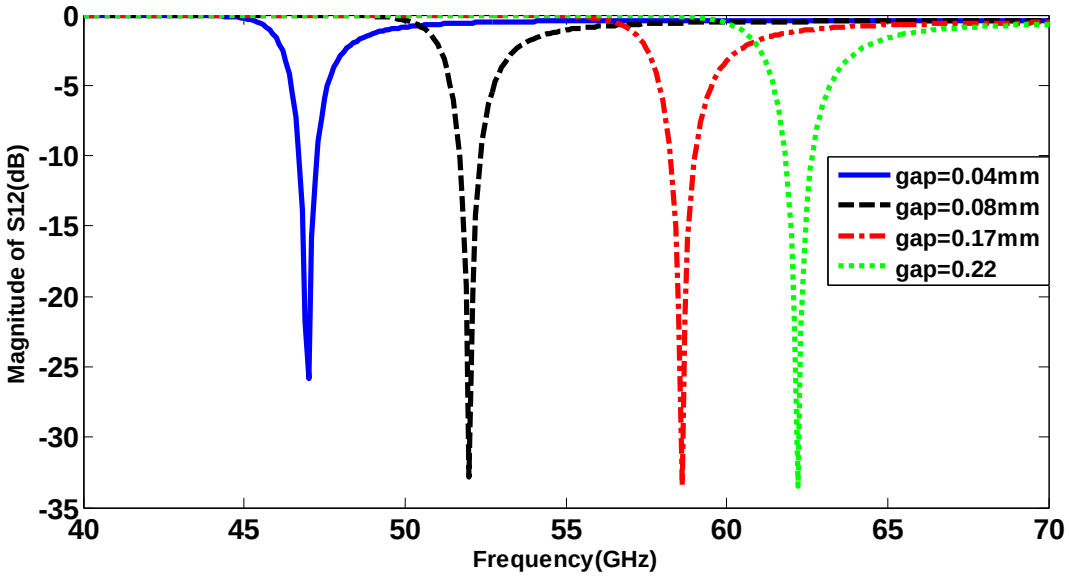

Figure 8-3: Magnitude of S12 of the proposed MNZ unit-cell structure as a function of the parallel coupled gap size.

The effect of the gap in the MNZ unit-cell on the insertion-loss response, shown in Fig. 8.3, indicates that when the gap is increased from 0.04 mm to 0.2 mm the anti-resonant frequency of the unit-cell shifts upwards in frequency from 46 to 64 GHz, respectively. This is attributed to the decrease in the capacitive coupling in the proposed MNZ unit-cell. The effect of the gap on the permeability of the MNZ unit-cell in Fig.8.4 shows it has a Lorenzian-type resonance. The magnetic resonance of the MNZ unit-cell shifts upward from 46 GHz to 64 GHz when the gap is increased from 0.04 mm to 0.2 mm, respectively. The MNZ unit-cell with a gap of 0.08 mm was selected as it artificially made the unit-cell to exhibit permeability less than 0.4 over 57–64 GHz. By integrating

an array of MNZ unit-cells in the azimuth plane of a radiating dipole antenna should refract the radiation beam as the MNZ array behaves as a metamaterial lens.

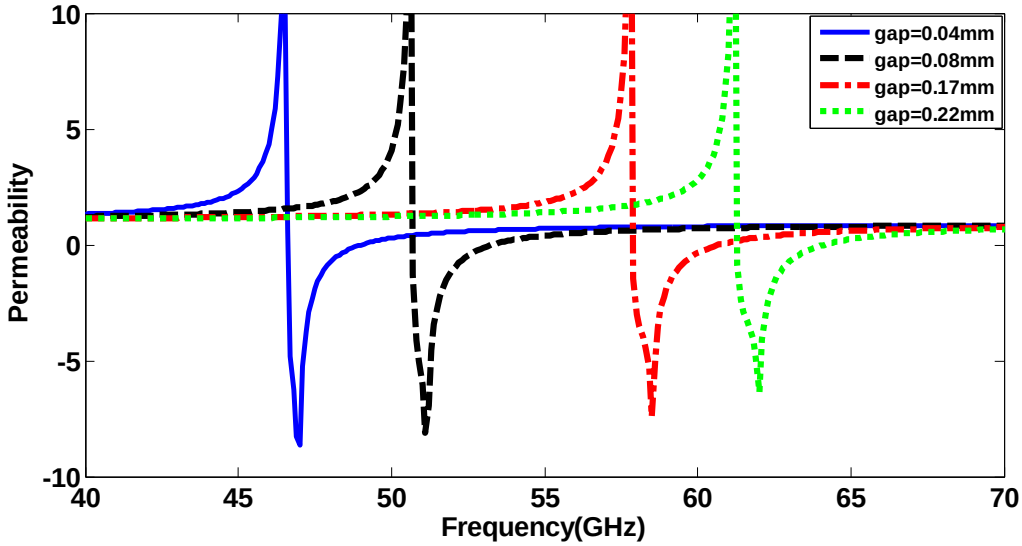

Figure 8-4: Real-part of effective permeability of the MNZ unit-cell.

The horizontal and vertical polarization of the proposed CLL unit-cell was obtained from its S-parameters. Fig.8. 5 shows the magnitude of transmission-coefficient when the E-field is polarized in the *x*-direction (horizontal polarization) and *y*-direction (vertical polarization), respectively. The results show that when the polarization is rotated by 90 degrees the resonant frequency of the unit-cell shifts by 2 GHz. This needs to be taken into account at the receiver.

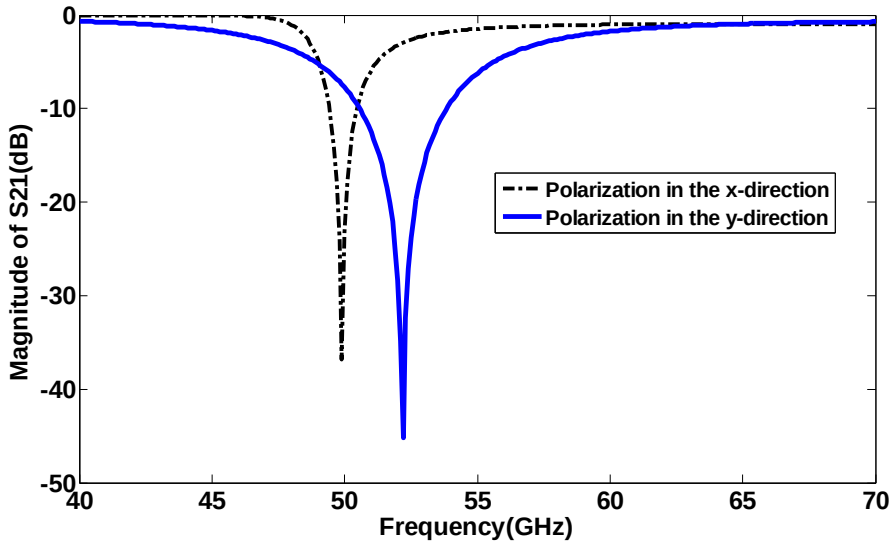

Figure 8-5: The magnitude of transmission coefficient with vertical and horizontal polarizations.

8.3 Beam Forming with a single antenna

In this section, the characteristics of a single-dipole antenna are explored when MNZ slabs are mounted vertically in front of one of the dipole arms, where the eight slabs are loaded with 4×10 array of MNZ unit-cells and the last two slabs loaded with 4×6 MNZ unit-cells in the azimuth plane (*xy*), as shown in Fig.8. 6. The distance between dipole and MNZ layers is $0.06\lambda_o$ to facilitate mutual interaction between the antenna and the slabs. The MNZ layers protrude by $1.12\lambda_o$ towards the end-fire direction. The dipole antenna used here is a modified version of the dipole antenna reported in [50]. The slabs were symmetrical loaded to prevent scanning in elevation plane.

The array of MNZ unit-cells are offset from the center of dipole antenna in the E-plane however the array is symmetrical in the H-plane. The same substrate was used to construct the array and antenna. The radiation pattern of the printed dipole antenna with and without MNZ inclusions in the E-plane is shown in Fig.8.7. The results show that when the MNZ layers are integrated vertically on the antenna substrate with respect to the azimuth plane, the direction of the main beam in the E-plane (*xy*) shifts by 34 degrees with respected to the end-fire direction (*y*-axis).

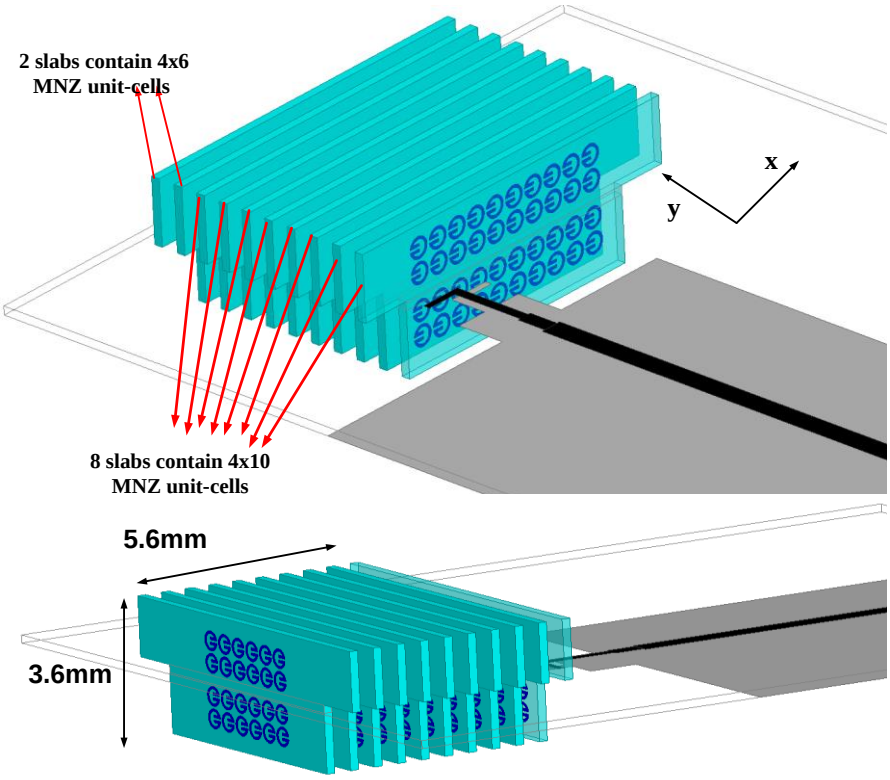

Figure 8-6: Configuration of proposed antenna integrated with 10 slabs of MNZ unit-cells.

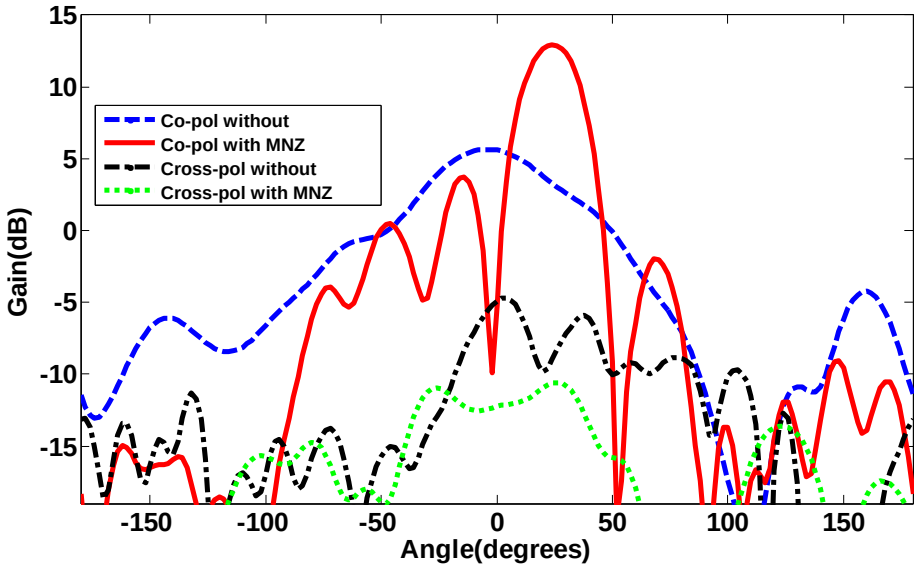

Figure 8-7: Co- and cross-polarization of the proposed antenna in the E-plane (xy) loaded with MNZ unit-cells, and a conventional dipole antenna at 60 GHz

In addition, this deflection is accompanied by 8 dB gain enhancement compared to dipole antenna with no MNZ unit-cell loading because the MNZ unit-cells effectively increase the aperture size of antenna. The cross-polarization of the dipole antenna loaded with MNZ layers is -22 dB, which is 2 dB better than cross-polarization of conventional antenna.

8.4 Parametric Study

In this section the results of a parametric study are presented. The initial dipole antenna design uses ten metamaterial slabs oriented in the *y*-direction on the top and bottom sides of the antenna, as shown in Fig.8.6. The effect of increasing the number of MNZ unit-cell inclusions along the *x*-direction from 4×3 to 4×10 results in the beam scanning angle to increase from 6 to 32 degrees, respectively, as shown in Fig.8.8. By creating a homogenous bulk of metamaterial medium is shown to improve the side-lobe level (SLL) and gain by 3 dB and 1 dB, respectively.

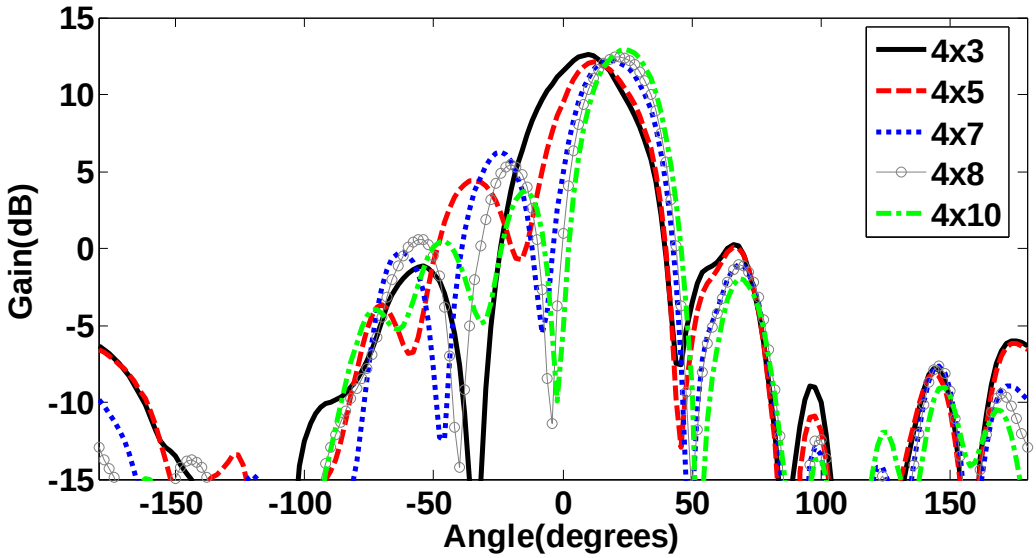

Figure 8-8: Radiation patterns of proposed antenna in the E-plane (xy) in terms of the number of MNZ slabs along the x-direction at 60 GHz

The peak realized gain of the antenna as a function of number of MNZ layers is shown in Fig. 8.9. The results show that by embedding two layers in front of the antenna enhances

its gain by 3.5 dB over 57–64 GHz compared to conventional dipole antenna. Also by increasing the layers from 2 to 5 enhances the gain from 8.5 to 9.8 dBi. However, by increasing the layers from 8 to 10 only improves the gain marginally by 0.6 dBi. Hence, in the final antenna design we have selected 10 layers.

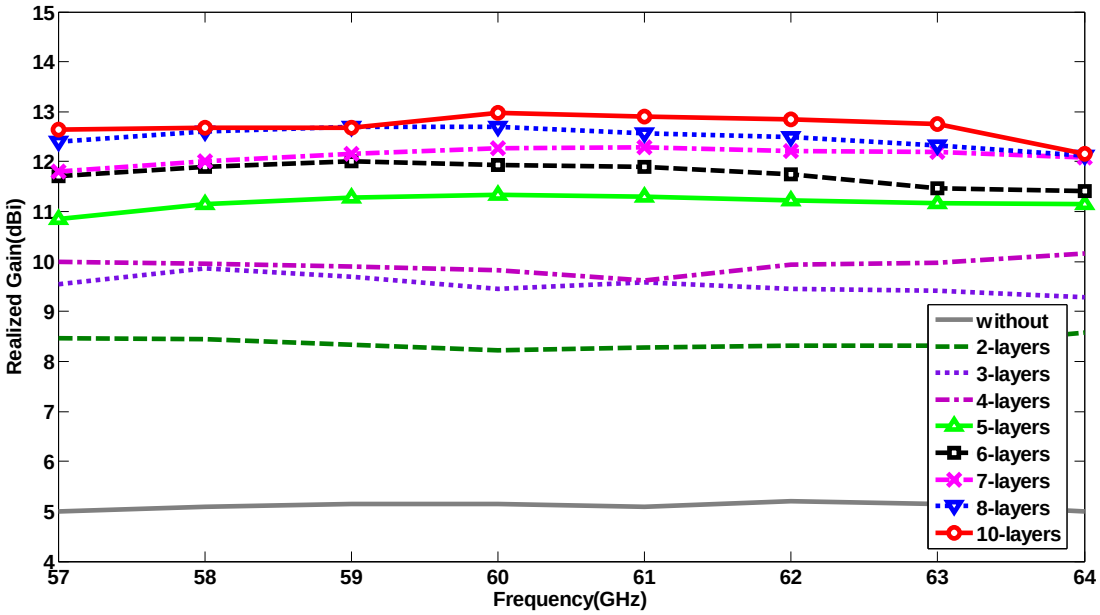

Figure 8-9: The peak realized gain of antenna as a function of different MNZ layers.

To demonstrate the versatility of the proposed antenna it is now shown the antenna's main beam can be steered in the azimuth plane (E-plane) by simply shifting the position of the dipole along the *x*-direction relative to the slabs. In the study tens slabs were used which were loaded with 4×10 array of MNZ unit-cells. Fig. 8.10 shows the antenna beam can be steered from -34 to 34 degrees when the position of the dipole is shifted from 0 to 6.5 mm, respectively. The results show the peak gain is maintained at 12.6 dBi over the steering angle.

Fig. 8.11 shows the antenna gain improves by 0.6 dB and SLL improves marginally when the last two layers consist of 4×6 unit-cells.

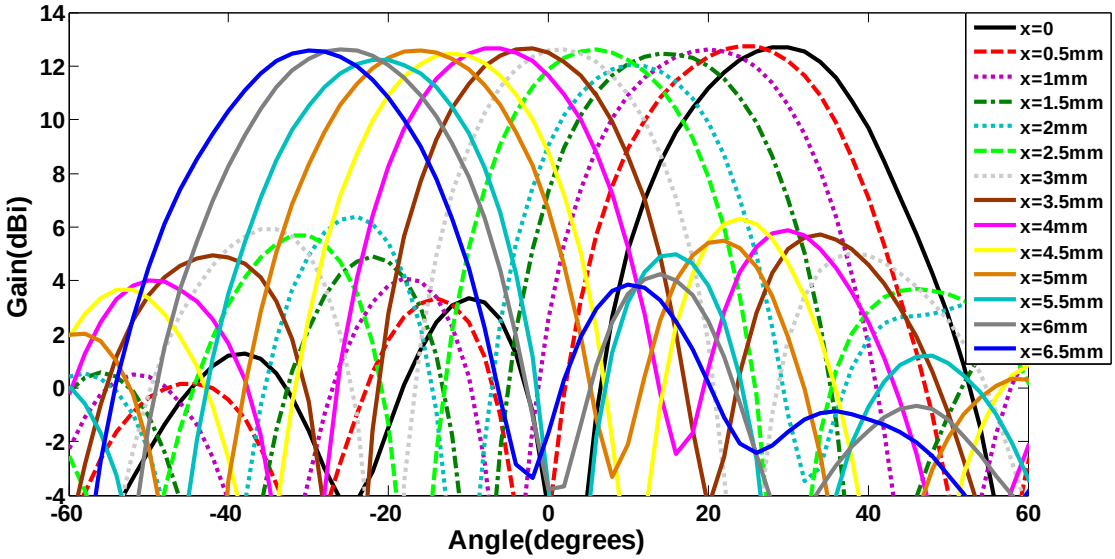

Figure 8-10: The Radiation patterns of proposed antenna in the E-plane (xy) as a function of the dipole antenna position along the x-direction at 60 GHz.

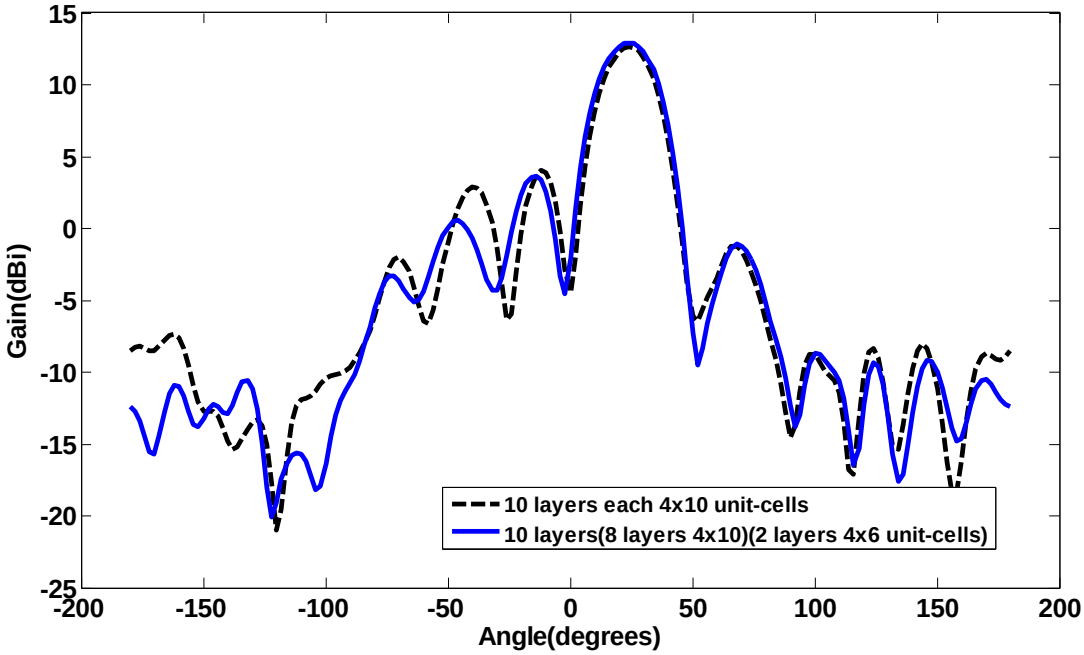

Figure 8-11: Radiation patterns of proposed antenna in the E-plane (xy) in terms of decreasing the number of unit-cells at two last layers at 60 GHz

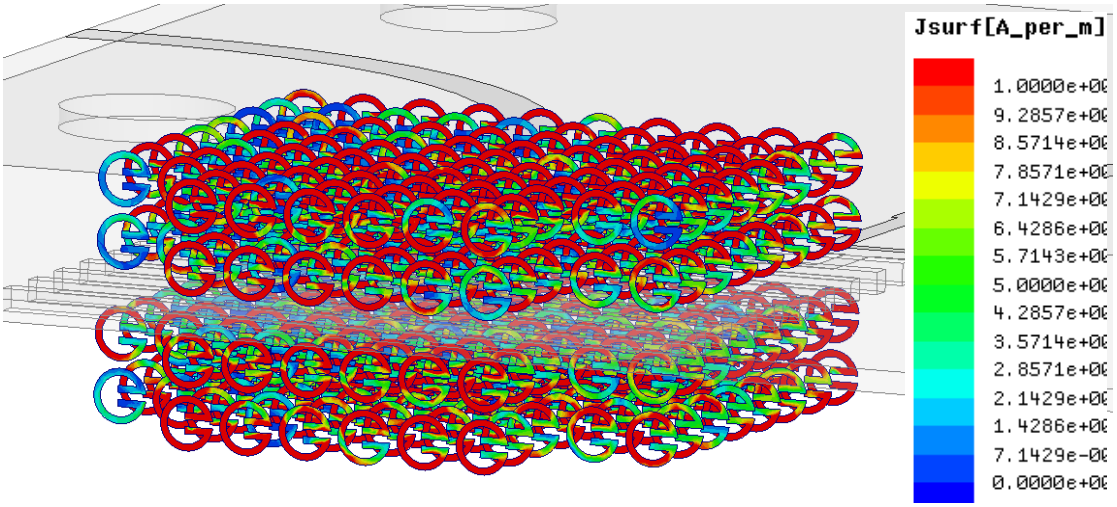

Figure 8-12: Surface current distribution on the MNZ unit-cells at 60 GHz.

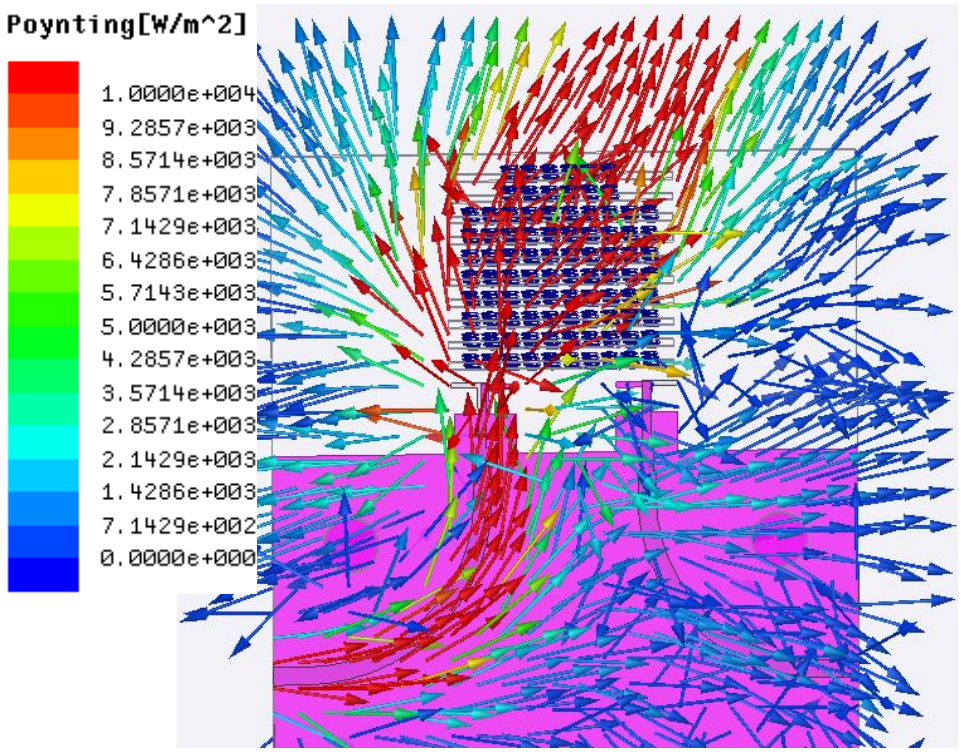

Figure 8-13: Poynting vector points in the E-plane (xy) at 60 GHz.

The surface current distribution over the metamaterial lens is shown in Fig.8. 12. This shows the interaction of the MNZ unit-cells with the radiation effectively increases the aperture size of the antenna to enhance its gain performance. The intensity of current at the outer MNZ slabs is less than at the center. So by reducing the number of MNZ unit-cells in the last two layers is like tapering the current distribution that results in improvement in SLL. The Poynting vector distribution at 60 GHz in Fig.8.13 confirms the radiated energy from the dipole antenna is significantly affected by the metamaterial region.

8.5 **Beam Switching Network In the Azimuth plane**

For application in a beam switching network where the main beam needs to be scanned in the E-plane from -34 to +34 degrees, it was necessary to include another dipole antenna on the opposite side of MNZ unit-cell slabs, as illustrated in Fig.8.14.

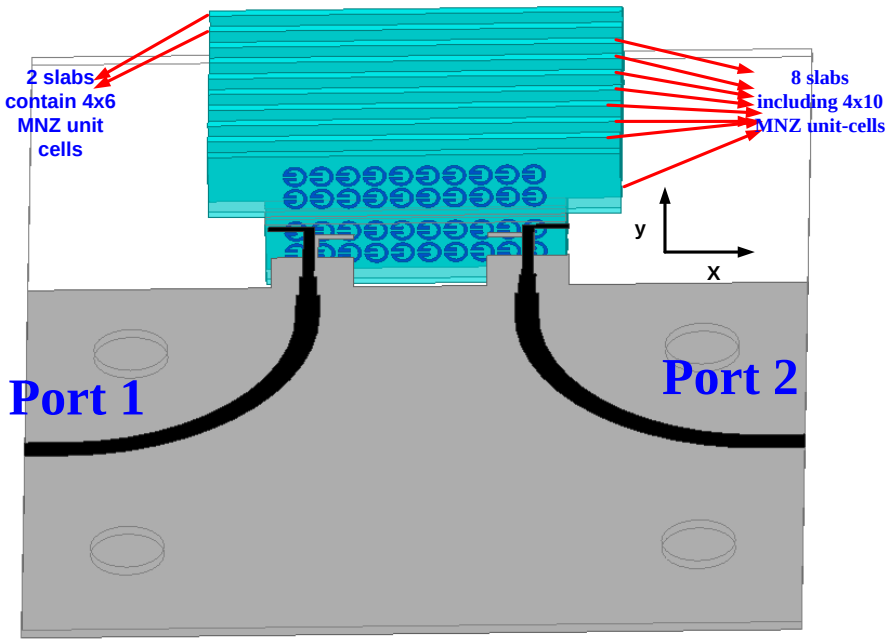

Figure 8-14: Configuration of two-dipole antenna when integrated with MNZ unit-cells.

When port 1 is switched ‘on’ while the port 2 is terminated in 50 ohm load, the main beam deflects to +34 degrees. Conversely, when port 2 is switch ‘on’ while the port 1 is terminated, the main beam deflects to -34 degrees. The radiation pattern of this antenna configuration is shown in Fig.8.15. These results suggest the direction of the beam can be electronically switched from -34 to +34 degrees.

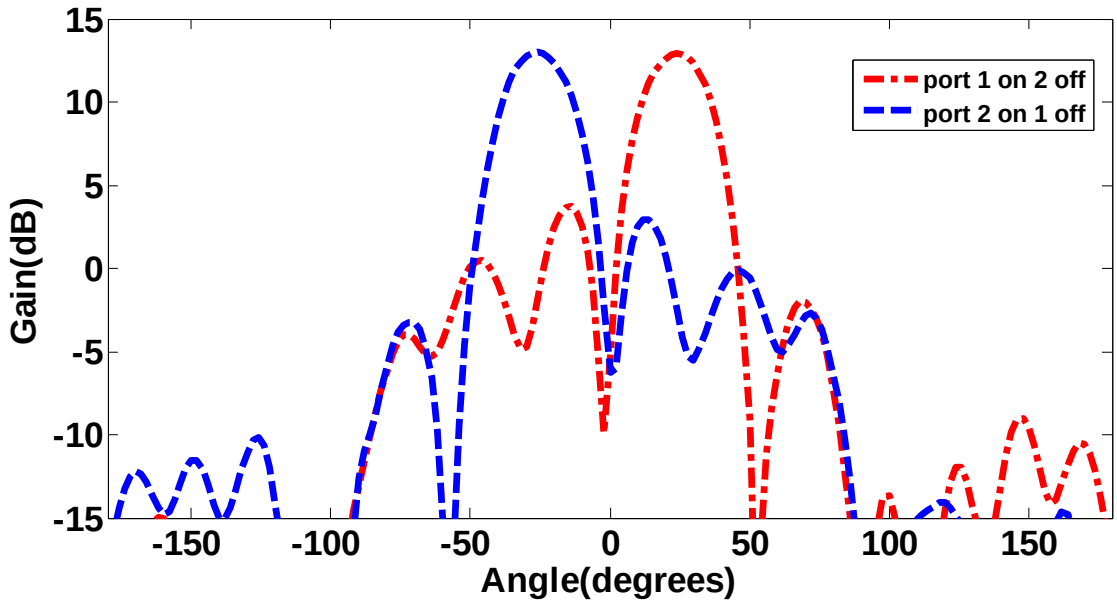

Figure 8-15: The radiation pattern in the azimuth plane at 60 GHz.

8.6 **Two-Dimensional Beam Tilting**

To achieve 2D beam scanning, 8 slabs were mounted on the double dipole antenna substrate, as illustrated in Fig.8.16. Each slab comprised 7×10 array of MNZ unit-cells. The radiation pattern of proposed double-dipole MNZ antenna in Fig.8.17 verifies that the E- and H-plane are refracted by 34 degrees (with respect to end-fire direction of 90 degrees) when port 1 is excited and port 2 is terminated with 50 ohm load. A beam deflection of 34 degrees is obtained in the E-plane (*xy*) and H-plane (*yz*) as the radiated EM waves from the dipole antenna interact with the MNZ medium.

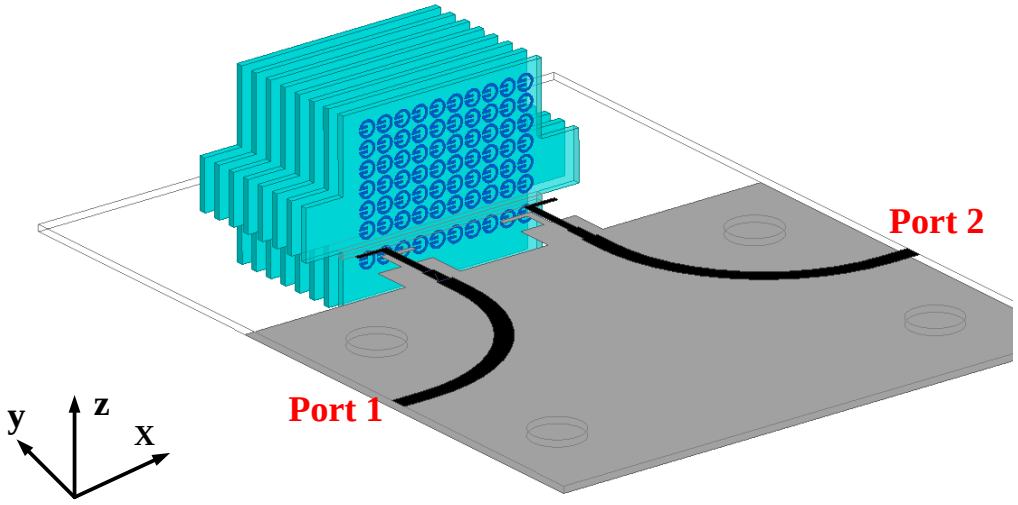

Figure 8-16: 3D configuration of the two-dipole antenna when integrated with MNZ unit-cells in both E-and H-planes.

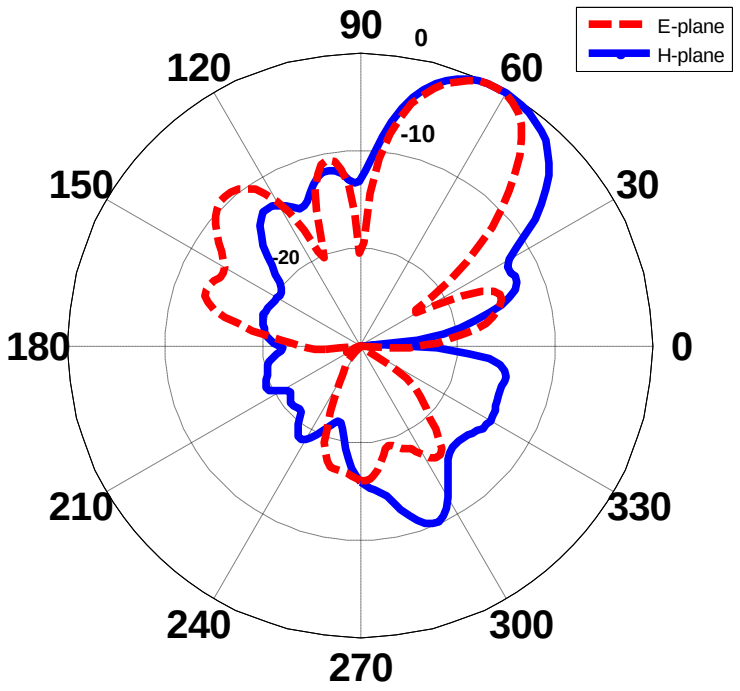

Figure 8-17:2D normalized E- and H-plane radiation patterns of the two dipole antenna when integrated with MNZ unit-cells in the azimuth and elevation planes.

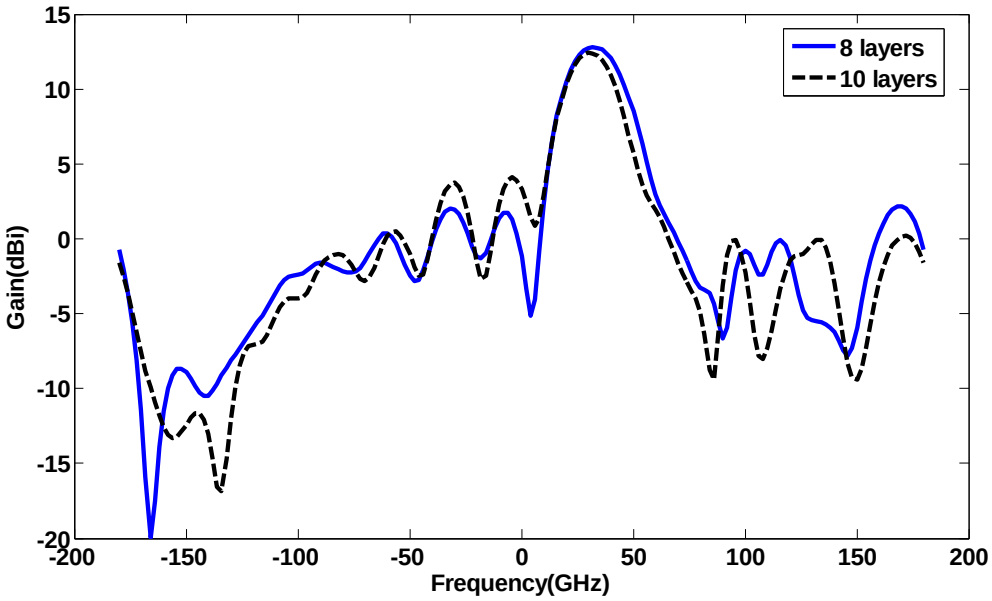

Figure 8-18: Radiation patterns of proposed antenna in the H-plane (yz) with different layers at 60 GHz.

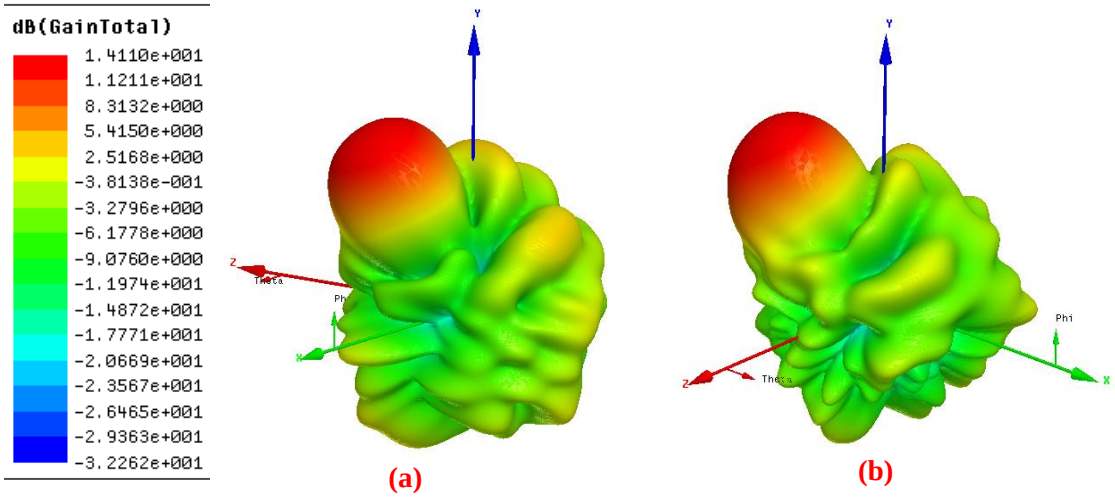

Figure 8-19: 3D radiation pattern of two-dipole antenna when integrated with MNZ unit-cells in both E-and H-planes when: (a) port 1 is excited and port 2 terminated, and (b) port 2 is excited and port 1 terminated.

By increasing the MNZ slabs from 8 to 10 the SLL deteriorates by 3 dB, as shown in Fig.8. 18. This, 8 slabs are selected as the optimum design for the 2D configuration.The 3D-radiation pattern in Fig.8. 19(a) proves that when antenna port 1 is excited and port 2 terminated with a 50 ohm load, the main beam in the azimuth (*xy*) and elevation (*yz*) planes tilt by 34 degrees with respects to the end-fire direction (*y*-axis). Conversely, when port 1 is terminated and port 2 is excited the main beam in the E-plane is directed towards -34 degrees while the direction of beam in H-plane tilts by +34 degrees with respects to the *y*-axis. The maximum gain of antenna is 14.11 dBi when the main beam direction is tilted.

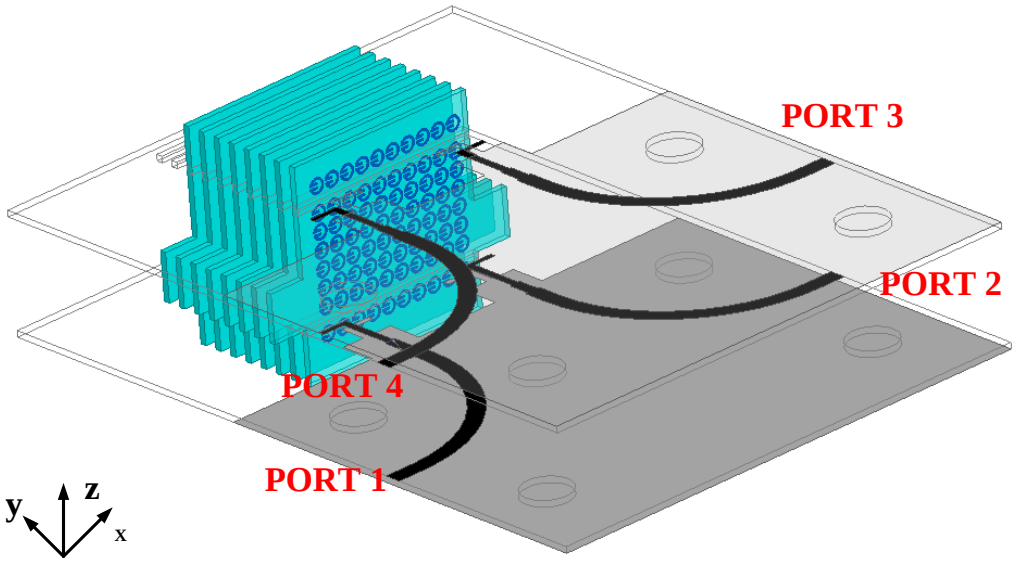

Figure 8-20: Configuration of two-dipole antenna when integrated with MNZ metamaterial unit-cells in the azimuth and elevation planes

A larger scan angle in the elevation plane can be realized by increasing the length of MNZ medium along the *z*-direction. To achieve a -34 degree beam deflection in the elevation plane, another identical double dipole antenna is stacked on the top of MNZ medium, as shown in Fig.8.20. By exciting the four ports one at a time with the other ports terminated appropriately four states of beam deflection can be implemented in the E- and H-planes.

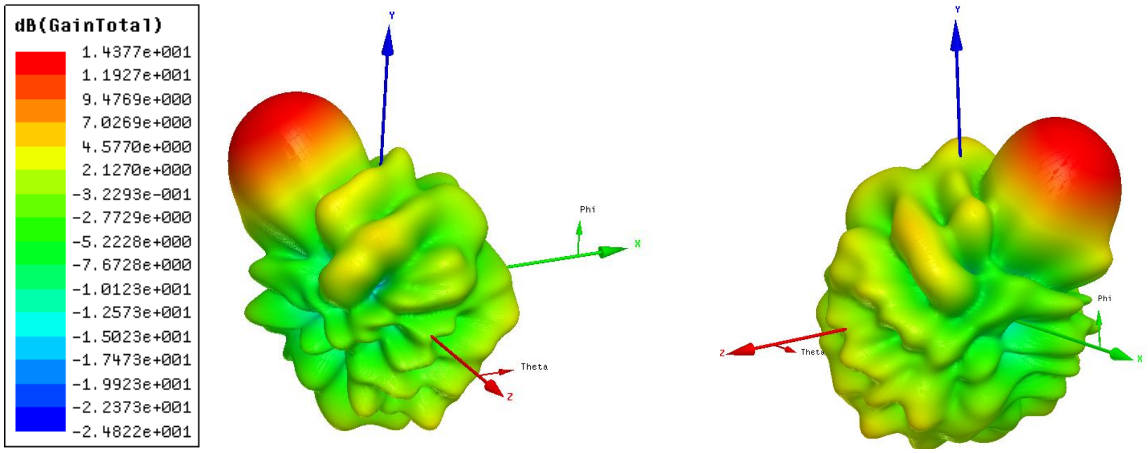

Figure 8-21: 3D radiation pattern of two-dipole antenna when integrated with MNZ unit-cells in both E-and H-planes when: (a) port 3 is excited, and (b) port 4 is excited.

8.7 Experimental Results

A photograph of the proposed two-dipole antenna with an array of MNZ unit-cells is shown in Fig.8.22. The 10 slabs are integrated in the E-plane of the antenna, where 8 slabs comprise of 4×10 array and 2 slabs comprise of 4×6 array. The measured reflection-coefficient of structure, shown in Fig. 8.23, is <-14 dB between 54–67 GHz. The measured results agree well with the simulation results. In the measurements a 1.85 mm end-launch connector (model no.1892-03A-5) was used. The Vector Network Analyzer used was Anritsu MS4647A. The system was calibrated with a standard short-open-load thru calibration procedure. The simulated and measured results presented agree well with each other showing the accuracy of the model is valid. The connector model was based on the datasheet from Southwest for the 1.85 mm end-launch connector [19]. Furthermore, the magnitude of S_{12} indicates mutual coupling between the two dipole antennas is less than -20 dB over 55–67 GHz.

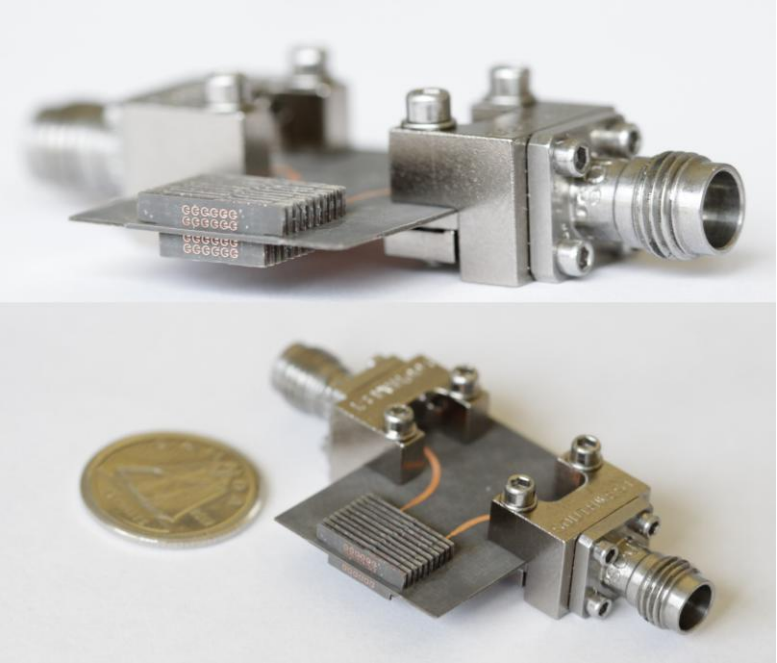

Figure 8-22: Photograph of the double feed antenna with MNZ loaded in the azimuth plane.

The simulated and measured radiation patterns of the two-dipole MNZ antenna in the E-plane at 58, 60, 62, and 64 GHz are shown in Fig.8.24 (a-c), respectively. The measured results confirm that the main beam of the antenna can shift by 34 degrees once the port 1 is exited and port 2 is terminated; conversely the main beam direction deflects by -34 degrees when the port 2 is excited and port 1 is terminated.

The antenna gain was measured using the comparative method that involves measuring the signal received by a reference antenna and by the antenna under test, and determining the relative difference in the gain of both antennas when both the reference antenna and antenna under test are working in the received mode With this information, the gain of the test antenna is determined. The microstrip line and the end-launcher connector loss, which is about -1.6 dB over frequency range of 58–64 GHz, were also taken into consideration. The measured gain of single feed antenna at a beam scan angle of 34 degrees is given in Table I.

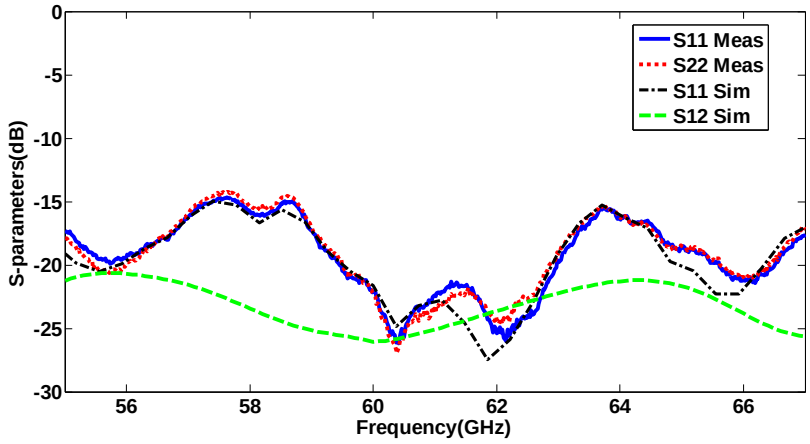

Figure 8-23: The measured reflection-coefficient of MNZ dipole antenna.

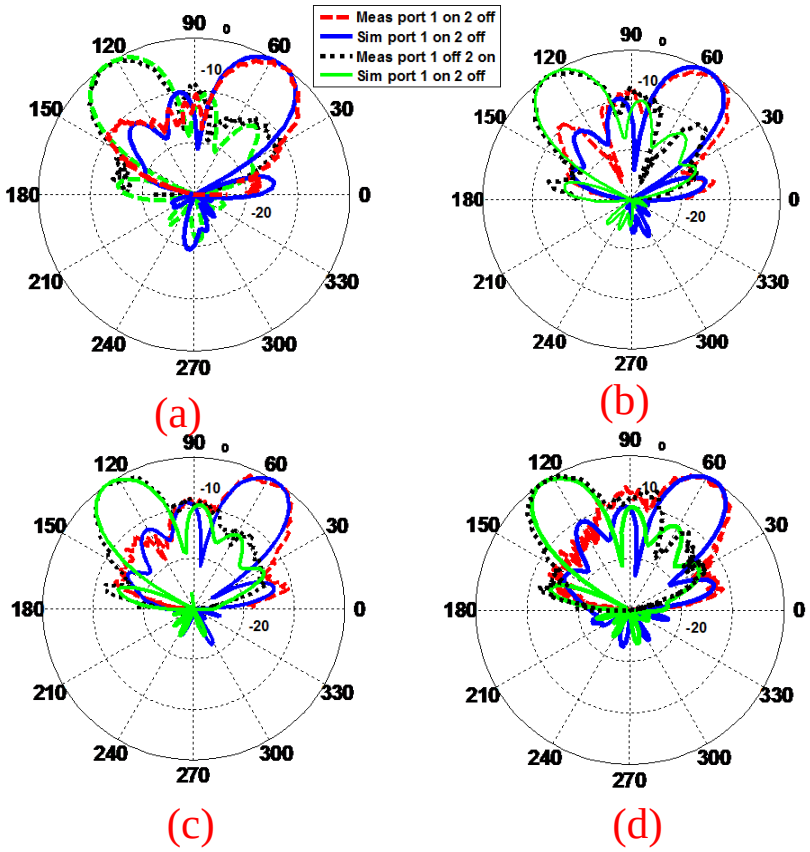

Figure 8-24: The normalized simulation and measured radiation patterns of double dipole antenna with 10 slabs of MNZ unit-cells in the E-plane (yz) at (a) 58 GHz, (b) 60 GHz, (c) 62 GHz, and (d) 64 GHz

The measured result shows a peak gain of 12.44 dB at 62 GHz, when the beam is swept by +34 degrees in azimuth plane. In addition, the measured gain is more than 12.38 dBi over of 58–64 GHz. The radiation efficiency of the antenna was measured by calculating the directivity and taking into account the measured gain. The radiation efficiency of the MNZ antenna is 88% at 60 GHz; the original dipole antenna has radiation efficiency of 95%. Reduction in the efficiency is attributed to ohmic losses.

Table 8-1: Measured and simulated peak gain of the proposed MNZ dipole antenna at beam scan angle of 34 degrees when port 1 is excited.

Freq. (GHz)	Simulated peak gain (dBi)	Measured peak gain (dBi)
58	12.85	12.30
60	13.00	12.41
62	13.10	12.44
64	12.90	12.35

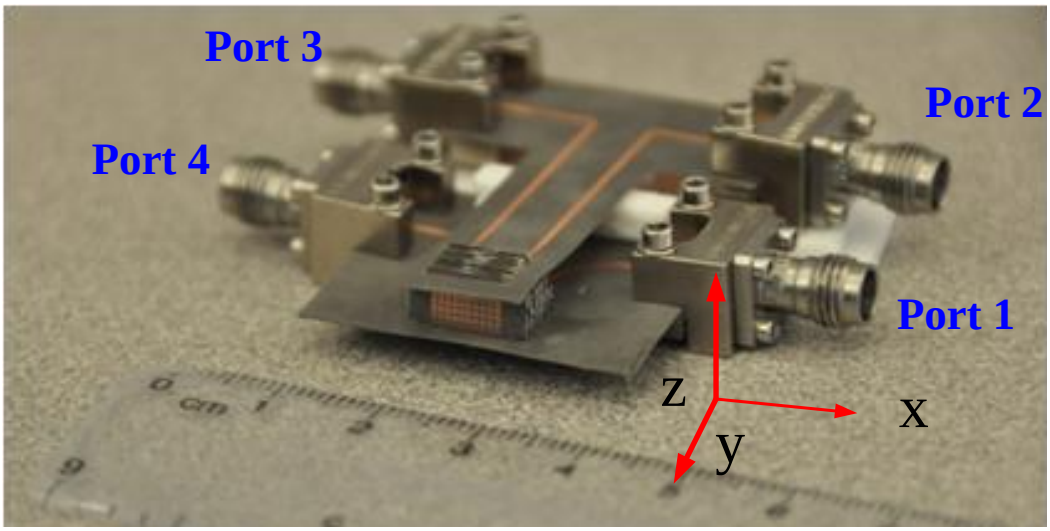

Figure 8-25: Photograph of the 2D beam-scanning MIMO antenna loaded by MNZ unit-cells in azimuth and elevation planes.

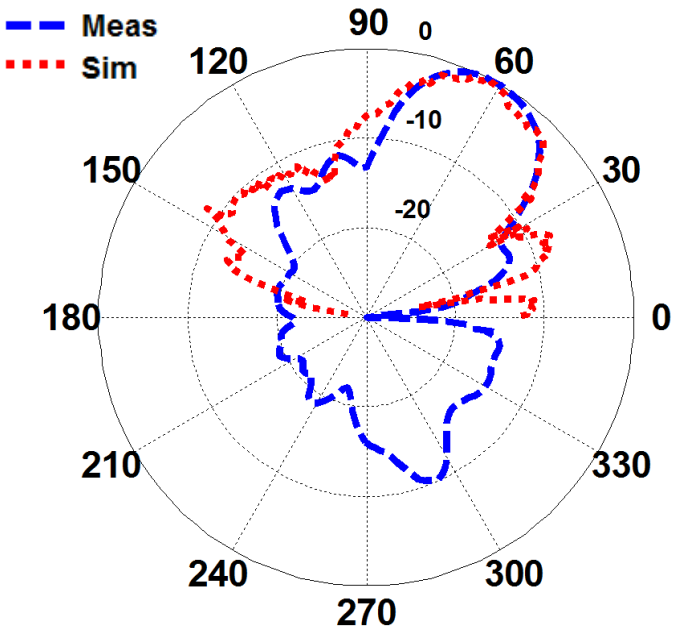

(a)

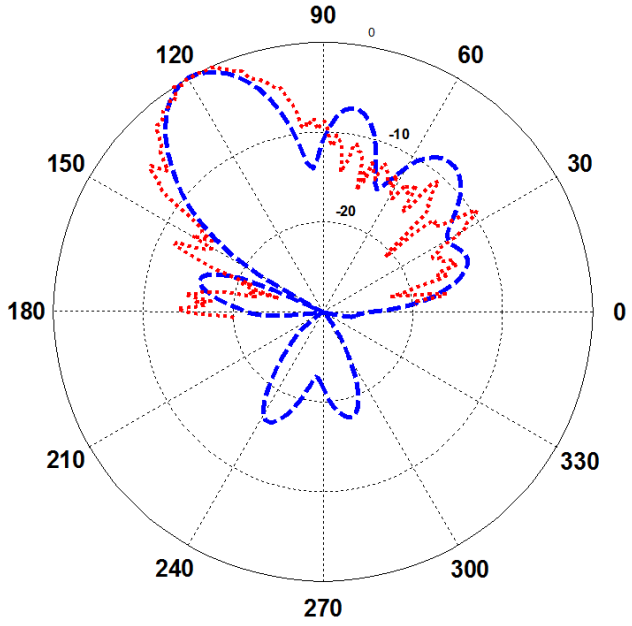

(b)

Figure 8-26: The normalized simulation and measured radiation patterns of two-dimensional dipole antenna with 8 slabs of MNZ unit-cells at 60 GHz when port 1 is excited in (a) H-plane (yz), and (b) E-plane (xy).

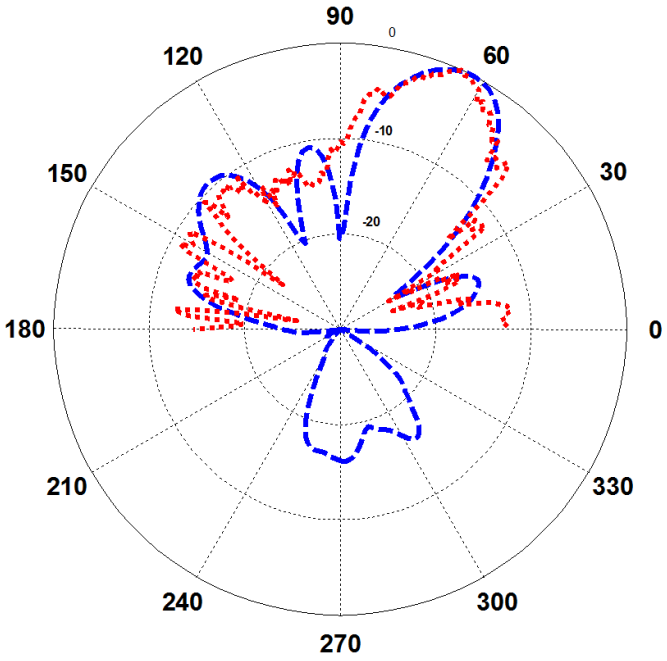

Figure 8-27: The normalized simulation and measured radiation patterns in E-plane (xy) when port 3 is excited at 60 GHz.

In order to show the versatility of the proposed antenna design, a 2D antenna structure shown in Fig.8.25 was fabricated. The antenna structure consists of four dipoles with 8 slabs, where each slab comprises 7×10 unit-cells. The measured and simulated radiation patterns at E(*xy*) and H(*yz*)-plane of this structure, in Fig.8.26 and 8.27, show that when port 1 is excited and the other ports are terminated the direction of the main beam in both E- and H-planes are deflected by 32 degrees. Conversely, switching port 3 and terminating the other ports results in beam deflection by -32 degrees in the E-plane. The discrepancy between simulation and measurement results, in particular, in the H-plane is due to the fabrication tolerance and the measurement setup.

8.8 **Conclusion**

Beamforming antenna has been performed by applying an array of MNZ metamaterial lens in the azimuth plane of the dipole antenna. The configuration of the MNZ unit-cell is essentially a split-ring structure with enhanced coupling. Ten slabs were embedded on the antenna substrate in front of the dipole, where eight slabs were loaded with 4×10 array of MNZ unit-cells and the two slabs were loaded with 4×6 unit-cells. The simulated and measured results confirm that the direction of the main beam can be refracted from -34 degrees to 34 degrees in the E-plane (azimuth plane). The peak gain of the antenna is 12.44 dBi at 62 GHz when the beam is tilted by 34 degrees. To realize 2D beamforming at the same time scanning in the H-plane is necessary. This was achieved by applying MNZ metamaterial inclusions along the *z*-direction of the elevation plane (*yz*). In this case eight slabs were mounted vertically in front of double dipole antenna where each slab was loaded with 7×10 unit-cells. The measured results shown confirm that 2D beamforming is possible. The main beam was swept by 34 degrees in both E- and H-plane simultaneously. The proposed structure can be scaled to the other frequency bands, e.g. 28 or 38 GHz for application in 5G MIMO systems.

Chapter 9 DUAL BEAM END-FIRE ANTENNA FOR 60 GHZ APPLICATIONS REALIZED BY MODIFYING THE PERMITTIVITY OF THE DIELECTRIC SLAB

9.1 Introduction

Performance of millimeter-wave communications at 60 GHz is adversely affected by: (i) interference effect that can degrade the signal level, and (ii) multipath effect that causes signal fading. In order to overcome these limitations and where coverage of multiple areas is required it is necessary to employ dual or multi-beam antennas. These antennas have the advantage of reducing the number of antennas and improve the link quality [83], which makes the network deployment easier. Recently, some work at millimeter-wave frequency band, in particular at 60 GHz, has attracted great attention by researchers as this band offers transmission rates of multi-gigabits per second, which is necessary for applications requiring video streaming and Internet-of-Things (IoT)/Machine-to-Machine (M2M) communications to be implemented in 5G wireless networks. Hence, various types of antennas with different functionalities are required. Working at this frequency band is quite challenging as there is substantial loss due to atmospheric absorption that can significantly degrade the quality of the communication link. End-fire radiating antennas, such as Yagi-Uda, dipole, as well as bow-tie, have been widely reported for millimeter-wave frequency band applications, in particular, beam switching networks, beam tilting and beam steering [84]-[87].

One approach to generate a multiple beams or dual-beams is to employ antenna arrays with adaptive radiation pattern using phased antenna arrays [88]. To implement this technique requires multiple antennas as well as phase shifters, which makes this approach costly and requiring a larger footprint size. To overcome these limitations, the authors in [22] have utilized gradient index of refraction media in the classical dipole antenna.

By switching the appropriate feed-line in the antenna structure, the direction of the main beam can be steered towards one of two specific angles. To achieve dual or multiple beams with this technique requires electronically controlled SPDT switches, which can introduce extra loss and complexity into the system.

Extensive investigation has been carried out to obtain dual-beam radiation pattern using leaky wave antennas [89]-[94]. The drawback of these antennas is the dual-beam radiation pattern is affected by the frequency, which restricts its applications. To overcome this limitation, the authors in [95] have excited higher TM_{02} mode in a U-slot patch antenna to realize a dual-beam with a wide beamwidth. Even though the radiation beam is fixed over the antenna's operating frequency range of 5.18–5.8 GHz, the antenna gain is relatively low for practical applications.

In this chapter, a technique is proposed to realize a dual-beam antenna for millimeter-wave applications over 57–64 GHz. This is realized on an end-fire bow-tie antenna by incorporating metamaterial inclusions which are implemented with stub-loaded H-shaped unit-cells. The array of 4×4 inclusions are tilted with respect to the end-fire direction. Reduction in the back-lobe radiation and antenna gain enhancement is achieved by loading a pair of H-shaped resonators next to the feed-line near the bow-tie radiators. The 3 dB beamwidth of the antenna is broadened by including an array of un-tilted 2×3 inclusions in the end-fire direction of the bow-tie radiators. The measured reflection-coefficient of the antenna is better than -10 dB over 57–64 GHz and the two radiation beams generated point at angles of 60 and 120 degrees with respect to the end-fire direction (90 degrees) with maximum peak realized gain of 9 dBi.

9.2 **Mechanism of Dual Beam**

Here dual-beam radiation is established from the dielectric slab mode TE in the printed bow-tie dipole antenna as described in [96][97]. To excite TE surface modes it is necessary to utilize high dielectric constant substrates [98]. It is well known that a high dielectric constant substrate can adversely affect the antenna's radiation efficiency and gain performance as the electromagnetic energy is confined within the substrate. Hence the bow-tie antenna used here was designed on a low dielectric constant RO5880 substrate with relative dielectric constant of 2.2.

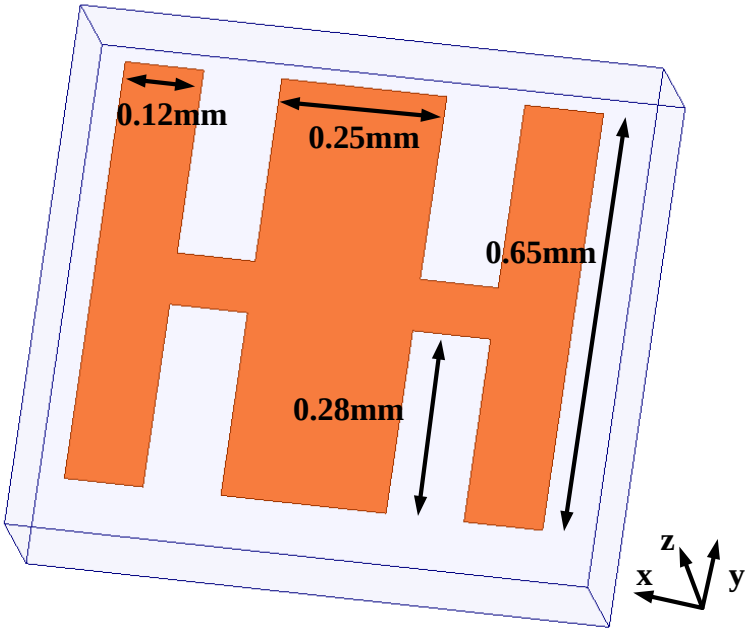

Figure 9-1: Geometry of the proposed H-shaped metamaterial unit-cell fabricated on the dielectric 5880 substrate.

The printed bow-tie antenna launches TE surface waves. The direction of the radiation emanating from the antenna was tailored towards a predefined angle by creating a region of high refractive index on the antenna. This was achieved by embedding metamaterial unit-cell inclusions described by the authors in reference [22]. Integration of metamaterial inclusions on the RO5880 substrate was designed to artificially increase the effective

dielectric constant of the substrate in order to refract the electromagnetic radiation from the bow-tie antenna. This technique was implemented here by using an array of stub-loaded H-shaped electric resonators or unit-cells depicted in Fig. 9.1.

The unit-cell's intrinsic parameters were extracted by locating the PEC and PMC boundary conditions in the *yz*- and *xy*-planes with the two wave ports in the *y*-direction [21]. Fig.9. 2 shows the real part of permittivity varies from 3.2–7.3 over the frequency range 57–64 GHz. The corresponding refractive-index varies from 1.81–2.22, which is larger than antenna substrate with effective refractive-index value of 1.28. By embedding the proposed unit-cells in front of end-fire radiation causes the antenna to excite surface waves whose phase velocity is less than the phase velocity of antenna substrate in order to alter the direction of the radiation.

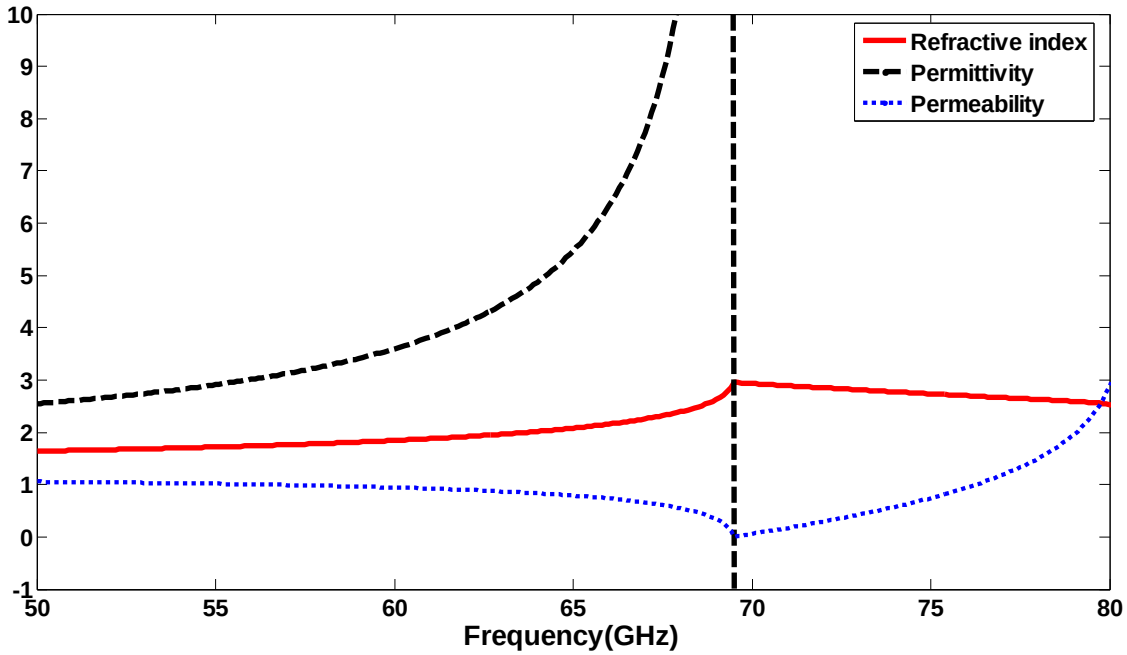

Figure 9-2: The extracted characterizing parameters of proposed unit-cell including permittivity, permeability and refractive index.

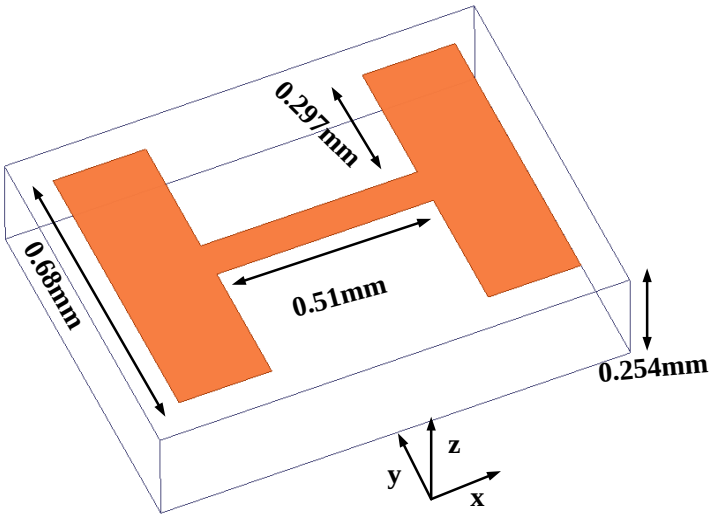

Figure 9-3: The structure of the H-shaped unit-cell.

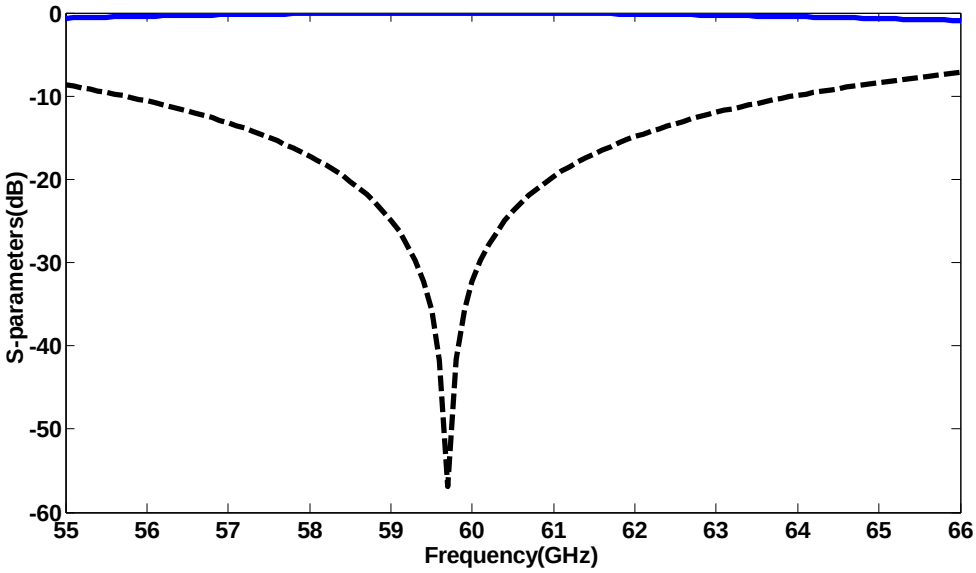

Figure 9-4: S-parameter (S12 and S11) response of the H-shaped configuration.

In order to improve the antenna gain and reduce the back-lobe radiation, a pair of H-shaped resonators was loaded on the antenna, as shown in Fig.9. 3. The S-parameter response of the resonators was obtained by exciting its two wave ports in the *y*-direction in order to induce electric and magnetic fields in the *x*- and *z*-directions, respectively. The transmission coefficient of proposed structure in Fig. 9.4 indicates that it has a band-stop

response over 57–64 GHz. In Section III, it is shown that by integrating the proposed H-shaped resonators at the back side of end-fire antenna results in the suppression of backward surface waves that are reflected at the edge of ground-plane [62].

9.3 Dual-Beam Radiation Pattern In the Azimuth plane

The proposed antenna, shown in Fig. 9.5, comprises printed bow-tie radiators constructed on Rogers 5880 substrate with relative dielectric constant 2.2 and thickness 0.254 mm.

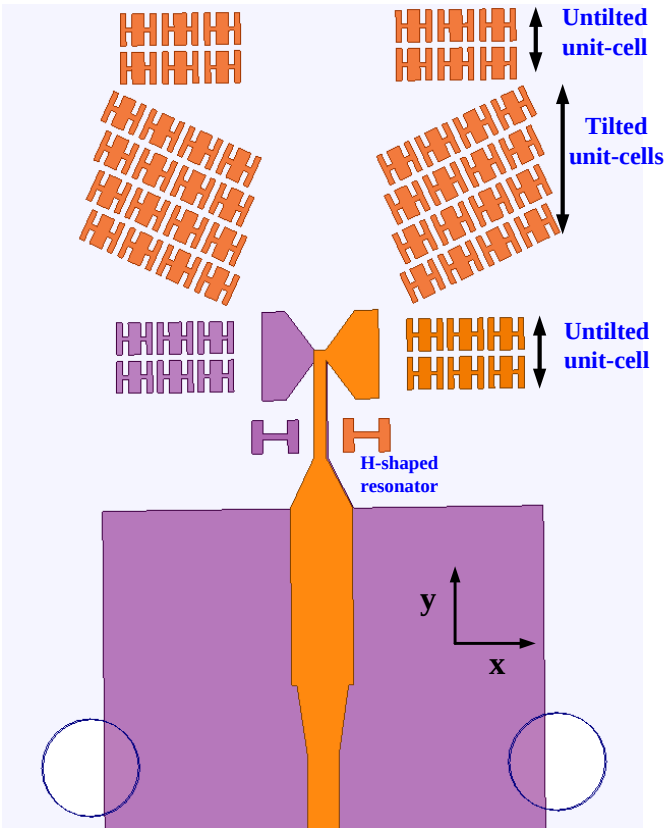

Figure 9-5: Configuration of the antenna embedded with a 3x4 array of the proposed HRIM unit-cells on upper surface of antenna substrate.

The bow-tie radiators are fed by microstrip lines that are tapered at its end to improve its impedance match. The antenna is loaded with two H-shaped resonators next to the feed-line and just below the bow-tie radiators to minimize the back-lobe and side radiation. Fig.9.6 shows these unit-cells effectively enhance the antenna gain by 2.66 dB from 4.1 dBi to 6.76 dBi.

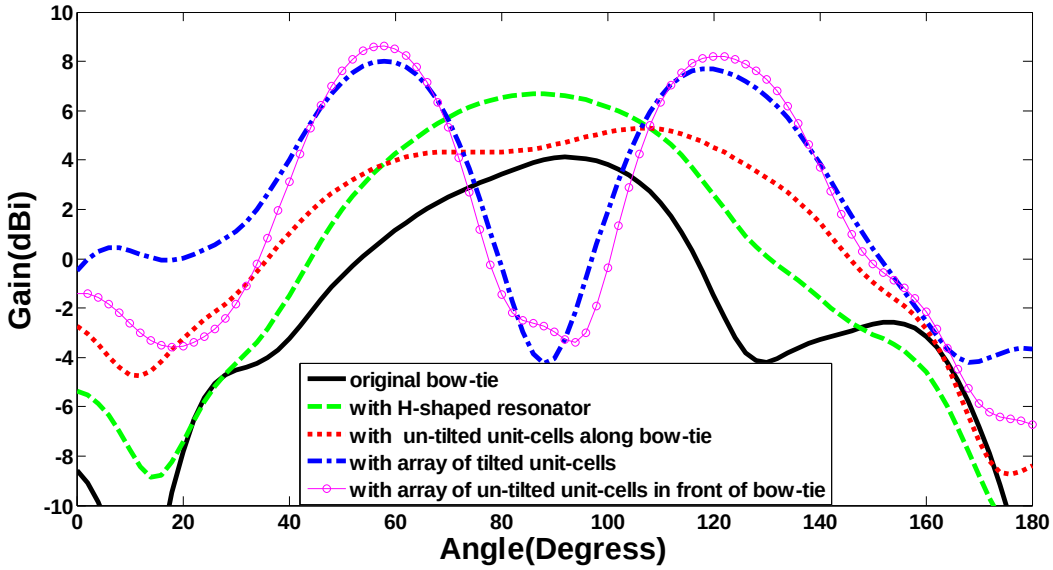

Figure 9-6: The radiation pattern of antenna in the E-plane with different arrangement of tilted and un-tilted unit-cells at 60 GHz.

Embedded in the antenna includes arrays of un-tilted stub-loaded H-shaped unit-cells placed along the *x*-direction of bow-tie antenna, as shown in Fig.9.5. The purpose of these unit-cells is to redirect the electromagnetic waves toward the *x*-direction and to broaden the radiation beamwidth in the azimuth plane. It can be observed in Fig. 6 that by loading the antenna with stub-loaded H-shaped unit-cells contributes in increasing the 3 dB beamwidth of the bow-tie antenna by 67 degrees from 53 to 120 degrees compared to conventional bow-tie antenna with 3 dB beamwidth of 53 degrees (62^{o}–115^{o}). This property can be used for providing a broader coverage for wireless communications over 57-64 GHz.

As mentioned in Section II, in order to excite TE surface waves it is necessary to integrate a higher refractive index medium in the end-fire region of the bow-tie antenna fabricated on Rogers 5880 substrate. This is achieved here by artificially creating a higher index of refraction using an array of stub-loaded H-shaped unit-cells that exhibit a higher effective permittivity and refractive index than antenna substrate as is evident in Fig. 9.2. In particular, the 4×4 arrays of stub-loaded H-shaped unit-cells were integrated in the end-fire direction (*y*-axis) of the bow-tie radiators, as shown in Fig.9. 5. The 4×4 arrays are tilted by 30 degrees with respect to the end-fire direction. The result of this arrangement, shown in Fig. 9.6, reveals that at 60 GHz the dual-beam radiation pattern is created with maximum peak gain of 7.9 dBi at 60^{o} and 120^{o} with respect to end-fire radiation (90 degrees). By introducing another 2×3 array of un-tilted stub-loaded H-shaped unit-cells in front of the tilted unit-cells enhance the antenna gain by 1 dBi. Furthermore, the 2×3 array reduces the side-lobe level by almost 4 dB.

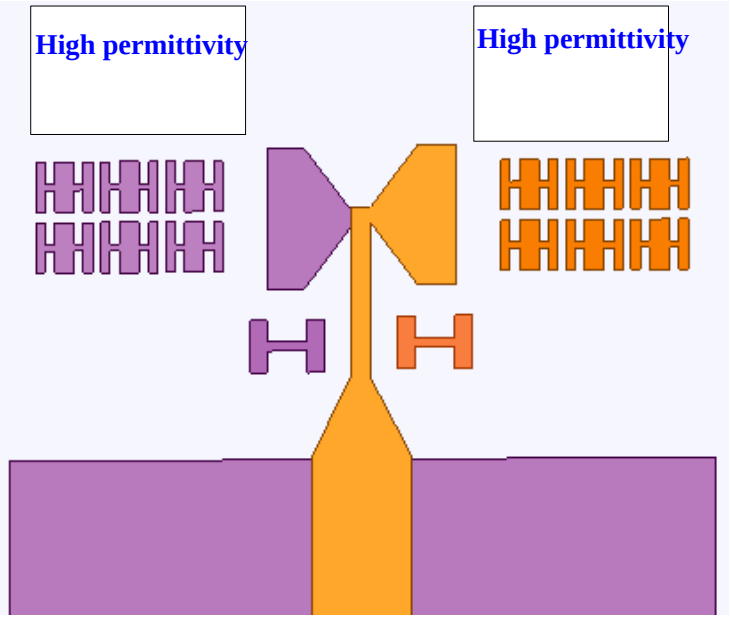

Figure 9-7: Configuration of the bow-tie antenna embedded with high dielectric constant material instead of stub-loaded H-shaped unit-cells.

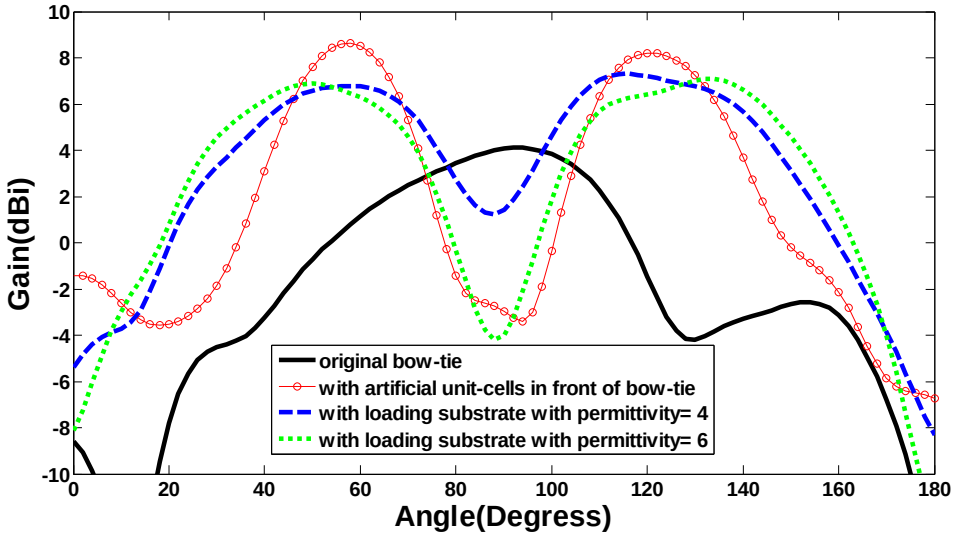

Figure 9-8: The radiation patterns of the antenna in the E-plane when loaded with higher dielectric constant substrate.

The TE mode surface waves were excited by artificially creating a high dielectric constant region in the end-fire vicinity of the bow-tie antenna by embedding arrays of stub-loaded H-shaped unit-cells. To demonstrate the validity of this technique we integrated into the antenna sections of high dielectric substrates with permittivity of 4 and 6, as shown in Fig.9.7. The antenna substrate had permittivity of 2.2. The result of this study in Fig.9.8 shows that when a substrate with dielectric constant 4 was used the antenna exhibits dual-beam radiation in the azimuth plane at 60 and 120 degrees with maximum gain of about 7 dBi, which analogous to loading the antenna with artificial metamaterial inclusions. When a substrate with dielectric constant 6 is used the antenna radiates dual-beam at 50 and 130 degrees with maximum gain of 7 dBi. Although the angle of maximum radiation beam of loading substrate is the same as artificial inclusions, the antenna gain with stub-loaded H-shaped unit-cells is higher by 3 dB.

The dual-beam radiation pattern in the E-plane of the final antenna design at 58, 60 and 62 GHz is plotted in Fig. 9.9. It is evident that at the three different frequencies, the antenna exhibits maximum radiation at +60 and 120 degrees. Also, the radiation null in the end-fire direction improves significantly from -10 dBi to -30 dBi with increase in frequency from 58 GHz to 62 GHz. The 3 dB beamwidth of the antenna tends to decrease from 32 degrees at 58 GHz to 23 degrees at 62 GHz.

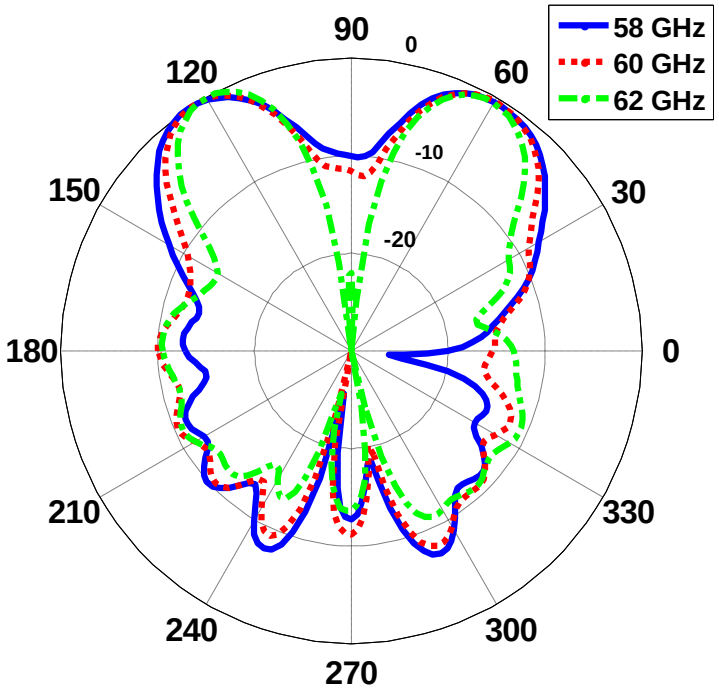

Figure 9-9: The normalized radiation patterns of the dual-beam bow-tie antenna in the E-plane (xy) at 58, 60, and 62 GHz.

Poynting vector distribution plot in Fig.9.10 gives an insight of how the antenna field is affected by integrating the array of stub-loaded H-shaped unit-cells in the bow-tie antenna. The interaction of the radiation field emanating from the bow-tie antenna with the array inclusions results in the redirection of the end-fire radiation into two distinct directions.

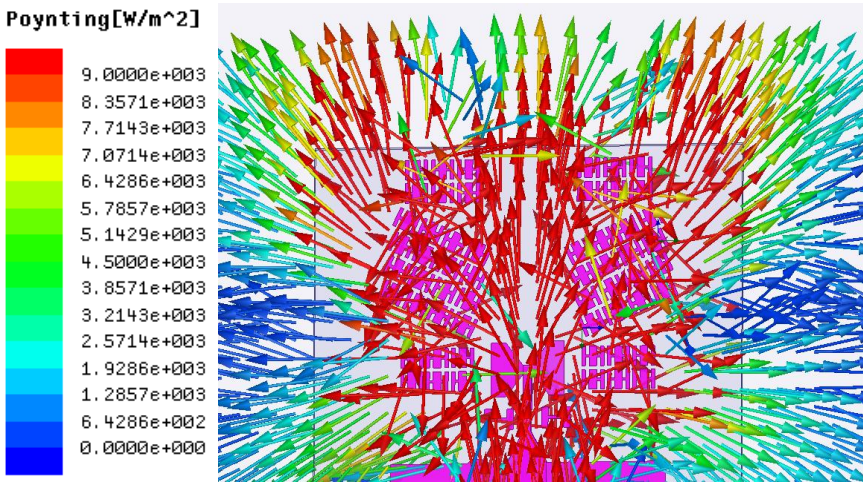

Figure 9-10: The poynting distribution normalized of dual beam antenna at 60 GHz.

9.4 **Experimental Results**

Photograph of the fabricated dual-beam bow-tie antenna with arrays of stub-loaded H-shaped unit-cells is shown in Fig.9.11.

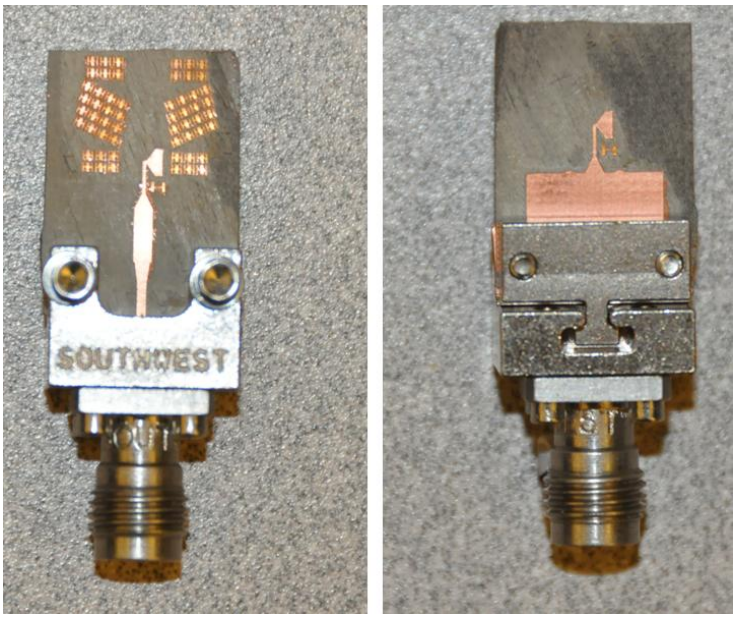

(b) (a)

Figure 9-11: Photograph of the dual-beam bow-tie antenna loaded with stub-loaded H-shaped unit-cells.

The proposed antenna was constructed on a Rogers RT5880. A 1.85 mm end-launch Southwest connector was utilized in the measurement of the antenna characteristics.

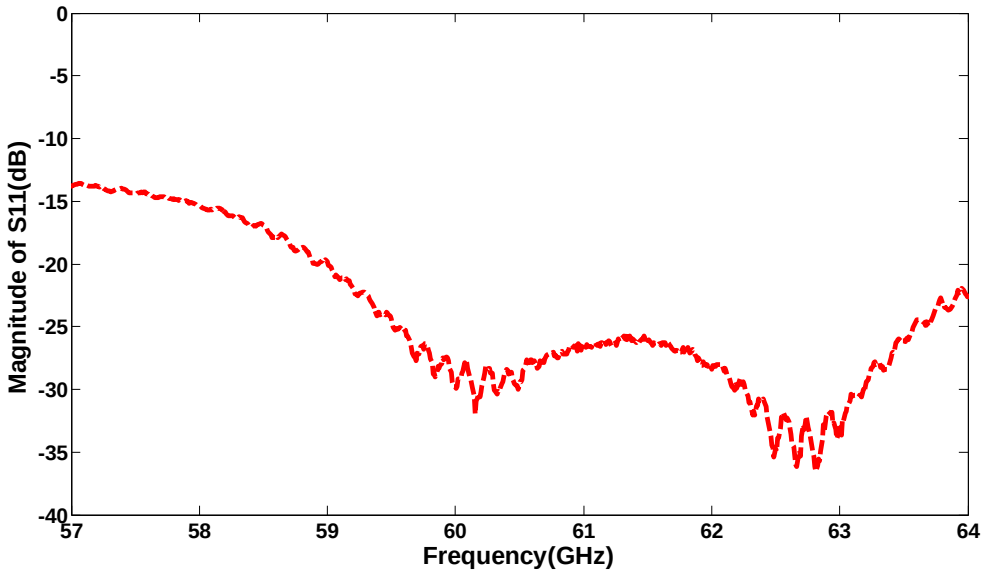

Figure 9-12: The measured reflection-coefficient of the dual-beam bow-tie antenna.

The measured reflection-coefficient of the proposed bow-tie antenna is shown in Fig.9.12. The magnitude of S_{11} is better than -10 dB over the frequency band of 55–65 GHz. The simulated and measured E-plane radiation pattern of the bow-tie antenna with at 58, 60, and 63 GHz are shown in Fig.9.13. The measured results show that the main beam direction of the antenna radiates at +60 and 120 degrees with respects to the end-fire direction (90 degrees). In addition, the magnitude of the normalized E-plane radiation in the end-fire direction corresponds to -10 dBi and -15 dBi at 58 and 63 GHz, respectively. The discrepancy between simulation and measured results is attributed to the fabrication tolerance.

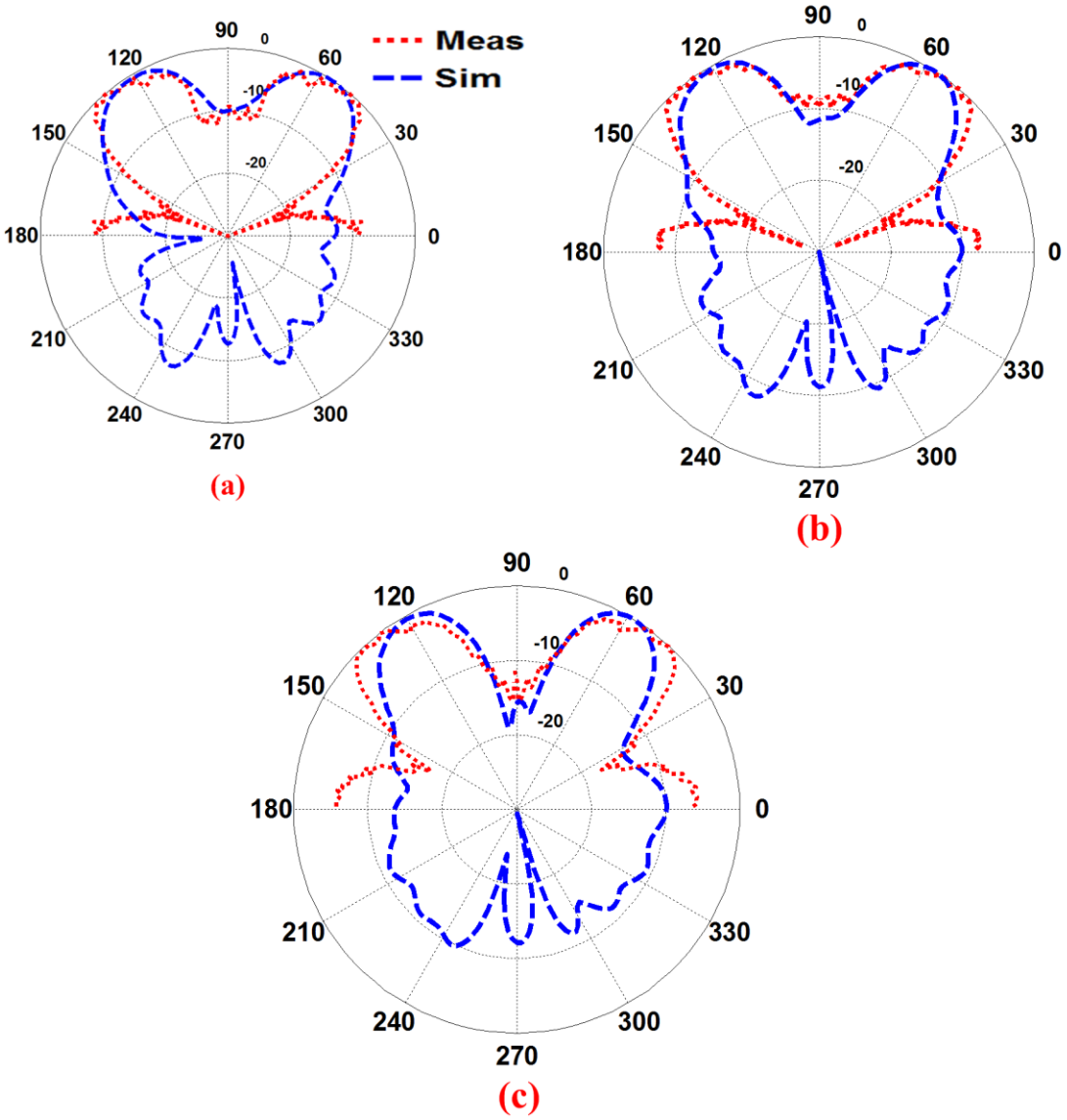

Figure 9-13: The normalized radiation patterns of the dual-beam bow-tie antenna using an array of stub-loaded H-shaped unit-cells in the E-plane (xy) at: (a) 58 GHz, (b) 60 GHz, and (c) 63 GHz.

The measured antenna gain at 58 GHz, 60 GHz and 63 GHz are 8.7 dBi, 8.9 dBi and 9.2 dBi, respectively. The proposed antenna is applicable for millimeter-wave indoor communication systems.

9.5 **Conclusion**

It has been demonstrated that by artificially manipulating the dielectric constant of the substrate in the end-fire direction of a bow-tie antenna a dual-beam radiation pattern can be realized in the E-plane at 60 GHz. This is achieved using 4×4 arrays of metamaterial inclusions implemented using stub-loaded H-shaped unit-cells. By appropriately tilting the inclusions with respect to the bow-tie axis a dual-beam was created at +60 and 120 degrees. In addition, it was shown that by including a pair of H-shape resonators in the vicinity of the feed-line and the radiators the back-lobe radiation is reduced and the antenna gain enhanced by 2.66 dB. Inclusion of a further 2×3 array of metamaterial inclusions was used to broaden the 3 dB beamwidth of the antenna and enhances its gain by 1 dB. The measured results of the prototype antenna agree well with the simulation results. This antenna exhibits desirable characteristics for indoor communications at 60 GHz.

Chapter 10 **CONCLUSION AND FEAUTURE WORK**

10.1 **Conclusion**

This dissertation presented an innovative approach for tilting the direction of the main beam from an end-fire antenna in both azimuth and elevation planes utilizing matasurface and metamaterial unit-cells. Tilting the antenna's main beam finds application in mobile base-stations to create smaller cells and increase system capacity. The metamaterial unit-cell was implemented using a novel electric resonator with meander-line H-shape geometry. Array of metamaterial unit-cells were integrated with the bow-tie antenna designed to operate between 7-8 GHz. In order to realize a larger tilt angle and high realized gain it was necessary to integrate into the bow-tie antenna an array of 5x4 unit-cells in the azimuth plane. The measured tilt angles was 17 degrees in the E-plane at 7.5 GHz with maximum peak realized gain of 9.3 dBi. Split-ring resonators (SRR) were used to enhance the tilt angle in the elevation plane of the bow-tie antenna. Integrating an array of inhomogenous SRRs in the elevation plane (H-plane) expended solely in the y- and z-directions provided a tilt angle of 30 degrees with gain enhancement of 5 dBi at 3.5 GHz. These results show the proposed approach is suitable for next generation of base-station antenna operating at the WiMAX frequency band. The side-lobe level (SLL) of radiation patterns in the H-plane is about -8 dB. To enhance the SLL it was necessary to increase the number of unit-cells in the end-fire direction, which however increases the protrusion dimension of antenna.

Millimeter-frequency band at 60 GHz is necessary to increase the transmission data rate more than 1.5 Gb/s because of its large bandwidth extending from 57-64 GHz. Operating at this frequency band incurs greater attenuation loss (10–16 dB/km) due to atmospheric absorption, which can be compensated by using high-gain antenna arrays. To avoid antenna arrays, the work in this thesis proposes using a bow-tie antenna fed by substrate integrated waveguide (SIW), which acts as a wideband balun over 57-64 GHz.

To increase the antenna gain entails (i) tilting the bow-tie radiators with respect to the end-fire direction, which increases the aperture size of the antenna and hence its gain, (ii) loading split-ring resonators at the back side of the bow-tie antenna to direct the energy toward the end-fire direction and improve its back-lobe level in the H-plane, and (iii) integrate in front of the bow-tie antenna an array of zero index metamaterial unit-cells to convert the spherical waves from the antenna into the planar waves. The measured antenna gain was 12.3 dBi over 57-64 GHz.

A high gain antenna makes the beamwidth narrower that makes signal alignment challenging between the transmitter and receiver. To deal with this issue a beamforming approach using phased antenna arrays was proposed. This involved using stub-loaded H-shape resonators, where the length and width of the stub is changed to alter its phase response over 57-64 GHz. By integrating an array of stub-loaded H-shape resonators in the off-axis of a classical dipole antenna is shown to deflect its peak radiation beam in the E-plane by 26 degrees. To implement a beam switching, another dipole antenna was embedded on the other side of GRIM unit-cells. By exciting the appropriate feed-line to the antenna its radiation beam can be switched from -26 to 26 degrees. The measurement results reveal that with this technique the radiation beam can be scanned from -58 to +58 degrees over 57-64 GHz. The gain of antenna when the beam is scanned was 10 dBi at 63 GHz.

To obtain a greater tilt angle and higher gain, an array of mu-near zero (MNZ) unit-cells created with split-ring resonator was proposed. Integrating an array of MNZ inclusions in the off-axis of the dipole antenna in both azimuth and elevation planes resulted in tilt angle of 35 degrees with gain enhancement of 8 dBi. In fact with this technique it was shown 2-dimensional beam scanning can be achieved with maximum peak gain of 14.3 dBi at 60 GHz.

Leaky wave antenna is another promising technique for creating dual beam radiation. In fact, dual beam radiation can be employed in WLAN and at millimeter-wave bands to improve the link quality. However, the radiation of leaky wave antenna changes with the frequency which restricts its application. Hence, in the thesis a novel technique is proposed to achieve a dual beam radiation with a fixed beam antenna for operation over 57-64 GHz. This was realized by integrating an array of stub-loaded H-shaped unit-

cells in front of bow-tie antenna. The measured result show that the peak radiation in the E-plane is directed at +30 and -30 degrees with respect to end-fire radiation over 57-64 GHz.

10.2 **Future work**

As shown above the beam tilting in both azimuth and elevation plane can be realized using array of metasurface and metamaterial unit-cells. To switch the radiation beam it is necessary to embed SP4T switch into the feed-line. In the above research work SP4T switch was not used due to time constraint however it has been shown this functionality can be included. Hence, electronic switching needs to be investigated to determine how the switch would affect the tilt angle and the overall antenna performance. Furthermore, the parametric study undertaken shows that by increasing the number of unit-cells in a desired direction leads to in the increase of the tilt angle. It would be interesting to integrate into the unit-cells PIN or varactor diodes to control the direction of the tilt angle and its beamwidth. This would enable the development of an antenna whose radiation pattern can be electronically reconfigured in both planes. In Chapter 5, a high gain bow-tie antenna was implemented using a single antenna with maximum peak gain of 12.3 dBi over 57-64 GHz. To obtain higher gain up to 18 dBi, it would be interesting to see how this can be achieved by deploying a larger number of arrays.

Chapter 11 **RESUME**

11.1 **Introduction**

La bande ISM 60 GHz (57-64 GHz) a suscité un grand intérêt chez plusieurs chercheurs et industriels pour sa large bande passante. Cette bande permet la transmission de données à un débit de plusieurs Gb/sde sortes à couvrir plusieurs applications dans le domaine des communications sans fil. Toutefois, en raison de la forte affaiblissement causé par le phénomène d'absorption atmosphérique dans cette bande, le signal propagé est considérablement réduit. Ce problème peut être résolu par l'utilisation des antennes à gain élevé. Cependant, l'alignement du faisceau rayonnant principal est un autre défi pour les antennes à gain élevé, où l'emplacement de l'émetteur ou le récepteur n'est toujours pas fixe. La solution pour régler ce problème est d'utiliser les réseaux à commutation ou à balayage de faisceaux comme dans les réseaux d'antennes à déphasage. Cependant, ces réseaux d'antennes à phasage souffrent énormément des pertes d'insertion causées par leur circuit d'alimentation, et ils sont aussi complexes à concevoir, ce qui les rend une solution moins attractive pour les systèmes de communication sans fil. Pour surmonter ces difficultés, on propose dans le cadre de cette thèse de nouvelles solutions pour contrôler électroniquement l'inclinaison de faisceau rayonnant en utilisant des structures en métamatériaux pour des applications en micro-ondes et en ondes millimétriques.

En premier lieu, nous avons conçu une structure en métamatériaux sous forme d'un réseau de résonateurs à ligne de méandre en forme de H, qui fonctionne comme une métasurface anisotrope dans bande C. Cette structure a été installée devant une antenne standard de type nœud papillon pour incliner la direction de faisceau principal dans le plan azimutal. De plus, pour incliner également le faisceau de rayonnement d'antenne dans le plan d'élévation, une seconde structure sous forme d'un réseau de résonateurs en anneau non-homogènes a été placée dans le plan du champ magnétique de l'antenne. Ces deux structures fournissent une solution viable pour contrôler simultanément

l'inclinaison du faisceau principal dans les deux plans de l'antenne. Ceci pourrait être une solution viable pour les antennes de station de base de la prochaine génération qui ont besoin de contrôler d'inclinaison de la direction de faisceau principal dans les deux plans (azimut et élévation). Cela comprend notamment les réseaux sans fil cellulaires 5G pour lesquels on envisage d'exploiter les ondes millimétriques. La technique proposée est également applicable à la bande C (7-8 GHz) et WiMAX bande (3,4-3,6 GHz).

En second lieu, nous avons conçu une antenne à gain élevé opérant dans les ondes millimétriques (57-64 GHz). Cette antenne utilise une configuration sous forme de nœud papillon et qui est alimentée par un guide d'onde intégré au substrat (Surface integrated waveguide :SIW). La technique qu'on propose pour accroitre le gain d'antenne implique (i) intégrer un résonateur en fente annulaire à l'arrière d'antenne en nœud papillon; (ii) incliner le faisceau de l'antenne en forme de nœud papillon selon la direction longitudinal (end-fire) ; (iii) intégrer un réseau de résonateurs repliés en forme de H afin de créer une région à indice de réfraction faible devant l'antenne pour convertir les ondes sphériques en ondes planaires. Les résultats obtenus indiquent que le gain d'antenne est amélioré pour atteindre 12 dBi de 57 à 64 GHz.

En troisième lieu, une autre technique a été proposée pour dévier le faisceau principal d'une antenne dipôle standard. Cette technique vise à créer un milieu à gradient d'indice de réfraction dans le plan azimutal. En utilisant cette approche, on a réussi à effectuer une commutation de faisceau de -58 à +58 degrés dans la bande entre 57 et 64 GHz et produire un gain maximal de 9.5 dBi à 60 GHz. De plus, afin de diriger le faisceau dans le plan d'élévation, on a utilisé des résonateurs repliés en forme de H chargés dans les plans magnétique et électrique. Cette configuration a permis d'obtenir une inclinaison ou une commutation de faisceau bidimensionnelle à 60 GHz. Toutefois, dans cette configuration le gain d'antenne se limite à 10 dBi et la déviation de faisceau se limite a 17 dégrées dans les deux plans.

En quatrième lieu, pour produire à un gain et un angle d'inclinaison plus élevés, un réseau de résonateurs enfentes annulaires a été placé devant une source quasi-TE générée par une antenne dipôle à 60 GHz. La résonance magnétique du réseau a produit un angle d'inclinaison de 34 degrés dans les plans d'azimutal et d'élévation et un gain maximal de 14 dBi dans la bande de 57 à 64 GHz.

Enfin, une dernière technique a été proposée qui utilise un réseau de résonateurs en forme de H et qui est placé devant une antenne en forme de nœud papillon pour obtenir un double faisceau et un rayonnement à large bande dans le plan azimutal de l'antenne. Les résultats obtenus indiquent que une l'inclinaison de faisceau est de +30 à -30 degrés dans le plan longitudinal de l'antenne et un gain maximal de 9 dBi à 60 GHz.

11.2 **Antenne à inclinaison de faisceau en utilisant des métamatériaux**

Cette section présente une technique pour réorienter le faisceau de rayonnement d'une antenne planaire dans une direction déterminée en utilisant une structure en métamatériau. Dans cette approche, on a exploité l'effet du changement de phase résultant de la propagation d'une onde électromagnétique en traversant d'un milieu à un autre ayant un indice de réfraction différant. Pour cela, une structure de cellule unitaire en métamatériau en forme de H a été conçue pour donner un indice de réfraction élevé qui a servi à mettre en œuvre l'inclinaison du faisceau d'une antenne en forme de nœud papillon. La cellule unitaire a été fabriquée et caractérisée en mesurant de ses paramètres S. Utilisant cette cellule unitaire, on a également construit un réseau bidimensionnel pour créer une région d'indice de réfraction élevé laquelle on a appliquée à proximité d'une antenne en forme de nœud papillon pour incliner le faisceau principal de l'antenne. Les résultats expérimentaux et les résultats simulés indiquent que le faisceau principal d'antenne dans le plan électrique est incliné de 17 degrés par rapport à la direction à rayonnement longitudinal aux fréquences : 7,3, 7,5 et 7,7 GHz. Les résultats montrent aussi que contrairement aux antennes classiques à inclinaison de faisceau, une chute du gain n'est pas remarquée quand le faisceau est incliné ; en fait, il résulte une amélioration du gain à 2,73 dB, comparativement à l'antenne originelle en forme de nœud papillon à 7,5 GHz. Le coefficient de réflexion d'antenne reste <-10 dB dans la gamme de fréquence d'opération.

11.2.1 Mécanisme de l'Inclinaison de Faisceau

Dans cette section, on explique le mécanisme de l'inclinaison du faisceau utilisant des milieux métamatériaux en deux couches déployés dans une structure d'antenne. Cette approche a été utilisée afin de développer une antenne de faible épaisseur avec un faisceau principal incliné. La Figure.11.1 montre qu'une source ponctuelle électromagnétique est disposée à proximité d'un milieu à deux couches avec deux indices de réfraction différents. L'onde électromagnétique dans chaque couche subit un déphasage différent. Le scenario présenté à la figure est analogue à un réseau d'antenne a deux éléments avec un déphasage β entre les éléments, qui est donné par :

$$\beta = k_o(n_2 - n_1)d \qquad (1)$$

Le rapport entre β et l'angle de rayonnement φ, dérivé de la théorie des antennes [12], donné par :

$$\beta = k_o l sin\varphi \qquad (2)$$

Donc, l'angle d'inclinaison est obtenu tirée des équations (1) et (2) :

$$\varphi = sin^{-1}\left[\frac{d(n_2 - n_1)}{l}\right] \qquad (3)$$

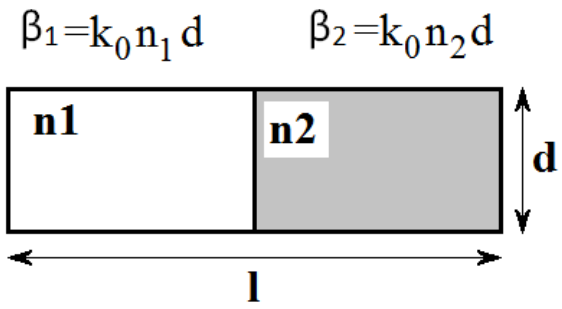

Figure 11-1: Le mécanisme d'inclinaison du faisceau en utilisant des milieux électriques a deux couches.

Selon l'équation (3), l'angle d'inclinaison est déterminé par la différence entre les indices de réfraction de deux milieux et leurs dimensions. Puisque, nous avons l'intention d'utiliser cette technique pour une antenne planaire à rayonnement longitudinal en forme de nœud papillon, le milieu à deux couches doit être situé sur le substrat de l'antenne. La meilleure solution pour modifier l'indice de réfraction d'une certaine partie du substrat de l'antenne a été de charger l'antenne avec une cellule unitaire métamatériau. La cellule unitaire devait (1) donner un indice de réfraction très élevé par rapport au substrat, et (2) pouvoir être directement intégrée au substrat diélectrique sans influer l'épaisseur de l'antenne. La section suivante décrit la structure de la cellule unitaire et ses paramètres, qui ont été validés avec les résultats expérimentaux.

11.2.2 La Cellule Unitaireen métamatériau

La structure de cellule unitaire en métamatériauest montrée à la Figure.11.2. Elle est en fait une version modifiée du résonateur en forme de H rapporté dans l'article [13]. La différence entre le résonateur en forme de H et la cellule unitaire présentée ici est que la structure comprend les lignes à méandres et dont l'épaisseur a été modifiée afin de réaliser un indice de réfraction plus élevé. Cette structure a été choisie car elle s'intègre

facilement dans l'antenne planaire en forme de nœud papillon. La géométrie de l'antenne indique la polarisation de l'onde électromagnétique est selon la direction de l'axe x ; il était donc nécessaire de créer un résonateur électrique afin de mettre à profit la résonance de la cellule unitaire.

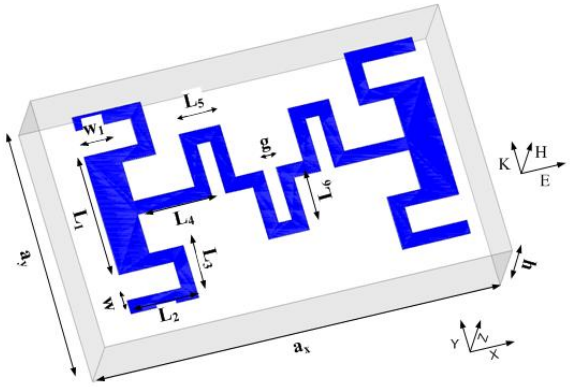

Figure 11-2: La géométrie de la cellule unitaire située sur un substrat diélectrique

11.2.3 L'antenne en forme de nœud papillon avec la cellule unitaire en métamatériau

Figure.11.3 illustre la disposition de l'antenne proposée utilisant des cellules en métamatériaux intégrées sur le même substrat.

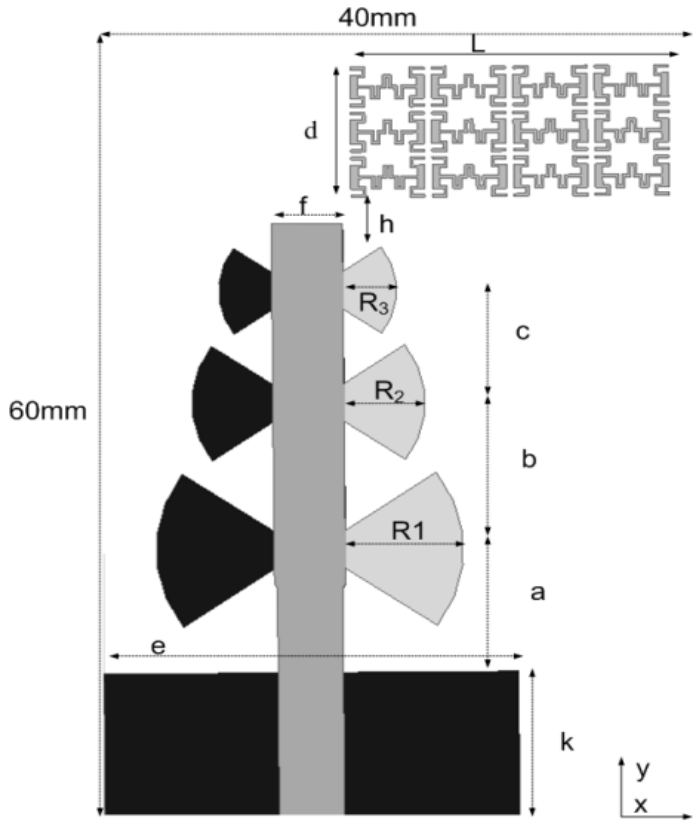

Figure 11-3: La configuration de l'antenne proposée utilisant des cellules en métamatériau sur la surface supérieure de substrat

Dans cette conception, l'antenne de référence est un réseau à trois éléments radiateurs en forme de nœud papillon connecté à une ligne d'alimentation micro-ruban [14]. Un réseau utilisant 3×4 celles unitaires en métamatériau a été imprimé sur le substrat d'antenne et placé devant l'antenne. Le chargement en métamatériau intégré à l'antenne a été imprimé sur un substrat Rogers RT5880 ayant une épaisseur de 1.575 mm. Les dimensions de l'antenne proposée sont : a=9,2 mm ; b=11 mm ; c=8,4 mm ; k=10,8 mm ; e=28 mm ; f=4,4 mm ; R_1=7,9 mm, R_2=5,4 mm ; R_3=3,6 mm. Le couplage entre le chargement en métamatériau intégré et l'antenne est obtenu grâce a l'interaction électromagnétique. Figure.11.4, illustre le diagramme du rayonnement de l'antenne en forme de nœud papillon avec et sans la structure du chargement en métamatériau incorporé dans le plan électrique de l'antenne.

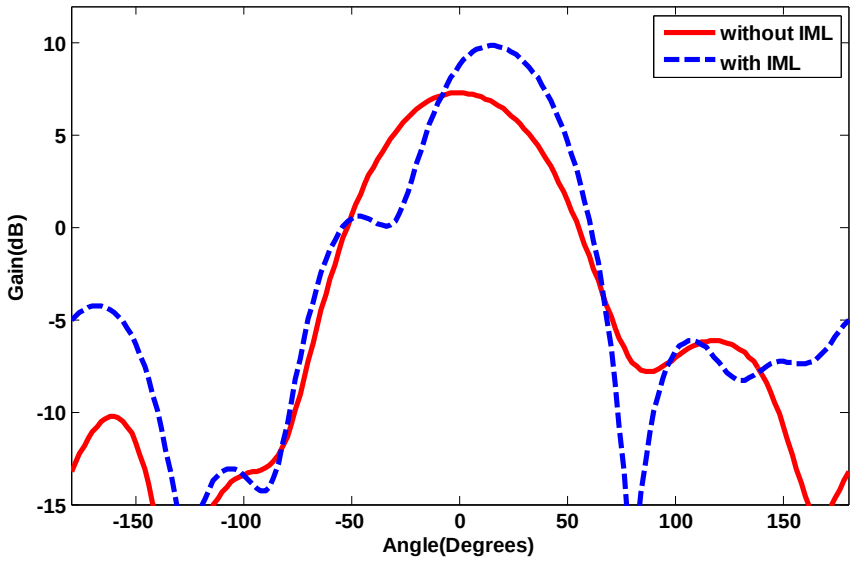

Figure 11-4 : Les diagrammes du rayonnement de l'antenne proposée dans le plan électrique (xy) avec les cellules unitairesen métamatériau intégré avec une antenne nœud papillon à 7,5 GHz.

11.3 L'antenne nœud papillon avec une cellule unitaire DGR

Dans cette section, on étudie les caractéristiques de l'antenne quand la lentille métamatériau est située dans le plan magnétique de l'antenne. Un réseau qui est constitué de cellules unitaires DGR est placé à proximité de l'antenne, tel que le montre la Figure 4.7. Les longueurs totales des réseaux 1×2 et 1×4 sont, respectivement, 36 mm et 72 mm. Selon les résultats de simulation, le réseau 1×4 incline le faisceau principal de 38 degrés dans le plan magnétique, et le réseau 1×2 incline le faisceau principal de 35 degrés dans le plan magnétique, comparativement à l'antenne sans lentille. D'après la Figure 4.7, l'amélioration du gain de 1,7 dB est réalisée grâce à la lentille métamatériau. Afin d'atteindre un gain élevé et un angle d'inclinaison maximal en même temps, quatre couches de lentille sont déployés. L'espace optimum entre les couches est déduit en utilisant des outils d'optimisation dans le simulateur de structure à haute fréquence. La configuration finale de DGR est un réseau 5×4 intégré à l'antenne nœud papillon, illustré à la Figure.11.5. Les dimensions de l'antenne sont : w_1=45 mm ; w_2= 72 mm ; h=7mm ; W=45 mm ; L=114 mm ; L_1=75,5 mm ; L_2=17,5 mm ; R_1= 17mm ; R_2=15 mm, et R_3=9,6

mm. La Figure 4.9 montre que la lentille métamatériau proposée a permis d'obtenir une inclinaison du faisceau principal de 31 degrés à 3,5 GHz et un gain maximal de 11 dB. L'angle d'inclinaison à 3,5 GHz peut être calculée en utilisant d'équation (1), ou θ=36,6 degrés, étant donne que n_{sub}=1,26, n_{DGR}=1,815, d=37 mm, a=8 mm, et L=72 mm.

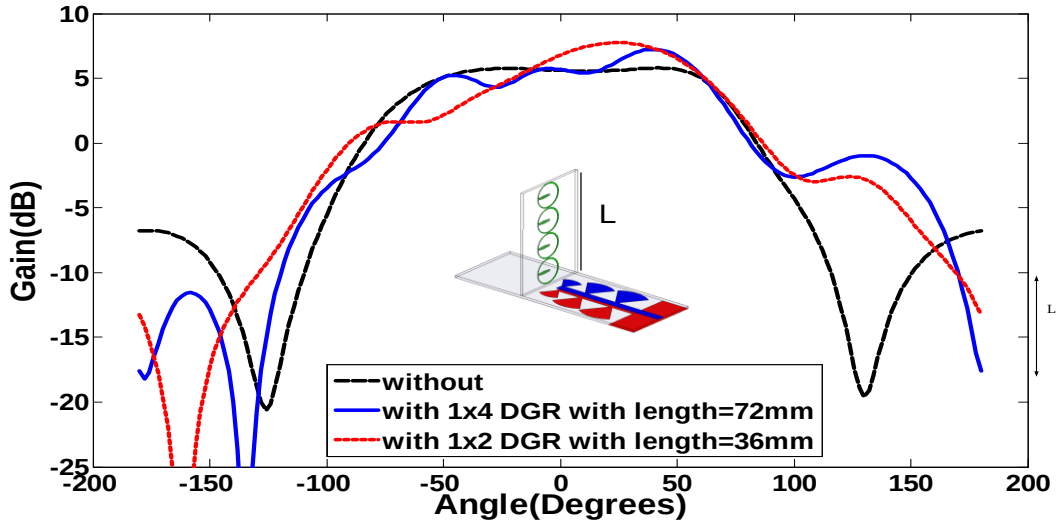

Figure 11-5: Le diagramme du rayonnement de l'antenne aux cellules unitaire DGR 1×2 et 1×4 située sur le substrat

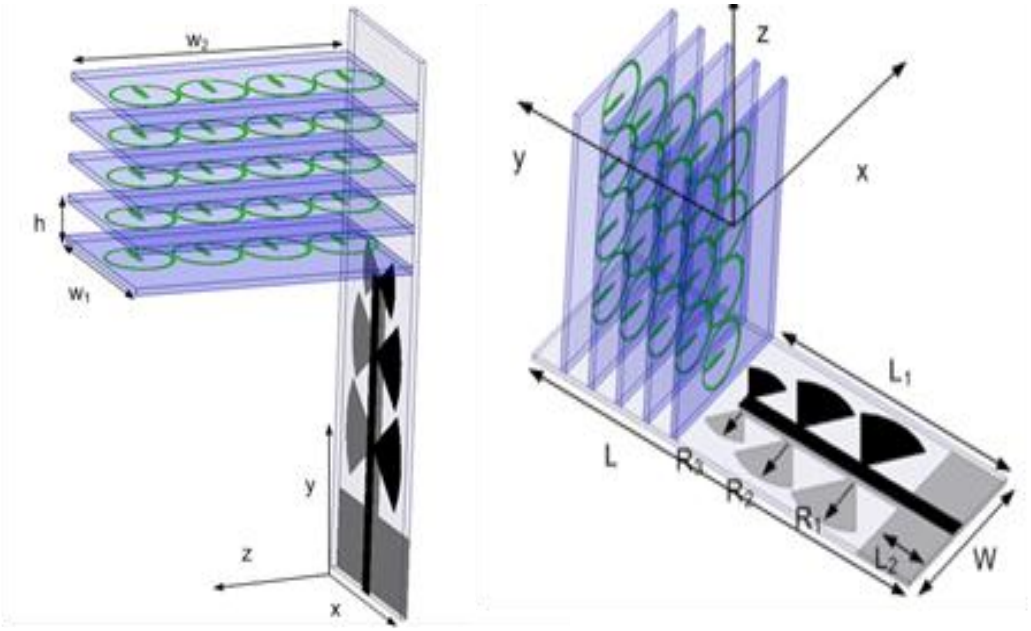

Figure 11-6: La configuration 3D de l'antenne proposée avec le réseau 5×4 de l'antenne DGR.

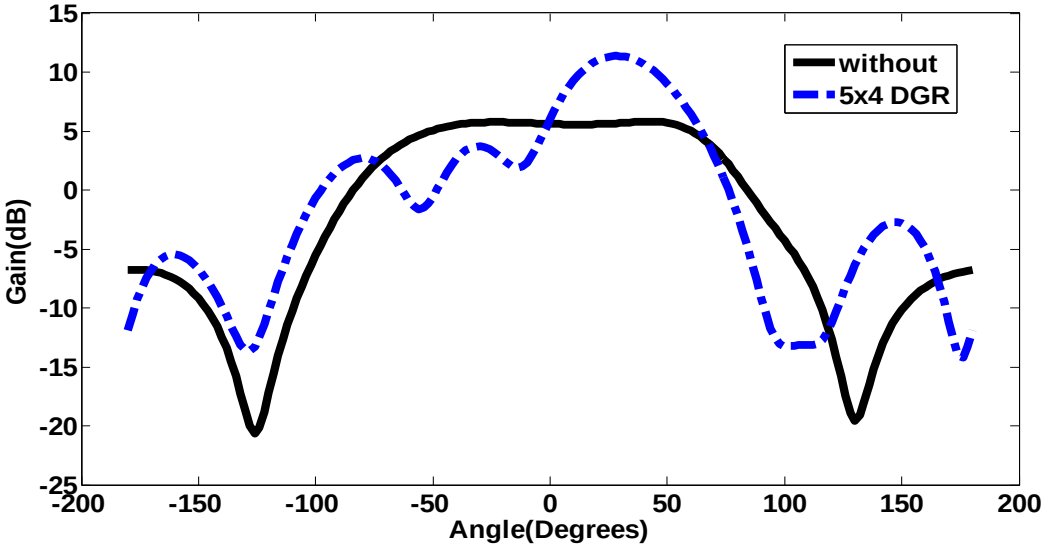

Figure 11-7 : Le diagramme du rayonnement de l'antenne dans plan magnétique avec ou sans le chargement DGR.

11.4 L'antenne nœud papillon à gain élevé en ondes millimétriques alimentée par un guide d'onde intégré au substrat

Une structure modifiée de l'antenne nœud papillon est proposée pour réaliser un gain élevé dans la bande de 57 GHz à 64 GHz. L'antenne comprend une paire de deux éléments rayonnants inclinés en forme de nœud papillon placés des deux cotés opposésdu substrat diélectrique commun. L'antenne est alimentée par une ligne d'alimentation en guide d'onde intégré au substrat (SIW). Les éléments rayonnants en forme de nœud papillon se croisent symétriquement afin d'améliorer le gain d'antenne et d'obtenir un diagramme du rayonnement désiré. Il est montré que le gain d'antenne peut

être considérablement élevé en chargeant l'antenne avec un réseau de cellules unitaires en métamatériau à indice zéro. L'antenne produit un gain mesuré de 11,5-12 dBi sur une gamme de fréquences de 57 GHz à 64 GHz avec un coefficient de réflexion moins de -11 dB. L'antenne proposée est facile à concevoir et à fabriquer à un prix moindre. Les caractéristiques de l'antenne la rendent adaptée pour les applications dans le domaine des communications intérieures sans fil à 60 GHz.

La géométrie de l'antenne proposée est montrée à la Figure.11.8, et elle comprend une structure alimentée par un guide d'onde intégré au substrat ressemblant à un tunnel rectangulaire créé entre les plaques de cuivre de substrat diélectrique en haut et au bas qui est entouré de deux colonnes de vias métalliques. Le tunnel est équivalent à un guide d'onde rectangulaire diélectrique, où les deux colonnes de vias métalliques sont équivalentes à ses parois. La configuration d'un guide d'onde intégré au substrat montré à la Figure.11.8 est une version modifiée de celle rapportée dans l'article [46]. Cette configuration crée une différence de phase de 180 degrés entre les courants le long des couches supérieures et inferieures de la structure du guide d'onde intégré au substrat. L'extrémité inferieure de la structure du guide d'onde intégré au substrat est effilée à une ligne d'alimentation micro-ruban, et l'extrémité supérieure est effilée à un élément rayonnant en forme de nœud papillon. Le coté inferieur du substrat comprend un plan de masse tronqué avec une antenne identique en forme de nœud papillon qui est montée de façon de se croiser symétriquement à l'antenne dipôle sur la couche métallique supérieure du substrat.

Les diagrammes normalisés du rayonnement dans le plan électrique (xy) et le plan magnétique (yz) de cette structure à 60 GHz sont illustrés à la Figure.11.9. Le niveau des lobes arrières dans plan magnétique est environ -0,6 dB, ce ne convient pas à des applications pratiques. Le niveau des lobes latéraux dans plan électrique (xy) est environ -7 dB. Du fait de l'amélioration de niveau des lobes arrières, plus de rayonnement est dirigé vers la direction longitudinal. Puisque le gain d'antenne est inversement proportionnel à largeur du faisceau, l'amélioration du niveau des lobes latéraux dans le plan électrique (xy) donnera lieu à une largeur du faisceau plus étroite et un gain renforcé.

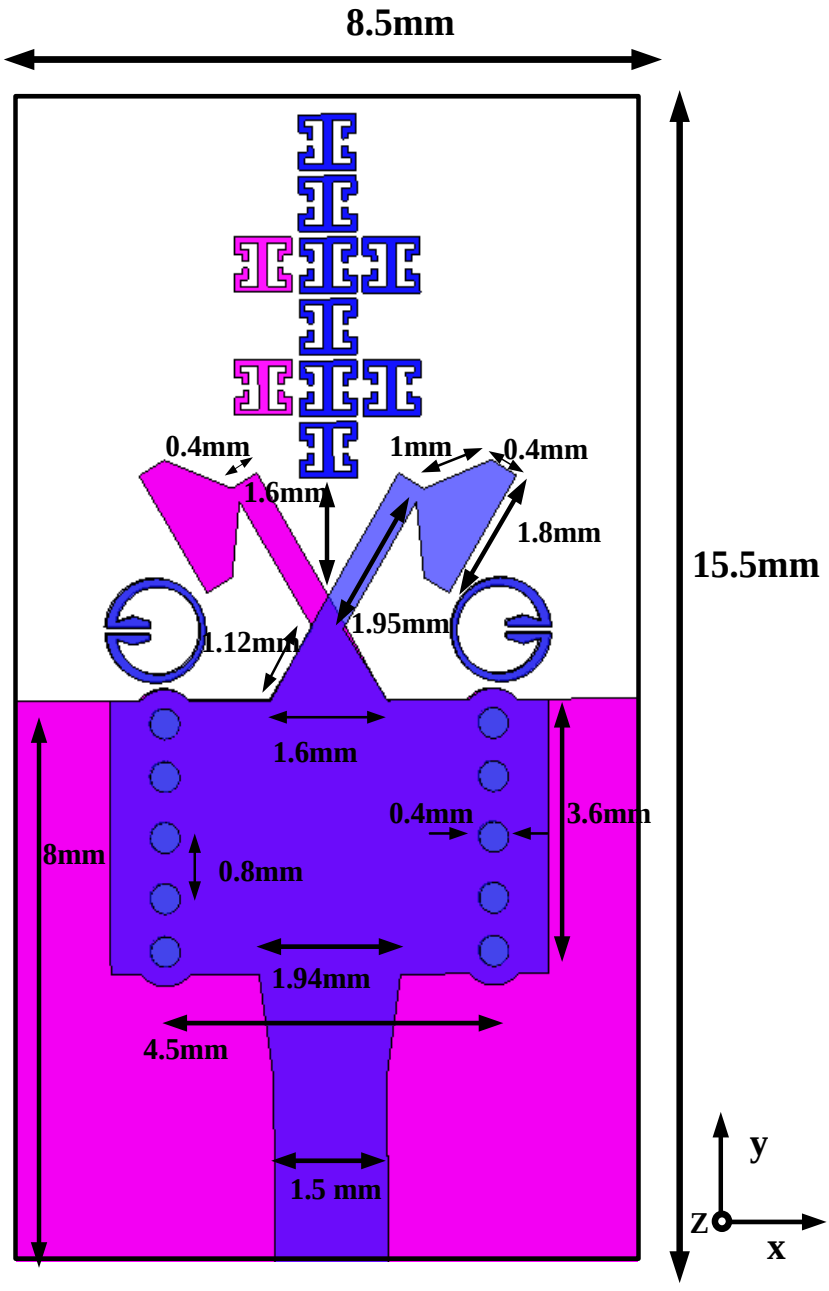

Figure 11-8 : La configuration de l'antenne inclinée en forme du nœud papillon avec DGR et un réseau des cellules unitaires en métamatériau un indice zéro

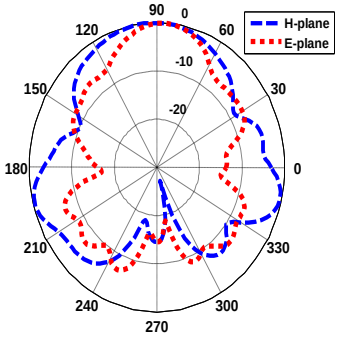

Figure 11-9 : Les diagrammes normalisés du rayonnement de l'antenne non-inclinée en forme du nœud papillon dans les plans magnétique et électrique à 60 GHz. L'angle est exprimé en degrés et le rayon est exprimé en dB.

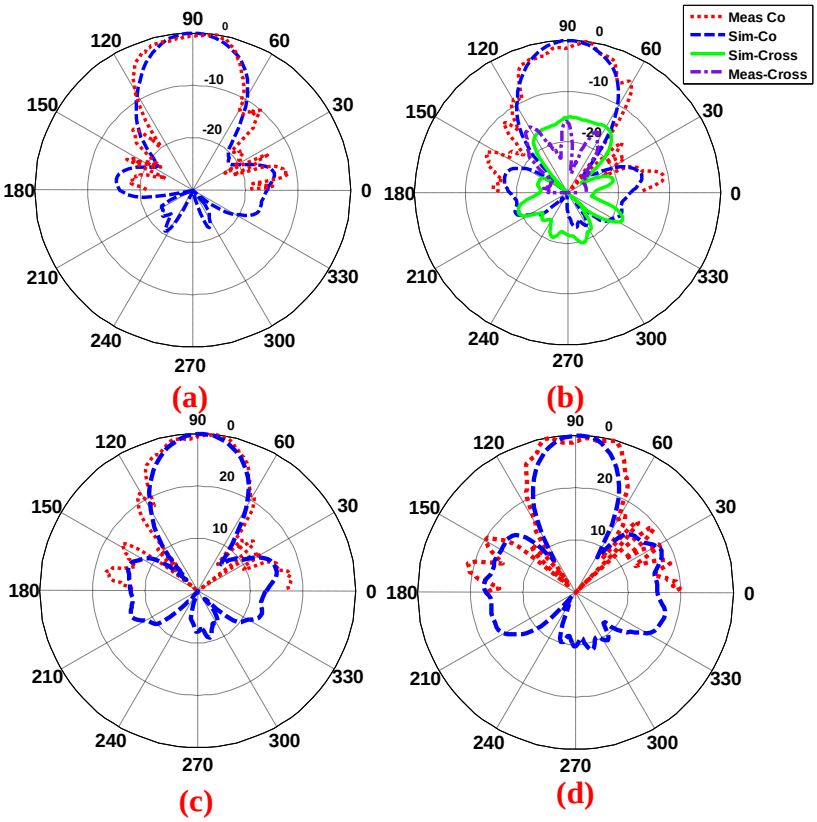

Figure 11-10 : Les diagrammes du rayonnement normalisés, simulées et mesurées pour l'antenne proposée dans le plan électrique (x-y) quand c'est intégrée par les résonateurs DGR et les cellules unitaires en métamatériau à indice zéro a : (a) 58 GHz, (b) 60 GHz, (c) 62 GHz, et (d) 64 GHz. L'angle est exprimé en degrés et le rayon est exprimé en dB.

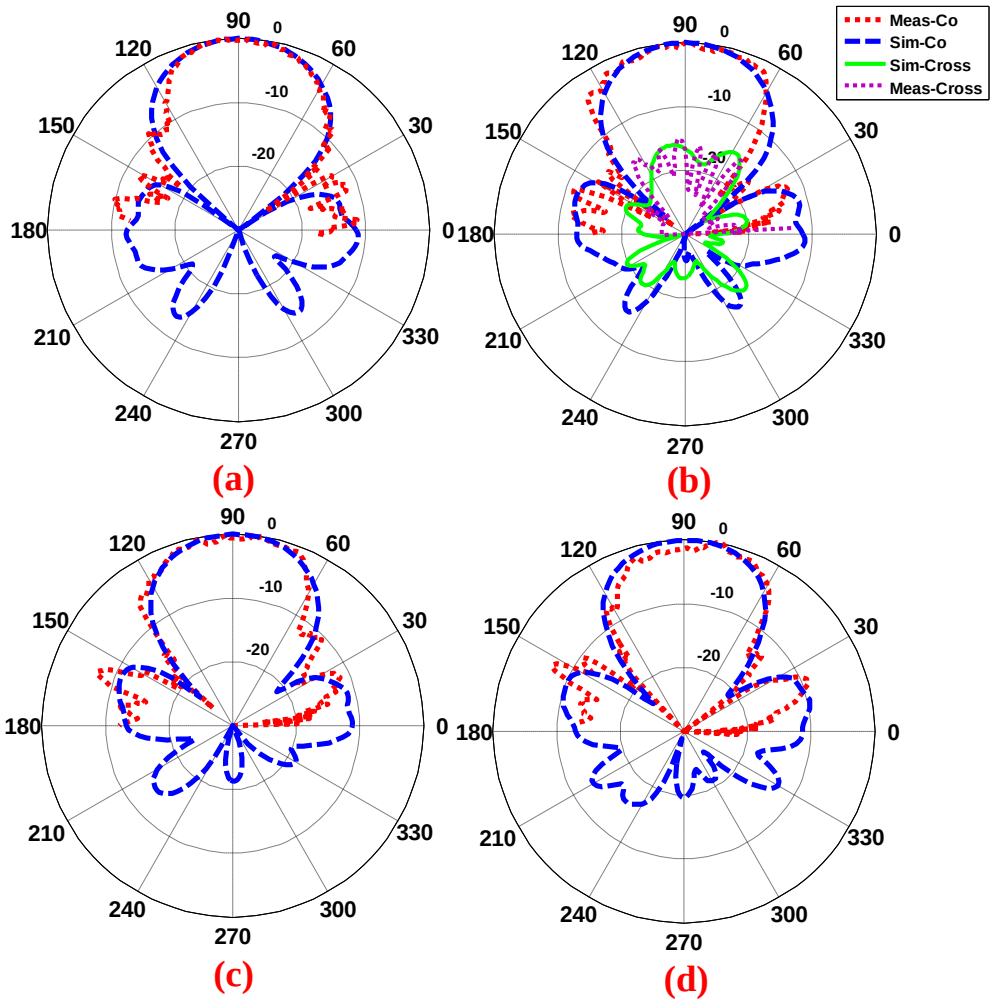

Figure 11-11 : Les diagrammes du rayonnement normalisés, simulées et mesurées pour l'antenne proposée dans le plan magnétique (yz) quand c'est intégrée par les résonateurs DGR et les cellules unitaires en métamatériau à indice zéro a : (a) 58 GHz, (b) 60 GHz, (c) 62 GHz, et (d) 64 GHz. L'angle est exprimé en degrés et le rayon est exprimé en dB.

Figure.11.10, et 11.11 montrent les diagrammes du rayonnement mesurés pour l'antenne en métamatériau à indice zéro en forme du nœud papillon dans le plan électrique (xy) et le plan magnétique (yz) quand les résonateurs DGR sont installés à l'arrière et les cellules unitaires en métamatériau à indice zéro devant l'antenne à 58, 60, 62 et 64 GHz. Il y'a une bonne concordance entre les résultats simulés et mesurés. Les résultats indiquent que le niveau des lobes latéraux de l'antenne dans le plan magnétique est moins de -11,5 dB à 60 GHz et moins de -9,7 dB à 64 GHz ; c'est mieux que les résultats de l'antenne Yagi-

Uda reportés dans l'article [50] avec un niveau de lobes latéraux de -5 dB ; le niveau du rayonnement arrière dans les deux plans est supérieur de -20 dB. En outre, la polarisation croisée de l'antenne dans le plan électrique (xy) et le plan magnétique (yz) est supérieur de -17 dB à 60 GHz, c'est mieux que l'antenne Vivaldi en métamatériau à 'indice zéro dans l'article [45] avec une polarisation croisée de -10 dB. L'efficacité de rayonnement de l'antenne est 91% à 60 GHz.

11.5 La déviation du faisceau en utilisant un milieu à gradient d'indice de réfraction pour l'antenne à rayonnement longitudinal à 60 GHz

Dans cette section, on montre les caractéristiques d'une antenne simple-dipôle utilisant un milieu métamatériau gradient d'indice de réfraction. L'antenne dipôle qu'on a utilisée est une version modifiée de l'antenne dipôle rapportée dans l'article [50]. Un réseau des cellules unitaires d'un milieu à gradient d'indice de réfraction a été introduit dans le substrat de l'antenne et posé devant l'antenne dipôle dans le plan azimutal, comme le montre la Figure.11.12. La structure de milieu à gradient d'indice de réfraction a été installée afin d'améliorer le couplage avec le dipôle de sorte à contrôler son rayonnement.

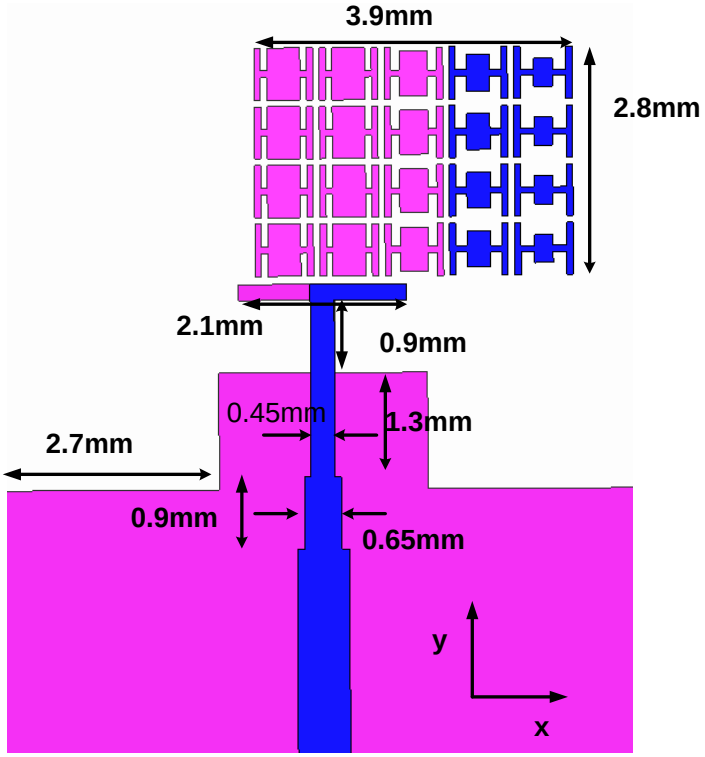

Figure 11-12: La configuration de l'antenne proposée avec un milieu à gradient d'indice de réfraction place sur les surfaces supérieure et inferieure du substrat.

Les dimensions de l'antenne proposée sont annotées dans la Figure 6.8. Le diagramme du rayonnement de l'antenne dipôle imprimée est illustrée à la Figure 6.9 avec et sans inclusions du milieu à gradient d'indice de réfraction dans le plan électrique de l'antenne. Les résultats présentés à la Figure.11.13 indiquent quand un milieu à gradient d'indice de réfraction est intégré au substrat de l'antenne, la direction du faisceau principal dans le plan électrique est inclinée d'un angle 26 degrés par rapport à la direction à rayonnement longitudinal. De plus, il y'a une amélioration de gain de 4 dB par rapport à l'antenne dipôle imprimée sans milieu à gradient d'indice de réfraction, parce que l'ouverture rayonnante est plus grande.

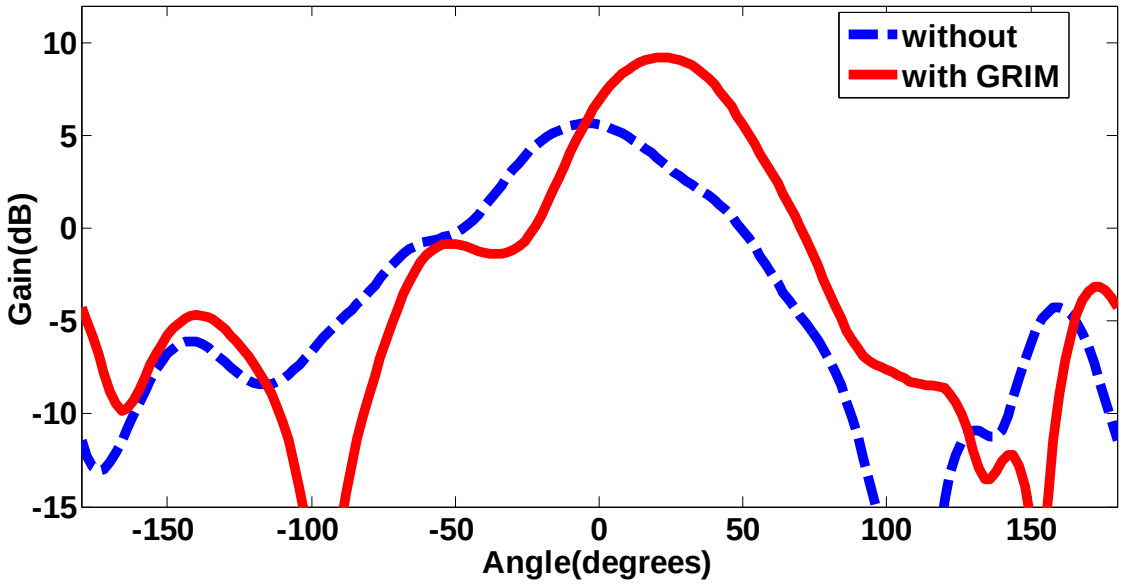

Figure 11-13 : Les diagrammes du rayonnement de l'antenne proposée dans le plan électrique (xy) équipée avec un milieu à gradient à indice de réfraction et une antenne dipôle classique à 60 GHz.

11.6 L'inclinaison de faisceau à deux dimensions (bidimensionnelle)

Dans cette section, on étudie les caractéristiques d'une antenne simple- dipôle chargée avec un réseau 3×4 de cellules unitaires HRIM dans le plan d'élévation (yz), comme illustré à la Figure.11.14. L'antenne dipôle a été construite sur un substrat Rogers RT5870 ayant une épaisseur de 0,254 mm et une permittivité de 2,3. L'indice de réfraction montrée à la Figure.7.4 est applicable à un volume infini des cellules unitaires HRIM.

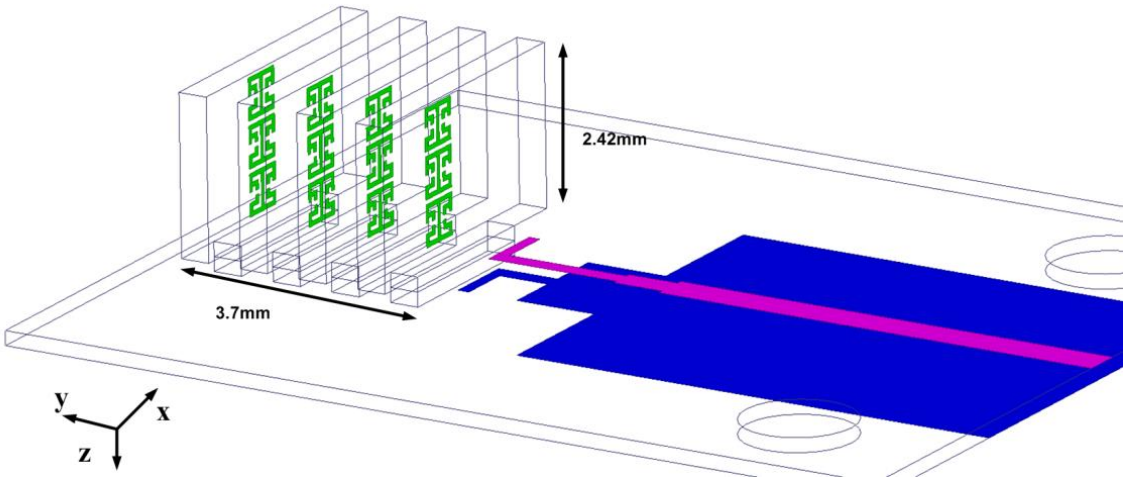

Figure 11-14: La configuration de l'antenne charge avec un réseau des cellules unitaires HRIM aux surfaces supérieure et inferieure du substrat.

Toutefois, on a construit seulement un petit morceau, ou un volume limité, du réseau des plaques illustré à la Figure.11.14. Le volume de ce réseau de plaques à un indice de réfraction inferieur est décrit par : $[(\varepsilon_{r1}t_1 + \varepsilon_{r2}t_2)/(t_1 + t_2)]^{1/2}$, où ε_{r1} (ε_{r2}) est la permittivité relative des plaques diélectriques (de la région d'air) et t_1 (t_2) est l'épaisseur de la région de la plaque (région d'air). Tel que construit, le métamatériau HRIM est vraiment un réseau de diffuseurs résonnants qui se situent dans le plan magnétique au lieu d'occuper la région tout entier associé aux plaques.

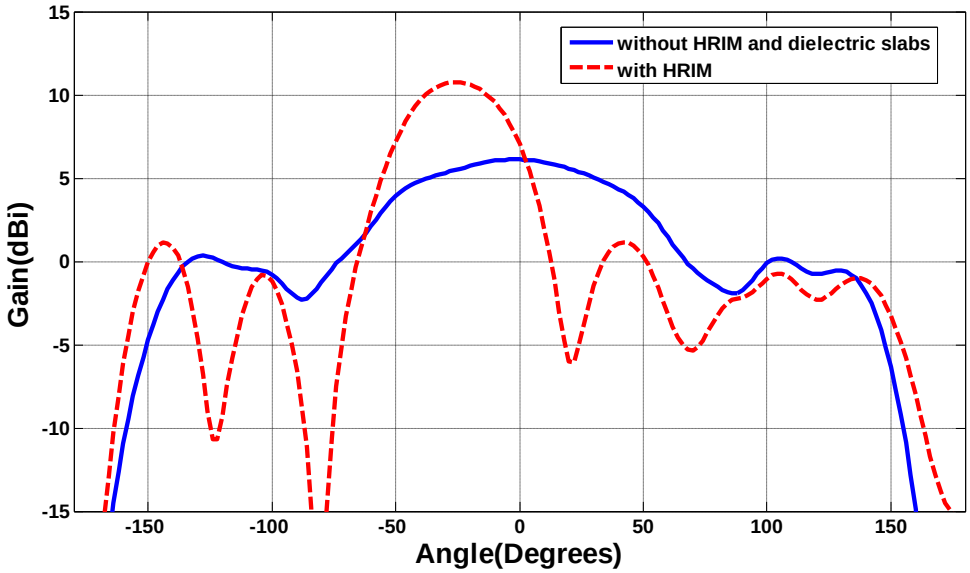

Figure 11-15: Les diagrammes du rayonnement de l'antenne proposée dans le plan magnétique (yz) avec et sans chargement HRIM à 60 GHz.

Les diagrammes du rayonnement de l'antenne avec ou sans chargement de la cellule unitaire dans le plan magnétique (yz) de l'antenne est illustré à la Figure.11.15. Les résultats indiquent que la direction du faisceau principal dans le plan magnétique est inclinée d'un angle -30 degrés par rapport à la direction à rayonnement longitudinal. De plus, il y'a un gain amélioré de 5 dB par rapport à l'antenne dipôle sans chargement de HRIM. Cela indique que le chargement de HRIM se comporte comme une lentille métamatériau qui augmente la largeur d'ouverture de l'antenne et provoque une amélioration de gain de l'antenne.

11.7 **L'antenne au balayage à faisceau monodimensionnel et bidimensionnel pour les applications MIMO en onde millimétrique**

Dans cette section, on étudie les caractéristiques d'une antenne dipôle simple avec des plaques MNZ montées verticalement devant les bras du dipôle. Cette configuration est composée de huit plaques composées de réseaux 4×10 unités cellulaires MNZ et deux dernières plaques de 4×6 MNZ placées dans le plan azimutal (xy), tel que le montre la Figure.11.16. L'espace entre les couches dipôle et MNZ est 0,06 λ_o afin de faciliter l'interaction mutuelle entre l'antenne et les plaques. Les couches MNZ avancent par 1,12 λ_o vers la direction à rayonnement longitudinal. L'antenne dipôle utilisée est une version modifiée de l'antenne dipôle rapportée dans l'article [50]. Les plaques ont été chargées symétriquement afin d'éviter le balayage dans le plan d'élévation.

Le réseau de cellules unitaires MNZ est décalé par rapport au centre de l'antenne dipôle dans le plan électrique ; toutefois, le réseau est symétrique dans le plan magnétique. Le même substrat est utilisé pour construire le réseau et l'antenne. Le diagramme du rayonnement de l'antenne dipôle imprimée est illustrée à la Figure.11.17 avec et sans inclusions de MNZ dans le plan électrique. Les résultats indiquent quand les couches MNZ sont intégrées verticalement au substrat de l'antenne par rapport au plan azimutal, la direction du faisceau principal dans le plan électrique (xy) est déplacée de 34 degrés par rapport à la direction à rayonnement longitudinal (axe y).

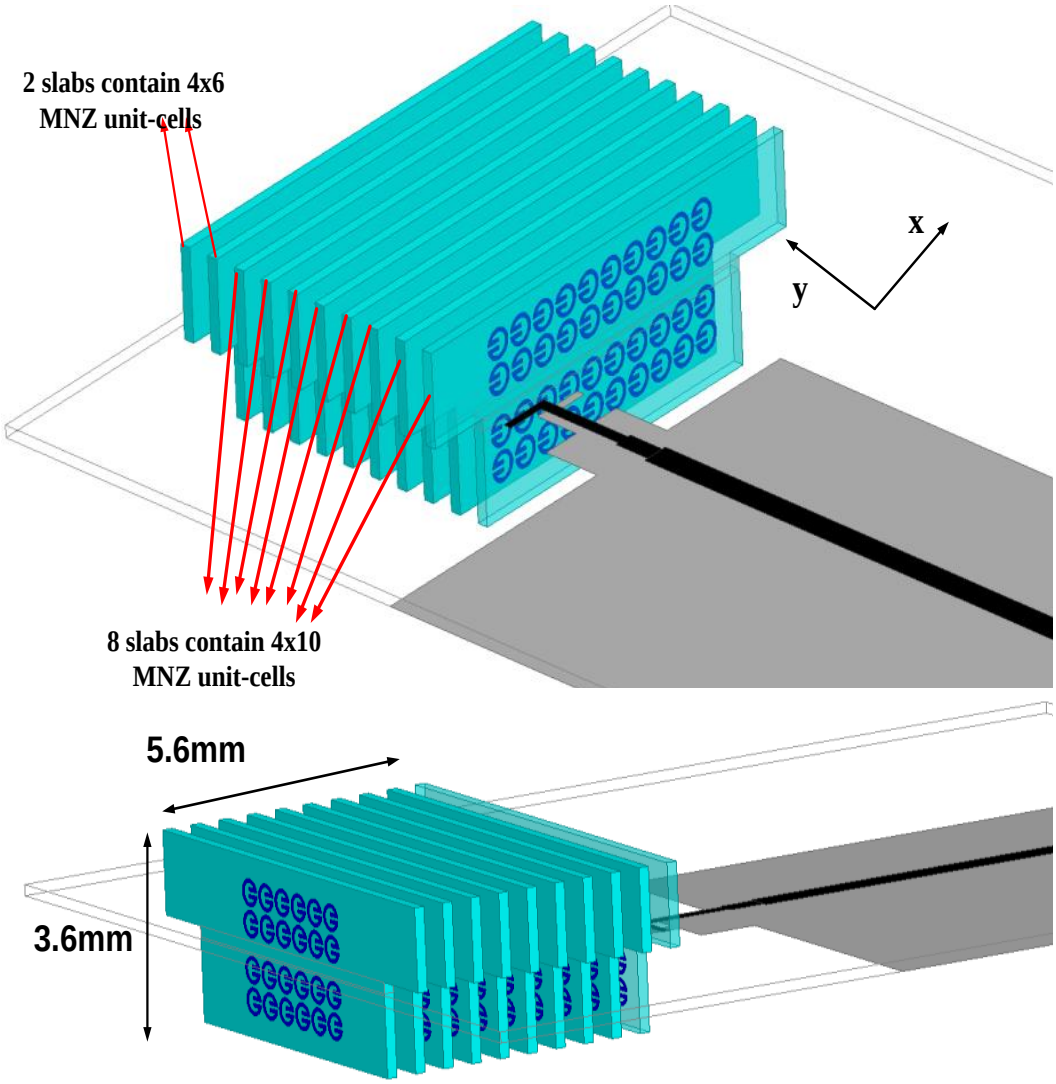

Figure 11-16: La configuration de l'antenne proposée avec 10 plaques des cellules unitaires MNZ.

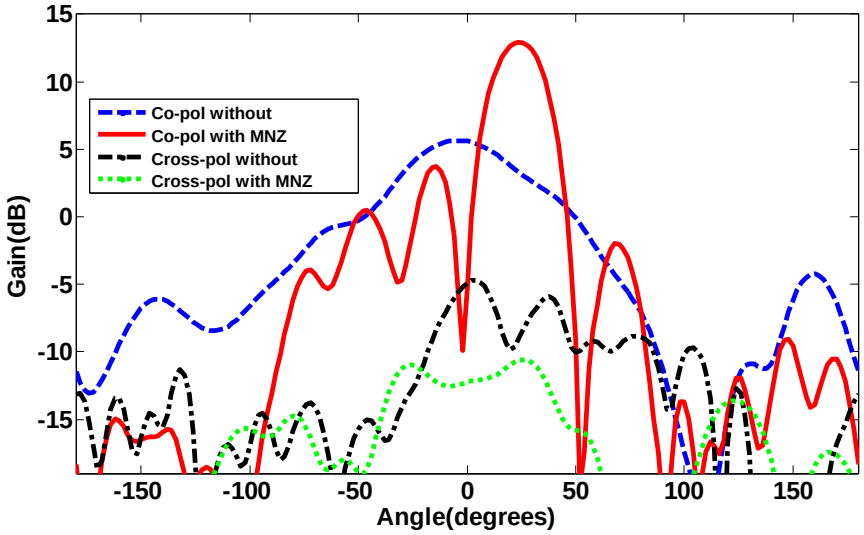

Figure 11-17: La polarisation croisée et copolarisation de l'antenne proposée dans le plan électrique (xy) avec et sans à 60 GHz.

En outre, cette réflexion est accompagnée de l'amélioration du gain à 8 dB par rapport à l'antenne dipôle sans chargement des cellules unitaires MNZ parce que les cellules unitaires MNZ augmentent la largeur de l'ouverture de l'antenne. La polarisation croisée de l'antenne dipôle avec MNZ est -22 dB, c'est 2 dB mieux que la polarisation croisée de l'antenne classique.

11.7.1 Le balayage de faisceau bidimensionnel

Pour obtenir un balayage de faisceau bidimensionnel, 8 plaques ont été montées au substrat de l'antenne dipôle, tel que le est montre la Figure.11.18. Chaque plaque comprend un réseau 7×10 de cellules unitaires MNZ. Le diagramme du rayonnement de l'antenne est illustré à la Figure.11.19, ce qui vérifie que les diagrammes de rayonnement dans les plans électrique et magnétique sont réfractés à un angle de 34 degrés (par rapport à la direction à rayonnement longitudinal de 90 degrés), quand la borne 1 est excitée et la borne 2 est terminée avec une charge adaptée de 50 ohm. Une réflexion du faisceau de 34 degrés est obtenue dans le plan électrique (xy) et plan magnétique (yz), alors que les ondes électromagnétiques rayonnées de l'antenne dipôle interagissent avec le milieu MNZ.

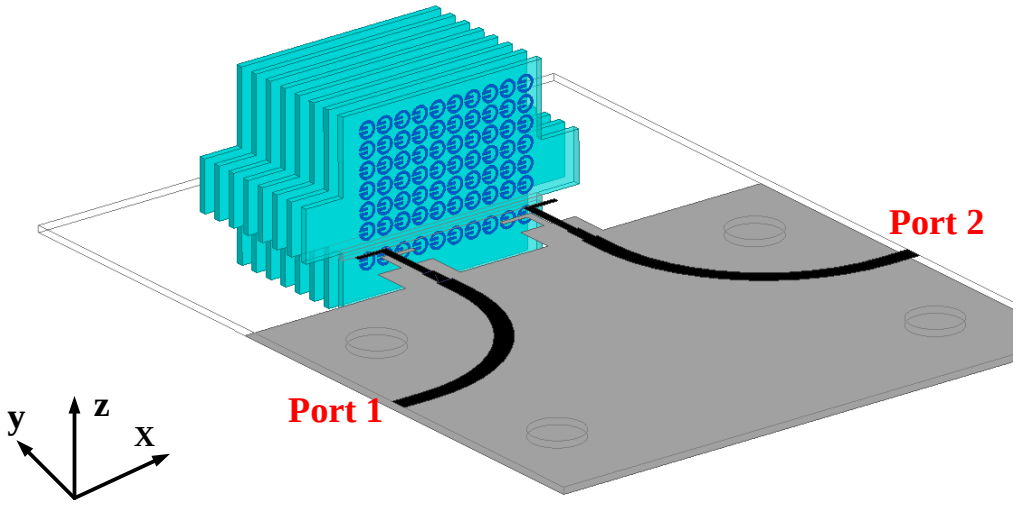

Figure 11-18 : La configuration 3D de l'antenne dipôle-double avec MNZ dans les plans électrique et magnétique

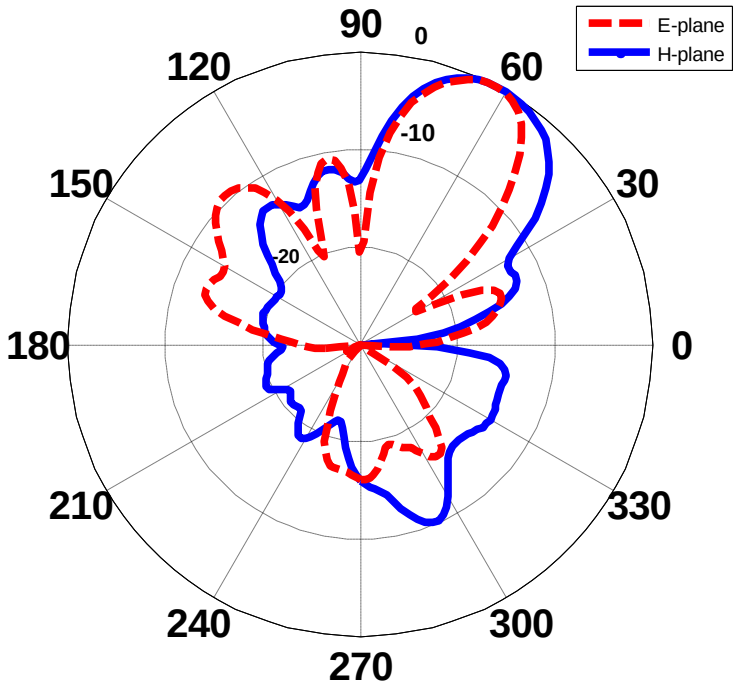

Figure 11-19 : Le diagramme du rayonnement bidimensionnel normalise dans les plans électrique et magnétique pour l'antenne dipôle et sans MNZ .

11.8 **Le diagramme du rayonnement à double faisceau dans le plan azimutal**

L'antenne proposée qui est montrée à la Figure.11.20. Cette antenne comprend deux éléments rayonnants imprimés en forme de nœud papillon et est construite sur un substrat Rogers 5880 ayant une constant diélectrique relative 2,2 et une épaisseur de 0,254 mm.
Les éléments rayonnants en forme de nœud papillon sont alimentés par des lignes d'alimentation micro-ruban qui sont effilés afin d'améliorer l'adaptation d'impédance. L'antenne est chargée avec deux résonateurs en forme « H » à coté de la ligne d'alimentation et juste en dessous des antennes en forme de nœud papillon (voir Fig.11-20) afin de minimiser le rayonnement des lobes arrières et latéraux. La Figure.11.21 illustre que ces cellules unitaires améliorent efficacement le gain d'antenne de 4,1 dBi à 6,76 dBi.

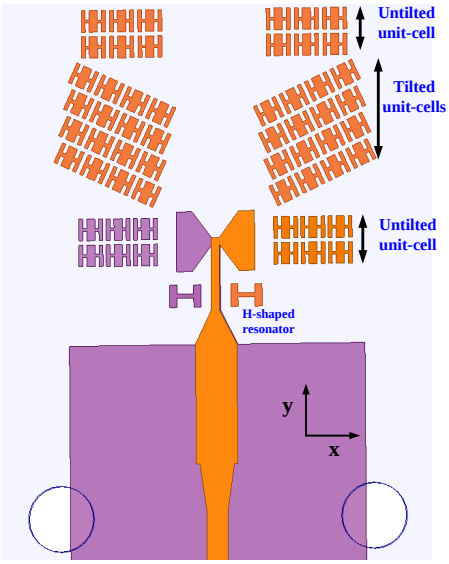

Figure 11-20 : La configuration de l'antenne intégrante un réseau 3×4 des cellules unitaires HRIM au surface supérieur du substrat de l'antenne

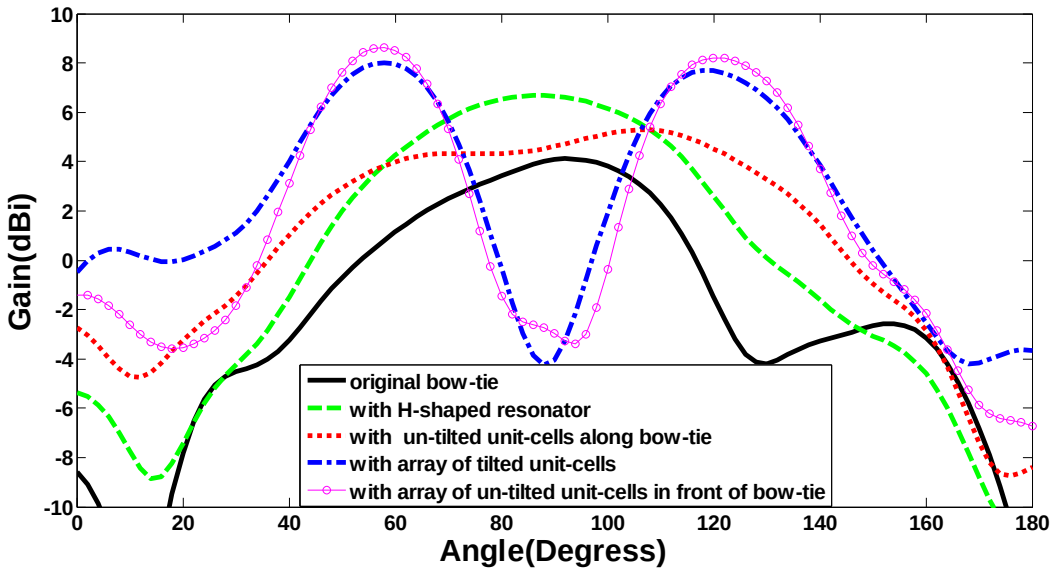

Figure 11-21: Le diagramme du rayonnement de l'antenne dans le plan électrique à un arrangement différent des cellules unitaires inclinés et non-inclinés à 60 GHz.

En utilisant des réseaux de cellules unitaires non-inclinés en forme de H situés le long de la direction x de l'antenne en forme de nœud papillon, comme le montre la Figure.11.20, le faisceau rayonnant peut être dirigé vers une direction donnée. Ces cellules unitaires ont pour objectif de réorienter les ondes électromagnétiques vers la direction x et d'élargir la largeur du faisceau rayonnant dans le plan azimut. Selon la Figure 6, on note que le chargement de l'antenne aux cellules unitaires en forme H contribue à augmenter la largeur du faisceau de l'antenne en forme de nœud papillon de 53 à 120 degrés par rapport à celui de l'antenne classique en forme de nœud papillon. Cette propriété peut être utilisée pour donner une couverture plus grande à communication sans fil dans la bande de 57 à 64 degrés.

11.9 **Conclusion et travaux à venir**

Dans le cadre de cette thèse, on a proposé de nouvelles approches pour contrôler l'inclinaison de la direction du faisceau principal d'une antenne à rayonnement longitudinal dans les plans d'azimut et d'élévation utilisant des cellules unitaires en métasurface et métamatériau. L'inclinaison de la direction du faisceau principal de l'antenne pourrait avoir des applications dans les stations de base des communications mobiles à contrôler la couverture des cellules plus petites de façon à accroitre la capacité du système. Les cellules unitaires en métamatériau ont été conçues en utilisant un nouveau résonateur électrique à ligne de méandre en forme de H. Un réseau de cellules unitaires en métamatériau a été intégré à une antenne nœud papillon conçue pour fonctionner de 7 à 8 GHz. Afin d'obtenir un plus grand angle d'inclinaison et un gain élevé, il était nécessaire d'intégrer un réseau de cellules unitaires 5×4 dans le plan azimutal. L'angle d'inclinaison mesuré a été 17 degrés dans le plan électrique à 7,5 GHz avec un gain maximal de 9,3 dBi. Les résonateurs à fente annulaire ont été utilisés pour améliorer l'angle d'inclinaison dans le plan d'élévation de l'antenne en forme de nœud papillon. L'intégration d'un réseau de résonateurs à fente annulaire non-homogène dans le plan d'élévation (plan magnétique) déployé seulement dans les directions y- et z- a fourni un angle d'inclinaison de 30 degrés avec une amélioration de gain de 5 dBi à 3,5 GHz. Ces résultats indiquent que l'approche proposée est convenable pour la prochaine génération d'antenne de station de base fonctionnant dans la bande de fréquence WiMAX. Le niveau des lobes latéraux des diagrammes du rayonnement dans le plan magnétique est autour de -8 dB. Pour améliorer le niveau des lobes latéraux, c'est nécessaire d'augmenter le nombre des cellules unitaires dans la direction du rayonnement longitudinal.

La bande de fréquence d'ondes millimétriques à 60 GHz est nécessaire pour accroitre le débit de transmission de données plus de 1,5 Gb/s en raison de sa large bande passante qui s'étendant de 57 à 64 GHz. Le fonctionnement dans cette bande de fréquences cause plus de perte d'affaiblissement (10-16 dB/km) en raison de l'absorption atmosphérique, ce qui peut être compensé à l'aide des réseaux d'antennes à gain élevé, qui sont

complexes et à cout élevé. Pour pallier ce problème, on a proposé dans cette thèse une nouvelle antenne alimentée par un guide d'onde intégré au substrat, qui permet d'opérer à une large bande de 57 à 64 GHz. Pour l'amélioration du gain d'antenne, on a besoin de (i) incliner les résonateurs en forme de nœud papillon par rapport à la direction du rayonnement longitudinal, ce qui augmente la taille d'ouverture de l'antenne, et par conséquent son gain ; (ii) charger les résonateurs à fente annulaire sur le coté arrière de l'antenne en forme de nœud papillon afin de diriger l'énergie vers la direction du rayonnement longitudinal et d'améliorer le niveau des lobes arrières dans le plan magnétique ; et (iii) intégrer un réseau des cellules unitaires en métamatériau à indice zéro devant l'antenne en forme de nœud papillon pour transformer des ondes sphériques de l'antenne en ondes planaires. Le gain d'antenne mesuré est 12,3 dBi de 57 à 64 GHz. Une antenne à gain élevé génère un faisceau plus étroit qui rend souvent l'alignement difficile entre l'émetteur et le récepteur. Pour régler ce problème, on a proposé une approche de formation de faisceau à l'aide d'un réseau d'antennes à commande de phase. Cette approche consiste à utiliser des résonateurs en forme de H chargés afin d'altérer la réponse en phase dans la bande de 57 à 64 GHz. Apres l'intégration d'un réseau des résonateurs en forme de H chargés à une antenne dipôle classique, le faisceau rayonnant de l'antenne est dévié dans le plan électrique de 26 degrés. Pour réaliser une commutation de faisceau, une autre antenne dipôle a été incorporée de l'autre coté des cellules unitaires en milieu à gradient d'indice de réfraction. Par excitation d'une ligne d'alimentation propre à l'antenne, le faisceau de rayonnement peut être commuté de -26 à 26 degrés. Les résultats de mesures montrent qu'en utilisant cette technique, le faisceau de rayonnement peut être balayé de -58 à +58 degrés dans la bande de 57 à 64 GHz. Le gain d'antenne au moment du balayage du faisceau est 9,5 dBi à 63 GHz.

Pour obtenir un angle d'inclinaison plus grand et un gain plus élevé, un réseau des cellules unitaires à mu-proche de zéro créé par un résonateur à fente annulaire a été proposé. L'intégration d'un réseau des inclusions à mu-proche de zéro à hors-axe de l'antenne dipôle dans le plan azimutal et plan d'élévation a permis d'obtenir un angle d'inclinaison de 35 degrés et un gain élevé de 8dBi. En fait, cette technique indique que

le balayage du faisceau bidimensionnel peut être réalisé avec un gain maximal de 14,3 dBi à 60GHz.

L'antenne à ondes de fuite est une autre technique efficace pour créer un rayonnement à double faisceaux. En fait, le rayonnement à double faisceaux peut être déployé pour les applications dans les réseaux locaux sans fil en ondes millimétriques pour améliorer la qualité de transmission. Toutefois, le rayonnement de l'antenne à ondes de fuite est modifié par la fréquence, cela limite son application. Alors, cette thèse propose une nouvelle technique pour réaliser un rayonnement à double faisceaux avec une antenne à faisceau fixe opérand dans la bande de 57 à 64 GHz. Ceci a été possible par l'intégration d'un réseau de cellules unitaires en forme de H chargés devant une antenne nœud papillon. Les résultats indiquent que le faisceau rayonnant dans le plan électrique est dirigée à +30 et -30 degrés par rapport au rayonnement longitudinal dans la bande de 57 à 64 GHz.

11.9.1 Travaux Futures

Comme indique ci-dessus, l'inclinaison de faisceau dans le plan azimutal et le plan d'élévation peut être réalisée à l'aide d'un réseau des cellules unitaires en métasurface et métamatériau. Pour commuter le faisceau rayonnant, c'est nécessaire d'intégrer un commutateur SP4T à la ligne d'alimentation. Le commutateur SP4T n'a pas été utilisé par la recherche susmentionnée faute de temps, mais c'était indiqué qu'on peut l'ajouter. Donc, la commutation électronique a besoin d'être étudiée afin de déterminer la façon dont le commutateur peut affecter l'angle d'inclinaison et les performances de l'antenne. En plus, l'étude paramétrique effectuée indique que l'augmentation de nombre des cellules unitaires à la direction voulue conduit à l'augmentation de l'angle d'inclinaison. Il serait intéressant d'intégrer les diodes PIN ou varactor aux cellules unitaires pour contrôler la direction de l'angle d'inclinaison et sa largeur de faisceau. Cela permettrait de développer une antenne dont le diagramme de rayonnement peut être

électroniquement reconfiguré dans tous les deux plans. Dans le Chapitre 5, une antenne en forme de nœud papillon à gain élevé a été appliquée en utilisant d'une antenne simple à un gain maximal de 12,3 dBi dans la bande de 57 à 64 GHz. Pour obtenir un gain plus élevé jusqu'à 18 dBi, c'est intéressant de voir comment ca peut être réalisé en utilisant plusieurs nombres de réseaux.

REFRENCES

[1] I. Kim, Y. Rahmat-Samii, "Electromagnetic band gap-dipole sub-array antennas creating an enhanced tilted beams for future base station," *IET Microw. Antennas Propag*., vol. 9, no. 4, pp. 319–327, 2015.

[2] R.A. Shelby, D.R. Smith, and S. Schultz, "Experimental verification of a negative index of refraction," Science, vol. 292, no. 5514, pp.77–79, 2001.

[3] A.Mehdipour, G.V.Eleftheriades, "Leaky-wave antennas using negative refractive index transmission line metamaterial supercells," I*EEE Trans. Antennas.and Prpagation*., vol.62, no.8, pp. 3929-3942, Feb. 2013.

[4] T. Jiang, Z.Y. Wang, D. Li, J.N. Pan, B. Zhang, "Low-DC voltage controlled steering-antenna radome utilizing tunable active metamaterial, " IEEE Trans. Microw. Theory Tech., vol.61, no.2, pp. 979-985, Feb. 2013

[5] J. R. Costa, E. B. Lima, and C. A. Fernandes, "Compact beam-steerable lens antenna for 60-GHz wireless communications," IEEE Trans. Antennas Propag., vol. 57, no. 10, pp. 2926–2933, Oct. 2009

[6] S. Lim, C. Caloz, and T. Itoh, "Metamaterial-based electronically-controlled transmission line structure as a novel leaky-wave antenna with tunable radiation angle and beamwidth," *IEEE Trans. Microw. Theory Tech*., vol.53, no.1, pp.161-173, Jan.2005

[7] J.J. Luther, S. Ebadi, and X. Gong, "A Microstrip Patch Electronically Steerable Parasitic Array Radiator (ESPAR) Antenna With Reactance-Tuned Coupling and Maintained Resonance," *IEEE Trans. Antennas Propagat.*, vol.60, no.4, pp.1803-1813, Sep.2012.

[8] E.R. Brown, "RF-MEMS Switches for Reconfigurable Integrated Circuits," *IEEE Trans. Microw. Theory Tech*., vol.46, no.11, pp.1868-1880, Nov.1998.

[9] J. Huang and A.C. Densmore, "Microstrip Yagi Antenna for Mobile Satellite Vehicle Application," *IEEE Trans. Antennas Propagat*., vol.39, no.7, pp.1024–1030, Jul. 1991.

[10] D.F. Filipovic, G.P. Gauthier, S. Raman, and G.M. Rebeiz, “Off-Axis Properties of Silicon and Quartz Dielectric Lens Antennas,” *IEEE Trans. Antennas Propagat.*, vol.45, no.5, pp. 760–766, May 1997.

[11] D-J. Kim and J-H. Lee, “Beam Scanning Leaky-Wave Slot Antenna Using Balanced CRLH Waveguide Operating above the Cutoff Frequency,” *IEEE Trans. Antennas Propagat.*, vol.61, no.5, pp. 2432–2440, May 2013.

[12] Marco A. Antoniades, and George V. Eleftheriades, “Multiband Compact Printed Dipole Antennas Using NRI-TL Metamaterial Loading,” *IEEE Trans. Antennas Propagat.*, vol.60, no.12, pp. 5613-5626, Dec. 201

[13] D. Li, Z. Szabó, X. Qing, E-P. Li, and Z. Chen, “A High Gain Antenna with an Optimized Metamaterial Inspired Superstrate,” *IEEE Trans. Antennas Propagat.*, vol.60, no.12, pp. 6018-6023, Dec. 2012.

[14] U.C. Hasar, and J.J. Barroso, “Permeability Measurement of Metamaterials with Split-Ring-Resonators Using Free-Space Calibration-Independent Methods," *Journal of Infrared, Millimeter, and Terahertz Waves,* vol.33, no.2, *pp.218*-227, Feb. 2012.

[15] X. Chen, T.M. Grzegorczyk, B.I. Wu, J. Pacheco Jr., and J.A. Kong, "Robust Method to Retrieve the Constitutive Effective Parameters of Metamaterials," *Phys. Rev. Lett.*, E 70, 016608, 2004.

[16] C.A. Balanis, Antenna Theory: Analysis and Design, 3rd ed. Nwe York: Wiley, 2005.

[17] R. Liu, C. Ji, J.J. Mock, J.Y. Chin, T.J. Cui, and D.R. Smith, “Broadband Ground-Plane Cloak,” *Science*, vol.323, no.5912, pp.366-369, Jan. 2009.

[18] S.-W. Qu, J.-L. Li, Q. Xue, and C.-H. Chan, “Wideband Periodic End- Fire Antenna with Bowtie Dipoles,” *IEEE Antennas Wireless Propag. Lett.*, vol.7, pp. 314–317, 2008.

[19] E. Öjefors, S. Cheng, K. From, I. Skarin, P. Hallbjörner, and A. Rydberg, “Electrically steerable single-layer microstrip traveling wave antenna with varactor diode based phase shifters,” IEEE Trans. Antennas Propag., vol. 55, no. 9, pp. 2451–2460, Sept. 2007.

[20] J. Schoebel et al., “Design considerations and technology assessment of phased-array antenna systems with RF MEMS for automotive radar applications,” IEEE Trans. Microw. Theory Tech., vol. 53, no. 6, pp. 1968–1975, Jun. 2005

[21] A. Dadgarpour, B. Zarghooni, B.S. Virdee, T.A. Denidni, “Beam tilting antenna using integrated metamaterial loading,” IEEE Trans. Antennas Propagat., vol.62, no.5, pp. 2874-2879, May 2014.

[22] A. Dadgarpour, B. Zarghooni, B.S. Virdee, T.A. Denidni, “Beam deflection using gradient refractive index media for 60 GHz end-fire antenna,” IEEE Trans. Antennas Propagat., vol. 63, no.8, pp.3768–3774, Aug. 2015.

[23] A. Dadgarpour, B. Zarghooni, B.S. Virdee, T.A. Denidni,“Improvement of gain and elevation tilt-angle using metamaterial loading for millimeter-wave applications,” IEEE Antennas and wireless propagation letters. Early access.

[24] J.D. Baena, L. Jelinek, and R. Marqués, “Towards a systematic design of isotropic bulk magnetic metamaterials using the cubic point groups of symmetry,” Phys. Rev. B, vol. 76, no. 24, pp. 245115/1–245115/14, Dec. 2007.

[25] J. Wu, Z. Zhao, Z. Nie, and Q-H. Liu, “Design of a wideband planar printed quasi-yagi antenna using stepped connection structure,” IEEE Trans. Antennas Propagat., vol.62, no.6, pp. 3431-3435, June 2014.

[26] D. Sugimura, M. Arai, K. Sakaguchi, K. Araki, T. Sotoyama, “A study on beam tilt angle of base station antennas for base station cooperation systems,” *IEEE 22nd International Symposium on Personal Indoor and Mobile Radio Communications,* pp. 2374-2378, 2011.

[27] J.J. Macial, J.F. Slocum, J.K. Smith, J. Turtle, “MEMS electronically steerable antennas for fire control radars,” *Proc. IEEE Radar Conf.*, pp. 677–682, 2007.

[28] S. Zhang, G.H. Huff, J. Feng, J.T. Bernhard, “A pattern reconfigurable microstrip parasitic arrays,” *IEEE Trans. Antennas Propagat.*, vol. 52, no.10, pp. 2773–2776, Oct. 2004.

[29] C-H. Ko, K.M.J. Ho, G.M. Rebeiz, “An electronically-scanned 1.8–2.1 GHz base-station antenna using packaged high-reliability RFMEMS phase shifters,” *IEEE Trans. Microw. Theory Tech.*, vol.61, no.2, pp. 979-985, Feb. 2013.

[30] C. Pfeiffer and A. Grbic, “A printed, broadband Luneburg lens antenna,” IEEE Trans. Antennas Propagat., vol. 58, no. 9, pp. 3055–3059, Sep. 2010

[31] L. Xue and V. Fusco, “Patch fed planar dielectric slab waveguide extended hemielliptical lens antenna,” IEEE Trans. Antennas Propagat., vol. 56, no. 3, pp. 661–666, Mar. 2008.

[32] I. Kim, Y. Rahmat-Samii, “Beam-Tilted Dipole-EBG Array Antenna for Future Base Station Applications,” *IEEE Antennas and propagation society International Symposium*, 2013.

[33] T. Debogović, J. Perruisseau-Carrier, “Array-Fed Partially Reflective Surface Antenna with Independent Scanning and Beamwidth Dynamic Control,” *IEEE Trans. Antennas Propagat.*, vol. 62, no. 1, pp. 446–449, Jan. 2014

[34] Z. Szabó, P.G. Ho, R. Hedge, E.P. Li, “A unique extraction of metamaterial parameters based on Kramers-kronig relationship,” IEEE Trans. Microw. Theory Tech., vol.58, no.10, pp.2646-2653, Oct.2010

[35] H-L. Wang, Y-X. Guo, W-X. Sheng, “Wideband high-gain 60-GHz LTCC L-probe patch antenna array with a soft surface," IEEE Trans. Antennas Propagat., vol.61, no.1, pp.153-161, Jan.2013.

[36] H.Chu, Y-X Guo, Z.Wang, “60-GHz LTCC wideband vertical off-center dipole antenna and arrays," IEEE Trans. Antennas Propagat., vol.61, no.1, pp.153-161, Jan.2013.

[37] K. Gong, Z.N. Chen, X. Qing, P. Chen, W. Hong, “Substrate integrated waveguide cavity-backed wide slot antenna for 60-GHz bands,” IEEE Trans. Antennas Propagat., vol.60, no.12, pp.6023-6026, Dec.2012.

[38] S.B. Yeap, Z.N. Chen, X. Qing, “Gain-enhanced 60-GHz LTCC antenna array with open air cavities,” IEEE Trans. Antennas Propag.,vol.59, no.9, pp.3470–3473, Sep. 2011.

[39] Y. She, R. Fujino, J. Hirokawa, M. Ando, D. Hanatani, M. Fujimoto, “LTCC oversized rectangular waveguide slot array antenna with air-layer in the radiating part in the millimeter-wave band,” IEEE Trans. Antennas Propag.,vol.61, no.4, pp.1777–1783, April. 2013.

[40] J. Xu, Z.N.Chen, X.Qing, W.Hong, "Bandwidth enhancement for a 60 GHz substrate integrated waveguide fed cavity array antenna on LTCC," IEEE Trans. Antennas Propag., vol.59, no.3, pp.826–832, March. 2011.

[41] K-S. Chin, W. Jiang, W. Che, C-C. Chang, H. Jin, "Wideband LTCC 60-GHz antenna array with a dual-resonant slot and patch structure," IEEE Trans. Ant. Propagat., vol. 62, no. 1, pp. 174-182, Jan. 2014.

[42] D. Wang, K.B. Ng, C.H. Chan, H. Wong, "A novel wideband differentially-fed higher-order mode millimetre-wave patch antenna," IEEE Trans. Antenna Propagat., vol. 63, no. 2, pp. 174-182, Feb. 2015.

[43] Y. Li, Z.N. Chen, X. Qing, Z. Zhang, J. Xu, Z. Feng, "Axial ratio bandwidth enhancement of 60-GHz substrate integrated waveguide-fed circularly polarized LTCC antenna array," IEEE Trans. Antennas Propagat., vol. 60, no. 10, pp. 4619-4626, Oct. 2012.

[44] M.J.Al-Hasan,T.A.Denidni, A.R.Sebak, "Millimeter-wave EBG-based aperture-coupled dielectric resonator antenna," IEEE Trans. Antennas Propagat., vol.61, no.8, pp.4354-4357, August 2013.

[45] M. Sun, Z.N. Chen,X.Qing, "Gain enhancement of 60-GHz antipodal tapered slot antenna using zero-index metamaterial," IEEE Trans. Antennas Propagation., vol.61, no.4, pp.1741–1746, April 2013

[46] G.H. Zhai,W. Hong, K. Wu, Z.Q. Kuai, "Wideband substrate integrated printed log-periodic dipole array antenna," IET Microwave Antennas Propagat., vol.61, no.6, pp.3009-3016, Feb 2010.

[47] R. Marqués, F. Mesa, J. Martel, and F. Medina, "Comparative analysis of edge- and broadside-coupled split ring resonators for metamaterial design-theory and experiments," IEEE Trans. Antennas Propag., vol. 51, no. 10, pp. 2572–2581, Oct. 2003

[48] R. Liu, A. Degrion, J.J. Mock, and D.R. Smith, "Negative index material composed of electric and magnetic resonators," Appl.Phys.Lett.,vol. 90, no. 26, Jun. 2007.

[49] X. Chen, T.M. Grzegorczyk, B.I. Wu, J. Pacheco Jr., J.A. Kong, "Robust method to retrieve the constitutive effective parameters of metamaterials," Phys. Rev. Lett., E 70, 016608, 2004.

[50] R.A. Alhalabi, G.M. Rebeiz, “High-gain Yagi-Uda antennas for millimeter-wave switched-beam systems,” IEEE Trans. Antennas Propagat., vol.57, no.11, pp.3672-3676, Nov. 2009.

[51] N. Celik, M.F. Iskander, R. Emrick, S.J. Franson, J. Holmes, “Implementation and experimental verification of a smart antenna system operating at 60 GHz band,” IEEE Trans. Antennas Propag., vol.56, no.9, pp.2790-2800, Sep. 2008.

[52] G. Grosskopf, R. Eggemann, H. Ehlers, A. Kortke, et al., “Maximum directivity beam-former at 60 GHz with optical feeder,” IEEE Trans. Antennas Propag., vol.51, no.11, pp.3040-3046, Nov. 2003.

[53] P. Deo, D. Mirshekar-Syahkal, L. Seddon, S.E. Day, F.A. Fernández, “60 GHz liquid crystal phased array using reflection-type phase shifter,” European conf. on Antennas and Propag., pp. 927-929, April 2013.

[54] C-H. Tseng, C-J. Chen, T-H. Chu, “Alow-cost 60-GHz switched-beam patch antenna array with butler matrix network,” IEEE Antennas and Wireless Propagation Letters, vol.7, pp.432-435, 2008.

[55] H. Chu, Y-X. Guo, Z. Wang “60-GHz LTCC wideband vertical off-center dipole antenna and arrays,” IEEE Trans. Antennas Propagat., vol.61, no.1, pp.153-161, Jan. 2013.

[56] W.F. Moulder, W. Khalil, J.L. Volakis, “60-GHz two-dimensionally scanning array employing wideband planar,” IEEE Antennas and Wireless propagation letters, vol.9, pp.818-821, 2010.

[57] Md. R. Islam, and M. Ali, “A 900 MHz beam steering parasitic antenna array for wearable wireless applications,” IEEE Trans. Antennas Propag., vol. 61, no. 9, pp.4520-4527, Sept. 2013.

[58] A. Artemenko, A. Maltsev, A. Mozharovskiy, A. Sevastyanov, V. Ssorin, R. Maslennikov, “Millimeter-wave electronically steerable integrated lens antennas for WLAN/WPAN applications,” IEEE Trans. Antennas propagat., vol.61, no.4, pp. 1665-1671, Apr. 2013.

[59] D.F. Filipovic, G.P. Gauthier, S. Raman, and G.M. Rebeiz, "Off-axis properties of silicon and quartz dielectric lens antennas," IEEE Trans. Antennas Propag., vol. 45, no. 5, pp. 760–766, May 1997.

[60] A.J. Guntapalli, T. Dejerafi, K. Wu, "Two dimensional scanning antenna array driven by integrated waveguide phase shifter," IEEE Trans. Antennas Propagat., vol.62, no.3, pp. 1117-1123, March 2014.

[61] N. Yu, P. Genevet, M.A. Kats, F. Aieta, J.P. Tetienne, et al., "Light propagation with phase discontinuities: Generalized laws of reflection and refraction," Science, vol. 334, pp. 333-337, Oct. 2011.

[62] A.Dadgarpour, B.Zarghooni, B. S.Virdee, T. A.Denidni, "Millimeter-Wave High-Gain SIW End-Fire Bow-tie Antenna," IEEE Trans. on Antennas and Propagation, vol. 63, No. 5, pp. 2337-2342, May. 2015.

[63] K. Hosoya, N. Prasad, K. Ramachandran, N. Orihashi, S. Kishimoto, S. Rampath, K. Maruhashi, "Multiple sector ID capture (MIDC): A Novel beamforming technique for 60 GHz band multi-Gbps WLAN/PAN systems," IEEE Trans. on Antennas and Propagation, vol. 63, No. 1, pp. 81-96, Dec. 2014.

[64] A. Artemenko, A. Maltsev, R. Maslennikov, A. Sevastyanov, V. Ssorin, "Beam steerable quartz integrated lens antenna for 60 GHz frequency band," European Conference on Antennas and Propagation, pp. 758- 762, 2011.

[65] G. M. Rebeiz, "Millimeter-wave and terahertz integrated circuit antennas," Proc. IEEE, vol. 80, no. 11, pp. 1748–1770, Nov. 1992.

[66] Y.J. Cheng, W. Hong, K. Wu, "Millimeter-wave multibeam antenna based on eight-port hybrid," *IEEE Microwave and Wireless components letters*, vol.19, no.4, pp. 212-214, Apr 2009.

[67] A.B.Guntupalli,Ke Wu, "Phase-steered fixed beams in one and two-dimensional scan space for substrate-integrated radar and radio systems at 60 GHz," *IET Microwaves, Antennas&propagation.* vol.8, no.11, pp. 819-828, Mar. 2014.

[68] H. Tanaka, T. Ohira, "A single-planar integrated self-heterodyne receiver with a built-in beam steerable array antenna for 60-GHz-band video transmission systems," *IEEE MTT-S Int. Microw. Symp.Dig.*J., vol.2, pp. 735–738, June 2004

[69] C.E. Patterson, W.T. Khan, G.E. Ponchak, G.S. May, J. Papapolymerou, "A 60-GHz active receiving switched-beam antenna array with integrated butler matrix and GaAs amplifiers," *IEEE Trans. Microw. Theory Tech.*, vol.60, no.11, pp. 3599-3607, Nov. 2012.

[70] H. Chu, Y-X. Guo, Z. Wang "60-GHz LTCC wideband vertical off-center dipole antenna and arrays," *IEEE Trans. Antennas Propagat.*, vol.61, no.1, pp. 153-161, Jan. 2013.

[71] Y.J. Cheng, X.Y. Bao, Y.X. Guo "60-GHz LTCC miniaturized substrate integrated multibeam array antenna with multiple polarizations," *IEEE Trans. Antennas Propagat.*, vol.61, no.12, pp. 5958-5967, Dec. 2013.

[72] A. Dadgarpour, B. Zarghooni, B.S. Virdee, T.A. Denidni, "Enhancement of Tilted-beam in Elevation Plane for Planar End-Fire Antennas using Artificial Dielectric Medium," accepted by IEEE Trans. Antennas Propagat.

[73] X. Wu, G. V. Eleftheriades, and T. E. van Deventer-Perkins, "Design and characterization of a single- and multiple-beam millimeter-wave circularly polarized substrate lens antennas for wireless communications," IEE

[74] O. Lafond, M. Himdi, H. Merlet, P. Lebars, "An active reconfigurable antenna at 60 GHz Based on plate Inhomogeneous lens and feeders," IEEE Trans. Antennas propagat., vol.61, no.4, pp. 1672-1678, Apr. 2013

[75] B. Schoenlinner, X. Wu, J. P. Ebling, G. V. Eleftheriades, and G. M. Rebeiz, "Wide-scan spherical-lens antennas for automotive radars," IEEE Trans. Microw. Theory Tech., vol. 50, no. 9, pp. 2166–2175, Sep. 2002

[76] A.B.Guntupalli, T. Djerafi, Ke Wu, "Two-dimensional scanning antenna array driven by integrated waveguide phase shifter," IEEE Trans. Antennas propagat., vol.62, no.3, pp. 1117-1123, Mar. 201

[77] W. Choi, K. Park, Y. Kim, K. Kim,Y. Kwon, "A V-band switched beam-forming antenna module using absorptive switch integrated with 4×4 butler matrix in 0.13-μm CMOS," IEEE Trans. Microw. Theory Tech., vol.58, no.12, pp. 4052-4059, Dec. 2010.

[78] W. Hong, A. Goudelev,K-H. Baek, V.A. Rkhipenkov, J. Lee, "24-element antenna-in-package for stationary 60-GHz communication scenarios," IEEE Microwave and Wireless components letters, vol.21, no.3, pp.142-144, March2011

[79] Y. Li, M.F. Iskander, Z. Zhang, Z. Feng, "A new low cost leaky wave coplanar waveguide continuous transverse stub antenna array using metamaterial-based phase shifters for beam steering," IEEE Trans. Antennas propagat., vol.61, no.7, pp. 3511-3518, July. 2013

[80] H. Attia, L. Yousefi, M.M. Bait-Suwailam, M.S. Boybay, O.M. Ramahi, "Enhanced-gain microstrip antenna using engineered magnetic superstrates," IEEE Ant. and Wireless Propag. Letters, vol.8, no., pp.1198-1201, 2009

[81] J.P. Turpin, Q. Wu, D.H. Werner, B. Martin, M. Bray, and E. Lier, "Low cost and broadband dual-polarization metamaterial lens for directivity enhancement," IEEE Trans. Antennas Propag., vol. 60, no. 12, pp. 5717-5726, Dec. 2012.

[82] A. Erentok, P. L. Luljak, and R. W. Ziolkowski, "Characterization of a volumetric metamaterial realization of an artificial magnetic conductor for antenna applications," IEEE Trans. Antennas Propag., vol. 53, pp. 160–172, Jan. 2005.

[83] K. Li, M. Ingram, and E. Rausch, "Multi beam antennas for indoor wireless communications," IEEE Trans. Comm., vol. 50, no. 2, Feb. 2002.

[84] R.A. Alhalabi, Y.-C. Chiou, and G. M. Rebeiz, "Self-shielded high-efficiency Yagi-Uda antennas for 60 GHz communications," IEEE Trans. Antennas Propag., vol. 59, no. 3, pp. 742–750, 2011

[85] S. Jafarlou, M. Bakri-Kassem, M. Fakharzadeh, Z. Sotoodeh, S. Safavi-Naeini, "A wideband CPW-fed planar dielectric tapered antenna with parasitic elements for 60-GHz integrated application," IEEE Trans. Antennas Propag., vol. 62, no. 12, pp. 6010–6018, Dec 2014.

[86] A. Dadgarpour, B. Zarghooni, B.S. Virdee, T.A. Denidni,"Improvement of gain and elevation tilt-angle using metamaterial loading for millimeter-wave applications," IEEE Antennas and Wireless Propagation Letters. Early access.

[87] A. Dadgarpour, B. Zarghooni, B.S. Virdee, T.A. Denidni, "High gain end-fire bow-tie antenna using artificial dielectric layers," IET Microw. Antennas Propag., May 2015.

[88] S-G. Kim and K. Chang, “Independently controllable dual-feed dual-beam phased array using piezoelectric transducers,” IEEE Antennas and Wireless Propagation Letters. vol.1, pp.81–83, 2002.

[89] A. Mehdipour and G.V. Eleftheriades, “Leakywave antennas using negative refractive-index transmission-line (NRI-TL) metamaterial supercells”, IEEE Trans. Antennas Propag., DOI 10.1109/TAP.2014.2322882.

[90] A. Mehdipour, J.W. Wong, and G.V. Eleftheriades, “Beam-squinting reduction of leaky-wave antennas using Huygens metasurfaces,” IEEE Trans. Antennas Propag., vol. 63, no. 3, pp. 978–992, March. 2015.

[91] W. Cao, W. Hong, Z.N. Chen, B. Zhang, and A. Liu, “Gain enhancement of beam scanning substrate integrated waveguide slot array antennas using a phase-correcting grating cover,” IEEE Trans. Antennas Propagat., vol.62, no.9, pp. 4584–4591, Sep. 2014

[92] T-L. Chen and Y-D. Lin, “Dual-beam microstrip leaky-wave array excited by aperture-coupling method,” IEEE Trans. Antennas Propagat., vol.51, no.9, pp. 2496–2498, Sep. 2003

[93] Z.L. Ma and L.J. Jiang, “One-dimensional triple periodic dual-beam microstrip leaky-wave antenna,” IEEE Antennas and Wireless Propagation Letters. vol.14, 2015

[94] C-C. Hu, C.F. Jou, and J-J. Wu “An aperture-coupled linear microstrip leaky-wave antenna array with two-dimensional dual-beam scanning capability,” IEEE Trans. Antennas Propag., vol. 48, no.6, pp. 909–913, Jun. 2000.

[95] A. Khidre, K-F. Lee, A.Z. Elsherbeni, and F. Yang, “Wide band dual-beam u-slot microstrip antenna,” IEEE Trans. Antennas Propagat., vol.61, no.3, pp. 1415-1418, March. 2013.

[96] A. Amadjikpe, D. Choudhury, C. Patterson, B. Lacroix, G. Ponchak, and J. Papapolymerou, “Integrated 60-GHz antenna on multilayer organic package with broadside and end-fire radiation,” IEEE Trans. Microw. Theory Tech., vol. 61, no. 1, pp. 303–315, Jan. 2013.

[97] K.M.K.H. Leong, Y. Qian, and T. Itoh, "Surface wave enhanced broadband planar antenna for wireless applications," IEEE Microw. Wireless Compon. Lett., vol. 11, no. 2, pp. 62–64, Feb. 2001.

[98] N.G. Alexopoulos, P.B. Katehi, and D.B. Rutledge, "Substrate optimization for integrated circuit antennas," IEEE Trans. Microw. Theory Techn., vol. MTT-31, no. 7, pp. 550–557, Jul. 1983.